THÈSE

Pour obtenir le grade de

DOCTEUR DE L'UNIVERSITÉ GRENOBLE ALPES

École doctorale : CSV- Chimie et Sciences du Vivant
Spécialité : Biologie Structurale et Nanobiologie
Unité de recherche : Institut de Biologie Structurale

Distribution et dynamique nucléaire de l'ADN glycosylase NTH1 avant et après un stress oxydant

Nuclear distribution and dynamics of the NTH1 DNA glycosylase before and after oxidative stress

Présentée par :

Mrinalini Lianne RAO

Direction de thèse :

Fabienne HANS MAITRESSE DE CONFERENCES HDR, UNIVERSITE GRENOBLE ALPES	Directrice de thèse
Joanna TIMMINS DIRECTRICE DE RECHERCHE, CNRS DELEGATION ALPES	Co-directrice de thèse

Rapporteurs :

Sébastien HUET
PROFESSEUR DES UNIVERSITES, Université de Rennes
Anna CAMPALANS
DIRECTRICE DE RECHERCHE, CEA centre de Paris-Saclay

Thèse soutenue publiquement le **1 décembre 2025**, devant le jury composé de :

Virginie FAURE, PROFESSEURE DES UNIVERSITES, Université Grenoble Alpes	Présidente
Fabienne HANS, MAITRESSE DE CONFERENCES HDR, Université Grenoble Alpes	Directrice de thèse
Joanna TIMMINS, DIRECTRICE DE RECHERCHE, CNRS délégation Alpes	Co-directrice de thèse
Sébastien HUET, PROFESSEUR DES UNIVERSITES, Université de Rennes	Rapporteur
Anna CAMPALANS, DIRECTRICE DE RECHERCHE, CEA centre de Paris-Saclay	Rapporteure
Judith MINE-HATTAB, CHARGEE DE RECHERCHE HDR, CNRS délégation Paris Centre	Examinatrice

Acknowledgments

Aboard the S.S. PhD battleship, for 3 years, I've navigated treacherous waters—from long days at the lab bench and late-night microscopy acquisitions to the exhilaration of unexpected discoveries. The twists and turns on this voyage taught me resilience, patience, and the importance of a strong crew — mentors, colleagues, friends, and family — without whom this journey would not have reached its harbor.

To my captains, my supervisors, Dr. Fabienne Hans and Dr. Joanna Timmins: thank you for steering me through the vast ocean of scientific discovery and nurturing my growth as an independent researcher. Fabienne, I am grateful for our moments at the lab bench, in the microscopy room, over data analysis, and the occasional aperitif. Your inquisitive nature fueled my curiosity and your support sustained my motivation. Joanna, I deeply value your patience, support, and admirable leadership. Your guidance and perspective inspired me to persevere and keep growing as a scientist and individual.

My sincere gratitude to my thesis jury members – Dr. Anna Campalans, Dr. Sébastien Huet, Dr. Judith Miné-Hattab and Dr. Virginie Faure, for taking your time in evaluating my Thesis Manuscript and attending my PhD Defense. My heartfelt gratitude to my CSI committee jury – Dr. Olivier Destaing, Dr. Karine Monier and Dr. Jean Breton, for your profound advise and guidance. I will always go by the motto 'Work hard, play hard'.

To my crew — the I2SR team, past and present — thank you. You have been my second family and I'm extremely grateful to have had the pleasure of working and interacting with each of you. Special thanks to Pierre Caron for your constant guidance and countless corridor discussions, and to Ahmad for your friendship and conversations. I am equally grateful to the GenOM team — Mohammad, Pierre Vauclare, Salva, Marjolaine, Jason, Loic and past M2 students — for your camaraderie.

Sasha and Jean-Philippe from the M4D platform, thank you for patiently answering my endless questions and navigating through long microscopy sessions and data analysis with good humor.

My fondest memories lie with the PIXEL team. Thank you to all the alumni members –Pascale, Angela, Arijit and Virgile. Special thank you to Pascale and Philippe (my M2 supervisor) for all your help and advise. I'll never forget the inspiring photophysics lunch discussions with Dominique and Jip, and the colourful conversations with Jérémy, Quentin, Oarii, and Ludwig. Your support and friendship will always be cherished, along with our lively coffee breaks.

To my IBS colleagues and friends — Espérance, Mai, Soumiya, Rebecca, Poushalee, Shivangi, Varun, Audrey, Céline, Borys, Andrea, and Rory — thank you for the scientific debates and weekend getaways that brightened many days. Special thanks to Ananya and Khushi, my external PhD squad, for your constant support and our Grenoble adventures.

To my family and friends in India, your love and encouragement carried me through. Thank you, Mom and Dad, for your steady belief in me, and for being my guiding conscience during this journey. Sanchia, ma petite sœur, thank you for holding down the fort at home and cheering me on through countless late-night conversations. I am deeply grateful to my wonderful friends—Andrea Thomas, Bhanu Priya, and Elinda—for their constant support and friendship.

Above all, I thank the Lord, whose invisible hand guided me through this journey and deepened my passion for science and discovery.

'Patience, Perserverence and Passion'

Cheers to the end of a transformative journey & to the beginning of another,

Mrinalini Lianne Rao

Abstract in English

In eukaryotic cells, nuclear DNA is constantly subjected to oxidative stress induced by reactive oxygen species (ROS), produced endogenously or by chemotherapeutic agents like cisplatin. To preserve genome stability, cells have evolved several DNA repair systems, notably the Base Excision Repair (BER) pathway, which eliminates small, non-helical distorting base lesions. BER is initiated by DNA glycosylases that recognize and excise the damaged bases, producing apurinic/apyrimidic sites, which are further processed to ultimately incorporate new and undamaged bases. Our team is particularly interested in NTH1, a bifunctional DNA glycosylase that recognizes and removes oxidized pyrimidines such as thymine glycols. Dysregulation of NTH1 expression or activity can lead to genomic instability and tumorigenesis. This thesis investigates the nuclear distribution and dynamics of NTH1 in cancer cells, before and after exposure to oxidative stress, using advanced fluorescence microscopy techniques, including confocal and single-molecule localization microscopy (SMLM), to achieve high spatial resolution.

For the first time, this study identified two distinct NTH1 populations: a freely diffusive nucleoplasmic pool and a chromatin-associated fraction forming foci. Using direct Stochastic Optical Reconstruction Microscopy (dSTORM, ~10 nm resolution), we further characterized these two populations at nanoscale resolution, revealing the existence of dense chromatin-associated clusters of NTH1 as well as more sparsely distributed NTH1 molecules. The foci observed by confocal microscopy were found to be typically composed of at least two NTH1 clusters. Following oxidative stress, we observed a two phase response. First, immediately after exposure to a strong oxidizing agent, chromatin-associated levels of NTH1 as well as the total number of NTH1 foci and clusters per nucleus were found to decrease. Second, between 4 and 8h post-treatment, chromatin-associated levels of NTH1 along with the number and density of NTH1 foci and clusters increased significantly, suggesting a major re-organization of NTH1 in response to oxidative DNA damage. Single-particle tracking experiments further revealed two populations of NTH1 molecules: (i) a mobile, slow-diffusing population, likely transiently chromatin-bound, whose proportion and diffusion coefficient increased markedly after oxidative stress, before returning to control levels upon recovery and (ii) a largely immobile, likely tightly chromatin-bound, whose diffusion coefficient decreased 4h post treatment. Together, these findings support a change in the mode of diffusion of NTH1 in the nuclear space in response to oxidative DNA damage. Preliminary dual-labelling with chromatin markers and BER factors is underway to further explore foci composition.

Altogether, our work has contributed to a better understanding of the spatial and temporal distribution and dynamics of NTH1, providing insight into the tight regulation of NTH1, in response to oxidative stress.

Résumé en français

Dans les cellules eucaryotes, l'ADN nucléaire est constamment soumis à un stress oxydatif induit par des espèces réactives de l'oxygène (ROS), produites de manière endogène ou par des agents chimiothérapeutiques tels que le cisplatine. Afin de préserver la stabilité du génome, les cellules ont développé plusieurs systèmes de réparation de l'ADN, dont la voie de réparation par excision de bases (BER), qui élimine les petites lésions non hélicoïdales déformant les bases. La BER est initiée par des ADN glycosylases qui reconnaissent et excisent les bases endommagées, produisant des sites apuriniques/apyrimidiques, qui sont ensuite traités pour finalement incorporer de nouvelles bases intactes. Notre équipe s'intéresse particulièrement à la NTH1, une ADN glycosylase bifonctionnelle qui reconnaît et élimine les pyrimidines oxydées telles que les thymine glycols. Une dérégulation de l'expression ou de l'activité de la NTH1 peut entraîner une instabilité génomique et une tumorigenèse. Cette thèse étudie la distribution nucléaire et la dynamique de la NTH1 dans les cellules cancéreuses, avant et après exposition à un stress oxydant, à l'aide de techniques avancées de microscopie de fluorescence, notamment la microscopie confocale et la microscopie de localisation de molécules uniques (SMLM).

Pour la première fois, cette étude a identifié deux populations distinctes de NTH1 : un pool nucléoplasmique et une fraction formant des foyers. À l'aide de la microscopie dSTORM, nous avons caractérisé ces deux populations à une résolution nanométrique, révélant l'existence de clusters de NTH1 associés à la chromatine ainsi que de molécules de NTH1 plus dispersées. Les foyers observés par microscopie confocale se sont avérés être généralement composés d'au moins deux clusters de NTH1. À la suite d'un stress oxydant, nous avons observé une réponse en deux phases. Immédiatement après traitement, les niveaux de NTH1 associés à la chromatine, le nombre total de foyers et de clusters de NTH1 par noyau diminuent. Ensuite, entre 4 et 8 heures après traitement, les niveaux de NTH1, le nombre et la densité des foyers et des clusters de NTH1 augmentent de manière significative, suggérant une rédistribution majeure de NTH1 en réponse aux dommages oxydatifs de l'ADN. Des expériences de sptPALM confirment deux populations de NTH1 : (i) une population mobile, probablement liée de manière transitoire à la chromatine, dont la proportion et le coefficient de diffusion augmentent après un stress oxydant, avant de revenir à son niveau basal, et (ii) une population plus lente, probablement fortement liée à la chromatine, dont le coefficient de diffusion diminue 4 heures après traitement. Ensemble, ces résultats confirment un changement dans le mode de diffusion de NTH1 en réponse aux dommages oxydatifs de l'ADN. Un double marquage préliminaire avec des marqueurs de chromatine et des facteurs BER est en cours afin d'étudier plus en détail la composition des foyers.

Dans l'ensemble, nos travaux contribuent à une meilleure compréhension de la distribution spatiale et temporelle ainsi que de la dynamique de NTH1, indiquant une régulation stricte de NTH1 en réponse au stress oxydant.

Table of Contents

Acknowledgments **2**

Abstract in English **4**

Résumé en français **5**

Abbreviations **10**

List of Figures **14**

List of Tables **19**

Preface **21**

INTRODUCTION **23**

Chapter 1: Chromatin organization and dynamics **24**

1.1 Chromatin organization 24

1.1.1 From nucleosomes to chromosomes 24

1.1.2 Biomolecular condensates 28

1.1.3 Self organization of chromatin 31

1.2 Regulation of chromatin and its dynamic nature 31

Chapter 2: DNA damage and chromatin **33**

2.1 Overview of DNA damage 33

2.2 Oxidative DNA damage 36

2.2.1 Hydrogen peroxide (H_2O_2) 39

2.2.2 Potassium bromate ($KBrO_3$) 40

2.2.3 Cisplatin 40

2.3 DNA damage response 40

2.4 Chromatin response to DNA damage 41

Chapter 3: DNA repair machinery **44**

3.1 Mismatch Repair Pathway 44

3.2 Nucleotide Excision Repair (NER) Pathway 46

3.3 Double strand break (DSB) repair pathways 48

3.3.1 Homologous recombination 49

3.3.2 Non-homologous end-joining (NHEJ) 50

3.3.3 DSB DNA repair foci 51

3.4 Base Excision Repair (BER) Pathway 53

3.4.1 DNA glycosylases 55

3.4.2 Lesion search by DNA glycosylases on chromatin fiber 57

3.4.3 Long and short patch BER 63
3.4.4 Role of PARP proteins in BER 63
3.4.5 Crosstalk between BER with other DNA repair pathways 64

Chapter 4: NTH1 - DNA glycosylase 67
4.1 NTHL1 gene structure and evolutionary conservation 67
4.2 Recognition and excision of DNA damage by NTH1 71
4.2.1 Substrate specificity and catalytic activity 72
4.2.2 NTH1 scanning and lesion accessibility involves chromatin dynamics 74
4.3 Regulation of NTH1 76
4.3.1 Regulation of NTHL1 gene expression 76
4.3.2 Regulation of NTH1 at the protein level 78

AIM OF THE THESIS 82

MATERIALS AND METHODS 83

1. Cell culture, transfections and oxidative treatment 84
1.1 Cell culture 84
1.2 Cell Transfection 84
1.3. Treatment of the cells with oxidizing DNA damaging agents 85
1.4 Cell-cycle measurements by flow cytometry 86

2. Western Blot 87

3. Immunofluorescence 88

4. Sample preparation for microscopy experiments 89
4.1 Immunofluorescence of fixed samples 89
4.2 Living samples 90

5. Microscope setup and data acquisition 90
5.1 Spinning disk confocal fluorescence microscopy 90
5.2 Single molecule localization microscopy (SMLM) 92
5.2.1 Overview of SMLM 92
5.2.2 Principle of SMLM 92
5.2.3 The ABBELIGHT SAFe360 system 94
5.2.4 dSTORM acquisitions 94
5.2.5 spt PALM acquisitions 95

6. Data analysis and statistics 96
6.1 Data analysis of confocal images 96
6.1.1 2D and 3D nuclear segmentation 96
6.1.2 2D NTH1 foci segmentation 96

6.1.3 Fluorescence intensity measurements 97
6.2 dSTORM 98
6.2.1 Reconstruction of super-resolved images 98
6.2.2 Cluster segmentation and quantification 99
6.3 Single Particle Tracking (SPT) PALM 100
6.3.1 Reconstruction of single molecule trajectories 100
6.3.2 Characterization of molecular dynamics from single molecule tracking analysis 102
6.4 spt simulations using SMIS 104
7. Graphs and statistical analysis 104

RESULTS 105

1. Heterogeneous nuclear distribution of NTH1 & existence of two nuclear pools. 106

2. NTH1 displays cell-cycle dependent expression. 108

3. Subcellular fractionation reveals a chromatin-associated NTH1 fraction and a nucleoplasmic NTH1 fraction. 109

4. Effects of various oxidizing agents on the nuclear distribution and abundance of NTH1.. 110
4.1 Cisplatin treatment mildly affects the distribution of NTH1 on chromatin 110
4.2 Hydrogen peroxide treatment increases NTH1 recruitment to chromatin. 114
4.3 $KBrO_3$ treatment increases recruitment of chromatin – associated NTH1 116
4.3.1 Dose-dependent effect of $KBrO_3$ on the survival of HeLa cells 116
4.3.2 Chromatin-associated NTH1 levels are significantly increased in response to $KBrO_3$ treatment. 118
4.3.3 Effects of $KBrO_3$ treatment on NTH1 foci formation. 119

5. Single-molecule localization microscopy reveals NTH1 clusters 122
5.1 Optimization of sample preparation for dSTORM imaging 122
5.2 Nuclear distribution of NTH1 reveals clusters within foci 124
5.3 $KBrO_3$ induces a redistribution and increase in chromatin-associated NTH1 131

6. Investigating the dynamics of NTH1 by single-particle tracking PALM. 136
6.1 Dynamics of NTH1 in untreated HeLa cells 136
6.2 Dynamics of NTH1 in HeLa cells exposed to oxidative stress 142
6.3 Integrating SPT simulations to elucidate NTH1 nuclear dynamics 148

DISCUSSION & PERSPECTIVES 153

DISCUSSION 154

CONCLUSION 162

FUTURE PERSPECTIVES 164
1. NTH1 in the context of BER partners 164
2. NTH1 in the context of chromatin 166

BIBLIOGRAPHY.....172

APPENDICES.....204

Abbreviations

NA Numerical Aperture

2D/ 3D 2 or 3 dimension

3C Chromsome Conformation Capture

3D-SIMS 3d-Structured Illumination Microscopy

6-4 PPs 6,4 – pyrimidine photoproducts

8oxoG 8oxoguanine

ACR ATP dependent chromatin remodelling

ChIP Chromatin immunoprecipitation

ChromEMT Chrom Electron Microscopy Tomography

COMET Cost function Optimized Maximal overlap drift Estimation

COSMIC Catalogue of Somatic Mutations in Cancer

CPDs Cyclobutane Pyrimidine Dimers

CRISPR-dCas9 Clustered Regularly Interspaced Short Palindromic Repeats – dead CRISPR associated protein 9

Dapp Apparent Diffusion coefficient

DDR DNA Damage Response

DNA Deoxyribonucleic acid

DSBs Double Strand Breaks

dSTORM directed Stochastic Optical Reconstruction Microscopy

EM Electron Microscopy

EPI Epifluorescence

F Fractionated

FCS Fluorescence Correlation Spectroscopy

FeSO4 Iron (II) sulphate

FOV Field of View

FRAP Fluorescence Recovery After Photobleaching

FRET-FLIM Förester Resonance Energy Transfer - Fluorescence-lifetime imaging microscopy

FROS Fluorescent Repressor – Operator System

GFP Green Fluorescent Protein

H_2O_2 Hydrogen peroxide

Hi-C High – thoroughput Chromosome Conformation Capture

HiLO Highly Inclined and Laminated Optical

iPALM interferometric Photoactivation Localization Microscopy

IR Ionizing radiation

JD Jump distance

$KBrO_3$ Potassium bromate

kDa kilo Dalton

LLPS Liquid-Liquid Phase Separation

MINFLUX Minimal Emission Fluxes

MJD Mean Jump Distance

MMS Methyl methanosulphate

MSD Mean Squared Displacement

n.a nuclear area

NAD^+ Nicotinamide adenine dinucleotide

NCP Nucleosome Core Particle

NF Non fractionated

NMFI Nuclear Mean Fluorescence Intensity

NT Non Treated

OGG1 8-oxoguanine glycosylase

PAINT Points Accumulation for Imaging in nanoscale Tomography

PALM PhotoActivated Localization Microscopy

PARP Poly (ADP-ribose) polymerase

PCA Point Cloud Analysis

PI – Propidium iodide

PNK Polynucleotide kinase

PRC-2 Polycomb-Repressive Complex 2

PSF Point Spread Function

PTFPs Photo transformable fluorescent proteins

PTM Post translational Modifications

px Pixel

ROI Region of interest

ROS/ RNS Reactive Oxygen Species/ Reactive Nitrogen Species

SA Surface Area

SAM S-adenosylmethionine

SAXS Small Angle X-ray Scattering

SHL Super helical locations

SMC Structural Maintainence of Chromsomes

SMLM Single Molecule Localization Microscopy

SRM Super Resolution Microscopy

SSBs Single Strand Breaks

STED Stimulated Emission Depletion

T0 Treated with 40 mM $KBrO_3$, 0.5h

TADS Topologically Associated Domains

TALE Transcription Activator-like Effector

TDG Thymine DNA glycosylase

Tg Thymine glycol

TIRFM Total Internal Reflection Fluorescence Microscopy

TX Recovery time point

UNG Uracil DNA glycosylase

UV Ultraviolet radiation

List of Figures

Figure 1: 3D hierarchy of chromatin organization, in mammals, at different genomic length scales.. 25

Figure 2: Genome elements brought together or isolated by the cohesin complex and CTCF. 26

Figure 3: Formation of chromatin domains or topological associated domains (TADS) containing multiple loops with clutches of nucleosomes. 27

Figure 4: Different types of phase-separated biomolecular condensates observed within eukaryotic nuclei. 29

Figure 5: Schematic representation of two binding modes observed within biomolecular condensates by phase separation. 29

Figure 6: Generation of reactive oxygen species (ROS) from endogenous and exogenous sources and their effects. 37

Figure 7: Illustration of the mechanism of action of hydrogen peroxide (blue), potassium bromate (green) and cisplatin (red), examples of endogenous and exogenous forms of ROS produced within the nucleus 39

Figure 8: Schematic illustration of the different components of the DNA damage response (DDR). . 41

Figure 9: Chromatin response to DNA damage at the nucleosome level 42

Figure 10: Examples of nuclear condensates with phase separation and their roles in maintaining genome integrity in the event of DNA damage. 43

Figure 11: Proposed model for mismatch repair during DNA replication, in mammalian cells. 45

Figure 12: Nucleotide excision repair in mammalian cells 48

Figure 13: Schematic representation of the canonical steps involved in the two pathways of double stranded break repair (DSB); homologous recombination (HR) and non-homologous end-joining (NHEJ). 49

Figure 14: Proposed model of the formation and development of DNA repair foci in mammalian cells. 52

Figure 15: Simplified schematic representation of the BER pathway in mammalian cells 54

Figure 16: Potential modes of target-site location of bifunctional DNA glycosylases (e.g. OGG1).... 60

Figure 17: Types of post translational modifications (PTMs) observed on DNA glycosylases in response to DNA damage, stimulating various DNA repair pathways..... 62

Figure 18: Schematic representation (linear) of isoform 3 of NTHL1 domain organization. 68

Figure 19: 3D structures of hNTHL1 obtained from X-ray crystallography and AlphaFold predictions. 71

Figure 20: A proposed general scheme of the catalytic activity – N-glycosylase and AP lyase activities of hNTH1. 73

Figure 21: Chromatin dynamics for inward and outward lesion accessibility depending on enzyme-substrate kinetics. 75

Figure 22: (A) Tissue – specific mRNA expression levels of hNTH1 and (B) schematic representation of consequences of dysregulation of NTH, leading to tumorigenesis. 78

Figure 23: Proposed mechanism of crosstalk between hNTH1 and its interaction with some key BER factors, on damaged DNA..... 81

Figure 24: Cartography of the p-mEos4B- NLS (A) and p-NTH1-mEos-4B (B) plasmids. 85

Figure 25: Schematic representation of SMLM (dSTORM and PALM) used in this thesis. 93

Figure 26: The microscopy setup in the M4D platform..... 94

Figure 27: Flowchart for NTH1 foci segmentation optimized for HeLa cells..... 97

Figure 28: Voronoi tessellation analysis performed on reconstructed dSTORM images of HeLa nuclei using the SR-Tesseler algorithm. 100

Figure 29: Flowchart of reconstruction of trajectories from single-molecule localizations. 101

Figure 30: Principle of mean jump distance and MSD analysis for the measurement of diffusion coefficient..... 103

Figure 31: GUI interface of SMIS on the left and the interface for analysing diffusion tracks on the right. 104

Figure 32: Detection of NTH1 by immunolabelling in HeLa cells of immunolabelling NTH1 and verification of labelling efficiency. 107

Figure 33: Expression of NTH1 during the cell cycle using FUCCI HeLa cells..... 108

Figure 34: Isolation of chromatin-bound fraction of NTH1 by in cellulo fractionation. 110

Figure 35: Dose- dependent effect of cisplatin on the nuclear level of NTH1 of HeLa cells..... 111

Figure 36: Comparison of the NTH1 expression levels in non-fractionated (NF) and fractionated (F) HeLa cells treated or not with cisplatin. 113

Figure 37: Increase in chromatin-associated NTH1 levels after treatment with H_2O_2 (-/+) $FeSO_4$. .. 115

Figure 38: $KBrO_3$ treatment effects on the cell cycle and NTH1 chromatin recruitment in HeLa cells. 117

Figure 39: The NTH1 chromatin bound fraction increase after Recovery from an oxidative stress induced by $KBrO_3$ treatment. 119

Figure 40: Effect of $KBrO_3$ on NTH1 foci formation. 120

Figure 41: Buffer combinations and fiducial markers tested for dSTORM. 123

Figure 42: Nuclear distribution of NTH1 in non-fractionated and fractionated HeLa cells, by dSTORM. 125

Figure 43: Voronoi tessellation applied on dSTORM images of NTH1 from fractionated HeLa cells. 126

Figure 44: Characteristics of NTH1 clusters from non-fractionated and fractionated HeLa cells. 128

Figure 45: Characterization of NTH1 clusters based on different density classes. 130

Figure 46: Comparing nuclear localizations inside and outside clusters. 132

Figure 47: Characteristics of cluster features in $KBrO_3$ treated and recovered HeLa cells. 133

Figure 48: $KBrO_3$ effect on the distribution of NTH1 clusters. 134

Figure 49: Characterisation of NTH1 cluster features based on different density classes in cells treated and recovered from $KBrO_3$. 135

Figure 50: Efficiency of NTH1-mEos4B and mEos4B-NLS transfections in HeLa cells..... 137

Figure 51: NTH1-mEos4B and mEos4B-NLS trajectories reconstructed using the Swift software.. 138

Figure 52: Comparison of the number of localizations per nucleus for NTH1-mEos4B and mEos4B-NLS transfected HeLa cells and the proportion of long (>4) tracks in both cases. 139

Figure 53: Mean jump distance (MJD) histograms measured for NTH1-mEos4B and mEos4B-NLS molecules. 140

Figure 54: Apparent diffusion coefficient (D_{app}) histograms measured for NTH1-mEos4B and mEos4B-NLS molecules. 141

Figure 55: Comparing localization properties between non-treated, treated (T0) and 4h recovered NTH1-mEos4B transfected cells. 143

Figure 56: $KBrO_3$ alters the diffusion kinetics of NTH1. 144

Figure 57: Mean jump distance (MJD) histograms of NTH1-mEos4B measured for (A) NT cells, (B) T0 cells and (C) T4 cells. 146

Figure 58: Apparent diffusion coefficient (D_{app}) histograms of NTH1-mEos4B measured in (A) NT, (B) T0 cells and (C) T4 cells. 147

Figure 59: Ground-truth diffusion kinetics for NTH1 simulated in HeLa cell nuclei before and after $KBrO_3$ treatment. 149

Figure 60: Preliminary attempt to reconstruct spt trajectories of diffusing NTH1 inside and outside NTH1 clusters. 150

Figure 61: Exchange rates between two diffusing NTH1 populations 151

Figure 62: Illustration of the nuclear organization and distribution of endogenous NTH1 changes in the distribution and composition of NTH1 clusters in response to oxidative stress. 155

Figure 63: Schematic illustration of diffusion properties of NTH1 in non-treated and $KBrO_3$ treated cells. 160

Figure 64: Illustration of our findings on the nuclear distribution and dynamics of NTH1 before and after oxidative stress..... 163

Figure 65: Co-immunofluorescence of NTH1 and APE1 before and after $KBrO_3$ treatment. 165

Figure 66: Optimization of Histone H3 by confocal and dSTORM, followed by 2-colour imaging strategies with NTH1. 167

Figure 67: Testing compatibility of fractionation step on Histone H3 immunolabelled HeLa cell nuclei. 168

Figure 68. Distribution of NTH1 and chromatin label Janelia 549 by DNA-PAINT. 169

Figure 69. Redistribution of NTH1 and effect of $KBrO_3$ on chromatin. 170

List of Tables

Table 1: Exogenous agents of DNA damage caused by environmental sources. 35

Table 2: Endogenous sources of DNA damage. 36

Table 3: DNA glycosylases of the BER pathway and the major substrates recognized in dsDNA. 56

Table 4: Comparison of characteristic features between NTHL1 orthologs in different species. 69

Table 5: List of concentrations of primary and secondary antibodies. 88

Table 6: (A) Calibrations details of image magnifications used during 3D acquisition of confocal images. (B) Laser properties and power densities used with different magnifications at the sample level during 3D acquisitions of confocal images. 91

Table 7: Hardware configurations and imaging parameters used during acquisitions on the Abbelight Olympus IXE. 95

Table 9: Summary of the characteristics of NTH1 foci obtained from confocal images. 121

Table 10: Comparing the mean and standard deviation of the localization properties between 10 non-fractionated (NF) and 8 fractionated (F) HeLa cells. 125

Table 11: Comparing the mean and standard deviation of the localization properties between non-treated (NT), treated (T0) and cells recovering from treatment at different time points (TX). 131

Table 12: Localization properties of cells transfected with either NTH1-mEos4B (N=10) or mEos4B-NLS (N=3). 138

Table 13: Localization properties of NTH1-mEos4B transfected cells in non-treated (NT), treated (T0) and recovered at 4h time point (T4h). 142

Table 14: Summary of NTH1 foci characteristics. Highlighted in bold italic red are low values and in bold italic green are high values for each parameter. 154

Table 15: Summary of NTH1 cluster characteristics. Highlighted in bold red are low values and in bold italised green are high values for each parameter. 156

Table 16: Summary of sptPALM data recorded for NTH1 molecules in HeLa nuclei before and after exposure to $KBrO_3$. 161

Preface

This thesis presents the aims, methodologies, and findings of my doctoral research on the nuclear distribution and dynamics of the DNA repair protein NTH1, a key glycosylase in the base excision repair (BER) pathway. BER is essential for repairing DNA lesions caused by reactive oxygen species (ROS) and safeguards genomic integrity. Since cancer cells rely on efficient DNA repair mechanisms to sustain uncontrolled proliferation, they provided a model to investigate NTH1's nuclear distribution and dynamic behavior.

To address this, I combined spinning disk confocal microscopy with advanced single-molecule localization microscopy (SMLM), enabling both ensemble-level imaging and nanoscale resolution. This multi-scale approach revealed novel insights into NTH1's nuclear organization and its response to oxidative stress.

The research was carried out at the Institut de Biologie Structurale (IBS) between 2022 and 2025, as part of the DYNAREP project, funded by the Université Grenoble-Alpes – IRGA program. Beyond the scientific outcomes, this thesis also reflects a personal journey: learning to master the challenges of high-resolution imaging, uncovering patterns within complex data, and integrating diverse methods into a coherent understanding of NTH1's role in nuclear DNA repair.

The introduction of this thesis is organized into four chapters. The first outlines the complexity of chromatin organization and nuclear dynamics in mammalian cells. The second explores how nuclear architecture and chromatin remodeling influence DNA repair. The third surveys the major DNA repair pathways, with a particular focus on the BER pathway and its participants. The fourth centers on NTH1, examining its structure, function, and regulation within the nucleus.

The methodology chapter summarizes experimental resources, imaging approaches, and analytical parameters, providing a framework for future studies employing similar strategies. The results are divided into three sections: the first describing the investigations of nuclear NTH1 within HeLa cells, and the second describing NTH1's response to different oxidizing agents. The third section disucsses the results of pilot investigations on NTH1 in broader context of BER enzymes and other DNA repair factors. Finally, the discussion reflects on the implications of these findings, proposes future research directions, and situates our pilot studies within a wider landscape of DNA repair biology.

My hope is that this thesis conveys not only the scientific findings but also the sense of curiosity that guided them. By taking the first steps toward defining a molecular signature of NTH1, through its distribution and dynamics, I aim to contribute to a deeper understanding of genome maintenance and to inspire further research with potential therapeutic implications.

INTRODUCTION

Chapter 1: Chromatin organization and dynamics

Eukaryotic cells face the challenge of compacting their long DNA genomes - 2 meters for a human - into a small nuclear volume – typically around 4200 μm^3 for a nuclear diameter of 10 µm. To make this possible, the genome is highly packaged into chromatin composed of DNA and histone proteins, and adopts a complex 3D architecture, comprising distinct structural domains. The multilayered organization of the chromatin — from chromosome to nucleosomes — critically influences the accessibility of DNA to all types of DNA machinery, including DNA repair factors, thereby modulating the cellular response to DNA damage. Chromatin is indeed a very dynamic and plastic structure, able to remodel and fine-tune its structures to make them compatible with genome activities that occur in a tightly controlled cell type- and cell cycle-dependent manner.

Over the past decade, novel experimental techniques like sequencing, imaging and synthetic biology have provided valuable and detailed insight into the spatio-temporal organization and dynamics of eukaryotic genomes and how this in turn modulates genome activity and cell fate (Johnstone et al., 2020; Misteli, 2020).

1.1 Chromatin organization

1.1.1 From nucleosomes to chromosomes

The first level of organization of the chromatin is the nucleosome or nucleosome core particle (NCP), which is the basic unit of chromatin. Kornberg, first described the NCP to be composed of 8 histones as a repeating unit in chromatin and further named as the 'nucleosome' (Kornberg, 1974; Kornberg & Lorch, 1999; Johnstone et al., 2020). The nucleosome is the focal point of transcription control, gene activation and repression at the promoter level, transcription units and whole chromosome domains.The first crystal structure of NCP showed that the nucleosome is composed of ~146 bp of DNA wrapped in 1.65 left-handed super helical turns around a histone core octamer composed of two H2A–H2B dimers and a H3–H4 tetramer (Luger, 1997), exhibiting a two-fold dyad axis. The amino-terminal tails of the core histones are positively charged and point out of the nucleosome and are subject to many different post translational modifications (PTMs). Individual NCPs are connected by 20-75 bp of linker DNA, interacting with linker histone H1, that "locks" the entry and exit sites of the nucleosomal DNA, each of which are delimitated by histone-DNA major groove contacts called Super Helical Locations (SHLs). Together the nucleosome and the linker DNA form repeating structures of 160-200 bp in a 'beads-on-a-string' arrangement (Kornberg, 1974), which is often referred to as the 10 nm chromatin fiber and was later confirmed by Luger, 1997; Cook & Delaney, 2022; García Fernández et al., 2023.

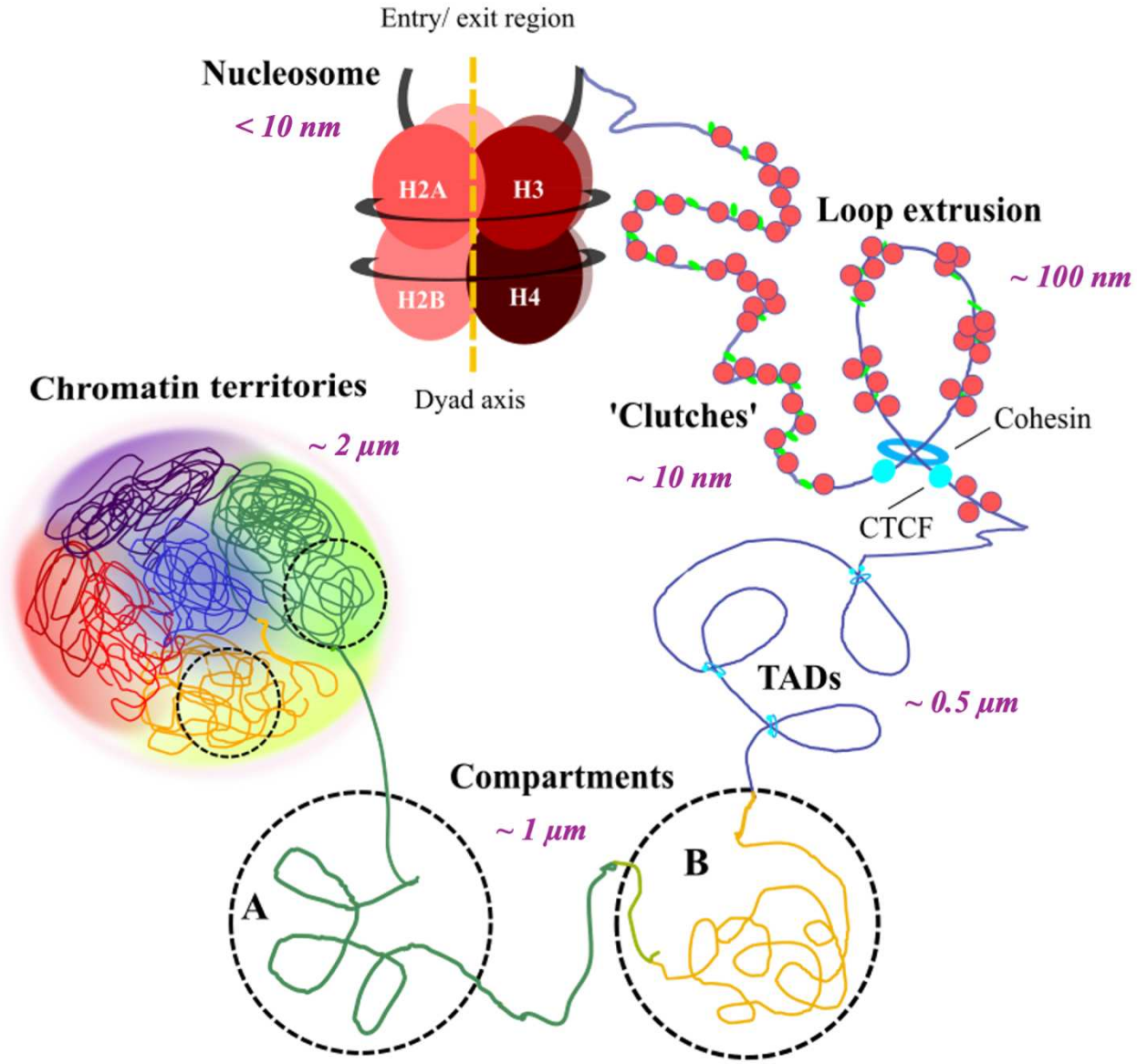


Figure 1: 3D hierarchy of chromatin organization, in mammals, at different genomic length scales. Schematic illustration, adapted from (Johnstone et al., 2020; Hoencamp & Rowland, 2023) of the different orders of DNA packaging, postulated to give rise to chromatin organization in the interphase nucleus. From left to right, the smallest unit of chromatin compaction is the nucleosome (~146 bp), which forms closely spaced heterogeneous clusters known as nucleosome 'clutches' (1-10 kb). These 'clutches' form chromatin loops (10-100 kb) held by the interphase SMC complexes, cohesin and CTCF. These chromatin loops form the base of topological associated domains (TADs)(<1 Mb) and depending on their level of compaction, can give rise to two types of chromatin compartments (> 3 Mb) – A (active) and B (inactive). Individual chromosomes occupy specific regions within the nuclear space, known as chromosome territories (100-3000 Mb).

The 10 nm chromatin fiber was further assumed to fold into compact 30 nm fibers. However, this model is now challenged due to the lack of observations of such fibers *in vivo* on vitrified chromosomes. Instead, the combination of electron microscopy (EM), electron tomography and the DNA labeling method, ChromEMT (ChromEM-tomography), showed chains of nucleosomes grouped without any apparent organization, termed clutches, forming a chromatin fiber with a diameter of ~ 5 to 24 nm (Ricci et al., 2015). This observation was confirmed by the super-resolution microscopy method, dSTORM (directed Stochastic Optical Reconstruction Microscopy), revealing heterogeneous groups of NCPs of varying sizes, interspersed with nucleosome depleted regions (Ricci et al., 2015; Johnstone et al., 2020).

Higher-order chromatin structure has been studied using a combination of state-of-the-art microscopy, biochemistry and genome-wide techniques, such as chromatin conformation capture (3C), that uncovered chromatin fibers assembling into dynamic chromatin loops of 10 to 100 kb, (Fudenberg et al., 2016; Johnstone et al., 2020; Parteka-Tojek et al., 2022; Hoencamp & Rowland, 2023) (Figure 2). The formation of these loops is proposed to occur following the loop extrusion model involving Structural Maintenance of Chromosomes (SMC) proteins forming a ring at the base of the loop and regulating the size of the loop. Two SMC monomers interact with each other through a hinge and two ATPase heads, bridged by a kleisin subunit (Figure 2). Cohesin, Condensin and SMC4/6 are three different SMC complexes involved in chromatin loop extrusion.

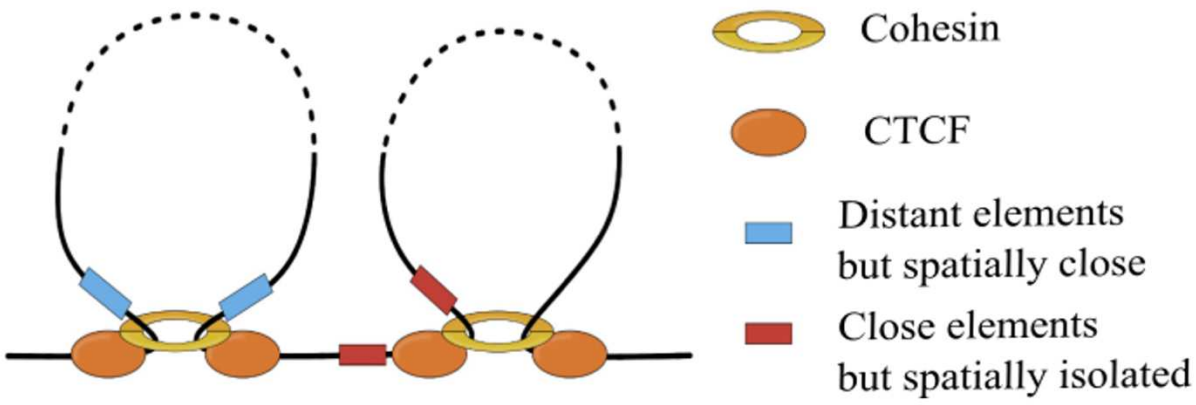


Figure 2: Genome elements brought together or isolated by the cohesin complex and CTCF.

The next level of higher chromatin structure corresponds to the energy-dependent folding of chromatin into larger domains, known as topological associated domains (TADs), that bring together multiple loops, physically insulated from one another by well-defined boundaries interacting with the architectural chromatin protein, CTCF (Figure 3). Inside TADs, chromatin loops can be stalled by either CTCF or a neighboring loop. Single-molecule imaging techniques such as dSTORM and 3D-SIM

(Structured Illumination Microscopy) have shown that TADs can dynamically assemble and dissolve (Fudenberg et al., 2016; Szabo et al., 2020).

In addition to their function in genome condensation, chromatin loops and TADs also play key roles in regulating the nuclear activity. In the case of transcription, the mechanism of chromatin loop extrusion allows, for example, two distant DNA sequences, such as an enhancer and a promoter, to come close together, to trigger transcription. On the contrary, two neighboring DNA sequences may be moved far away from each other upon loop organization. CTCF also interacts with tissue-specific transcription activators or repressors and RNA polymerase II, thereby regulating the function and size of the loops and TADs. Through Hi-C (High-throughput Chromosome conformation capture) maps and interferometric PALM (Photoactivated Localization Microscopy), chromatin loops appear often, forming at least once per cell cycle (15–30 h), and play a role in gene regulation, through interactions with CTCF and nucleosome stacking (Fudenberg et al., 2016).

Other higher-order chromatin structures—nucleosome domains (~ 200 nm), chromonema fibers (100–200 nm), and chromatin blobs (~ 45–90 nm)—have been described in the literature, some of which share physical and functional properties with TADs (Nozaki et al., 2017; Barth et al., 2020). Spatial analysis revealed chromatin domains of ~ 220 nm in diameter in live cells, slightly reduced to ~ 160 nm in fixed cells due to motion blur effects confirming the presence of compact chromatin domains in live cells and validating the utility of high-resolution tracking and imaging to study chromatin organization and dynamics (Nozaki et al., 2017).

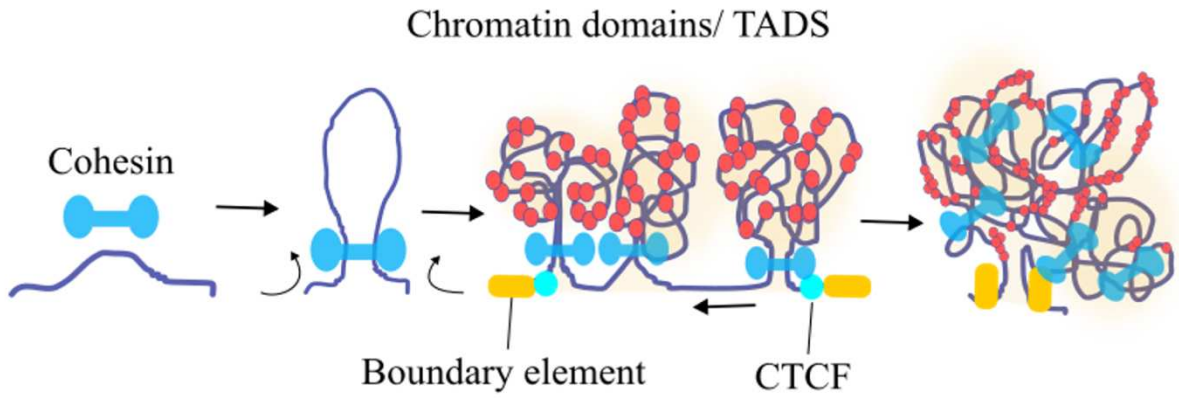


Figure 3: Formation of chromatin domains or topological associated domains (TADS) containing multiple loops with clutches of nucleosomes.

TADs are further embedded within larger A and B compartments, which reflect the chromatin's functional and structural state (J.-H. Su et al., 2020) (Figure 1). Compartment A is defined as gene-rich, transcriptionally active euchromatin, while compartment B is gene-poor, transcriptionally inactive

heterochromatin. These compartments arise from enriched or depleted cis- and trans-interactions. Cis-interactions are usually found within cohesin complexes, like SMC1 or SMC2, using ATP-binding motifs. On the other hand, trans-interactions occur between chromosome compartment A-A and B-B as inter-chromosomal interactions. These types of interactions are influenced by nucleosome composition and loop density. Phase separation mechanisms **(see section 1.2.2.1)** and cohesin activities contribute to the spatial segregation of A/B compartments, with partial overlaps between A and B compartments as confirmed by Fluorescence *in situ* Hybridization (FISH) imaging (Carré-Simon & Fabre, 2021; García Fernández et al., 2023).

At the highest level of chromatin organization, chromosomes are arranged into discrete three-dimensional nuclear regions called chromosome territories, first revealed by FISH in human neuronal and fibroblast cell (Manuelidis, 1985). Later studies confirmed by Hi-C and advanced microscopy that these 'dynamic' territories, ranging from 100 to 3000 Mb, exhibit limited intermingling and are needed to maintain nuclear architecture (Carré-Simon & Fabre, 2021; García Fernández et al., 2023).

To sum up, over the years, the study of each level of chromatin structure and organization has offered deep insights into the arrangement of DNA in the nucleus, revealing a highly ordered, multilayered architecture.

1.1.2 Biomolecular condensates

Membrane-less biomolecular condensates, such as liquid-liquid phase separations (LLPS), have also been shown to play a role in chromatin organization. They function by concentrating proteins and nucleic acids and are becoming increasingly important in understanding chromatin compartmentalization and its regulation.

LLPS is a small-scale biophysical process (Figure 4), in which a homogeneous mixture, in this case, a liquid, separates into distinct phases by demixing (Chiollo, 2025). In the context of chromatin, compartmentation when the phase separation begins, chromatin readers accumulate at their binding sites to form clustered binding (Figure 4a). This increase in the local concentration of these factors triggers the formation of LLPS condensates (Figure 4b), mediated by dynamic soluble interactions.

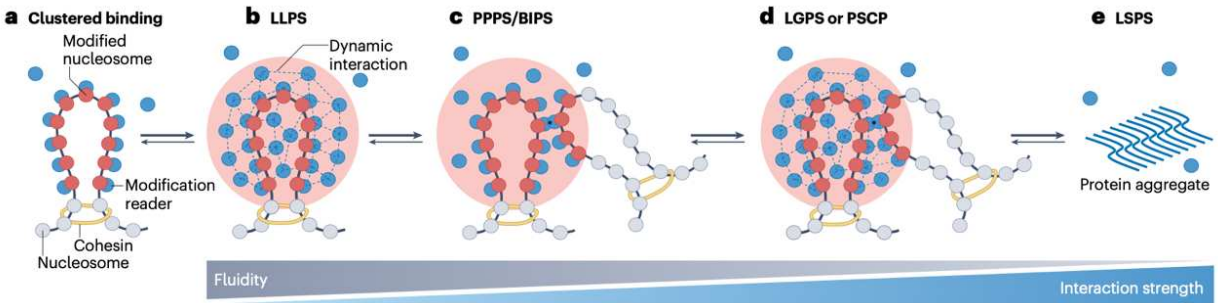


Figure 4: Different types of phase-separated biomolecular condensates observed within eukaryotic nuclei (Chiolo et al., 2025).
Clustered binding sites can locally enrich the capacity of self - associating proteins, promoting phase separation. Here, liquid-liquid phase separation (LLPS) involves formation of dynamic multivalent interactions and interactions with associated polymers can form polymer-polymer phase separation or bridging induced phase separation (PPPS/ BIPS). Depending on the strength of the viscoelastic network between polymers, a liquid – gel phase separation or phase separation coupled to percolation (LGPS/ PSCP) can occur. Finally, liquid – solid phase separation (LSPS) can form as a result of aberrant phase separation or protein aggregation (Chiolo et al., 2025).

LLPS may evolve to polymer-polymer phase separation (PPPS) or bridging induced phase separation (BIPS) (Figure 4c) inside which interactions between chromatin fiber polymers dominate. Depending on the strength of the polymer-polymer interactions, these PPPS can lead to gelation forming liquid-gel phase separation (LGPS) that could eventually give rise to liquid-solid phase separation or irreversible protein aggregate. Throughout this process of phase separation, the fluidity of the condensates decreases concomitantly with an increase of chromatin polymer-polymer interactions linked to an increase in viscoelastic networks (Figure 5). Each of the phase separation types are not mutually exclusive and may cooperate within the complex nuclear environment to shape DNA repair condensates and their interactions with other nuclear structures, like the nuclear envelope or nucleoskeleton, in a context specific and time dependent manner (Chiolo et al., 2025).

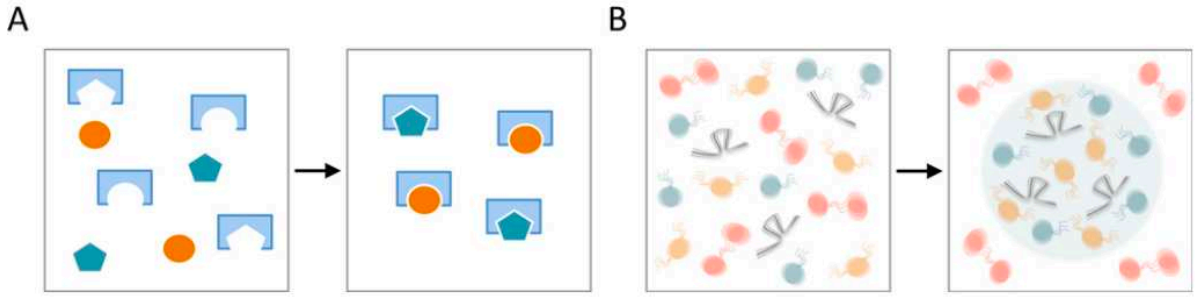


Figure 5: Schematic representation of two binding modes observed within biomolecular condensates by phase separation (from Spegg & Altmeyer, 2021).
A) Stochiometric one – on – one binding like a lock and key or induced fit association. B) Highly dynamic multivalent interactions involved in phase separation. Attractive π-π interactions between aromatic rings, electrostatic or dipole-dipole interactions (including hydrogen bonding) can promote protein assembly by phase separation (Spegg & Altmeyer, 2021).

Interestingly, *in vitro* reconstituted chromatin, in the presence of physiological salt concentrations, can form highly compact, dynamic liquid-like droplets (Banani et al., 2017). These droplets reach a nucleosome concentration close to ~ 340 µM, which corresponds to a 10,000-fold

increase compared to the bulk chromatin (10 nM) in the starting solution, and is similar to the nucleosome concentration found in the nucleus (80–520 μM), demonstrating that LLPS is sufficient to drive genome-scale compaction *in vitro* (Gibson et al., 2019). Both the linker Histone H1, known to compact chromatin, and the length of the linker DNA have been shown to influence the droplet density resulting from LLPS. Acetylation of histone tails, a mark of transcriptionally active chromatin, reduces droplet density and suppresses LLPS formation, whereas the presence of bromodomain-containing proteins like BRD4, that recognize and bind to acetylated chromatin, favors the formation of distinct phase-separated droplets. This supports a model where active transcriptional foci (e.g., super-enhancers) arise through chromatin–reader co-phase separation (Gibson et al., 2019).

LLPS has been observed in bacteria, yeast, plants, animals and also viruses where it contributes to genome compartmentalization (Villaseñor & Baubec, 2021). Biomolecular condensates, like nucleoli speckles and paraspeckles, PML nuclear bodies, repair condensates and stress granules, are naturally present within eukaryotic cells (Spegg & Altmeyer, 2021). Depending on different cell cycle stages, a wide variety of chromosomal processes can be phase separated. For instance, the human heteroprotein HP1α protein can undergo phase separation, forming droplets upon phosphorylation or DNA binding, while the unmodified form remains soluble. Single-molecule assays show a phase separation-deficient HP1α mutant forming fewer and smaller nuclear puncta, suggesting that chromatin compaction and gene silencing may involve dynamic sequestration within HP1α-driven condensates (Larson et al., 2017). This increased local concentration enhances regulatory activity and is crucial for processes like transcription and DNA repair.

Although the concept of LLPS within the self-organizing genome is not new, there remains an active debate about whether phase separation, as classically defined, truly underlies biomolecular assemblies *in vivo* (McSwiggen et al., 2019; Zhai et al., 2025). It is widely speculated that LLPS facilitates cellular reactions by concentrating specific components while excluding others, thereby enhancing reaction kinetics and spatial organization (Gibson et al., 2019; Zhai et al., 2025). *In vitro* studies with purified proteins such as FUS have shown that intrinsically disordered regions can drive droplet formation under controlled conditions, supporting this model (Patel et al., 2015). However, these simplified systems often rely on elevated concentrations and lack the molecular crowding, RNA, and ATP-dependent processes present in cells (Bancaud et al., 2009). *In vivo*, condensates such as stress granules, transcriptional hubs, or DNA repair foci form in highly dynamic, non-equilibrium environments, and not all structures that appear droplet-like are bona fide examples of LLPS (Banani et al., 2017; McSwiggen et al., 2019). Moreover, disrupting condensate formation does not always abolish biological function, raising questions about how quantitatively these assemblies are regulated and whether their formation is functionally essential or instead a consequence of other cellular processes (Spruijt, 2023) . Current efforts therefore combine endogenous tagging, optogenetic tuning of interaction valency, single-molecule tracking, super-resolution microscopy, and more physiologically relevant

reconstitution systems to rigorously test when classical LLPS operates in cells versus alternative assembly mechanisms (McSwiggen et al., 2019; Mittag & Pappu, 2022).

1.1.3 Self organization of chromatin

Genome organization and gene expression are inherently stochastic and heterogeneous, since each cell type exhibits its own transcriptional program to fulfil its function. Single-cell analyses has revealed that genetically identical cells exhibit variable gene expression due to transcriptional bursting, where genes oscillate between active and inactive states (Rodriguez & Larson, 2020). This randomness arises from the dynamic behavior of the transcription machinery and low probabilities of simultaneous allele activation. Similarly, chromatin structures like loops and TADs vary between cells and even between alleles within the same nucleus (Misteli, 2001, 2020).

1.2 Regulation of chromatin and its dynamic nature

Chromatin is highly dynamic, enabling the genome to respond flexibly to regulatory cues across all levels of its organization (Misteli, 2020). Higher-order chromatin structures are regulated by the interplay between drivers and constraints. Drivers include polymer-polymer interactions and homotypic clustering. Conversely, constraints include architectural features that physically interact with genomic regions to increase their mobility and location (Villaseñor & Baubec, 2021).

Multivalent polymer-polymer interactions and homotypic clusters: Key features of chromatin organization like loops, chromatin domains and compartments spontaneously emerge in thermodynamic stable states. Chromatin can be visualized as a polymer driven by intra-polymer interactions (Misteli, 2020). Polymer-self interactions include architectural, chromatin remodelers, transcription binding proteins and functional machineries. Transcriptionally inactive and active regions fold into themselves forming domains, as homotypic clusters. Multiple homotypic domains interact within a single chromosome and/ or between domains of distinct chromosomes to form compartments. This generates transcription hubs and centromere aggregates containing distinct chromosomes and centromeres, respectively (Misteli, 2020; Villaseñor & Baubec, 2021). Within these polymer chains, histone tails and DNA undergo cooperative binding to enhance their affinity and residence time on chromatin (Villaseñor & Baubec, 2021). Cohesin and CTCF, are two of the most prominent chromatin binders that determine the formation of loops and domains, originally identified to demarcate insulator sequences that separate functionally distinct genome regions, in the case of TADs (Rowley & Corces, 2018).

Interaction of chromatin with stable architectural elements: Chromatin interacts with the nuclear lamina, forming lamina-associated domains (LADs) enriched in repressive marks and confined to the periphery, thereby repressing gene expression and maintaining LAD clustering. Their loss relocates LADs inwards, disrupting the 3D chromatin organization. Nuclear bodies like nucleoli and splicing

speckles also act as internal constraints, with active regions associating with speckles and inactive regions with nucleoli. Mechanisms likely involve histone modification readers anchoring chromatin to lamins. Together, these elements create a spatial framework that organizes and regulates genome function through physical positioning in the nucleus (Misteli, 2020).

Heterogeneity and stochasticity of individual chromatin regions: Genome organization and gene expression are inherently stochastic and heterogeneous. Transcriptional single-cell heterogeneity is a major contributor to disengagement of the transcription machinery and oscillates between dynamic on and off states, leading to 'transcriptional bursting'. Single-cell analyses have revealed that genetically identical cells exhibit variable gene expression due to transcriptional bursting, where genes oscillate between active and inactive states (J. Rodriguez & Larson, 2020). This randomness arises from the dynamic behavior of the transcription machinery and low probabilities of simultaneous allele activation. Similarly, chromatin structures like loops and TADs vary between cells and even between alleles within the same nucleus (Misteli, 2001, 2020).

Post-translational modifications: At the nucleosome level, over 550 potential post translational modifications (PTM) serve as interaction hubs for regulatory proteins, ensuring the correct deposition to the genome, essential for DNA replication, transcription, chromatin compaction and also DNA repair (Davie, 1996; Misteli, 2001; Villaseñor & Baubec, 2021). These chromatin marks rely on coordinated activities of reader, writer and eraser enzyme functions, depending on complex multicomponent regulatory circuits (Villaseñor & Baubec, 2021). This was observed for modifications such as H3K9me3, for constitutive heterochromatin and H3K27me3 for facultative heterochromatin. This recognition can allosterically activate the writer enzyme, promoting the spread of the modification to neighboring nucleosomes and creating a positive feedback loop (Villaseñor & Baubec, 2021). Such feedback loops help reinforce specific chromatin states; for instance, H3K9 methylation can recruit DNA methyltransferases, resulting in DNA methylation, thereby maintaining a self-perpetuating, repressed chromatin environment (Almouzni & Cedar, 2016).

Crosstalk Between PTMs: Different histone modifications can influence each other in the form of "crosstalk". This can be stimulatory, where one modification enhances the writing activity of another, reinforcing or maintaining a particular chromatin state. For instance, the conserved interplay between H3K9 methylation and DNA methylation reinforces a repressed heterochromatin chromatin state. Conversely, it can be inhibitory, where one modification interferes with the readout or deposition of another, acting as a negative feedback mechanism (Villaseñor & Baubec, 2021). An example is the inhibition of Polycomb-repressive complex 2 (PRC2) activity, a histone methyltransferase by H3K4me3 or H3K36me2/3, leading to genome-wide anticorrelation between H3K27me3 and H3K36me3 (H. Huang et al., 2015; Poepsel et al., 2018).

Even if the chromatin is highly dynamic, participating in all activities of the genome, the mechanisms by which DNA repair proteins recognize and locate DNA lesions are far from being completely understood.

In recent years, the development of super-resolution microscopy techniques such as Single-Molecule Localization Microscopy (SMLM), has facilitated the study of different cellular processes at the nanoscale, providing a multi-scale overview of chromatin behavior in response to all nuclear activities including DNA repair (García Fernández et al., 2023). The next chapter discusses how DNA damage influences the multilayered organization of chromatin and how chromatin responds to this DNA damage. **(see Chapter 2 for more details).**

Chapter 2: DNA damage and chromatin

In cells, genomic DNA is constantly assaulted by numerous endogenous and environmentally damaging agents, leading to the formation of a variety of DNA damage, such as, oxidation, alkylation, and deamination of nitrogen bases, intra and inter strand DNA cross links as well as single and double strand breaks. This damage activates, the DNA damage response (DDR) pathway, that locates the site of DNA damage, signals its presence and mediates its repair, in order to maintain the integrity of the genome, and thereby avoid disease, in particular, cancer development (Jackson & Bartek, 2009). In eukaryotic cells, DNA is highly susceptible to chemical modifications. It is constantly exposed to numerous sources, leading to the formation of a diverse variety of DNA damage. If unrepaired, this damage can lead to genetic instability, cancer development and eventually, cell death.

In this Chapter, an overview of DNA damage will be presented, then focusing on oxidative DNA damage. It will be followed by a presentation of DNA damage repair considering the organization of chromatin in the genome.

2.1 Overview of DNA damage

DNA damage can be categorized into two types: (i) environmental or exogenous, when induced by sources such as ultra-violet (UV) light, ionizing radiation, environmental pollutants or cytotoxic agents, and (ii) endogenous, resulting from cellular metabolic processes such as mitochondrial activities or oxidative stress. Tables 1 and 2 describe these different sources of DNA damage and their effect on the DNA, that compromises the integrity of the genome.

Endogenous DNA damage resulting from hydrolytic reactions or DNA methylation and oxidation accumulate at measurable rates in cells (Chatterjee & Walker, 2017; Lindahl & Barnes, 2000). Depurination is the most frequent, with ~10,000 bases lost daily. Cytosine deamination and SAM (S-adenosylmethionine)-induced methylation also occur, generating mutagenic or cytotoxic lesions like 3-

methyladenine and 7-methylguanine (Lindahl & Barnes, 2000). Chromatin structure may slightly reduce depurination but does not significantly protect against methylating agents. Oxidative DNA damage, though harder to quantify due to unknown concentrations of reactive oxygen species (ROS) in the nucleus, generates lesions such as 8-oxoguanine (8oxoG), thymine glycols (Tg), many of which are substrates for DNA repair enzymes, particularly of the nucleotide and base excision repair pathways. The identification of these lesions and the use of repair-deficient mutants or knockout models have helped reveal the physiological relevance and cumulative threat of endogenous DNA damage to genome stability (Lindahl, 1993; Lindahl & Barnes, 2000; H. Nakamura & Takada, 2021).

Table 1: Exogenous agents of DNA damage caused by environmental sources.
UV: ultraviolet, CPD: cyclobutene pyrimidine dimers, 6-4PPs: 6-4 photoproducts, 4-ABP: 4-Aminobiphenyl, AqC: 6-Aminoquinolyl-N-hydroxysccinimidyl carbamate, BPDE-G: BaP-diol-epoxide-guanine adducts, MMS: methyl methane sulfonate, EMS: ethyl methane sulfonate; BER – Base Excision Repair; NER – Nucleotide Excision Repair; TL – Translesion synthesis; ICLs – Interstrand crosslinks

Source	Major DNA lesions	Mutagenic Consequences	Repair Pathway	Mechanism	References
Ionizing radiation (IR): X-rays, gamma rays	Direct: SSBs, DSBs; Indirect: ROS-induced lesions (e.g. 8-oxoG, thymine glycol); Clustered DNA damage	Large deletions, translocations, chromosomal rearrangements, point mutations at oxidized sites	BER (oxidized bases, SSBs), NHEJ and HR (DSBs), SSBR	Direct ionization of DNA; Indirect via water radiolysis and ROS	(R. Kumar et al., 2013; Ghosh & Ghosh, 2021)
Ultraviolet radiation (UV): UV-A, UV-B, UV-C	CPDs, 6-4 PPs, Dewar isomers, oxidative base damage, SSBs, DNA-protein crosslinks	C>T transitions at dipyrimidine sites (UV signature), frameshift mutations, replication fork collapse	NER (CPDs, 6-4PPs), BER (oxidative lesions), TLS (damage bypass)	Photoreaction with DNA bases; ROS generation	(Kciuk et al., 2020; Roy, 2017)
Aromatic amines: 4-ABP, AqC	DNA adducts; base substitutions; frameshift mutations	Base substitutions (especially G>T), frameshift mutations, replication blockage	NER, TLS	Metabolic activation by P450 enzymes forms DNA-reactive intermediates	(Hammons, 1997; Ebert et al., 2017)
Polyaromatic hydrocarbons: (BaP)	Bulky DNA adducts (e.g. BPDE-G); helix distortion; replication errors	G>T transversions (especially in p53), error-prone replication	NER, TLS	P450-mediated metabolic activation to reactive epoxides	(Hammons, 1997; Thompson et al., 1981)
Alkylating agents: MMS, EMS, nitrogen mustards, nitrosoureas	N7-alkylguanine, N3-alkyladenine, O6-alkylguanine, abasic sites, crosslinks	G>A transitions (e.g., in oncogenes), abasic site-induced strand breaks, insertion/deletion mutations	Direct reversal (MGMT), BER, MMR (O6-MeG:T mismatches)	Alkyl group transfer to nucleophilic DNA sites	(Fu et al., 2012; Fahrer & Christmann, 2023)
Non-alkylating crosslining agents: Cisplatin, formaldehyde	Intra-/inter-strand crosslinks (e.g. GpG), DNA-protein crosslinks, replication fork stalling	Chromosomal breaks, stalled replication forks, large deletions	NER, HR (ICLs), Fanconi anemia pathway, TLS	Covalent binding (e.g. N7 of purines); UV-activated crosslinking (e.g. psoralen)	(Basu & Krishnamurthy, 2010; Haynes et al., 2015; Baiken et al., 2021)

Table 2: Endogenous sources of DNA damage.

OGG1: 8-Oxoguanine glycosylase, BER: Base Excision Repair, AP sites: Abasic sites, MGMT: O6-methylguanine-DNA methyltransferase, dNTP: deoxyribonucleoside triphosphate, SSB: single-strand break, DSB: double-strand break, HR: Homologous Recombination.

Source of Damage	Major DNA Lesions	Mutagenic Consequences	Repair Pathway(s)	Mechanism	References
Oxidation (ROS)	8-oxo-Guanine (8-oxo-G), Thymine glycol	Base mispairing (e.g., G>T transversion), replication errors	BER (OGG1); cooperation with NER (XPC, etc)	Reactive oxygen species generated during metabolism react with DNA bases	Cadet et al., 2003; Kumar et al., 2020, 2022
Hydrolysis	AP sites, deamination of uracil from cytosine	Strand breaks, DNA-protein crosslinks, interstrand crosslinks, transition mutations (e.g., C>T)	BER for uracil/AP sites; complex repair for crosslinks	Spontaneous hydrolysis of glycosidic or amine bonds	Lindahl, 1993; Chatterjee & Walker, 2017
Methylation (Alkylation)	O6-methylguanine (O6-MeG), N7-methylguanine	G>A transition mutations, abasic sites if unstable	Direct repair by MGMT (O6-MeG) or BER	Non-enzymatic alkylation by agents like nitrosylation byproducts	Chatterjee & Walker, 2017
Replication Errors	Base mismatches, indels, mis paired tautomer's	Substitution mutations (e.g., A>C), frameshifts	Mismatch Repair (MMR); proofreading by DNA polymerase	DNA polymerase misincorporation, dNTP	Kunkel, 2004, 2009; Kimsey et al., 2018
Topoisomerase-DNA Cleavage Complexes	Covalent Topo-DNA adducts, SSBs, DSBs	Blocked replication/ Transcription or cell death	Tyrosyl-DNA phosphodiesterase; HR for DSBs	Trapped DNA intermediates	(Pommier et al., 2022)

2.2 Oxidative DNA damage

ROS and reactive nitrogen species (RNS) are natural byproducts of cellular metabolism, generated by various physiological processes such as respiration and redox reactions. RNS are highly reactive nitrogen-based molecules, often formed by interactions between nitric oxide (NO•) and ROS intermediates (Cadet & Wagner, 2013; Lindahl & Barnes, 2000). Low to moderate levels of ROS serve as crucial signaling molecules in cellular processes and high levels of ROS lead to irreversible DNA damage and cell death (Figure 6) (Nakamura & Takada, 2021). Oxidative stress created by an imbalance between ROS and the antioxidant defense system (thiols like glutathione and cysteines) causes DNA

base oxidation, leading to an increase in oxidative DNA damage (Averill-Bates, 2023). ROS leads to the formation of oxidatively induced DNA damage like base modifications such as formamidopyrimidines – FapyA and FapyG, 8-oxoguanine (8oxoG), 5-hydroxycytosine (5-OHC) and thymine glycol (Tg) along with strand breaks and interstrand crosslinks (Greenberg, 2012; Cadet & Wagner, 2013) (Figure 6).

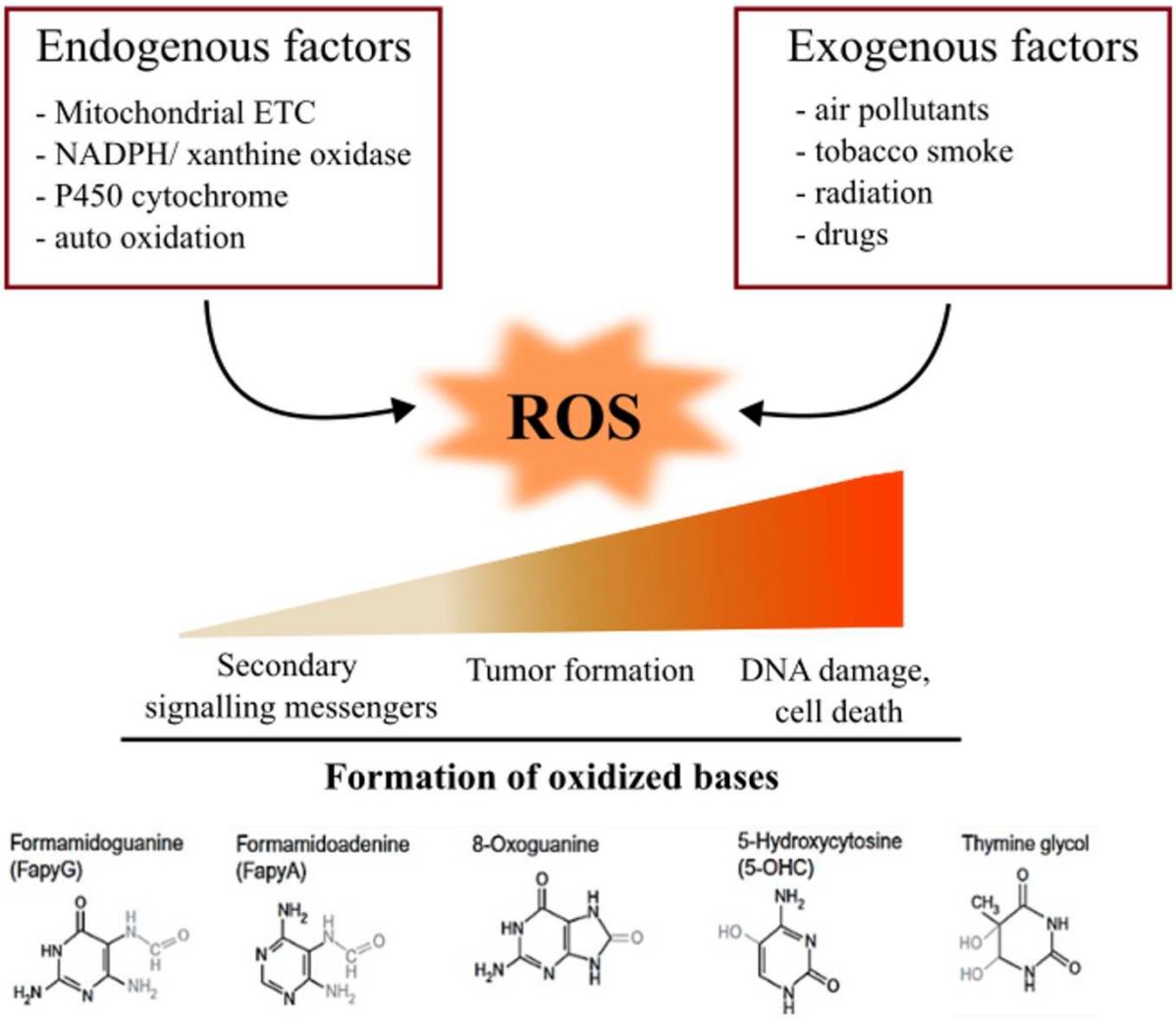


Figure 6: Generation of reactive oxygen species (ROS) from endogenous and exogenous sources and their effects.

Depending on the severity of ROS generated, secondary signalling messengers are produced that stimulate tumour formation and antioxidant inhibition leading to the formation of oxidized base lesions causing oxidative DNA damage (Nakamura & Takada, 2021). The common types of oxidized DNA base lesions produced are Formamidopyrimidines (FapyG and FapyA), 5-hydroxycytosine (5-OHC), 8-oxoguanine (8oxoG) and thymine glycol (Tg) (Dizdaroglu et al., 2017). Illustration adapted from Nakamura et al 2021.

Endogenous ROS, including oxygen free radicals [superoxide anion (O_2^-)], hydroxyl radical (OH^-)] or non-radical ROS like hydrogen peroxide (H_2O_2), are produced to a large extent during oxidative respiration (Lindahl & Barnes, 2000; Averill-Bates, 2023). Figure 7 simplifies the mechanisms of action of three oxidative DNA damaging agents. Even though its intracellular concentrations remain quite stable (1-100 nM), H_2O_2 can be converted in the presence of transition metals, such as Fe (II), producing high levels of ROS (Freinbichler et al., 2011). Exogenous ROS are instead generated by genotoxic or chemotherapeutic agents like cisplatin. Some oxidizing agents, like potassium bromate ($KBrO_3$), can also induce oxidative DNA damage independently of ROS (Lindahl & Barnes, 2000).

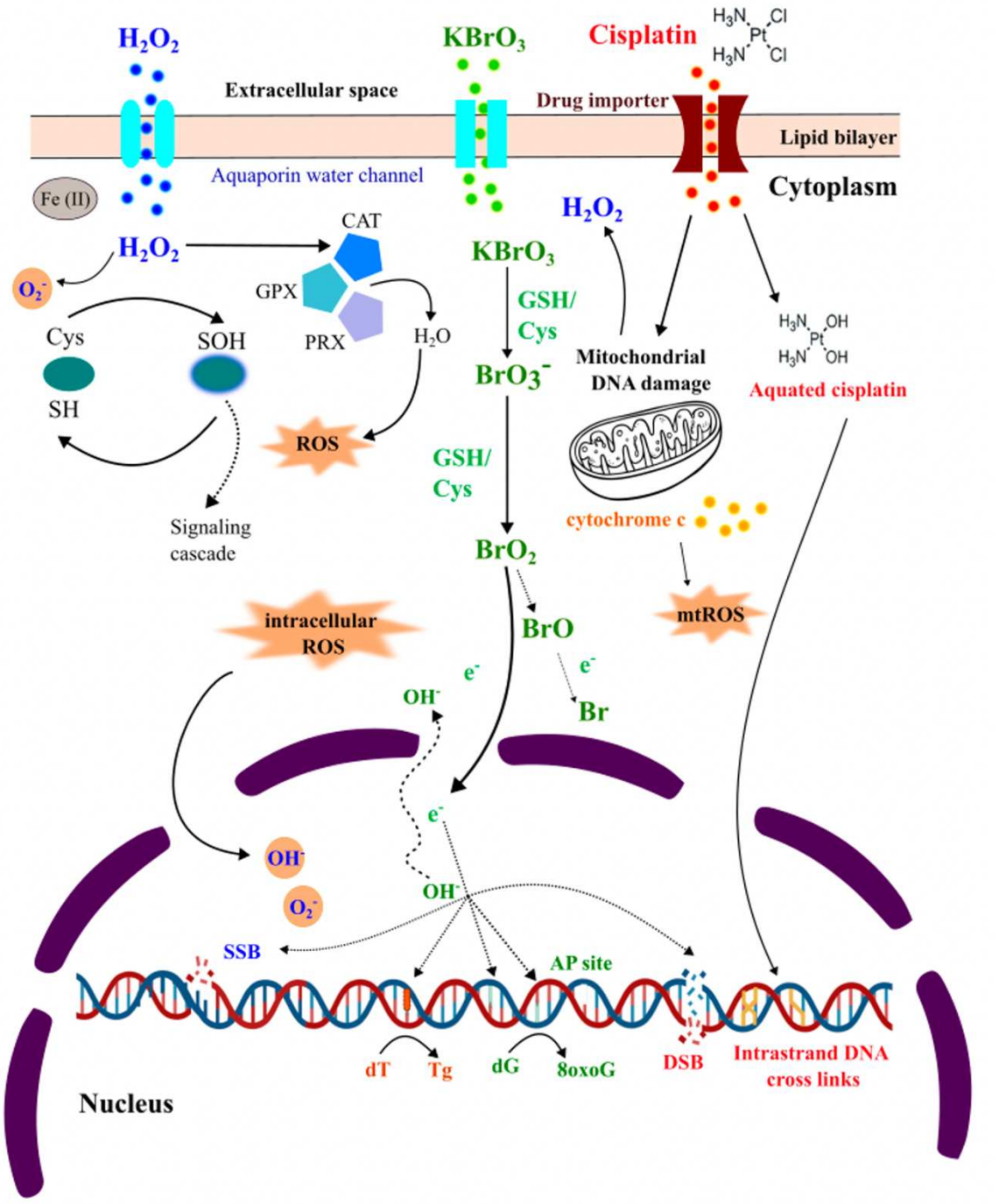


Figure 7: Illustration of the mechanism of action of hydrogen peroxide (blue), potassium bromate (green) and cisplatin (red), examples of endogenous and exogenous forms of ROS produced within the nucleus.

Through the aquaporin water channel, hydrogen peroxide (H_2O_2) can cross the cellular membrane and activate ROS signalling, by an oxidative modification of the critical redox sensitive Cys signalling proteins. H_2O_2 can target cellular oxidant systems like catalase (CAT), glutathione peroxidases (GPXs) and peroxiredoxins (PRXs) to maintain redox homeostasis. This could lead to single strand breaks (SSBs) by oxygen radicals (OH^- and O_2^-). $KBrO_3$ directly interacts with nuclear DNA by reducing $KBrO_3$ (BrO_3^-) to BrO_2 by one-electron oxidation of guanine (dG) to 8oxoguanine (8oxoG) or thymine (dT) to thymine glycol (TG), in the presence of GSH/ Cys, forming an AP site. On the other hand, a fraction of aquated cisplatin reacts with thiols like glutathione (GSH) and cysteine (Cys) or with mtDNA producing mtROS, indirectly increasing levels of intracellular ROS. A fraction reacts with nuclear DNA to form cisplatin induced inter- and intrastrand cross links, or double strand breaks (DSBs) known to be repaired by nucleotide excision repair (NER) and mismatch repair pathways (MMR). Illustration adapted from (Di Marzo et al., 2018 (H_2O_2); Goffart et al., 2021; Kawanishi & Murata, 2006 ($KBrO_3$); Kar et al., 2024; Kothandapani et al., 2011 (cisplatin)).

2.2.1 Hydrogen peroxide (H_2O_2)

Hydrogen peroxide (H_2O_2) is a crucial metabolite involved in cellular redox metabolism. It is involved in sensing, modulating and signaling redox processes in tightly regulated mammalian subcellular compartments (Di Marzo et al., 2018). It functions as a secondary messenger along with hydrogen sulfide (H_2S), and nitric oxide (NO), activating downstream metabolic responses to cell proliferation, survival and death. It is produced by enzymatic reactions catalyzed by superoxide dismutase (SOD), that converts superoxide radicals into H_2O_2 and oxygen (Averill-Bates, 2023). As figure 7 highlights, H_2O_2 directly affects binding of growth factors to their receptors (e.g EGF or PGDF), to trigger downstream events using the NOX-2 complex. This produces $O_2^{\bullet-}$ radicals through superoxide dismutase-3 activity (SOD3). Moreover, H_2O_2 can cross the cellular membrane through aquaporin transport channels and activate intracellular ROS signaling cascades, targeting transcription factors, mitogen-activated protein kinases and protein tyrosine phosphatases. This produces oxygen free radicals, OH^- and O_2^-, that in turn lead to the formation of single-strand breaks (SSBs) in the DNA, as illustrated in figure 7 (Averill-Bates, 2023; Di Marzo et al., 2018). Additionally, H_2O_2 can be detoxified by antioxidants generating hydroxyl radicals (OH•) through a Fenton reaction, that also cause severe cellular damage to proteins and lipids. The intracellular concentration of H_2O_2 is tightly controlled to maintain homeostatic concentrations ranging from 1 to 100 nM (Freinbichler et al., 2011). This balance fluctuates along the cell cycle. H_2O_2 intracellular concentrations increase from the G1 phase to mitosis,

regulating the effect of cyclin – dependent kinases (Cdks) and anaphase promoting complexes (APC) (Heo et al., 2020).

2.2.2 Potassium bromate ($KBrO_3$)

Potassium bromate ($KBrO_3$) is a carcinogenic agent, previously used as a food additive ('flour enhancer') and for ozonation of drinking water. The oxidative stress caused by $KBrO_3$, leads to downregulation of transcription and translation activity, in eukaryotes. $KBrO_3$ induces specific formation of 8oxoG in the presence of glutathione/ cysteines (GSH/ Cys) through a one-electron oxidation of guanine (Kawanishi & Murata, 2006). The efficient activation of $KBrO_3$ to bromine oxides (BrO) and bromine radicals (Br•) is indeed strongly dependent on the high intracellular levels of GSH/ Cys, causing bromate-induced oxidative DNA damage (Figure 7). Therefore, studies have shown that the mechanism of bromate-induced oxidative DNA damage is different to the general mechanism of oxidative stress induced by other ROS species like H_2O_2 and superoxide anions (O_2•) (Goffart et al., 2021).

2.2.3 Cisplatin

Cisplatin [$Pt(NH_3)_2Cl_2$] is a platinum-based chemotherapeutic drug that induces cisplatin-DNA adducts, blocking replication and transcription, leading to cell cycle arrest at the G2 checkpoint and subsequently apoptosis (Kar et al., 2024). Figure 7 illustrates a general mechanism of the influx/ efflux of cisplatin through the plasma membrane of the cell that is mediated by either passive diffusion or copper transporters. Once in the cytoplasm, cisplatin undergoes aquation to form $[Pt(NH_3)_2Cl(OH_2)]^+$ and $[Pt(NH_3)^2(OH_2)_2]^{2+}$, a process that is facilitated by low concentrations of chloride ions. Aquated cisplatin is known to play three major roles in inducing cisplatin-related DNA damage: i) Cisplatin enters the cells by passive diffusion. Cisplatin forms aquated cisplatin interacts with nuclear DNA, forming 1,2 – intrastrand crosslinks such as., Pt-d(GpG) and Pt-d(ApG) adducts or interstrand crosslinks such as, G-Pt-G. ii) Aquated cisplatin also interacts with cellular thiols such as, glutathione/ cysteine (GSH/Cys). The Pt atom is chelated by glutathione forming glutathione-Pt complex which is effluxed from the cell. iii) It can also react with mtDNA producing mtROS and indirectly increasing intracellular ROS levels. However, ROS generation leading to oxidative damage appears to be independent of the amount of cisplatin-induced nuclear DNA damage (Basu & Krishnamurthy, 2010).

2.3 DNA damage response

DDR is an integrated signaling and genome – maintenance network. It helps to locate the site of DNA damage, signal its presence and mediate its repair, thus maintaining the integrity of the genome and avoiding a rapid decay of genetic information by operating collectively (Jackson & Bartek, 2009). The presence of DNA damage or stalled replication forks during the S-phase of the cell cycle alerts

DNA damage sensor proteins. These sensors initiate and amplify signaling pathways, inducing a number of cellular responses, including cell cycle arrest, autophagy, apoptosis, chromatin remodeling and DNA repair, as illustrated in figure 8 (Lindahl, 1993; Jackson & Bartek, 2009). Therefore, the activation of the DDR, by stimulating the DNA repair of a cell ensures mitigation of both environmental and endogenous stressors in cells by decreasing i) opportunities for genetic effects, ii) malignant transformation compromising genetic integrity, iii) enhanced cancer development and iv) arresting a cells' DNA repair ability.

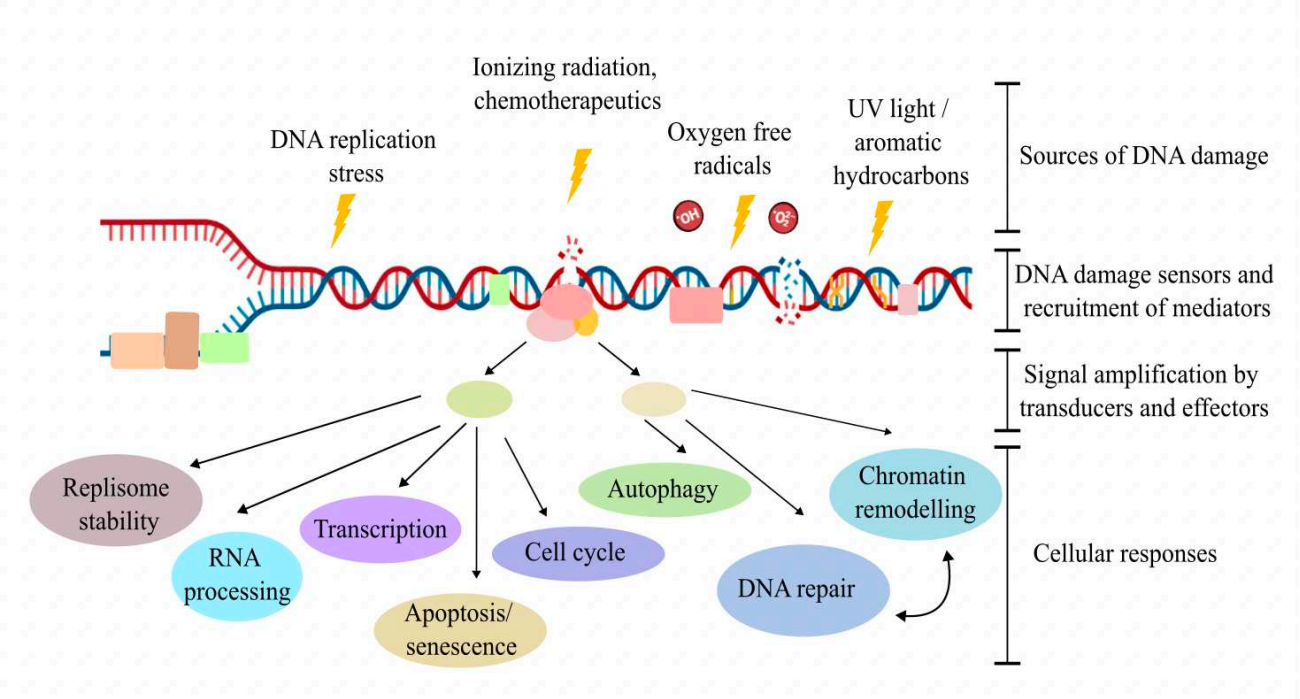


Figure 8: Schematic illustration of the different components of the DNA damage response (DDR). A lesion formed as a result of endogenous or exogenous DNA damage is recognized by various DNA damage sensors (green and brown). These sensor proteins recruit mediators (pink), transducers and effectors to amplify the signaling pathways, leading to downstream cellular responses (Friedberg et al., 2004; Jackson & Bartek, 2009).

2.4 Chromatin response to DNA damage

DDR impacts a wide range of cellular events, including the various levels of chromatin organization and the accessibility of sites of DNA damage (Figure 9). Structural changes that occur in chromatin in response to DNA damage include chromatin decondensation, nucleosome repositioning, histone modification, compartmentalization, recruitment of chromatin modelers and increased mobility to facilitate access to the repair machinery (Figure 9A) (Carré-Simon & Fabre, 2021; Cook & Delaney, 2022). Chromatin organization is affected at all levels, starting from the smallest scale. Indeed, at the level of nucleosomes, histones are subject to PTMs leading to phase separation, histone eviction and

chromatin remodeling. At the medium scale, loop extrusion by SMC protein complexes is activated and sites of DNA damage undergo passive or directed mobility within the nucleus. At the large scale, chromatin attachment to the nuclear envelope and global chromatin arrangement are altered to form functional nuclear compartments. Each organizational scale exhibits a two-way communication and coordination displaying an interconnection between different scales of organization (Figure 9B) (Chiolo et al., 2025).

Chromatin dynamics at the nucleosomal level, was observed in irradiated cells. It begins with chromatin decompaction, which allows increased accessibility of nucleases to trigger the repair process, as observed in human cells exposed to UV-C light. Chromatin immunoprecipitation (ChIP) has also shown that UV-A laser induced DNA damage leading to the accumulation of double-strand breaks (DSBs) induces transient nucleosome disassembly. This greatly facilitates the release and degradation of histones (Ferrand et al., 2021). The geometry and position of the nucleosomes is vital for nucleosome – mediated epigenetics and to encode spatial and structural information in the genome. Therefore, histones control the chromatin response accessibility and repair at sites of DNA damage. Thus, chromatin is not only a victim of DNA damage, but also an active participant in the cellular response to it (Chiolo et al., 2025; Ferrand et al., 2020).

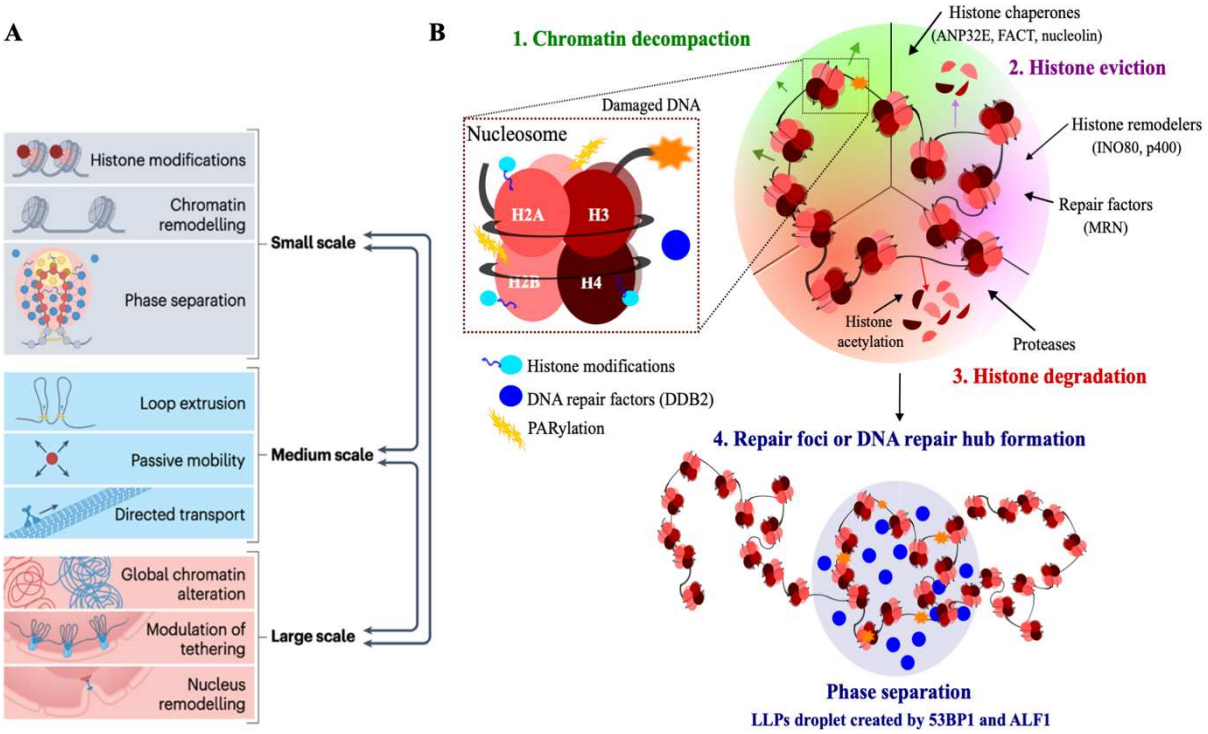


Figure 9: Chromatin response to DNA damage at the nucleosome level

An integrated overview of (A) DNA repair structures at the nucleosome and genomic organization at different chromatin levels. The diagram illustrates the main chromosomal rearrangements at sites of

DNA damage sites that occur at different genomic spatial and temporal scales. (B) At the small scale (nucleosomes), chromatin decompaction (green) exposes the DNA damage to the action of dedicated nucleases, causing histone eviction (purple) and histone degradation (red) by proteases. This allows histone chaperones, modelers and repair factors to form repair hubs or foci (blue) as a result of DNA damage. Adapted from Ferrand et al 2020 and Chiolo et al 2025.

DNA repair foci are microscopically discernable entities in which DNA repair proteins accumulate in the vicinity of DNA damage sites. These nuclear condensates have been extensively studied in eukaryotic species. The stoichiometric binding between structured domains and multivalent interactions drives phase separation for condensate formation. Figure 10 illustrates some intriguing examples of DNA repair foci, formed at DNA damaged sites, that contribute to maintaining genomic integrity (Spegg & Altmeyer, 2021).

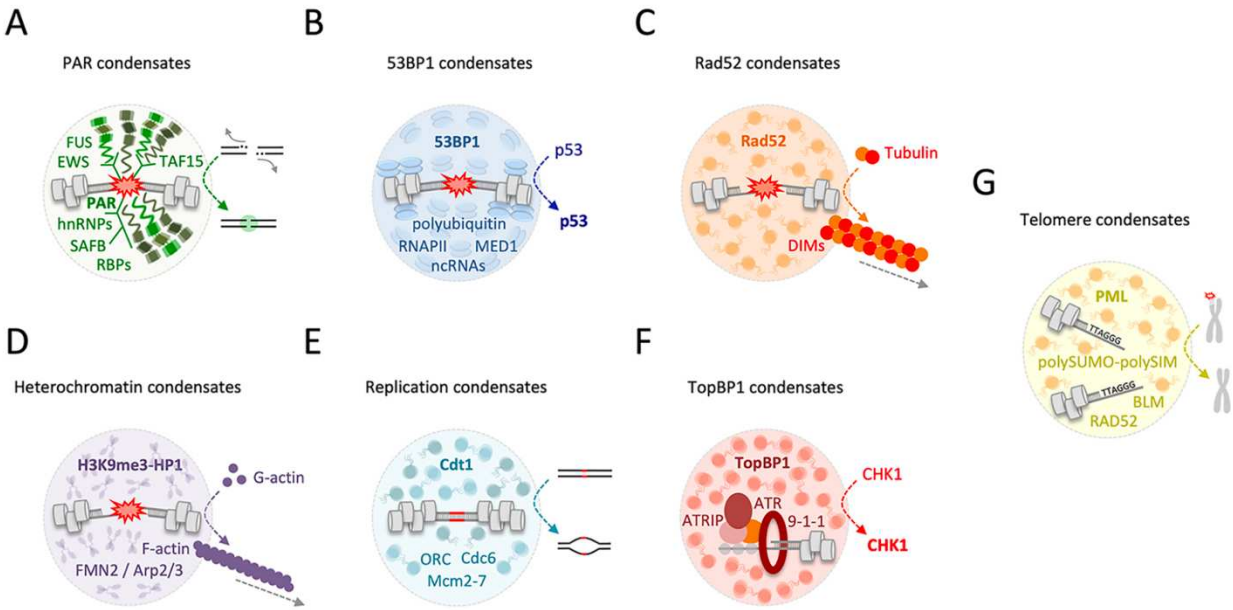


Figure 10: Examples of nuclear condensates with phase separation and their roles in maintaining genome integrity in the event of DNA damage.
(A) Poly (ADP-ribose) (PAR) induces assembly of disordered and RNA-binding proteins for chromosome tethering. (B) At DSB sites, 53BP1 condensates form through multivalent interactions with chromatin and promote p53 signaling via co-condensation. (C) Rad52 forms condensates in yeast that facilitate the mobility of repair condensates along intranuclear microtubule filaments. (D) In human cells, heterochromatin domains relocate to the nuclear periphery for repair, a process dependent on the actin nuclear skeleton. (E) Replication condensates formed by ORC, Cdt1, and Cdc6 have also been shown to phase – separate. (F) TopBP1 condensation activates ATR/ CHK1 signaling during replication stress. (G) PML (Promyelocytic leukemia) bodies phase separate for telomere clustering and recombination (Spegg & Altmeyer, 2021).

To summarize, mammalian DNA is continuously exposed to damaging agents of both endogenous and exogenous origin, leading to diverse lesions that threaten genomic integrity. At the onset of DNA damage, the structure of chromatin dynamically reorganizes at multiple levels, to facilitate repair, highlighting its dual role as both a barrier and active participant in genome maintenance. DNA damage activates the DNA damage response (DDR), a signaling network that coordinates repair, cell cycle arrest, or apoptosis. In the next chapter, I will focus on the DNA repair pathways that recognize and repair the DNA.

Chapter 3: DNA repair machinery

Mammalian cells have developed highly specialized DNA repair pathways to handle a variety of different DNA lesions, as mentioned in the previous section. Such damage must be repaired immediately to ensure the smooth, error-less transfer of genetic information from one generation to the next. Each repair pathway targets a specific type of DNA damage. For example, homologous recombination (HR) and non-homologous end joining (NHEJ) repair DSBs, while mismatch repair pathway (MMR), base excision repair (BER) and nucleotide excision repair (NER) target smaller base lesions (R. Huang & Zhou, 2021).

3.1 Mismatch Repair Pathway

MMR mainly operates in the presence of mismatches (non-Watson-Crick base pairs or indels) resulting from errors during replication that have escaped proofreading by δ/ε polymerases. Indels (insertions or deletions) located on the newly synthesized strand are generated by a slippage of the polymerase. The fundamental principles of MMR are quite conserved from prokaryotes to eukaryotes (Hsieh & Zhang, 2017). Although eukaryotic MMR is not fully understood, a generally agreed model of its mechanism has been proposed, and is illustrated in Figure 11 (Hsieh, 2001).

The MMR pathway begins with the recognition of a base mismatch by MutS homologues such as MSH. MutSα, also known as MSH2-MSH6, detects the presence of base-to-base mismatches and small indels of ~1-2 nucleotides and MutSβ, also known as MSH2-MSH3, detects longer indels of 1-15 nucleotides. MSH6 is recruited to the chromatin by interacting with trimethylated histone H3 (H3K36me3). To avoid repairing the template strand, the repair machinery needs to be targeted to the newly synthesized strand. In the case of the lagging strand, the new strand is recognized by the presence of gaps, resulting from the Okazaki fragments. Targeting of the MMR machinery to the leading strand is less understood. However, discontinuities may arise from incorrect insertion of ribonucleotides (Putnam, 2021). The mismatch is detected by the MutSα/β complexes leading to ATP hydrolysis that promotes diffusion of the MutS complex along the DNA. Next, the recruitment of MutLα heterodimer

(MLH1-PMS2), activated by PCNA, incises the damaged DNA strand on each side of the mismatch. From here, there are two downstream pathways proposed. The EXO1 dependent repair pathway involves the recruitment of either the exonuclease EXO1 (5' → 3') or the endonuclease Rad27 to help eliminate a section of the DNA, often around 100 bases long, that contains the mismatch (Hsieh & Yamane, 2008). The resulting single-strand DNA will be protected by RPA proteins and final resynthesis takes place by polymerases δ/ε and relegation by ligase I after EXO1. On the other hand, in the Rad27/ FEN1 dependent repair pathway, when Rad27 is recruited, the polymerase δ (alone) resynthesizes the damaged strand by displacing the old one.

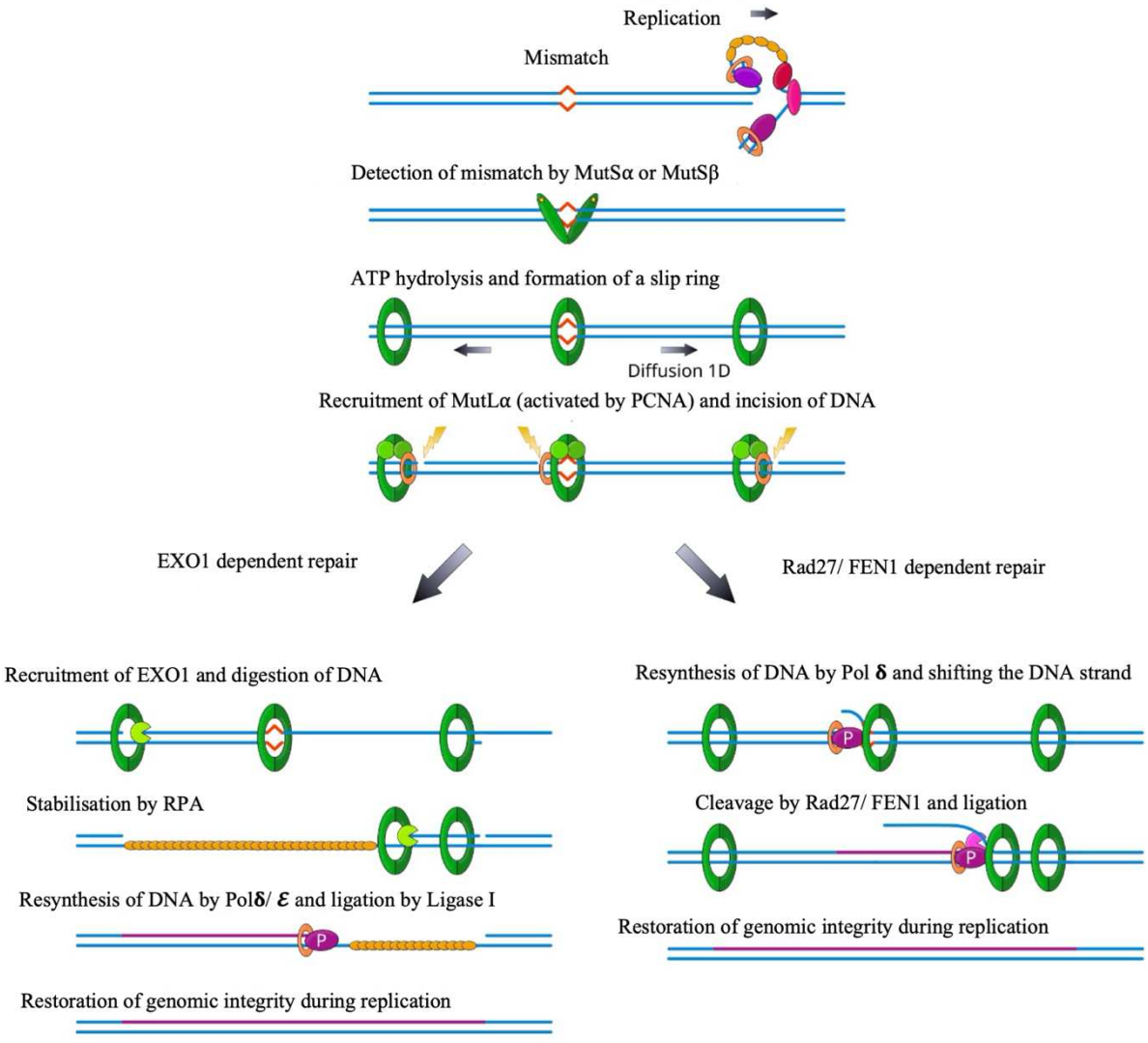


Figure 11: Proposed model for mismatch repair during DNA replication, in mammalian cells. The mismatch repair (MMR) pathway begins with mismatch recognition by MutSα for base-base and small indels, and MutSβ for larger indels. MutS binding and ATP hydrolysis recruit MutLα, which incises the error-containing strand. Repair proceeds via EXO1-dependent excision and resynthesis by

polymerases δ/ε, or Rad27/FEN1-dependent displacement synthesis. Illustration adapted from Dr. Ostiane D'Augustin PhD thesis (D'Augustin, 2022).

Chromatin remodeling during MMR begins with nucleosome eviction. This is achieved through collaboration of MSH2 with the chromatin remodeler SMARCAD1 to displace nucleosomes at repair sites, followed by recruitment of MutLα. The next step involves the recruitment of MutSα with the MSH2 subunit facilitated by the subunit of SWI/SNF, ARID1A. To ensure that the mis-paired bases are not incorporated into the nucleosomes, MSH6 interacts with CAF-1 to prevent nucleosome assembly. Finally, it is suggested that the SWR-C complex deposits H2A.Z to promote mismatch repair, although the mechanism is not fully understood (Huang & Li, 2020). These MMR chromatin remodelers (SMARCAD1, SWI/SNF and CAF-1) are regulators of the repair process, in the context of chromatin, maintaining genomic stability, to avoid tumorigenesis. Therefore, many of these chromatin remodelers are potential targets for cancer therapy, aiding to increase MMR activity in response to alkylating damage (Hsieh & Yamane, 2008; Huang & Li, 2020).

3.2 Nucleotide Excision Repair (NER) Pathway

The NER pathway repairs lesions that distort the DNA helix. The main types of lesions recognized by the DNA damage sensors, XPG and DDB2, include cyclobutane pyrimidine dimers (CPD), 6,4 – pyrimidine photoproducts (6,4-PP), Benzo[a]pyrene (BaP), intrastrand crosslinks and other helix-distorting lesions, that are generally induced by UV radiation or environmental pollutants or chemotherapeutic agent as cisplatin (Dizdaroglu et al., 2017; Apelt et al., 2021).

NER broadly encompasses the following steps: damage recognition, pre-incision complex assembly, dual incision and repair synthesis. As illustrated in figure 12, NER can be divided into two sub-pathways, depending on whether the lesion is present in a transcribed region or not. the first pathway is the Transcription-coupled NER pathway (TCR-NER), that detects the blockage of RNA polymerase II (RNA pol II), due to bulky DNA adducts, generated for example, by cisplatin-induced DNA damage (Chiou et al., 2018). The second pathway is the Global Genome NER (GG-NER) that directly detects the lesion, independent of the presence of the polymerase. In TCR-NER, RNA pol II detects the blockage caused by the lesion and is dissociated after dual incision by the translocase CSB (Cockayne Syndrome B), initiating the repair process. Subsequently, CSB recruits CSA (Cockayne Syndrome A) and then UVSSA (UV stimulated scaffold protein A). The CSA/UVSSA complex, stabilized by CSB, in turn allows the recruitment of the transcription factor TFIIH.

After the initial steps of lesion recognition, the recruitment of the TFIIH complex is common to these two pathways. Recent studies have demonstrated that RNA pol II needs to be completely dissociated from the DNA during TCR-NER (Chiou et al., 2018).

GG-NER, in contrast, is initiated through the direct recognition of the lesion-induced DNA helix distortion by a complex composed of XPC (Xeroderma pigmentosum group C), HR23B (Human Rad23 homolog B) and Centrin 2, aided by the UV-DDB complex that facilitates the recognition of helix-distorting lesions – cyclobutane pyrimidine dimers (CPDs) and 6-4 Photoproducts (6-4PPs), that distort the DNA helix. XPC subsequently recruits TFIIH. After these initial steps of lesion recognition and the recruitment of the TFIIH complex, the end processing step is common to the two pathways. The two TFIIH subunits, XPB and XPD, activate their helicase properties, opening the DNA to create a repair bubble. When XPD is blocked by the lesion, this stimulates recruitment of the pre-incision complex (PIC) factors: XPA, RPA and XPG. The order of recruitment of these factors is currently the subject of some debate. However, XPG displaces XPC and initiates formation of the PIC. Subsequently, XPA recruits the endonuclease ERCC1/XPF allowing incision of the DNA on the 5' side of the lesion and DNA synthesis is initiated by DNA polymerases δ/κ/ε, before the 3' incision by XPG. The final step involves the DNA ligase III/XRCC1 complex or Ligase I, to seal the nick.

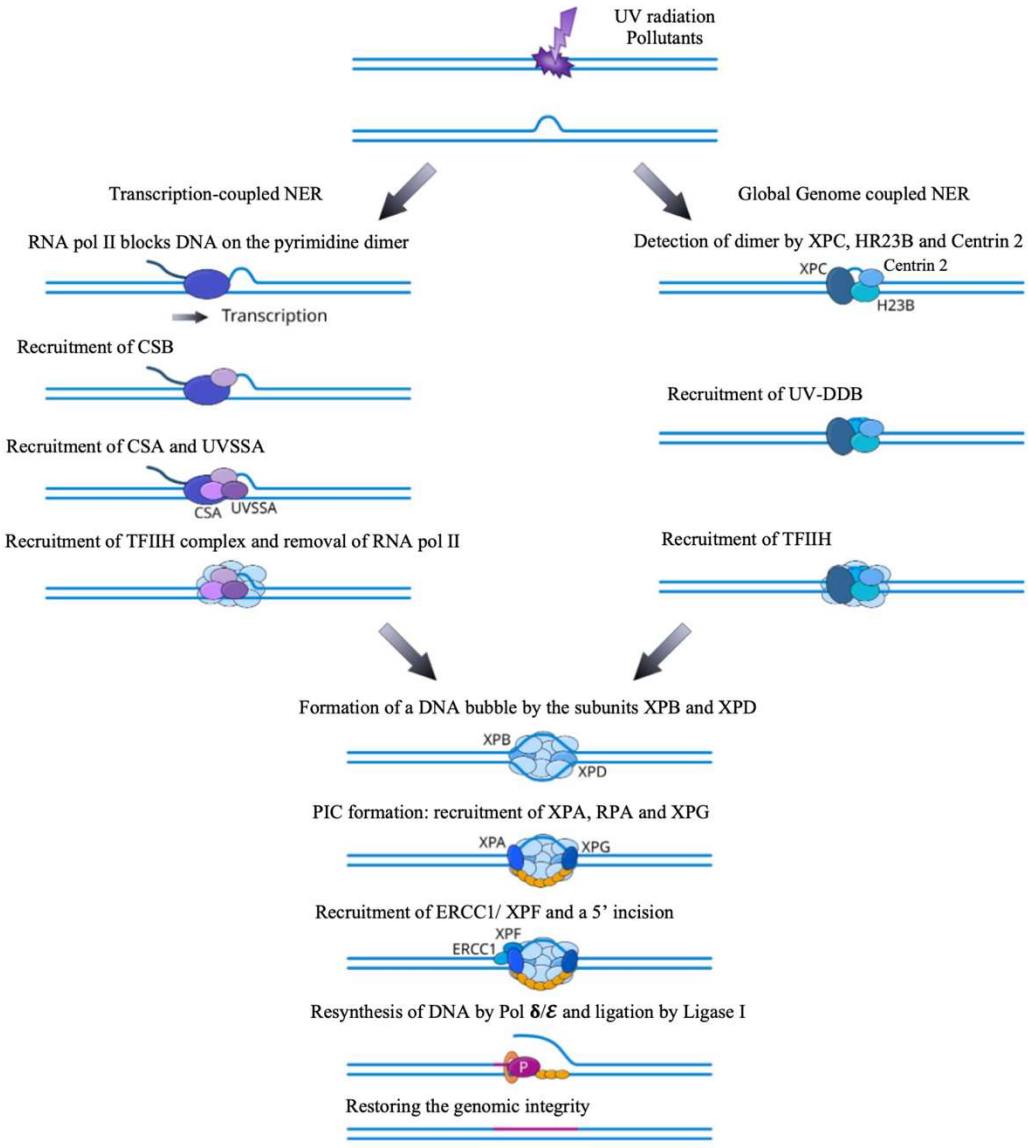


Figure 12: Nucleotide excision repair in mammalian cells.
Depending on whether the lesion is present in the transcribed region, repair can follow either the TCR-NER pathway, which detects stalled RNA polymerase II at lesions, or the GG-NER pathway, which recognizes helix distortions via the XPC-HR23B-Centrin2 complex, aided by UV-DDB. Both converge on recruitment of TFIIH, whose XPB/XPD helicases unwind DNA to form a repair bubble. Assembly of the pre-incision complex (XPA, RPA, XPG) follows, with ERCC1/XPF and XPG mediating 5′ and 3′ cuts. Repair is completed by polymerases δ/κ/ε and ligation by Ligase I or XRCC1/Ligase III. Illustration adapted from Dr. Ostiane D'Augustin PhD thesis (D'Augustin, 2022).

NER activity is greatly inhibited on nucleosomal DNA and highly modulated by PTMs of histones. *In vitro* studies have demonstrated that recruitment of XPC to DNA lesions is stimulated by PARP1 – mediated PARylation. In cases of UV damage, DDB2 is observed to stimulate the recruitment of XPC, by SUMOylation at K309. DDB2 can also form a complex with CUL4B-RING1B that ubiquitinates the histone H2A at K119 and another complex CUL4B-RBX1, ubiquitinating the Histones H3 and H4 in response to UV. PARP1 can also interact with DDB2, PARylating it, and thereby regulating its ubiquitination and chromatin retention (Apelt et al., 2021). Many studies have also described the role of NER in cisplatin resistance within solid tumors (Slyskova et al., 2018). However, it is unknown which NER genes are upregulated in these tumors during cancer treatment (Slyskova et al., 2023). Systematic analysis of protein and mRNA levels of NER factors at different stages of drug treatment may hold the key to uncover treatment-induced changes of specific NER proteins (Bowden, 2014). Additionally, small molecule inhibitors of NER factors could be useful tools to manipulate NER repair capacity in cells (Duan et al., 2020).

3.3 Double strand break (DSB) repair pathways

DSBs are considered the most harmful and toxic type of DNA lesion. They cause cell cycle arrest and can induce genomic instability, cell senescence and ultimately, cell death (Chapman et al., 2012). They are generated through various means: replication stress, DNA crosslinks, unusual DNA secondary structures (e.g. loop extrusions) or stalling of the transcription machinery leading to the formation of a replication fork (Huang & Zhou, 2021). Persistence of the replication fork can ultimately lead to a collapse of the fork and generation of DSBs (Caldecott, 2024). High energy radiation, like X-rays and gamma rays, also directly cleave the DNA double helix, causing DSB formation (Chatterjee & Walker, 2017).

DSB repair pathways have been extensively studied. There are two main pathways responsible for repairing DSBs: homologous recombination (HR) and non-homologous end joining (NHEJ). They differ significantly in their mechanism, accuracy of repair and cellular context (Figure 13).

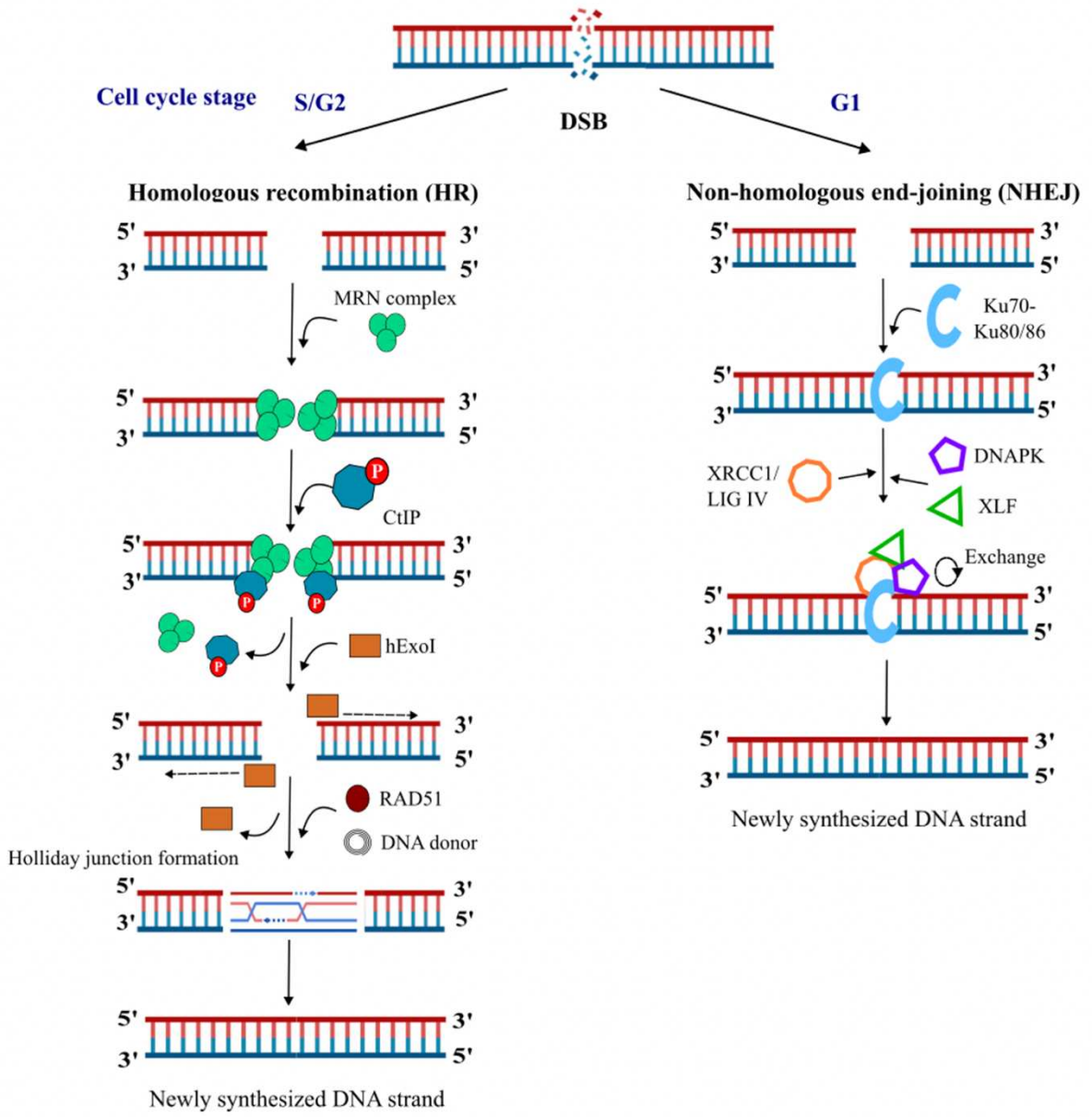


Figure 13: Schematic representation of the canonical steps involved in the two pathways of double stranded break repair (DSB); homologous recombination (HR) and non-homologous end-joining (NHEJ).

Illustration adapted from (Jensen et al., 2011)

3.3.1 Homologous recombination

Homologous recombination is a high-fidelity DSB repair pathway utilizing DNA strand invasion and template-directed synthesis (Figure 13). This pathway requires a homologous sequence or sister-chromatid and is thus only active during the S and G2 phases of the cell cycle. The first stage of recognition determines the extent and type of DSB. First, the MRN (MRE11-RAD50-NBS1) complex recognizes the DSB and initiates the HR pathway by binding to each end of the DSB (Figure 13). In parallel, it recruits ATM and TIP60, the latter activating ATM and subsequently phosphorylating

γH2AX. γH2AX anchors MDC1, which in turn is phosphorylated by ATM to function as a scaffold for the two ubiquitin E3 ligases, RNF8 and RNF168. The subsequent ubiquitination of γH2AX by these two E3 ligases acts as a docking site for the tumor suppressors, 53BP1 and BRCA1. Extensive studies have shown that BRCA1 and 53BP1 play antagonistic roles (Georgieva et al., 2024). BRCA1 successfully counteracts 53BP1, thereby initiating downstream HR processes (Chapman et al., 2012; Georgieva et al., 2024). First, a 5' to 3' nucleolytic degradation generates 3' overhangs committing to the HR pathway. Second, the endonuclease activity of MRN causes initial resection with CtIP, followed by a longer resection by EXO1 or BLM together with DNA2. This is followed by coating of the exposed bases of the 3' overhangs by RPA. RAD51 displaces RPA generating a nucleoprotein filament, formed by BRCA2 and PALB2. This nucleoprotein filament invades a neighboring DNA duplex forming a D-loop. To integrate the template DNA, RAD54 and RAD54B displace RAD51, allowing to begin synthesis by Polymerases δ, κ and ν (Chatterjee & Walker, 2017). Depending on the length of DNA to be synthesized, either the synthesis-dependent strand annealing (SDSA) factors are recruited or a Holliday junction is established by the BLM-TOPOIII-RMI1-RMI2 complex, GEN1 endonuclease, the MUS81-EME1 complex and the SLX1-SLX4 complex (Song et al., 2022; Chatterjee & Walker, 2017). Apart from this canonical HR pathway, SDSA and break-induced repair are two other variations of the HR pathway (Chatterjee & Walker, 2017). On the other hand, pre-existing and DSB induced histone PTMS in euchromatin and heterochromatin regions promote transcriptional activation (H3K36me and H3K4me2) and transcriptional repression (H3K9me3), both promote DSB repair by HR through interactions with distinct factors (Z. Chen & Tyler, 2022).

3.3.2 Non-homologous end-joining (NHEJ)

In NHEJ, there is no template strand required for the repair of DSBs and it is thus active throughout the cell cycle and notably during the G1 phase when HR is inactive. As a result, it is also error-prone, causing insertions or deletions of DNA bases at the sites of DSB. As illustrated in figure 13, the Ku complex (composed of Ku70 and Ku80) recognizes the DSB and immediately prevents end resection, serving as a scaffold for the recruitment of other NHEJ components, such as DNAPKs, XRCC4, LIG4 and XLF (XRCC4-like factor), forming the NHEJ complex. For example, the recruitment of DNA-PKcs has been shown to phosphorylate other NHEJ factors and itself (Yue et al., 2020). At the same time, XRCC4, a scaffolding protein, helps to stabilize the NHEJ complex by tethering the two DNA ends. Downstream factors, including Artemis, PNKP, APLF, WRN, APTX and Ku, then initiate DNA end processing (Chatterjee & Walker, 2017). Any gaps remaining after end resection are filled by DNA polymerases (POL μ) in a template-dependent manner and LIG4 ligates the non-homologous ends (Jensen et al., 2011).

3.3.3 DSB DNA repair foci

The regulation of chromatin compartmentalization in response to DNA DSBs is dependent on the state of the chromatin, repair-protein condensates, chromosome topology, chromatin loop extrusion and a variety of signaling pathways (Chiolo et al., 2025). Hi-C data has revealed that DNA damage initiates compartmentalization of the chromatin, but this effect differs depending on the genomic location of the DSB. A few studies have reported a change in the nature of the chromatin compartment in which DSBs occur, from compartment B (inactive) to compartment A (active), resulting in an increased accumulation of DSB sites in the latter (Arnould et al., 2023). Moreover, Hi-C maps have shown that sub compartments may be segregated into subsets of heterochromatin (compartments B1-B4) and euchromatin (A1-A2) following DSB induction, and PCA analysis of differential Hi-C maps suggest another segregated D compartment (for DSB induced) is formed composed of DSB sites within the euchromatin compartment (Arnould et al., 2023). Further investigations using RNAseq data showed an upregulation of the genes in the D-compartment pointing to a potential role in shepherding DDR proteins to DSB sites. Upregulated expression of DDR genes at DSB sites was notably observed in damaged TADs decorated with large clusters of γH2AX and 53BP1 bodies (Arnould et al., 2023; Chiolo et al., 2025). The upregulation of DDR genes causes the formation of R-loops, triple stranded structures formed by local retention of transcribed RNA within the DNA double helix. R-loops are key regulators within chromatin compartments and nuclear substructures and they have recently been shown to play a role in the formation of the D-compartment, also known as DNA repair foci (Arnould et al., 2023), with some examples illustrated in figure 14.

Recent studies are starting to reveal the nature and composition of these specialized membrane-less compartments formed after DSB induction, which are sometimes referred to as DNA repair foci (Figure 14). Poly (ADP-ribose) polymerase 1 (PARP1) is one of the earliest responders to DNA damage. Its enzymatic PARylation activity involves production of short or long, branched chains of poly (ADP-ribose) (PAR) from NAD^+ that are used to modify target proteins. PARylation has been proposed to control the initial response to DNA damage notably by increasing the accessibility of the chromatin and by facilitating the recruitment of DNA repair factors to sites of damage (García Fernández et al., 2025; Chaudhuri & Nussenzweig, 2017). Negatively charged PAR chains also strongly participate in phase separation through weak multivalent interactions, notably between intrinsically disordered regions (IDRs) of repair factors (Figure 14B). Furthermore, *in vitro* studies have shown that auto modification of PARP1 promotes dissociation of PARP1 from the break sites due to steric hindrance or electrostatic repulsion, making the sites available for further processing (Fijen & Rothenberg, 2021). ATM phosphorylation of histone H2AX causes chromatin relaxation. This increases the accessibility of proteins to the damage site, confining them within a TAD. The spread of γH2AX then promotes chromatin decondensation **(see chapter 2.4)** (Fijen & Rothenberg, 2021). This in turn facilitates the

recruitment of 53BP1 to form 53BP1 repair foci. 53BP1 interacts with the site of DSB formation in multiple ways, and in particular by binding to the demethylated histone H4K20 (Fijen & Rothenberg, 2021).

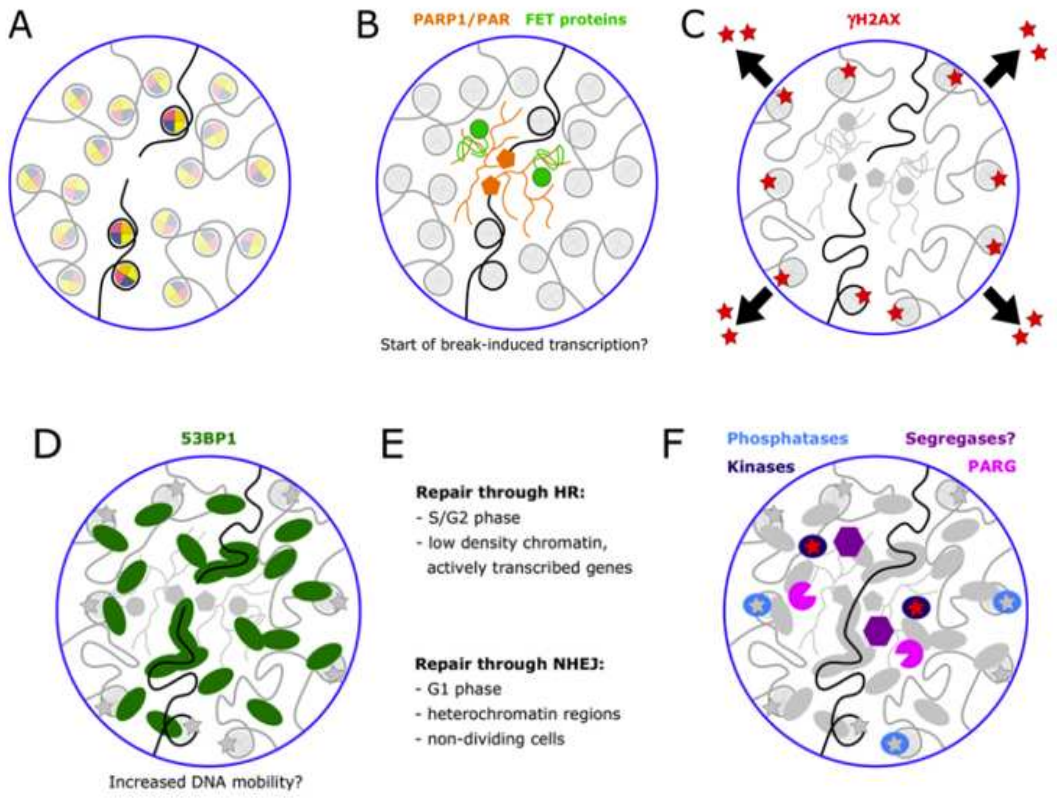


Figure 14: Proposed model of the formation and development of DNA repair foci in mammalian cells. (A) A DSB occurs leading to (B) a phase separated domain created by PARP1 by synthesizing PAR chains. This triggers recruitment of PAR chain binding motif and RNA binding proteins (FUS, EWS and TAF15) into the phase separated domain. (C) Phosphorylation of γH2AX by ATM is confined around the break site, leading to local chromatin decondensation. (D) 53BP1 is recruited to the break site, followed by (E) repair by HR or NHEJ double strand break repair pathways. Lastly, dissolution of the condensates is triggered by either PTMs or hydrolysis of the PAR chains (Fijen & Rothenberg, 2021).

The formation and regulation of these DNA repair foci still remain unclear. Understanding exactly how PTMs regulate DNA repair foci formation will be of importance, as will determining whether other DNA repair pathways are also associated with DNA repair foci.

3.4 Base Excision Repair (BER) Pathway

The BER pathway is a versatile repair process, specialized in the removal of small, non-helical – distorting base lesions (mutagenic or cytotoxic), such as oxidized bases (Figure 6) induced by reactive oxygen species (ROS), but also alkylated or deaminated bases, induced by endogenous or exogenous agents.

As illustrated in figure 15, the BER pathway can be divided into five stages: (i) recognition and (ii) removal of the base lesion, (iii) incision of the DNA to produce a single-strand break (SSB), (iv) end-processing of SSB ends, followed by (v) *de novo* repair synthesis (Krokan & Bjoras, 2013). In the first stage, the base lesion is recognized by monofunctional or bifunctional DNA glycosylases, which flip the damaged base out of the DNA helix into the selective catalytic site pocket and remove the base lesions via N-glycosidic bond cleavage generating abasic (apurinic/ apyrimidinic) (AP) sites (Krokan & Bjoras, 2013; Moe et al., 2022). In the case of monofunctional glycosylases, an activated water molecule is used for a nucleophilic attack on the N-glycosidic bond. The resulting AP sites are then incised on their 5' side by the AP endonuclease 1 (APE1) that acts downstream of the DNA glycosylase to create a SSB. This enzyme also removes 3'-blocking sugar moieties at strand breaks and generates a 3'-OH and 5' deoxyribose phosphate (5'-dRP). After removal of the damaged base, bifunctional DNA glycosylases, in contrast, can also nick the DNA backbone to introduce a SSB, but this time on the 3' side of the AP site. This is achieved thanks to the AP lyase activity of these bifunctional enzymes and a hydrolytic reaction involving the formation of a Schiff base intermediate. The resulting DNA contains either a 3' α,β-unsaturated aldehyde (β-elimination) or a 3'-phosphate (β,δ-elimination) that are converted to a 3'-OH by APE1 and a 5'-phosphate (Jacobs & Schär, 2012). Despite this bifunctional activity, in mammalian cells, APE1 has been shown to take over AP sites after excision of the damaged base by OGG1 (Vidal, 2001) and NTH1 (Liu et al., 2003; Marenstein et al., 2003). During the fourth stage of end processing, several downstream cofactors and enzymes prepare the damaged site for *de novo* synthesis via short or long patch repair, notably by removing the 5'-dRP. Here, DNA polymerase I fills the gap with one single nucleotide (short-patch BER) or 5-10 nucleotides (long-patch BER). The final stage of repair synthesis takes place when the newly synthesized strand is sealed by DNA ligase enzymes to complete its repair, restoring the original DNA sequence (Krokan & Bjoras, 2013; Freudenthal, 2017).

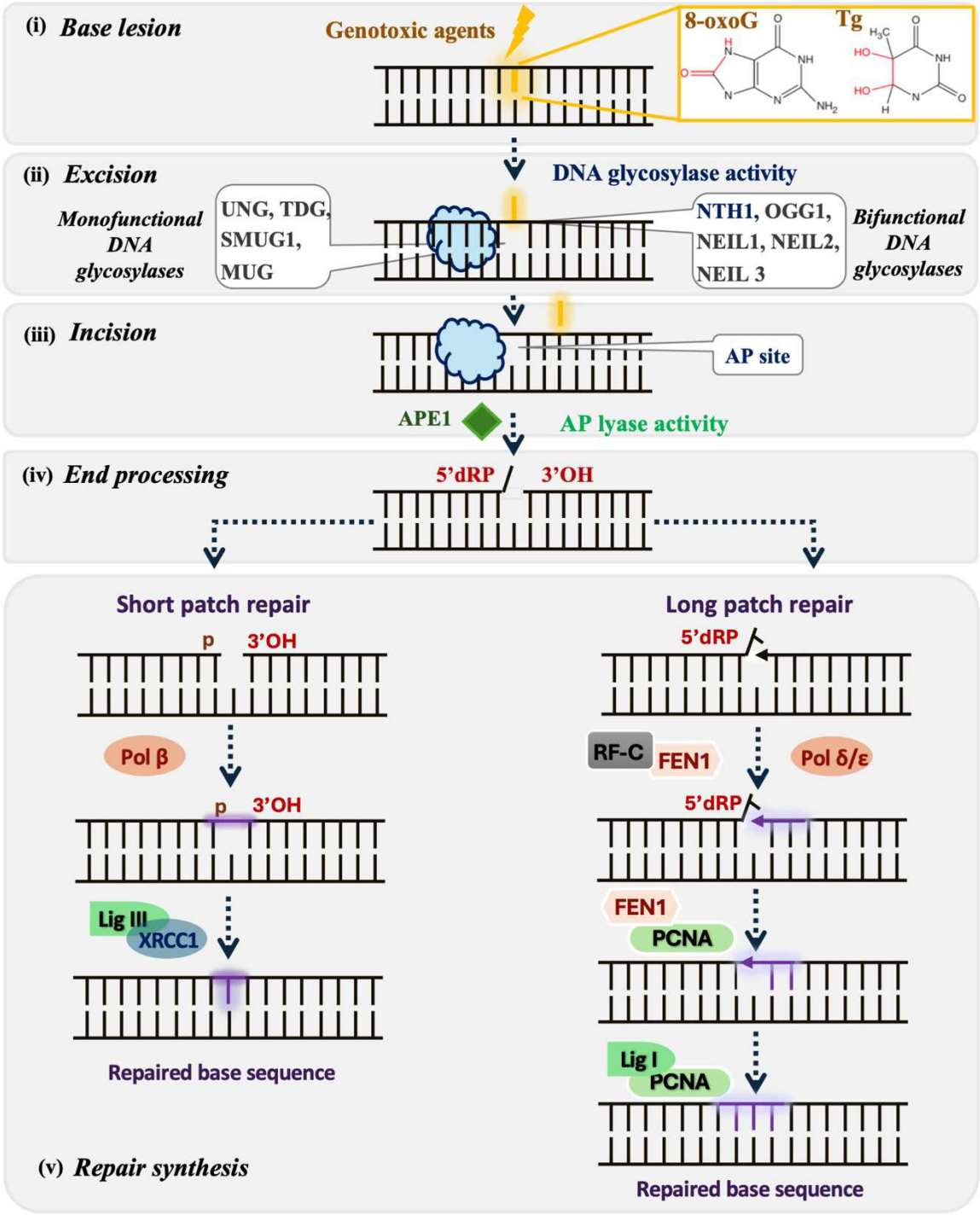


Figure 15: Simplified schematic representation of the BER pathway in mammalian cells.
A damaged base (yellow), for example, 8oxoguanine (8-oxoG) or thymine glycol (Tg) is recognized and flipped out of the DNA double helix by a mono or bifunctional DNA glycosylase enzyme (blue) that mediates base removal. Several cofactors and enzymes prepare the damaged site for de novo synthesis via short or long patch repair. Here, DNA polymerase β (orange) fills the gap with one single nucleotide

(short-patch BER) or 5-10 nucleotides (long-patch BER). The newly synthesized strand is sealed by ligase I and III (green). Adapted from (Krokan & Bjoras, 2013; Hans et al., 2020).

3.4.1 DNA glycosylases

DNA glycosylases are key initiation enzymes of the BER pathway involved in recognition and removal of base lesions (Hans et al., 2020, Dizdaroglu et al., 2017). They catalyzes the cleavage of the N-glycosidic bond between the substrate base and the 2'-deoxyribose to remove the damaged base efficiently (Carroll et al., 2021; Jacobs & Schär, 2012). Out of eleven known DNA glycosylases, discovered in mammals, six have been shown to recognize oxidative base lesions in humans and a summary of their characteristics and functions are described in table 3 (Jacobs & Schär, 2012; Krokan & Bjoras, 2013). Each DNA glycosylase exhibits a specific selectivity for a subset of chemically related base lesion, with some substrate overlap between different DNA glycosylases. This overlap became apparent in single-glycosylase mice knockout models, which showed no obvious phenotype (Krokan & Bjoras, 2013). In contrast, double OGG1 and MUTYH knockout mice models are strongly susceptible to a shortened life span or cancer (Krokan & Bjoras, 2013). Among the BER bifunctional DNA glycosylases, NTH1 and NEIL1 both repairs oxidized pyrimidines and ring-opened purines. They serve as backups for one another due to their overlapping substrate specificities (Chan et al., 2009). Similarly, triple knockout mice models targeting both uracil DNA glycosylases, UNG and SMUG1 together with MSH2 (MMR) cause shortened lifespans and lymphomas (Kemmerich et al., 2012).

DNA glycosylases involved in removal of oxidized bases can be classified into three structural families depending on their folds. OGG1 and NTH1 as well as MBD4 and MUTYH, are Hairpin-helix-hairpin (HhH) family members as they are possessing an HhH DNA-binding domain and a Gly/Pro-rich motif followed by a GPD motif, with Asp being the catalytic residue. The second family is the Fpg/Nei or H2TH family, whose DNA binding domain is a Helix-2-turns-Helix (H2TH) domain, and which also contains a β-sandwich and a long α-helix in its N-terminal (N-ter) domain whose end is the catalytic group. This group contains the three NEIL DNA glycosylases. The third family (UNG1 and UNG2, SMUG1 and TDG), includes DNA glycosylases organized around a β-sheet located between two α-helices fold. Finally, the fourth family comprises only one member, -the 3-methyladenine-DNA glycosylase (MPG) which does not contains any characterized specific fold and targets the damage caused by alkylation instead of oxidative stress (Hans et al., 2020). All known DNA glycosylases, regardless of the organism, and regardless of the family to which they belong, detect the lesion for which they are responsible by inserting an amino acid with an aromatic ring into the DNA double helix, thus serving as a sensor (Friedman & Stivers, 2010).

Once the lesion is found, it is extruded into the catalytic site, allowing its excision (Dizdaroglu et al., 2005; Sampath et al., 2012). As described above, DNA glycosylases can be either monofunctional

or bifunctional, depending on their catalytic activities. Monofunctional DNA glycosylases only possess DNA glycosylase activity, while bifunctional enzymes additionally possess an AP lyase activity to cleave the DNA backbone (Hans et al., 2020). However, the DNA ends left by bifunctional DNA glycosylases must be cleaned to allow DNA resynthesis. In the case of HhH family DNA glycosylases, this step is performed by AP-endonuclease 1 (APE1), while for NEIL proteins (H2TH family), the kinase PNK (polynucleotide kinase) takes over (Das et al., 2007). These two families exhibit different modes of action, thus generating chemically different ends.

Table 3: DNA glycosylases of the BER pathway and the major substrates recognized in dsDNA.

DNA glycosylase	Structural Motif Superfamily	Type	Substrate specificity	Recognized DNA structures	References
AAG/MPG (Tag-like)	MPG	Monofunctional	εA; 3-meA; 7-meG; 3-meG ; hypoxanthine	DSBs	(O'Brie & Ellenberger, 2003)
UNG and SMUG1 (UDG like)	α /β fold	Monofunctional	ss U; U:G; U:A; 5-hmU; 5-hoU; 5-fU	SSBs and DSBs	(Pettersen et al., 2007; Zharkov et al., 2010)
TDG (UDG like) and MBD4	α /β fold (HhH)	Monofunctional	T:meG; U:G; T:G	DSBs (CpG islands)	(Bellacosa, 2001; Hashimoto, 2014)
Adenine DNA glycosylase (MUTYH)	(HhH)	Bifunctional	Bases opposite 8oxoG/C/G	DSBs	(T. Nakamura et al., 2021)
8-OxoG DNA glycosylase 1 (OGG1)	(HhH)	Bifunctional	8-oxoG:C, FapyG:C	DSBs	(D'Augustin et al., 2022)
Endonuclease III-like protein 1 (NTH1)	(HhH)	Bifunctional	Tg, 5-OHC, 5-OHU, FapyG, FapyA	Bubbles, replication forks, SSBs and DSBs	(Ikeda et al., 1998; Carroll et al., 2021;

					Moe et al., 2022)
Endonuclease VIII-like 1, 2 and 3 (NEIL1, NEIL2, and NEIL 3)	(H2TH)	Bifunctional	Tg, 5-OHC, 5-OHU, FapyG, FapyA in general and NEIL2, specifically detects bubbles and loops.	Bubbles, replication forks, SSBs and DSBs	(Dou et al., 2008; Liu et al., 2013)

3.4.2 Lesion search by DNA glycosylases on chromatin fiber

The quest to understand how proteins, and in particular DNA repair factors, navigate the crowded nuclear environment in search of their rare DNA substrates (1D or 3D diffusion, DNA scanning, hopping between DNA molecules) has driven the development of cutting-edge experimental techniques capable of capturing single-molecule dynamics in real time (Misteli, 2020; D'Augustin et al., 2022; Schaich & Van Houten, 2021). In the case of DNA glycosylases, research has shown that they apply multiple modes of diffusion to maximize their speed and accuracy to search for DNA damage.

TIRFM (Total Internal Reflection Fluorescence Microscopy), was one of the first optical microscopy techniques used to study single proteins moving along individual DNA molecules. An evanescent field is created by reflecting a laser off the microscopic slide interface and buffer containing the sample. Here, individual long DNA molecules (in most cases, λ-DNA) are stretched along the surface and purified proteins (concentration < 10 nM) can be tracked and visualized along its entire contour length, within a penetration depth of 100 – 200 nm (Gorman & Greene, 2008). The eukaryotic recombinase RAD51, a member of the RecA family of DNA recombinases essential for homologous recombination, was the first DNA repair enzyme to experimentally demonstrate one dimensional unbiased diffusion, with a mean diffusion coefficient between 1.0 x 10^{-3} to 2.1 x 10^{-1} μm^2 s^{-1} that was consistent with theoretical calculations (Blainey et al., 2006; Granéli et al., 2006).

Similarly, TIRFM studies showed that hOGG1 (human 8-oxoguanine DNA glycosylase) also exhibits similar lateral diffusion properties with a mean diffusion coefficient of 0.55 ± 0.13 μm^2 s^{-1} (5 x 10^6 bp^2/s). hOGG1 demonstrated random bidirectional movement along the DNA and differences in binding lifetimes, depending on the buffer flow within the chamber (Blainey et al., 2006). Two prominent modes of diffusion patterns have been described for hOGG1 and TDG: (i) sliding along the DNA, while remaining bound to the DNA, termed as 1D diffusion, and (ii) hopping, where the protein

dissociates from one location and rebinds to the DNA in a new location (D'Augustin et al., 2020; Schnable et al., 2024). In some cases where the diffusion patterns might be altered, for example, in inaccessible stretches of DNA, the protein would be forced to dissociate and choose between sliding and hopping mechanisms. This type of diffusion is termed as intersegmental transfer and was observed in the case of TDG. However, for hOGG1, a 3D diffusion model was proposed termed as facilitated diffusion where the DNA glycosylase stochastically binds and diffuses along the DNA to locate its target site (Obmolova et al., 2000; Blainey et al., 2006; Gorman et al., 2007; Dey & Bhattacherjee, 2019). These characteristic modes of diffusion are illustrated in figure 16.

These potential modes of target-site location have been proposed and verified through *in vitro* single-molecule experiments that observe DNA glycosylases and have demonstrated diffusion coefficients in agreement with the Schurr rotation model (Blainey et al., 2009; Schaich et al., 2023). This model proposes that many proteins make non-specific contacts with DNA through electrostatic interactions with the DNA phosphate backbone. The diffusion property of the protein is dependent on the radius of the particle and so, the particle size scales differently for linear versus rotation diffusion. Therefore, as they move along the DNA helix, they rotate along the DNA helical axis by lateral movement, preventing the protein from skipping target sites via hopping or intersegmental transfer (Gorman et al., 2007; Blainey et al., 2009). In these studies, low salt concentrations were used to facilitate DNA binding and collect longer diffusion trajectories. Unfortunately, this does not represent the physiological salt concentrations, the pH dependence present *in vivo,* and does not provide information on transitions from one diffusion state to another (Gorman & Greene, 2008; Schaich & Van Houten, 2021). Also, importantly, the behavior of the enzyme depends on several factors: (a) its concentration, (b) the level of DNA compaction, which regulates the accessibility to base lesions, (c) the protein shape, which allows it to either diffuse or scan the DNA more freely or in a restricted manner, and (d) molecular crowding within the nucleus (Dey & Bhattacherjee, 2019; Carroll et al., 2021; D'Augustin et al., 2023). TIRFM studies cannot fully recapitulate *in vivo* conditions were the heterogeneous nuclear environment poses many obstacles. Higher-order chromatin compaction for instance provides stationary roadblocks like nucleosomes that inhibit the diffusion of repair proteins (Blainey et al., 2006; Gorman & Greene, 2008; Blainey et al., 2009; Schaich et al., 2023).

Instead of using purified proteins to study single – molecule dynamics, a novel technique known as SMADNE (Single-Molecule analysis of DNA binding proteins from Nuclear Extracts), combines TIRF C-trap and single-molecule FRET, to investigate native DNA repair proteins, namely hOGG1, APE1, PARP1, Pol β within a nuclear fraction. This allows rapid screening of variants, determining the reaction kinetics of binding events ('k_{on}' and 'k_{off}' rates), binding substrate specificity and movement of DNA glycosylases along the DNA, providing simultaneous information on the intermediate environment of purified proteins and the heterogeneity of the nucleus. SMADNE on the Lumicks C-trap instrument places the optical tweezers in the middle of the flow cell and not at the bottom in classical

TIRFM, avoiding possible nuclear debris (Gorman & Greene, 2008; Schaich et al., 2024). Interestingly, hOGG1 was found to bind more weakly to oxidative DNA damaged sites in nuclear extracts, than when used as a purified protein, suggesting it may be modified in these extracts (Schaich et al., 2024).

Since its early discovery in the 1990's, *in vitro* studies using recombinant hOGG1 have elucidated its central role in repairing 8-oxoguanine, one of the most abundant DNA lesions generated by ROS. Its structural and enzymatic activity discovered earlier on, catapulted its fame as a model bifunctional DNA glycosylase. Single-molecule characterization of recombinant hOGG1 expressed in nuclear extracts revealed the average diffusivity of the DNA glycosylase to be 0.55 $\mu m^2 s^{-1}$ similar to results obtained from classical TIRFM (Gorman & Greene, 2008; Schaich & Van Houten, 2021; Kim & Pak, 2024a). However, the data collected was modeled by a two-state model: faster diffusion of one state and slower diffusion in the second state, potentially generated by two physical conformations of hOGG1 as it moves along the DNA (Hu et al., 2005; Schaich & Van Houten, 2021). A three-state diffusion model for hOGG1, translocating along DNA, derived from all-atom molecular dynamics simulations showed 3 key conformational states: L1 (helical sliding), L2 (groove tracking) and L3 (freely diffusing) exhibiting distinct diffusion constants (DL1 < DL2 < DL3) and transition barriers, with L1 experiencing a 6 kBT free-energy barrier. The model aligns with experimental findings, elucidating how hOGG1 efficiently locates damaged DNA bases through thermal transitions and rotational adjustments. Enhanced sampling methods enabled determining detailed free energy landscapes, revealing that hOGG1 predominantly resides within a 34 Å radius from the DNA axis, facilitating rapid damage detection and repair (Kim & Pak, 2024a, 2024b). Single-molecule studies on stretched DNA showed that hOGG1 slides in persistent, rotation-coupled contact with the duplex, achieving near-theoretical diffusion rates ($\approx$1 kb $\cdot$ 0.1 s^{-1}) and then performs short 2D/3D hopping steps when it encounters obstacles or tightly packed chromatin. During scanning, hOGG1 induces sharp DNA kinks that extrude bases into an "exosite". FCS performed on OGG1-GFP in the nucleus of living cells further shows impaired lesion-dependent mobility changes in hOGG1 mutants compared to wild type, reinforcing the importance of lesion binding for effective recruitment (D'Augustin et al., 2023). Fluorescence-recovery after photobleaching (FRAP) is also an extremely powerful ensemble approach used to probe the diffusive properties of proteins within their cellular environment. FRAP measurements have notably shown that the nonspecific DNA binding constants of DNA glycosylases may be orders of magnitude weaker than the binding constants at the damage site. It is therefore believed that DNA glycosylases would rather be present in a weakly bound state than in an unbound state, permanently residing on the DNA double helix (D'Augustin et al., 2020; Schaich & Van Houten, 2021).

Upon oxidative stress ($KBrO_3$ or H_2O_2 treatment), soluble hOGG1 rapidly (within seconds) accumulates on chromatin, as seen by FRAP and live-cell imaging of hOGG1-GFP. When a focused laser (Campalans et al., 2013; D'Augustin et al., 2023) or proton beam (Robeska et al., 2024) creates a local 8-oxoG burst, hOGG1 is similarly recruited to the damage site within a few seconds. Live-cell

imaging of OGG1-GFP shows a rapid increase of fluorescence at the irradiated region, reaching a clear focus by ≈10 s and persisting for tens of seconds to minutes as repair proceeds. This swift accumulation is accompanied by a drop in nuclear mobility: FRAP experiments reveal that the mobile fraction of hOGG1 becomes markedly reduced after laser-induced lesions, indicating that the enzyme is now bound to chromatin rather than freely diffusing. Recruitment occurs independently of PARP1 activity, as PARylation inhibition does not prevent OGG1's arrival at the laser stripe. Therefore, laser-induced 8-oxoG lesions trigger an immediate, PARP-independent recruitment of OGG1, a rapid immobilization on chromatin, and a retention period that mirrors the enzymatic removal of the lesion (D'Augustin et al., 2020, 2023)

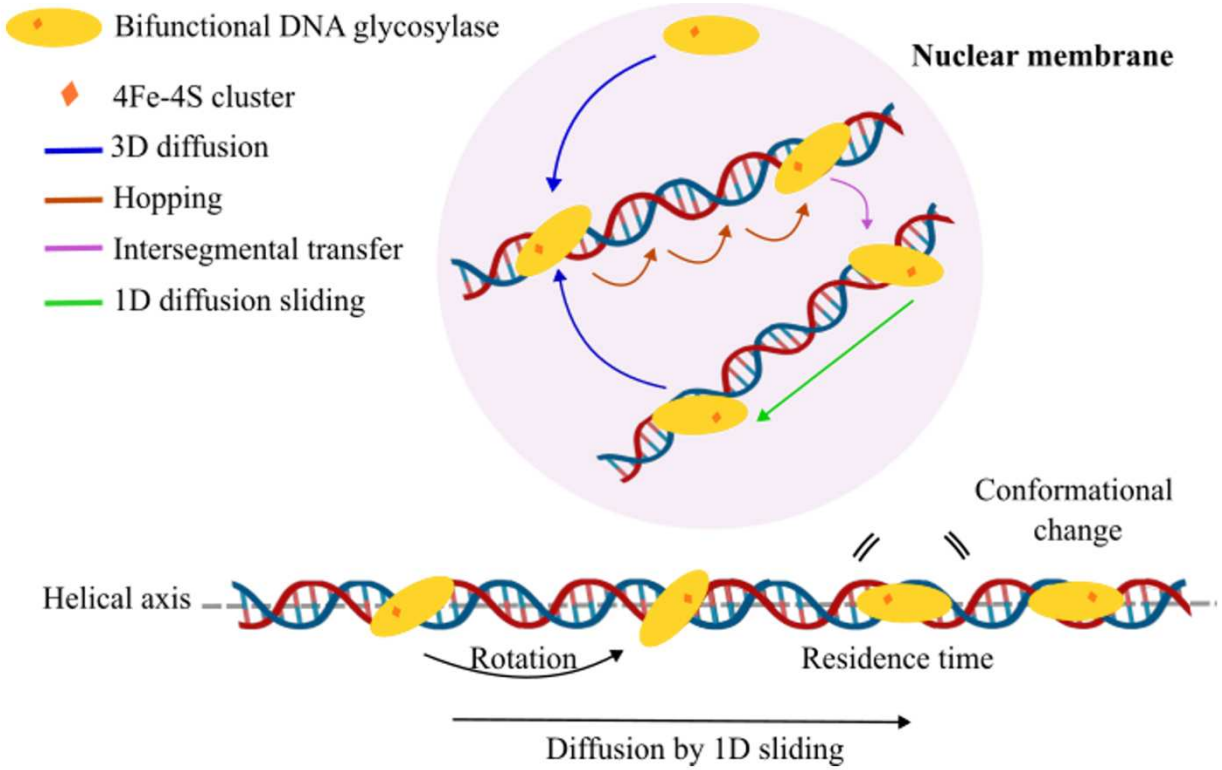


Figure 16: Potential modes of target-site location of bifunctional DNA glycosylases (e.g. OGG1). Potential modes of target-site location have been proposed and verified through single-molecule experiments that observe DNA glycosylases (yellow) like hOGG1 undergoing 3D diffusion (blue line), hopping from one target sequence to the next (orange line), intersegmental transfer (pink line) by completely skipping a part of the DNA sequence and 1D diffusion by sliding (green line) along the dsDNA. The energy landscape of the protein suggests that they could rotate around the helical axis of dsDNA ensuring they stay bound to the DNA at all times. Due to obstacles encountered along the length of dsDNA, they may halt their diffusion for short periods of time known as 'residence time'.

Information derived from experiments on how DNA repair proteins find their substrates, their residence time at repair sites, the assembly and disassembly during repair processes using endogenous

or ectopically expressed target proteins, provide important insights into their dynamics within the heterogeneity of the nuclear environment (Schaich & Van Houten, 2021).

In addition, SMLM techniques like dSTORM or (spt) PALM, are beginning to offer new insights into the dynamics of single molecules in live cells. Like in the case of Rad52, a functional homolog of BRCA2 in yeast. By using single-particle tracking, the initial two diffusive behaviours of Rad52 was found to be slower and exhibit confined motion within DSB repair foci (Miné-Hattab et al., 2021). This similar change in diffusive behavior was also discovered by Heyza and team. They systematically analyzed the recruitment kinetics of 21 Halo-tagged DNA damage response factors, in U2OS cells, to micro irradiated sites containing DSBs. This work describes most DNA repair proteins of the NHEJ and HR pathways, having two distinct nuclear populations of molecules, representing a freely diffusive fraction and a chromatin-bound fraction (Heyza et al., 2023). However, further investigations and challenges remain in understanding how DNA glycosylases navigate across compact chromatin, how PTMs and chromatin remodeling enable repair *in vivo*, and how they play equally important roles in regulating the process of lesion recognition.

Remodeling of chromatin is generally thought to act in two stages. The first is coordinated by histone PTMs, while the second is driven by ATP-dependent chromatin remodelers (Madders & Parsons, 2020). Histone H2B ubiquitination by Mdm2 in position K120 was found to be induced in response to oxidative DNA damage and is associated with chromatin remodeling (Rodriguez et al., 2018). Histone acetylation has also been shown to stimulate OGG1 activity on H2B mononucleosome substrates (Madders & Parsons, 2020; Rodriguez et al., 2018). For the second stage, *in vitro* studies have demonstrated that ATP-dependent chromatin remodeling (ACR) by the SWI/SNF complex is needed for efficient repair of 8-oxoG, allowing hOGG1 and APE1 access to the lesion site (Krokan & Bjoras, 2013; Odell et al., 2013). A member of the SNF2 superfamily of chromatin remodelers, Amplified in Liver Cancer 1 (ALC1) has also shown to be recruited to sites of laser micro-irradiation in U2OS cells in a PAR-dependent manner, promoting chromatin relaxation (Ahel et al., 2009).

PTMs also directly regulate the dynamics of DNA glycosylases. Figure 17 provides an overview of the different PTMs and their functions in regulating DNA glycosylases during the various steps from DNA damage recognition to DNA repair. Several reports have highlighted the role of PTMs in DNA repair coordination and regulation, without requiring *de novo* protein synthesis. PTMs can regulate DNA glycosylase proteins levels, their catalytic activities, substrate specificity, protein trafficking and interactions with other protein partners. Consequently, dysregulation of PTMs can cause major DNA repair problems, leading to genomic instability (Bai et al., 2020). The most abundant PTMs, such as phosphorylation and acetylation, have been identified on DNA glycosylases including UNG, hOGG1 and NEIL1. PTMs like ubiquitination and SUMOylation of protein substrates are known to regulate protein degradation, cellular re-localization and serve as a protein binding platform with alternate

binding partners. These events are tightly controlled by both E3 ubiquitin/SUMO ligases and deubiquitinases/deSUMOylases (S. Su et al., 2020). For example, SUMOylation of the BER enzyme, Thymine DNA glycosylase (TDG) removes mis paired thymine or uracil opposite guanine and alters its DNA-binding affinity resulting in increased enzymatic turnover on G: U-containing substrates and impaired activity on G:T substrates. Furthermore, a recent study also suggests that SUMOylation of TDG may facilitate the recruitment of other partner proteins to the sites of DNA damage (Pidugu et al., 2024).

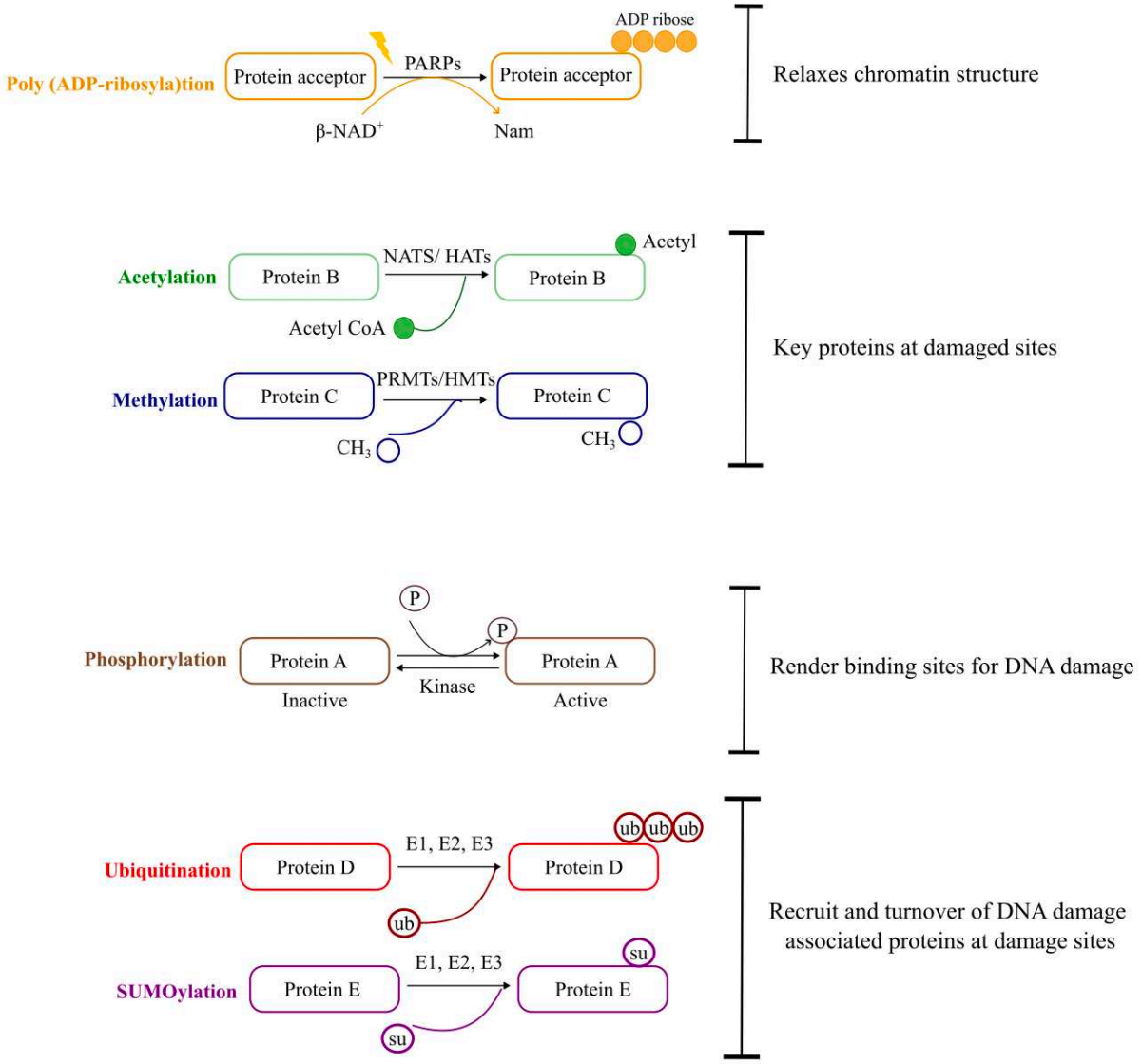


Figure 17: Types of post translational modifications (PTMs) observed on DNA glycosylases in response to DNA damage, stimulating various DNA repair pathways.
Illustration adapted from (Bai et al., 2020)

A dominating view is the requirement for chromatin remodelers and PTMs to facilitate BER enzymatic activity at sites of DNA damage, particularly within occluded nucleosomal regions. BER functioning within the cellular chromatin environment is still largely unexplored. Elucidating the

mechanisms behind ACRs directed to sites of BER and their target activity on either tightly packaged chromatin domains or global DNA damage also remain to be investigated to help us understand how BER enzymes actively search for DNA damage (Madders & Parsons, 2020).

3.4.3 Long and short patch BER

After the creation of the SSB, the downstream BER steps can be subdivided into two sub-pathways: the short-patch BER (sp-BER), which allows the replacement of a single nucleotide, and the long-patch BER (lp-BER), which excises and replaces 2 to 8 nucleotides. The use of one pathway over the other is dictated by the recruited DNA glycosylase, the physiological state of the cell, the type of lesion and the availability of BER factors (Krokan & Bjoras, 2013). Monofunctional DNA glycosylases appear to be able to initiate both pathways, but bifunctional DNA glycosylases (particularly hOGG1 and NTH1) preferentially engage in sp-BER (Figure 15) (Freudenthal, 2017). Furthermore, while sp-BER appears to be active in proliferating and non-proliferating cells, lp-BER may be implemented during or after replication (Dizdaroglu, 2005; Krokan & Bjoras, 2013). sp-BER occurs in three main steps after the generation of an AP site, by a DNA glycosylase. First, XRCC1 (X-ray repair cross-complementing protein 1), a scaffolding protein essential for the proper execution of BER, is recruited by DNA glycosylases and serves as an anchor for all subsequent repair factors. Incision of the AP site by APE1 leaves a one-nucleotide gap or SSB that is filled by DNA pol β. Finally, the newly incorporated nucleotide is sealed to the rest of the strand by ligase III (Figure 15) (Krokan & Bjoras, 2013; Wallace, 2014). During the whole process, the lesion and the repair intermediates are never left alone. Repair proteins are displaced one after the other by the following ones, in order to protect the DNA and avoid more serious consequences (degradation by endonucleases, breaks (single or double strand), chromosomal rearrangements, etc). lp-BER is more complex, comprising more steps and involving more proteins. The first steps are similar to sp-BER, the lesion is recognized and excised by a DNA glycosylase and the resulting AP site is taken over by APE1. This is where the two pathways diverge. Replication Factor C (RFC) loads PCNA, which is necessary for DNA pol β to initiate repair synthesis. The rest of the synthesis is carried out by replicative DNA pol δ/ε, thus generating a DNA flap, released by FEN1 (Flap Endonuclease 1). Finally, ligase I allows ligation to the old strand (Figure 15) (Krokan & Bjoras, 2013).

3.4.4 Role of PARP proteins in BER

PARP proteins were briefly introduced in **section 3.3.3**, when describing their role in DNA repair foci formation (Figure 13). Apart from this, they are also implicated in the BER pathway, (specifically, PARP1 and PARP2), by the addition of PAR chains and PAR moieties via mono PARylation to proteins in the vicinity of the damaged DNA, including itself and histones (Dantzer et al., 1999; Krokan & Bjoras, 2013). PARP1 has been implicated in cellular signaling, playing an

important role in sensing SSBs and recruiting downstream DNA repair proteins during oxidative stress (Krokan & Bjoras, 2013; Sergeeva et al., 2024). PARylation induces chromatin relaxation allowing access to repair proteins. Conflicting reports found that PARP1-deficiency or PARP1 inhibition may or may not cause hypersensitivity to alkylating agents (for example with MMS), known to cause base lesions (Pachkowski et al., 2009). However, PARP1 is required for downstream processing of single-stranded breaks (SSBs) (Caldecott, 2024; Dantzer et al., 1999). One of the main proteins to be recruited via PARylation is XRCC1, however, its recruitment can also be PAR-independent in the case of BER (Campalans et al., 2013). Interestingly, YB1 has also been shown to interact with several key BER proteins, including PARP1 and PARP2 along with pol β, NEIL1 and APE1. YB1 exhibits a dual role in regulating Poly (ADP-ribose) (PAR) synthesis by PARP1 (Sangermano et al., 2020). At low levels of DNA damage, YB1 can interfere with PARP1 activation on lesions. However, in conditions with excessive DNA damage, YB1 actively stimulates PARP1 activity (Shaw et al., 2024). This study suggests that YB1 may act as a "molecular glue" within the BER pathway, facilitating the assembly of repair complexes, or "BERosomes." This highlights a shift in understanding BER from a "passing the baton" model to dynamic "BERosomes," where accessory proteins like YB1, with intrinsically disordered structures and multivalent interactions, may act as platforms to stabilize dynamic repair complexes through multiple weak interactions (Guay, Evoy, et al., 2008; Alemasova et al., 2016; Senarisoy et al., 2020).

3.4.5 Crosstalk between BER with other DNA repair pathways

The interplay between DNA repair pathways ensures that processes are tightly regulated and integrated within the global cellular response to DNA damage. Here, I discuss how some BER repair factors are implicated in other DNA repair pathways or recognize and stimulate repair of other substrates.

In most cases, SSBs are formed from oxidative damage to DNA, from abasic sites or by erroneous activity of DNA topoisomerase (TOP1) during gene transcription, when Okazaki fragments form unligated intermediates during DNA replication (Hegde et al., 2008; Chatterjee & Walker, 2017; Pommier et al., 2022). Studies have observed an overlap between different SSB repair pathways such as, the BER (Caldecott, 2024), NER (Marteijn et al., 2014), MMR (Ghodgaonkar et al., 2013) and ribonucleotide excision repair (Kellner & Luke, 2020). The canonical single-strand break repair (SSBR) pathway is stimulated by PARP1 activity. If SSBs remain unrepaired for a long time, this leads to hyperactivation of PARP1, the major SSB sensor protein, leading to rapid poly(ADP) ribosylation, and recruitment of the scaffold protein XRCC1. This protein, in turn, recruits XRCC1 and most of the end - processing enzymes such as polynucleotide kinase phosphatase (PNKP), aprataxin (APTX), DNA polymerase β (POL β) and DNA ligase III (LIGIII), initiating the SSB repair pathway (Caldecott, 2024). On the other hand, the long patch SSB repair involves the DNA topoisomerase (TOP1), in a variant of

the PARP1-dependent long patch repair of the BER. Here, the end processing is carried out by the TDP1 (tyrosyl-DNA phosphoesterase 1) that removes TOP1 from the 3' end (Chatterjee & Walker, 2017; Mei et al., 2020; Caldecott, 2024).

A study conducted by Sergeeva and coworkers, describes the crosstalk between BER and NHEJ pathways by investigating the expression levels of XRCC1, LIG3 and APE1 from BER and the Ku70/ Ku80 genes in NHEJ, in telomerase-immortalized hTERT-modified cells (human bronchial epithelium cell line - NBE1) (Sergeeva et al., 2024). Suppressing the expression of hTERT in NBE1 cells demonstrated that both scaffolding proteins XRCC1 and XRCC4 rely on each other and are possibly regulated by intermediate steps in both repair pathways. This may be linked to transcriptional regulation or mRNA metabolism. XRCC4 depletion elevated Sp1 and p53 levels, inducing a G1/S delay in the cell cycle, in normal but not hTERT-overexpressing cells, where the opposite effect occurred. These findings indicate that loss of a single DNA repair scaffold triggers broader cellular responses, extending beyond repair systems (Sergeeva et al., 2024). Therefore, the crosstalk between BER and NHEJ is suggested to reflect an integrated regulatory network essential for maintaining genome stability and coordinating cell-cycle responses.

Several reports provide supporting evidence of an active crosstalk between the BER and NER pathways. The model organism, *C. elegans* has been extensively used to study the crosstalk between NER factors, such as ERCC4, CSB and ATXN3, and BER nuclear factors ATR, TPD1, NEIL1, OGG1 and APE1 contributing to neurodegenerative diseases (NDDs) (Gupta et al., 2021). For example, neuroinflammation, observed in Alzheimer's disease (AD), Parkinson's disease (PD), and Amyloid Lateral Sclerosis (ALS) promotes oxidative DNA damage while suppressing DNA repair. This mechanism of inflammatory signaling forms a vicious cycle that amplifies neurodegeneration (Gupta et al., 2021). AD brains show DNA damage, with reduced activity of DDR proteins (ATM, BRCA1, DNA-PK) and BER enzymes (hOGG1, NEIL1, POLβ) (Rao et al., 2000). This suggests lower POLβ expression in aging and AD impairs repair, while Polβ-deficient mice display memory loss and neuronal death, strongly correlating defective DNA repair to AD pathology (Lovell et al., 2000). In Parkinson's disease (PD), BER glycosylases (hOGG1, MTH1, MUTY1) are elevated in dopaminergic neurons, with hOGG1 loss causing 8-oxoG accumulation and behavioral defects. PD genes, including Parkin, regulate APE1, linking BER to SSBs (Murakami et al., 2007). Elevated AP sites, α-SYN aggregation, and PARP1/PARylation further connect DDR dysfunction to PD pathology (Mastrocola et al., 2013). In ALS, DNA glycosylases APE1 and hOGG1 are upregulated in brains and motor neurons, likely reflecting compensatory responses to oxidative stress, supported by promoter hypomethylation. DDR defects also involve TARDBP/TDP-43 and FUS, which impair NHEJ through defective recruitment of XRCC4/LIG4 and PARP1 interactions (Mitra et al., 2019). Furthermore, during transcription, the NER factor CSB (Cockayne Syndrome Protein B) has been shown to specifically recruit XRCC1 to BER-generated SSBs (Wallace, 2014; Menoni et al., 2018).

Extensive studies using advanced imaging technology on the BER DNA glycosylases hOGG1 have opened up new avenues to explore other cross talks between DNA repair pathways (D'Augustin et al., 2020). For example, UV-DDB1, a NER damage sensor is also implicated in BER, detecting 8oxoG. However, its affinity for 8oxoG: C pairing is weaker than hOGG1, and its recruitment to 8oxoG sites on telomeres, stimulating increased enzymatic activity of hOGG1, MYH and APEl (Kumar et al., 2022).

The following Chapter is entirely dedicated to NTH1 but we can already refer to the work of Gautam et al., 2023, who observed that human RPE-1 cells follow a BER-dependent pathway to repair a subset of UV photodimers (6-4PPs and CPDs), suggesting an additive yet alternative repair pathway independent of NER participation. During the early stages post UVC radiation, NTH1 and APE1 are triggered to the damage site, and actively recruit downstream BER factors such as PARP1, XRCC1 and FEN1. On the other hand, loss of PARP1, XRCC1 and FEN1 slows down the repair rate and sensitizes cells to UVC radiation by 2-fold (Gautam et al., 2023). NTH1 may also sequester XPG, an NER endonuclease, thereby reducing the repair of thymine glycol or cisplatin - adducts (Klungland et al., 1999; Kar et al., 2024) **(see chapter 4.3.2 for further details).**

Chapter 4: NTH1 - DNA glycosylase

One of the key DNA glycosylases of primary interest to our team at IBS, is the human DNA glycosylase NTH1. It is an evolutionary conserved endonuclease-III bifunctional enzyme (37 kDa) belonging to the HhH superfamily of DNA glycosylases. It primarily recognizes and excises oxidatively damaged pyrimidines including 5-OHC and Tg (Ikeda et al., 1998; Marenstein et al., 2003; Sarre et al., 2019), but has also been reported to excise the ring-opened FapyA, resulting from a hydroxyl radical attack on adenine (see figure 6 for the formula of the oxidized bases recognized by NTH1) (Hu et al., 2005). Here, I present a comprehensive review of our current understanding of its structure, function and regulation in the context of chromatin and oxidative stress.

4.1 NTHL1 gene structure and evolutionary conservation

The human NTHL1 gene encoding for the protein NTH1 is a housekeeping gene of 317 residues. NTH1 is composed of two regions (Figure 18): a largely disordered mammalian-specific N-terminal domain (NTD – residues 1-89) and the well folded catalytic core (residues 90-317).

The intrinsically disordered NTD domain bears a bipartite nuclear localization signal (NLS) sequence within residues 36-60 and a mitochondrial targeting signal (MTS) within residues 1 to 30 (Figure 17). Both NLS sequences are needed to transport the protein into the nucleus (Luna et al., 2000; Ikeda et al., 2002). Several studies have reported that hNTH1 was sorted into the nucleus and mitochondria of HeLa and COS-7 cells (Takao et al., 1998; Luna et al., 2000; Takao, 2002; Ikeda et al., 2002). However, within mammalian eukaryotes, the full-length hNTH1 fused to EGFP was found exclusively in the nucleus of HeLa cells, whereas the mouse NTH1 (mNTH1) protein was mainly transported to the mitochondria, with a relatively small amount observed in the nucleus. Despite ~ 85% sequence homology between hNTHL1 and mNTHL1, the NTD regions are quite different (with ~ 60% sequence identity), which may explain these different subcellular distributions. The intracellular sorting of hNTH1 into the mitochondria was first demonstrated by substituting three arginine residues, with alanine or aspartic acid (R49A and R49D) in the NLS sequence of hNTH1, resulting in the translocation of the protein into the mitochondria (Ikeda et al., 2002; Luna et al., 2000). Oxidative damage of mtDNA is one of the primary causes of mutations and mtDNA instability. In humans, seven of the eleven known DNA glycosylases have MTS sequences. For example, hOGG1 is a key enzyme for the repair of oxidative damage in mtDNA (Rong et al., 2021; Sampath et al., 2012; Takao, 2002). Using *in vitro* biochemical assays and *in cellulo* molecular biology techniques, HEK293 and U2OS cells with deleted hNTHL1, demonstrated an unexpected increase in mitochondrial – copy number (CN) even though there was high accumulation of mtDNA damage with altered transcript levels of mitochondrial – related genes. This correlated with an increase in oxidative phosphorylation (OXPHOS) protein levels and enhanced mitochondrial respiratory activity. It was suggested that loss of hNTH1 activity may confer

cellular resilience through compensatory mechanisms, to sustain mitochondrial function rather than leading to cellular dysfunction (Hubers et al., 2024).

Because of its intrinsically disordered nature, the NTD region was deleted for successful crystallization of the catalytic core of NTH1 and its structure determination (Carroll et al., 2021).The catalytic core comprises two globular helical domains connected by two linkers, namely Linker 1 and Linker 2. The first globular domain, hereby addressed as the 4Fe-4S domain, is composed of the N- and C-terminal regions of the catalytic core and contains a [4Fe-4S] cluster that plays a essential role in DNA binding and substrate recognition. The second globular domain, addressed here as the hairpin domain, is a six-helical bundle containing the HhH DNA binding motif. Linkers 1 and 2 are located in proximity to the six helical bundle and HhH motif respectively (Carroll et al., 2021; Moe et al., 2022).

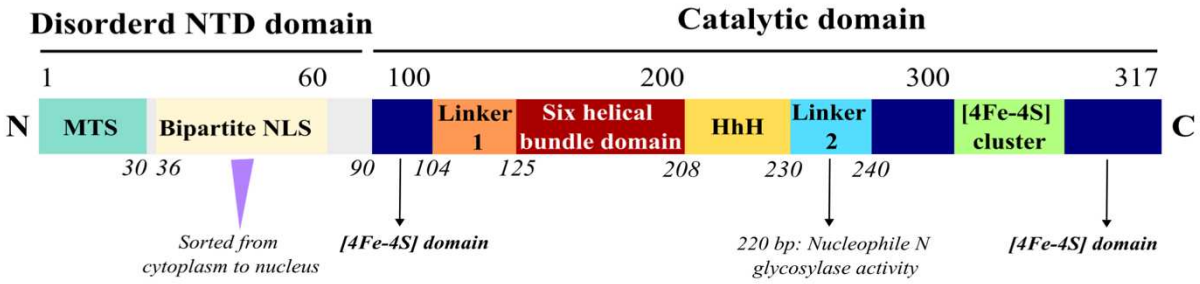


Figure 18: Schematic representation (linear) of isoform 3 of NTHL1 domain organization.
From the N-terminus to C-terminus, the illustration highlights the disordered NTD domain and catalytic domain. NTD: MTS (mitochondrial targeting signal) and Bipartite NLS (nuclear localization signal). In the catalytic domain, linker 1 (orange), six helical bundle domain (red), hairpin-helix-hairpin DNA motif (HhH – yellow), linker 2 (cyan), iron-sulphur [4Fe-4S] cluster (green) within the [4Fe-4S] domain.

NTHL1 is an evolutionary conserved gene across different species (Table 4). In Eukarya, human and mouse NTHL1 share ~ 85-90% of sequence identity. Therefore, mice NTHL1 knockout models are widely employed to investigate the mechanisms of tumor susceptibility (Chan et al., 2009; Vallabhaneni et al., 2013). In lesser eukaryotes, such as the nematode *Caenorhabditis elegans*, NTHL1 has ~ 60-70% sequence identity with the human ortholog and ~ 40% with *Saccharomyces cerevisiae*. *C. elegans* is extensively used to study the BER pathways' response to oxidative stress, particularly the role of NTH1 in repairing single DNA base damage. Furthermore, it is utilized in models of human tauopathies to examine the involvement of DNA glycosylases in neurodegenerative disease development and progression (Elsakrmy et al., 2020; Tiwari et al., 2024).

In the yeast species, *Saccharomyces cerevisiae* and *Schizosaccharomyces pombe,* NTHL1 orthologs, known as Ntg1/2, are studied in the context of stress response and repair due to fewer BER

enzymes and notably, *S. cerevisiae* Ntg1/2 does not have an 4Fe-4S cluster (Ikeda et al., 1998; Osman et al., 2003; A. Chen et al., 2024). Bacterial and eukaryotic homologs are known to share ~ 30% sequence homology. For example, both *E. coli* and human NTH1 homologs are involved in DNA binding and catalysis using key residues such as, the lysine (K220) from the hairpin domain and the aspartate (D239) from the 4Fe-4S cluster domain. However, unlike their bacterial counterparts, mammalian NTH1 contains an additional NTD (Ikeda et al., 1998) proposed to act as a site for PTMs and protein-protein interactions, in addition to harboring the NLS and MTS signals (Carroll et al., 2021; Moe et al., 2022; Odstrcil et al., 2024).

Table 4: Comparison of characteristic features between NTHL1 orthologs in different species.

Domain	Species	Gene	Sequence Similarity to Human	Localization	Biological Function	Evolutionary Conservation	References
Eukarya	*H. sapiens*	NTHL1	Reference	Nuclear/ Mitochondria	Repairs oxidized pyrimidines; BER	Highly conserved across domains	(Carroll et al., 2021; Moe et al., 2022)
Eukarya	*M. musculus*	Nthl1	~85–90%	Nuclear	Tumor susceptibility in KO	Conserved in vertebrates	(Chan et al., 2009; Hu et al., 2005; Vallabhaneni et al., 2013)
Eukarya	*C. elegans*	nth-1	~60–70%	Predicted nuclear	Genome stability under oxidative stress	Single functional homolog	(Elsakrmy et al., 2020; SenGupta et al., 2021; Tiwari et al., 2024)
Eukarya	*S. cerevisiae; S. pombe*	Ntg1/ Ntg2	~30–40%	Nucleus/ Mitochondria	Stress response & repair	Functional analogs	(B.-C. Chen & Lin, 2022; Chen et al., 2024)
Bacteria	*E. coli*	nth	~50%	Cytoplasmic	BER prototype enzyme	Archetypal homolog, ancestral origin	(Ikeda et al., 1998; Osman et al., 2003)

Endonuclease III (EndoIII or NTH) was first identified in *E. coli* as a nuclease (Thayer et al., 1995) that generates single-strand nicks in UV – irradiated double stranded DNA (Radman, 1975). It was the first DNA glycosylase discovered to possess an iron-sulphur (Fe-S) cluster (Cunningham et al., 1989) and was rapidly found to be present across all domains of life (Figure 19A). The Fe-S cluster was initially proposed to play more of a structural role, but subsequent studies that elucidated NTH1's mode of DNA binding involving a dual strand engagement (lesion and DNA complementary strand) process, suggested that the Fe-S cluster may contribute to stabilizing the DNA strands for lesion recognition and catalysis (Fromme, 2003; Fromme et al., 2004). Oxidation of Fe-S clusters in purified proteins was observed in bacterial DNA glycosylase homologs, EndoIII and MutY, and was found to promote enhanced binding affinity for DNA. The Fe-S cluster loop binding motif (FCL) was thus later proposed

to also play a role in the process of search for damaged bases (Lukianova & David, 2005; Carroll et al., 2021; Moe et al., 2022).

Several crystal structures of bacterial EndoIII enzymes such as, from *E. coli* (ecEndoIII) (Thayer et al., 1995), *Deinococcus radiodurans* (drEndoIII1 and drEndoIII3) (Sarre et al., 2019) and *B. stearothermophilus* (bstEndoIII) (Fromme, 2003) have been determined in their apo- and DNA-bound form. Commonly, EndoIII bears an elongated bilobal structure with a positively charged DNA binding cleft separating the two domains, as seen in figure 19B. This cleft contains a highly conserved DNA-binding HhH motif and three less conserved DNA – interacting loops (FCL, DIL1, DIL2) surrounding the active site. This comprises the catalytic core and is linked by two loops, suggesting binding to B-DNA to scan the DNA for lesions (Sarre et al., 2019).

The first X-ray crystal structure of human NTH1, in a DNA-free state and missing most of the NTD, revealed an unexpected 'open' conformation of NTH1, in marked contrast with earlier structures of bacterial EndoIII enzymes, all of which adopt a 'closed' conformation (Figure 19C and D). In the 'open' conformation, the six-helical barrel domain comprising the HhH DNA binding motif is rotated away from the 4Fe-4S cluster domain requiring a large conformational change to reconstitute a functional catalytic site and adopt the closed conformation required for DNA binding and base excision (Carroll et al., 2021; Odstrcil et al., 2024). Small angle X-ray scattering (SAXS) experiments performed on both full length and NTD-truncated NTH1, also suggested that full length NTH1, unlike its NTD-truncated form, does not adopt an open conformation in solution (Moe et al, 2022). Furthermore, by combining SAXS data and AlphaFold2 predictions, Moe and colleagues demonstrated that the disordered NTD is directly involved in DNA binding and undergoes a major conformational change upon DNA binding. In the absence of DNA, the NTD indeed adopts a variety of extended conformations, while upon DNA binding it wraps tightly around the catalytic core and DNA, to adopt a much more compact structure, similar to the 'closed' conformations reported previously for bacterial EndoIII enzymes (Moe et al., 2022) (Figure 19D). Taken together, these structural studies suggest that human NTH1 is a dynamic protein that can adopt multiple conformational states. This flexibility appears to be provided by both the disordered NTD and the two linker regions (Moe et al., 2022).

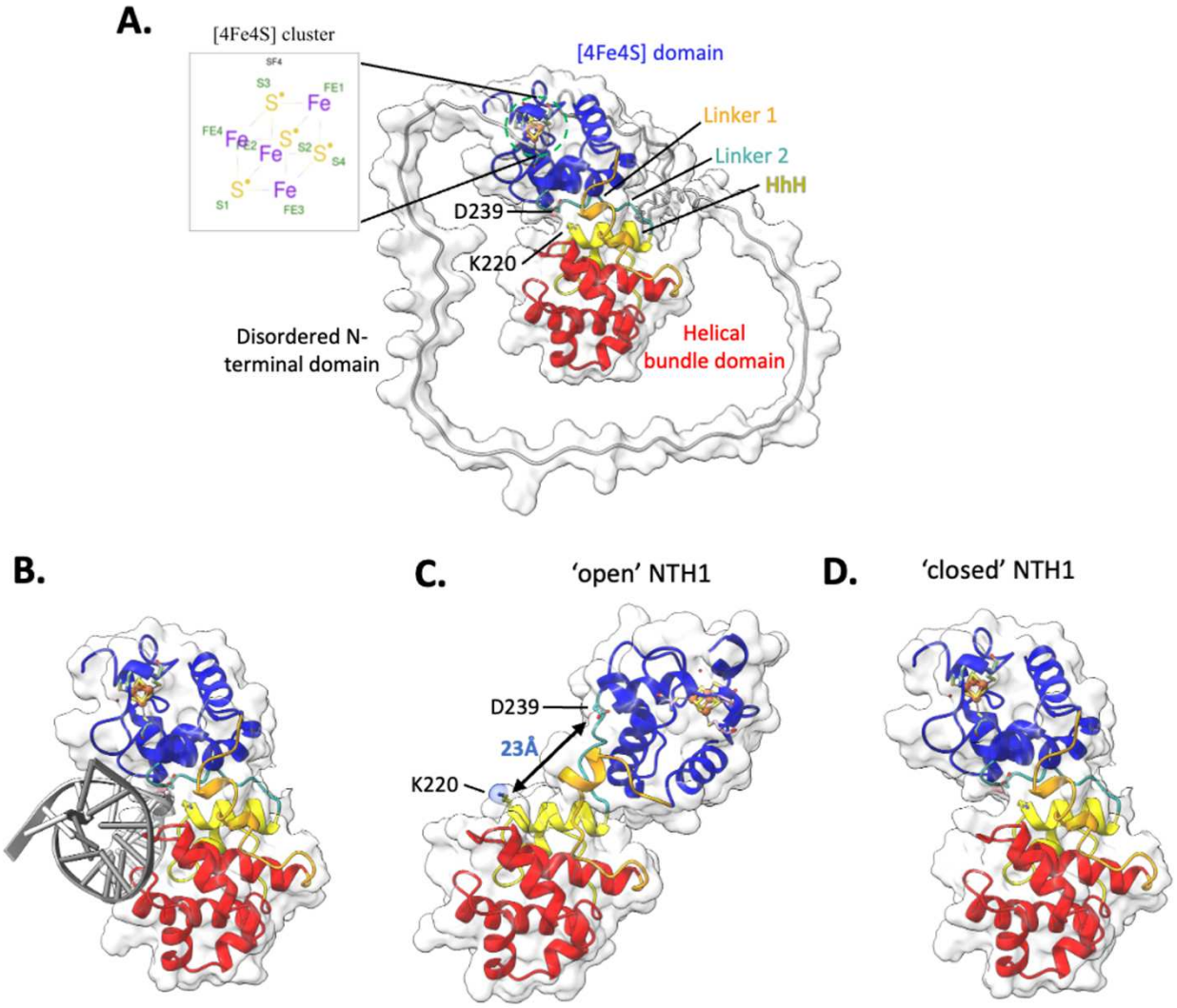


Figure 19: 3D structures of hNTHL1 obtained from X-ray crystallography and AlphaFold predictions. A) X-ray crystallographic structure of hNTHL1 with each domain highlighted in similar color-code to figure 17 and a close-up of the 4Fe-4S cluster organization (PDB: 7RDS) (Carroll et al., 2021). B, C, D) AlphaFold prediction models of DNA bound NTH1 (without NTD), the 'open' and 'closed' conformation of hNTHL1 (Moe et al., 2022).

4.2 Recognition and excision of DNA damage by NTH1

The capability of a protein to locate specific target sequences or structures among the expanse of non-specific DNA is determined by its energy landscape. Comprehensive free energy landscapes provide information on protein translocation along the DNA helix (dynamics), its substrate specificity and stability of its binding to dsDNA in between stretches of non-specific sequences (Misteli, 2001). To locate their target sequences, proteins undergo conformational changes that govern their function and movement. The development of single-molecule detection techniques has allowed direct visualization

of proteins diffusing across DNA and is helping to elucidate their mechanisms within the crowded nuclear environment (Misteli, 2001; Gorman & Greene, 2008).

4.2.1 Substrate specificity and catalytic activity

E. coli EndoIII and hNTH1 are homologous DNA glycosylases but differ in terms of substrate specificity and biological roles. EndoIII acts as a broad-spectrum enzyme, efficiently excising a wide range of oxidized pyrimidines, including Tg, 5-hydroxyuracil (5-OHU), 5-OHC, and ring-opened pyrimidines such as thymine urea (Dizdaroglu et al., 1993), reflecting its role as a generalist in bacteria with fewer backup enzymes. In contrast, human NTH1 has narrower specificity, showing higher activity toward Tg and oxidized cytosine derivatives (cytosine glycol, 5-OHC), but reduced activity against ring-opened pyrimidines (Marenstein et al., 2003), when these are situated opposite guanines in DNA. The substrate specificity of hNTH1 is indeed strongly influenced by the base opposite the lesion in DNA, which affects recognition and cleavage efficiency (Marenstein et al., 2003). For example, NTH1 excises Tg efficiently when paired with adenine and to a reduced level when paired with guanine, likely due to steric and hydrogen-bonding mismatches that destabilise Tg recognition. It has a strong substrate preference for cytosine glycol, that protects it from C → T mutations. For 5-OHU, it has consistent activity that is natural to its C:G pairing (Ikeda et al., 2002; Marenstein et al., 2003). When acting upon the AP: A site, the addition of human APE1 (AP endonuclease-1) to hNTH1 leads to increased dissociation of hNTH1 from the DNA, which in turn abrogated its AP lyase activity and boosted its N-glycosylase turnover. Conversely, APE1 did not inhibit the AP lyase activity of hNTH1 when acting on Tg:G sites. Interestingly, the addition of YB-1, in conjunction with APE1, resulted in a cumulative increase in both N-glycosylase and AP lyase activities of hNTH1 (Figure 20), irrespective of the base pairing context (Marenstein et al., 2003).

Unlike its bacterial counterpart, hNTHL1 has been shown to function as a dimer at high concentrations. This dimerization has been shown to be primarily mediated by the catalytic core and also to some extent by the N-terminal tail. This process of dimerization was observed by Liu and coworkers both *in vitro* and *in vivo* using HeLa cells. In these experiments, the catalytic turnover of full-length hNTHL1 exhibited a positively cooperation as a function of protein concentration and the NTD appeared to be responsible for the specific homodimerization of hNTHL1. Furthermore, the high nuclear (2.3 μM) and cytosolic (0.65 μM) concentrations of hNTH1 observed in *in vivo* experiments with HeLa cells indicate potential oxidation of cysteine residues of endogenous NTH1, leading to homodimerization (Liu et al., 2003; Marenstein et al., 2003). Thus, dimerization may influence the processivity and efficiency of base excision and strand cleavage. Dimerization may also stabilize the DNA-enzyme complex allowing longer association times and sequentially promoting coupling of N-glycosylase activity and AP lyase activity, within the same enzyme molecule. On the other hand, disruption of this dimerization may promote release of the enzyme from the DNA after base excision,

but before β-elimination or strand cleavage, leading to uncoupling of both DNA glycosylase and AP lyase activities, thereby reducing AP lyase efficiency (X. Liu et al., 2003; Marenstein et al., 2003; Sarre et al., 2019). Most studied EndoIII enzymes display a higher N-glycosylase activity and reduced AP lyase activity, as a consequence of hNTH1's poor affinity towards the intermediate, abasic or AP site, leading to dissociation of the enzyme-Ap-DNA complex before β-elimination (Sarre et al., 2019) (Figure 19).

Uncoupling of hNTH1 causes individual reaction steps to take place in a concerted manner resulting, in two separate pathways (Sarre et al., 2019). As illustrated in figure 19, in situations where these two reaction steps are not directly coupled, the enzyme can dissociate from the abasic site DNA (NTH1+DNA_{AP}) after the glycosylase reaction. This uncoupling leads to a mix of DNA substrates, some containing abasic sites and others still containing oxidized bases. The enzyme can then proceed through one of two pathways: it can re-engage in DNA glycosylase activity on new oxidized DNA substrates (DNA_{ox}), or it can perform AP-lyase activity on DNA with abasic sites (DNA_{AP}). The degree to which NTH1 follows either of these pathways is influenced by the concentrations of the various species involved in the reaction (NTH1, DNA_{ox}, DNA_{AP}, and DNA_n or even other factors as chromatin state) and by other factors that can either boost or hinder specific stages of the reaction. Marenstein et al explains the uncoupling of hNTH1 due to the proteins' poor affinity towards the intermediate, the abasic site or the AP site. This leads to dissociation of the enzyme-AP-DNA complex prior to β-elimination (Marenstein et al., 2003; Sarre et al., 2019). The significance of this uncoupling was observed by Liu and coworkers, where a single point mutation at the active site (K212R) uncoupled NTH1's glycosylase activity with its AP lyase activity. This suggested a possible direct attack of the nonionized guanidino group of arginine forming an unstable Schiff base. Prior to β-elimination, this hydrolyzes by the hydroxide ion results in cleavage of the glycosylic bond (Liu & Roy, 2001).

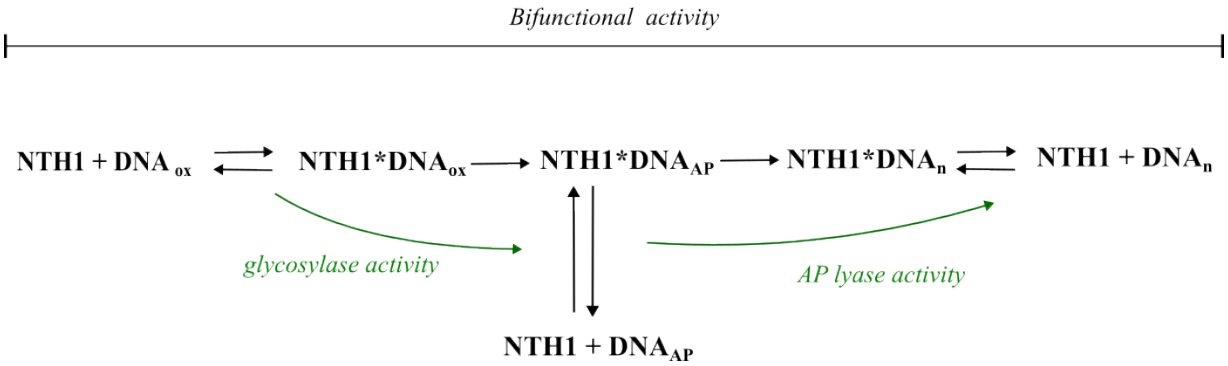


Figure 20: A proposed general scheme of the catalytic activity – N-glycosylase and AP lyase activities of hNTH1.

The enzyme (NTH1) binding to its substrate DNA containing an oxidized base (DNA_{ox}), forming an enzyme-substrate complex ($NTH1*DNA_{ox}$). This binding facilitates the removal of the oxidized base, resulting in an NTH1-abasic site complex ($NTH1*DNA_{AP}$). This complex is then processed further through a lyase reaction, yielding an NTH1-nicked DNA complex ($NTH1*DNA_n$). Finally, the fully processed DNA product, after a β-elimination step, is released from the enzyme ($NTH1+DNA_n$) (Marenstein et al., 2003).

4.2.2 NTH1 scanning and lesion accessibility involves chromatin dynamics

The mechanism of search and recognition of 8oxoG by hOGG1, has been the object of several studies (Campalans et al., 2013; D'Augustin et al., 2020; Robeska et al., 2024). For hNTH1, in contrast, such studies are very limited. Based on the crystal structure of hNTH1, Carroll and colleagues proposed a model in which hNTH1 uses a one-dimension sliding motion to search, identify and excise lesions, based on its kinetic cooperativity (Carroll et al., 2021). This model speculates that hNTH1 begins as an apo enzyme existing in an open configuration or a 'scanning conformation' as it scans the length of the DNA searching for a lesion. On encountering a lesion, hNTH1 would close upon the lesion, forming a closed or active complex, followed by processing and releasing the damaged base, thereby allowing the DNA glycosylase to continue its search along the DNA (Carroll et al., 2021). This accounts for both the 'open' and 'closed' conformations discovered by X-ray crystallography and is similar to the diffusion model proposed for hOGG1, illustrated in figure 20. However, more recent SAXS data suggests that the 'open' conformation of hNTH1 observed in the crystal structure may be a consequence of truncating the flexible NTD (Moe et al., 2022). Further studies are therefore needed to refine this model and determine the factors that may influence the mode of lesion search and recognition by hNTH1 (Carroll et al., 2021; Moe et al., 2022; D'Augustin et al., 2023).

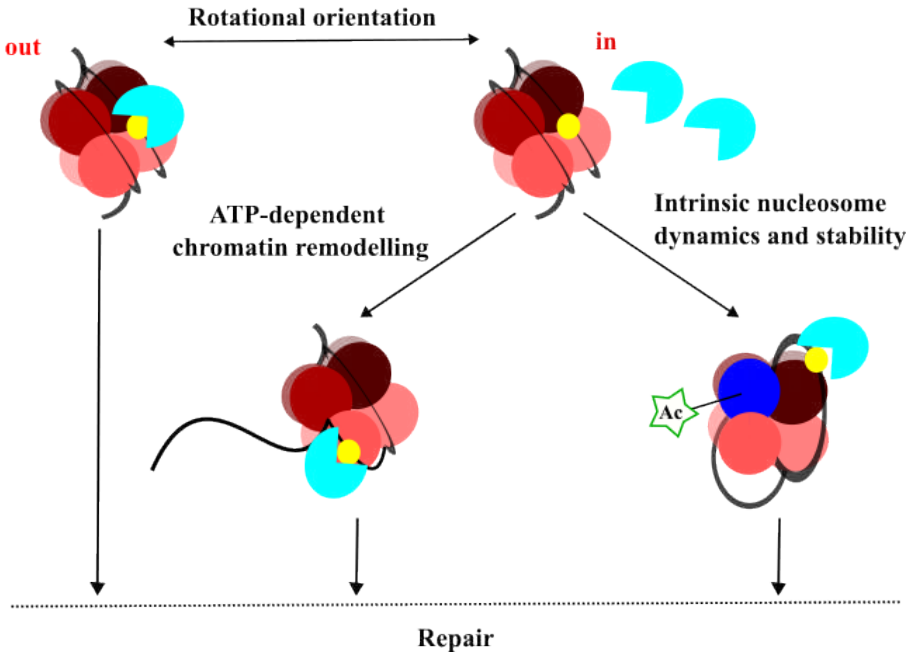


Figure 21: Chromatin dynamics for inward and outward lesion accessibility depending on enzyme-substrate kinetics.

Rotational orientation of the nucleosome determines lesion accessibility for hNTH1. If the lesion is facing away from the dyad axis of the histone core, then it is easily recognized by hNTH1, followed by excision of the lesion and the steps involving the downstream repair process. However, if the lesion faces inward, either ATP-dependent chromatin remodeling or intrinsic nucleosome dynamics allows the lesion to be accessed by hNTH1, to excise the lesion.

Chromatin dynamics, particularly the transient unwrapping of nucleosomal DNA, plays a critical role in regulating hNTH1's ability to recognize and excise oxidized lesions. The activity of hNTH1 was indeed found to vary depending on whether the lesions face inward toward the histone core or outward into the solvent (Prasad et al., 2007). Prasad and colleagues tested the efficiency of purified hNTH1 to process Tg lesions, introduced into reconstituted nucleosomes, at positions 51(outward facing lesion) or 46 (inward facing lesion) (Tg-51 or Tg-46), and into corresponding naked DNAs (Prasad et al., 2007). Interestingly, as the concentration of hNTH1 increased to a physiological level, i.e., ~ 2.3 µM in the nucleus and ~ 0.65 µM in the cytosol, the efficiency of cleavage of inward-facing sterically occluded lesions increased substantially. hNTH1 cleaved more inward facing lesions in the nucleosome Tg-46 as a function of enzyme concentration, reaching ~ 50% of the cleavage observed on naked DNA with 200 to 800 nM hNTH1. Further experiments demonstrated that hNTH1 binding to inward facing lesions was limited by the frequency and duration of the transient unwrapping of DNA from the histone octamer and the capacity of hNTH1 to capture this lesion during the times of unwrapping. These observations thus suggest that cleavage of Tg lesions that were inward facing occurred without nucleosome disruption, through the formation of enzyme nucleosome ternary complexes (Prasad et al., 2007). A proposed mechanistic model of the excision of oxidatively damaged bases from sterically

occluded nucleosomal positions is described in five steps (Figure 21): a) a spontaneous conformational change that exposes the damaged base to the solvent, b) binding of the DNA glycosylase to the damaged base to form an ES complex, c) excision of the damaged base by the DNA glycosylase to form an apurinic site, d) dissociation of the DNA glycosylase and e) re-wrapping of the processed DNA (Maher et al., 2013).

4.3 Regulation of NTH1

DNA glycosylases repair a myriad of DNA lesions in various differentiated and embryonic tissues, by functioning in a coordinated manner. For this, their activity needs to be tightly regulated, both temporally and spatially (Hans et al., 2020). In this section, we will look at some of the key aspects of NTH1 regulation occurring at either the transcriptional level (in a cell cycle and cell type dependent manner) or the protein level (role of PTMs and interacting partners).

4.3.1 Regulation of NTHL1 gene expression

The hNTH1 gene is composed of 6 exons and 5 introns and undergoes alternative splicing to produce a variety of spliced coding and non-coding variants, with only one of the known mRNA variants encoding for a functionally intact catalytic domain. Transcription of the hNTHL1 gene has also been shown to be initiated at three different initiation codons to produce three isoforms of the protein, existing with different N-terminal sequences (Luna et al., 2000; Boldinova et al., 2019).

When mRNA from synchronized HaCat cells (human skin keratinocytes) were collected at different time points during the cell cycle, they showed low expression of hNTH1 during G_0 to G_1 phases, but significantly increased expression during the early- and mid S-phase (Luna et al., 2000; Takao, 2002). This Northern blot analysis demonstrated, for the first time, that hNTH1 expression is also cell-cycle dependent (Luna et al., 2000). Not only is hNTH1 differentially expressed throughout the cell cycle and transcriptionally regulated, it seems that an additional regulatory role is its tissue-specific expression (Sampath et al., 2012). hNTH1 is ubiquitously expressed in human tissues, but mRNA levels are higher in heart, brain, and in thyroid fibroblasts, but comparatively lower in liver and lung tissues (Karahalil et al., 2003).

mRNA expression levels derived from various cancers (*www.cBioPortal.org*) showed NTH1 undergoing amplification or upregulation in many cancerous tissues (Shao et al., 2019). This increased expression is highly correlated to increased copy number variations caused by duplication or inversion of the hNTHL1 gene and to transcriptional regulation, as seen in the scatter plot presented in figure 22A. For example, hNTHL1 is observed to be overexpressed in colorectal adenocarcinoma and undergo amplification in invasive breast carcinoma cells. In these cells, hNTHL1 overexpression may be a response to increased levels of DNA lesions formed, and could have deleterious effects, such as the

accumulation of toxic repair intermediates (Chae et al., 2016; Shao et al., 2019; Hans et al., 2020). The effect of hNTHL1 overexpression was studied by transiently expressing hNTHL1 or a catalytically dead variant, hNTHL1 (CATmut) in HBEC (non-transformed human bronchial epithelial) cells, which resulted in replication stress signaling and decreased activity of homologous recombination (HR). 17% mRNA upregulation of hNTHL1 was also observed in non-small cell lung cancer cell lines (NSCLC), A549 and H460. In these cases, hNTHL1 overexpression led to genomic instability and cellular transformation over time, independent of the proteins' catalytic activity. Galick and colleagues demonstrated that expressing the catalytically inactive germline variant, bearing the D239Y mutation, of hNTHL1, occurring in ~ 6.2% of the global population, in human MCF10 cells leads to accumulation of γH2AX, an indicator of DSBs in the S- and G2/M cell cycle phases. Additionally, treatment with 30 mM H_2O_2 and recovered at different time points, led to higher expression of the hNTHL1 D239Y variant compared to the hNTHL1 wild type, which in turn led to genomic instability and cellular transformation (Galick et al., 2013). Similarly, the R33K germline variant of hNTHL1 expressed in MCF10A cells, reported by Marsden and coworkers, is associated with increased cellular transformation, with no impact on cellular localization, substrate specificity and its enzymatic activity (Marsden et al., 2020). Furthermore, the absence of hNTHL1 leads to accumulation of oxidized bases, yielding mutations, genetic instability and ultimately, tumorigenesis (Limpose et al., 2018). Therefore, a proper balance between NTH1 and its substrates is needed to maintain genomic stability, as depicted in figure 22B (Galick et al., 2013; Marsden et al., 2020).

Tumor – associated variants of DNA glycosylases, including hNTH1, have also been identified revealing genetic connections between DNA glycosylases and cancer (Hans et al., 2020). For instance, several hNTHL1 variants, identified by tumor mutational signatures, have an autosomal recessive inheritance, leading to polyposis development, known previously as hNTHL1 – associated polyposis. This was first reported by Weren and his coworkers, who reported three Dutch families with the same homozygous truncating hNTHL1 variant (c.244C>T p. (Gln82Ter) according to NM_002528.7, with CLIN Var ID 192319) and confirmed a homozygous germline nonsense mutation in NTHL1 by whole – exome sequencing. Here, biallelic inactive hNTHL1 causes accumulation of somatic variants, mostly with C>T transitions observed in hNTHL1-deficieint tumors, causing disruption of the BER pathway (Weren et al., 2015). Whole – genome sequencing of hNTHL1 KO colonic stem cells reported an accumulation of C>T base substitutions, approximately two-fold higher than normal human colonic stem cells (Drost et al., 2017). This was confirmed by Grollerman and his team, who reported that tumors of biallelic hNTHL1 variants carry a distinctive single base substitution COSMIC (Catalogue of Somatic Mutations in Cancer) signature 30 (SBS30) characterized by the abundance of C>T transitions, particularly at non-CpG sites, causing a lifetime risk of developing colorectal polyposis, colorectal cancer (CRC) and breast cancer (Grollerman et al., 2019; Pinto et al., 2023). Research confirms hNTHL1's association with a multi-tumor phenotype, including polyposis, colorectal cancer, and breast

cancer, with the addition of uterine lesions, basal cell carcinoma, and pancreatic cancer observed (Belhadj et al., 2019; Pinto et al., 2023). Recently, three new families with hNTHL1 tumor syndrome, two with a recurrent pathogenic variant and one with a novel likely pathogenic variant were identified. The analysis of tumor mutational signatures, particularly SBS30, was instrumental in classifying the novel variant and highlighted its predominance in hNTHL1-associated tumors. However, polyposis remains the primary characteristic for hNTHL1 tumor syndrome, and heterozygous carriers do not appear to have a clinically significant increased risk. For a broad-spectrum multi-tumor syndrome, other types of malignancies or non-malignancies could occur, that have been so far hard to identify and characterize, from the scarce number of families identified (Pinto et al., 2023). A recent medRxiv preprint by Walker and coworkers described an enrichment of SBS30 signature in adenomas at comparable portions to CRCs, hoping to use adenomas to identify biallelic cases, facilitate variant classification and CRC prevention (Walker et al., 2024). Analyzing these mutational signatures could allow researchers to identify DNA repair deficient patterns linked to specific types of DNA damage associated with hNTHL1 deficiency in tumors. This approach is crucial to understand the spectrum of NTHL1-germline mutations and propose potential clinical interventions (Drost et al., 2017).

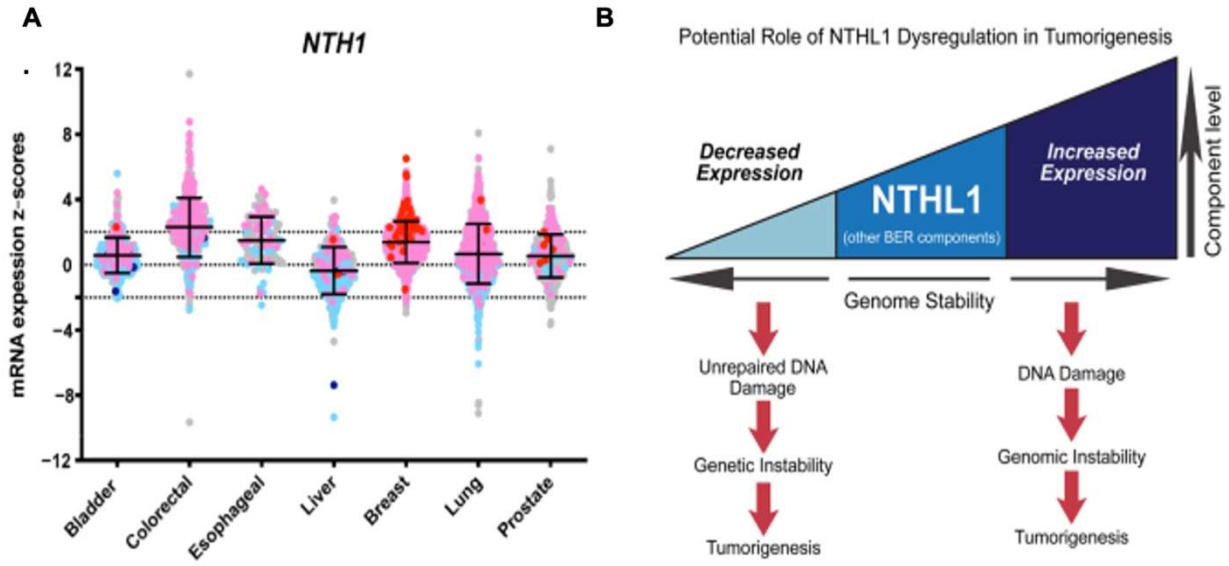


Figure 22: (A) Tissue – specific mRNA expression levels of hNTH1 and (B) schematic representation of consequences of dysregulation of NTH, leading to tumorigenesis.
Illustrations taken from Limpose et al., 2018.

4.3.2 Regulation of NTH1 at the protein level

At the protein level, enzymes are known to be regulated by PTMs and their interactions with other cellular partners. So far, there have been very few studies of PTMs on hNTH1. A well-documented

in vitro study demonstrated the broad specificity of TRIM26, an E3 ubiquitin ligase tripartite motif 26, that can target multiple DNA glycosylases for polyubiquitination (Konis et al., 2022). TRIM26 catalyzes the polyubiquitylation of hNTH1 at lysine 67, thereby stimulating its degradation and affecting the cellular response to oxidative stress (Williams & Parsons, 2018). Two *in vivo* studies reported, using different sources of oxidative stress (H_2O_2 and X-ray radiation) to investigate the regulation of NEIL1 and hNTH1 protein levels by TRIM26 (Williams & Parsons, 2018; Konis et al., 2022). Upon treatment with H_2O_2, hNTH1 protein levels were found to increase ~ 1.3-1.8-fold, and its accumulation on chromatin was further exacerbated in the absence of TRIM26, underlining its importance in maintaining hNTH1 stability and protein levels during oxidative stress (Konis et al., 2022). Furthermore, the siRNA depletion of TRIM26 in HCT116 cells (human colon cancer cell line) resulted in ~ 1.6-fold increase in the stability of hNTH1, leading to accelerated DNA repair kinetics (Williams & Parsons, 2018). Although hNTH1 is predicted to undergo a number of PTMs other than polyubiquitylation (COSMIC database), there is so far no experimental evidence for this *in vivo*. Performing such an analysis would thus provide valuable information into the mechanisms of post-translational regulation in response to oxidative stress (Drost et al., 2017; Williams & Parsons, 2018).

Protein – protein interactions (PPIs) are also heavily involved in regulating protein function. DNA glycosylases are known to interact not only with repair factors belonging to the same DNA repair pathway, but also with factors from other repair pathways (Almeida & Sobol, 2007; Hans et al., 2020; Rathnaiah & Sweasy, 2025). These interactions may be either direct or indirect. The AP lyase activity of hNTH1 is dependent on its binding affinity for the AP site resulting from its DNA glycosylase activity. APE1 – assisted dissociation of hNTH1 from AP-DNA is an illustration of an indirect interaction and results in reduced AP lyase activity (Marenstein et al., 2003). In the presence of high protein levels of APE1, hNTH1 has indeed been proposed to act mostly as a monofunctional glycosylase, particularly on Tg paired with adenine (Tg:A), and to handover the AP site to APE1 for the cleavage step (Demple & Harrison 1994).

Figure 23 illustrates the known interactions of NTH1 to several DNA repair factors. *In vitro* experiments with HeLa whole cell extracts revealed a direct interaction between hNTH1 and XRCC1, a scaffolding protein involved in both BER and single strand break repair (SSBR) pathways (Campalans et al., 2005; Almeida & Sobol, 2007; Ström et al., 2011). Pull-down assays also confirmed a direct physical interaction between XRCC1 and both hNTH1 and NEIL2. In this case, the BRCT1 domain of XRCC1, whether alone or in combination with other XRCC1 domains like N-B1 and H-B1, was sufficient for hNTH1 binding (Campalans et al., 2005). Interestingly, the NTD region of hNTH1 could also interact with the hinge regions (N-H) of XRCC1, suggesting two possible interacting sites. 10% of the repair foci in HeLa cell nuclei, formed after a 1 hour treatment with 5 mM H_2O_2 showed colocalization between XRCC1 and hNTH1 (Campalans et al., 2005). This suggests a weak or transient

assembly of XRCC1 with BER factors allowing for a dynamic assembly and disassembly to repair the damaged base.

Several NER factors have also demonstrated direct interactions with hNTH1, supporting a crosstalk between these two repair pathways, which together eliminate lesions occurring at the nucleobase level. *In vitro* studies describe the interaction between XPG (Xeroderma Pigmentosum Complementation Group G), a structure specific endonuclease of the NER pathway, and hNTH1, that favors NTH1's catalytic efficiency (Bessho, 1999; Kar et al., 2024; Klungland et al., 1999). Interestingly, studies suggest different roles of XPG on interaction with hNTH1. Klungland et al., 1999 reports that hNTH1 may interact more efficiently with an XPG-DNA complex, bound to small, oxidized base lesions. Therefore, XPG could potentially bend the DNA at the site of damage, helping to expose the damaged base, so that hNTH1 might be able to recognize, flip out and excise the damaged base. In special cases involving XPG point mutations, this would lead to a deficient excision of the damaged base by hNTH1 and an early onset of Cockayne syndrome (Klungland et al., 1999; Limpose et al., 2018). In a more recent study, Kar et al., 2024 also observes the interaction between NTH1 and XPG proteins *in vivo*. In non-small cell lung cancer (NSCLC) and HBEC-3KT cells, elevated levels of hNTH1 showed increased co-immunoprecipitation of NTh1 with endogenous XPG. This would indicate that, transiently overexpressing NTH1 could sequester XPG, inhibiting NER mediated repair of cytotoxic DNA lesions, particularly cisplatin – induced DNA intrastrand crosslinks (Kar et al., 2024).

Pull-down experiments using NTH1-GST tagged protein expressed in the A549 adenocarcinoma cell line also revealed an association of hNTH1 with the well-known tumor suppressor protein, p53, and the sliding clamp PCNA. The activity of p53 is downregulated by the ubiquitin proteosome pathway but is found to be upregulated during oxidative DNA damage. This results in an accumulation of p53, enhancing its transactivation activity (Oyama et al., 2004; Rathnaiah & Sweasy, 2025).

hNTH1 has also been reported to interact with YB1, a damage-inducible transcription factor. Several laboratories have demonstrated that YB1 is directly involved in the cellular response to genotoxic stress (Marenstein et al., 2001; Senarisoy et al., 2020). YB1 is known to directly affect the steady-state equilibrium between the covalent hNTH1-AP site Schiff base ES intermediate and the non-covalent ES intermediate containing the AP aldehydic sugar and ε-amino group of the lysine of hNTH1. YB1 has been shown to bind specifically to the auto-inhibitory NTD of hNTH1, thereby stimulating its AP lyase activity, thus acting as a modulator of hNTH1 activity (Guay, Garand, et al., 2008; Marenstein et al., 2003; Senarisoy et al., 2020). Interestingly, the complex formed by hNTH1 with a C-terminally truncated form of YB1 showed a medium binding affinity with a k_d in the low micromolar range. This interaction was proposed to be associated with increased cisplatin resistance in breast cancer cells (Guay et al, 2008). This proposal was further supported by the identification of two inhibitors that block the

hNTH1-YB1 interaction *in vitro* and which were found to partially resensitize MCF7 cells to cisplatin *in vivo* (Senarisoy et al, 2020). This study also confirmed hNTH1 as a relevant target to potentiate cisplatin cytotoxicity in YB1 overexpressing tumor cells.

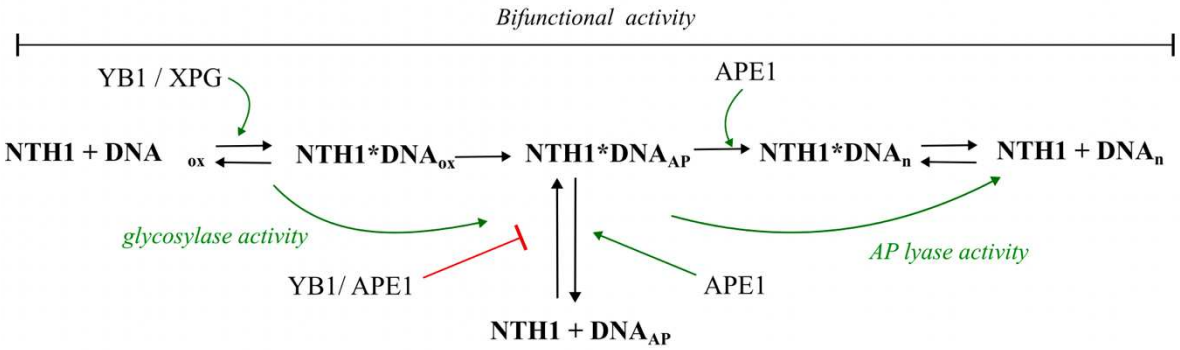


Figure 23: Proposed mechanism of crosstalk between hNTH1 and its interaction with some key BER factors, on damaged DNA.

Following the same description as figure 20, YB1 or XPG are known to stimulate the catalytic activity of hNTH1, although it is unknown if both the glycosylase and AP lyase activity is stimulated by XPG or one. YB1 affects the steady – state equilibrium of hNTH1-AP Schiff base intermediate and stimulates the AP lyase activity of hNTH1. High levels of APE1 cause hNTH1 to act as a monofunctional DNA glycosylase, promoting dissociation of hNTH1 from the AP site. APE1 then takes over to further process the AP site.

AIM OF THE THESIS

So far, little is known about how BER enzymes are organized in the nuclear space. In particular, very little information is available regarding the distribution and dynamics of NTH1 within the nuclear landscape. Evidence for DNA repair foci formation has been described in the literature at sites of DSB forming liquid-liquid phase droplets were DNA repair factors accumulate (Spegg & Altmeyer, 2021, Chiolo, 2025). These structures have notably been studied by SMLM in living cells to get information on the dynamics and interactions of the proteins inside the repair foci (Miné-Hattab et al., 2021; Heyza et al., 2023).

The main aim of my thesis was thus to investigate the nuclear distribution of endogenous NTH1 and its dynamics in response to oxidative stress. To reach this goal, we imaged HeLa cells, using a combination of 3D spinning disk confocal microscopy and 2D SMLM techniques - dSTORM and PALM, to obtain the highest possible spatial resolution (~10 to 20 nm), therefore allowing us to follow the dynamics of single NTH1 molecules.

The thesis was sub-divided into the following four main objectives:

Objective 1: Establish the nuclear distribution of endogenous NTH1 in HeLa cells using a combination of 3D confocal imaging and 2D dSTORM to achieve high spatial and temporal resolution.

Objective 2: Explore the changes in the nuclear levels and distribution of chromatin-associated NTH1 in response to oxidative stress.

Objective 3: Investigate the dynamics of NTH1 at the single-molecule level using sptPALM, before and after exposure to oxidative stress.

Objective 4: Map the distribution of chromatin markers and/or other BER factors alongside NTH1, by dual labeling experiments using either dSTORM or DNA-PAINT imaging.

Note: Due to a number of technical difficulties encountered on the way and a lack of time, objective 4 has not been completed, but some initial experiments have been performed, which are presented in the final Discussion and Perspectives section of my thesis.

MATERIALS AND METHODS

This chapter outlines the experimental materials and methods used to study the spatial organization and dynamic behavior of the DNA glycosylase NTH1 in human cells. HeLa and HeLa NTH1 knockout cell lines were employed to assess the role of NTH1 in DNA repair. A combination of molecular biology techniques and advanced fluorescence microscopy, including 3D confocal microscopy, 2D dSTORM and sptPALM, was used to analyze NTH1 localization and mobility. Detailed descriptions of cell culture, treatments, imaging procedures, and data analyses are provided in the following sections.

1. Cell culture, transfections and oxidative treatment.

1.1 Cell culture

HeLa and HeLa NTH1 knockout cells - NTH1 KO (the latter kindly provided by *Prof. Andriy Khobta*; Sarmini et al., 2023), were cultured and maintained as a sub-confluent monolayer culture at 37°C in 5% CO_2 using Dulbecco's Modified Eagle's Medium (DMEM) supplemented with 10% FBS and 1% penicillin/ streptomycin, non-essential amino acids (0.1 mM) and sodium pyruvate (1 mM). All experiments were performed using cells at passage no. between 1-7, to preserve similar genomic integrity within the cells.

We have also used fluorescence ubiquitin cell cycle indicator: (FUCCI)-HeLa cell line (kindly provided by *Dr. Jean-Philippe Kleman from the M4D platform, Institut de Biologie Structurale*) to follow the cell cycle progression. Engineered FUCCI HeLa Cells expressing Cdt1 and Geminin, during the G0/1 and S/G2/M phases of the cell cycle, respectively, are fused with two different fluorescent proteins; mCherry and GFP respectively. So, fluorescence imaging of each nucleus allows us to predict the cell cycle phase of each cell (Sakaue-Sawano et al., 2011).

For cell cycle analysis and western blot (WB), after growth, cells were trypsinized with 3.5 ml of trypsin-EDTA at 37˚C followed by neutralizing the trypsin with 4ml of DMEM with FBS. The cell suspensions were centrifuged at 1500 rpm, for 5 minutes at room temperature. The supernatant was discarded, and the cells were resuspended in 1ml of PBS 1X, washed twice by centrifugation at 1500 rpm, for 5 minutes at room temperature. The pellets were kept at -20°C for western blot.

For immunofluorescence and super resolution experiments, cells were further cultivated as described, in the following sections.

1.2 Cell Transfection

To assess for NTH1 antibody specificity, cells were transfected with siRNA for NTH1 (5'-GUGGCUUUACGCUUCAGG-3'), (5'-UCCUGAAGCGUAAAGCCAC-3') and with a control siRNA (5'-AGGUAGUGUAAUCGCCUU-3'), (5'-CAAGGCGAUUACACUACUACCU-3') using Lipofectamine RNAiMax (Invitrogen, Thermo Fisher Scientific). Cells were seeded the day before in

6-well plates at an appropriate density of 200,000 cells. The siRNA complexes were prepared using Lipofectamine RNAiMax in Opti-MEM (Gibco), following the manufacturer's instructions. Each complex sample contained siRNA at a concentration of 36 nM per well. The complexes were incubated at room temperature for 15-30 minutes. After rinsing the cells with fresh medium, the siRNA complex was added to the cells at a final concentration of 5 nM, and the cells were incubated for 4-6 hours at 37°C. After incubation, the media was replaced with complete growth media and cells were further grown.

For sptPALM experiments, cells were transfected with either the plasmid, p-mEos4B- pNLS or p-NTH1-mEos4B constructed by *Dr. Fabienne Hans (Institut de Biologie Structurale)* (Figure 24). Transfection was performed with FuGENE HD Transfectant (Promega E2311) in a ratio of 3:1. In brief, 875 ng of plasmid was diluted in 125 µl of Opti-MEM and further complemented with 2.6 µl of FuGENE HD (Promega). After incubation for 10 minutes at room temperature, the mixture was added to the cells.

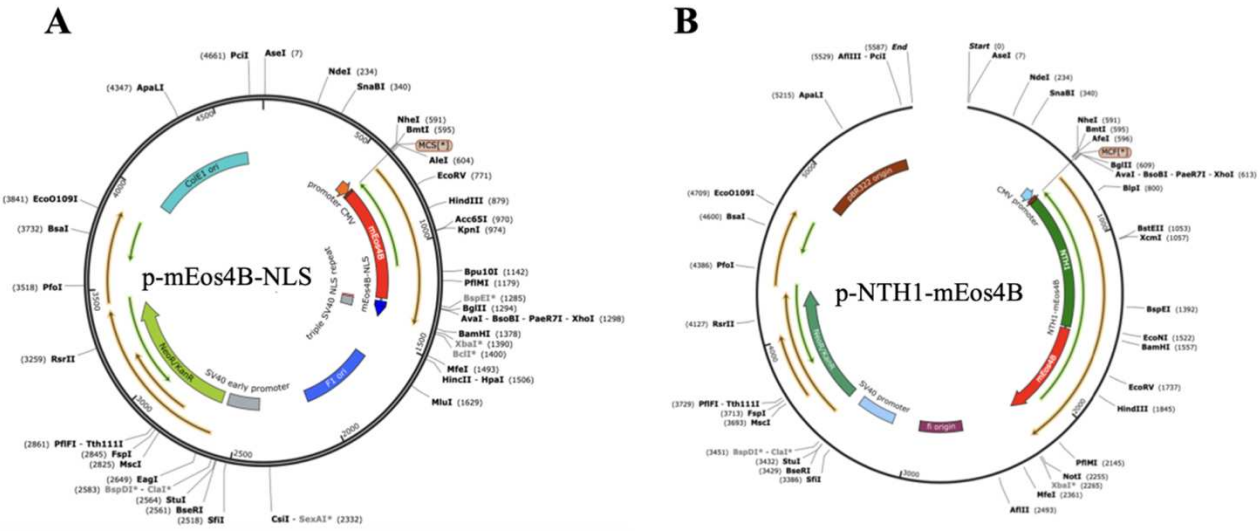


Figure 24: Cartography of the p-mEos4B- NLS (A) and p-NTH1-mEos-4B (B) plasmids. p-mEos4B-NLS and plasmid pNTH1-mEos4B were prepared by replacing the sYFP coding sequence from p-sYFP-NLS and p-NTH1-sYFP (Senarisoy et al., 2020) by the coding sequence of mEos4B. Plasmid DNA was purified using NucleoBond kits column (Macherey-Nagel), according to the manufacturer's instructions. Nuclear Localization Signal (NLS).

1.3. Treatment of the cells with oxidizing DNA damaging agents

In order to investigate the response of NTH1 to oxidative stress, we treated cells with H_2O_2 or $KBrO_3$, two commonly used oxidizing agents for BER studies, (Amouroux et al., 2010) or with cisplatin, a chemotoxic drug commonly used in cancer therapy (Kar et al., 2024).

Cisplatin (Sigma) was weighed and resuspended with 0.9% w/v NaCl to a stock concentration of 1 mM, with repeated pipetting for 5 minutes to ensure complete dissolution. Intermediate solutions were diluted 10x in DMEM media and were 10x concentrated compared to the final working concentration. The cells were incubated with cisplatin-media at 37˚C for indicated periods of time.

A stock solution concentrated at 5 mM H_2O_2 (Sigma) without or with 5 mM $FeSO_4$ was prepared in FluoroBrite DMEM medium (9.8 M stock solution). $FeSO_4$ acts as a catalyst, stimulating Fenton's reaction. This involves the formation of two different oxygen-radical species, $H^+ + OH^-$, as the final products which contribute to increased levels of oxidative stress.

A stock solution of 400 mM $KBrO_3$ (Sigma) was prepared in DMEM or FluoroBrite DMEM media. A final concentration of 40 mM potassium bromate was prepared in DMEM or FluoroBrite DMEM media. Cells were treated with 40 mM $KBrO_3$ for 30 minutes at 37ºC. The media was discarded, and cells were recovered in fresh DMEM or Fluorobrite DMEM media for indicated periods of time before subcellular fractionation or fixation.

By convention, throughout this manuscript, cells that have not been treated with $KBrO_3$ will be named **NT cells (Not Treated)**, cells treated with $KBrO_3$ for 0.5 hours will be named **T0 cells** and cells treated with $KBrO_3$ for 0.5 hours followed by a period of recovery will be called **TX cells**, with 'X' defined as the period of recovery, recorded in hours.

1.4 Cell-cycle measurements by flow cytometry

For fixation, the cell pellets containing 1 x 10^6 cells, were resuspended in 2 ml 2.4% paraformaldehyde at 37˚C for 15 minutes. The tubes were inverted twice during incubation with the fixative to homogenize the cells in the fixative, followed by two washes via centrifugation in PBS 1X at 2000 rpm for 5 minutes. The cells were permeabilized in 1ml of 0.2% Triton X100, 1X PBS, for 5 minutes at room temperature and washed in 1ml PBS 1X twice with centrifugation at 2000 rpm for 5 minutes. Cells were resuspended in 2ml of PBS 1X and stored on ice. Cells were then incubated in a solution of primary antibodies for 45 minutes followed by two washes in 2ml PBS 1X and centrifuged at 2000 rpm for 5 minutes. Incubation in a solution of rabbit polyclonal Alexa Fluor 488 secondary antibodies was done for 45 minutes, followed by two washes in 2ml PBS 1X and centrifuged at 2000 rpm for 5 minutes **(Please refer to table 5 for the working antibody concentrations).**

The samples were diluted in 300 µl of labelling solution containing 4 µM sodium citrate, 10% Triton X100 and 0.01mg/ml RNAse. Automated sample uptake was set-up on the MACSQuant VYB system at the *M4D platform (Institut de Biologie Structurale)*. 1:100 propidium iodide (PI) (1mg/ml) was added automatically to each sample before measurement. 50 µl of the control samples were used to adjust the number of events captured by FSC (forward scatter) and SSC (side scatter) before measuring a volume of 300 µl (~ 0.5 x 10^6 cells/ sample) The sample volume was homogenized and allowed to

flow at a low rate for single cells to pass through the fluidic system, illuminated with 488 nm laser to measure the fluorescence intensity of NTH1 at the single cell level. The SSC vs FSC (granularity of the cell vs size of the cell) plot was used to gate 50,000 cells/sample. The data was analyzed using the MACSQuantify software (v2.13.3). SSC-H (height) vs SSC-A (area) graphs were plotted to select only singlets from a mixed population of cells. Histograms of the PI labelled singlet cells were plotted to quantify the cell populations present at different stages of the cell cycle followed by isolating the expression of NTH1 at each cell cycle stage. The online available software *Floreada.io*, designed for flow cytometry analysis was used to represent the data.

2. Western Blot

Previously prepared cell pellets (**described in section 1.1 Materials and Methods)** were denatured in 100 µl denaturing lysis buffer (20mM Tris-Cl, pH 7.5, 50 mM NaCl, 0.5% IGEPAL (NP40), 1% sodium deoxycholate, 1% SDS, 5mM $MgCl_2$, 50 µl of protease inhibitor cocktail and 50 µl of phosphatase inhibitor cocktail, qsp dH_2O). 1 µl of Turbo nuclease (Jean Biosciences -116446) was added and the cell suspensions were left on ice for 12 minutes. The samples were centrifuged at 10,000 rpm at 4˚C for 10 minutes. The supernatant was transferred to fresh Eppendorf tubes without touching the pellet. Protein quantification was performed according to the Micro BCA Protein assay kit provided by the manufacturer (Thermofisher 23235). 2 µl of the sample was diluted in 498 µl of distilled water. 150 µl of each standard and sample was pipetted into a 96-well plate and measured on UV/ vis absorbance on a plate reader CLARIOStar Plus (BMG Labtech). According to the concentration of the samples, they were aliquoted and stabilized with denatured Laemmli 1X and, stored at -20˚C.

20 µg of protein samples were separated in a 12% polyacrylamide (TGX Stain-Free Fast Cast Acrylamide 12% Kit 161-0185) gel together with 5 µl of protein ladder (BioRad, Precision Plus All Blue Ladder 250 kDa). Gel migration was performed on the BioRad apparatus at 120V till the level of the stacking gel and increased to 150V during migration in the resolving gel. After gel migration, the stain-free gel was activated on the ChemiDoc MP. The proteins were transferred onto a nitrocellulose membrane for 7 minutes at 25V. After transfer, the stain-free blots were washed in PBS 1X-Tween 20 0.1%, before imaging under the ChemiDoc.

To visualize NTH1 protein on the membranes, the blots were saturated with 5% milk-PBS 1X-Tween 20 0.1% for 1 hour at room temperature. The blot was incubated with the primary antibody (Table 5) for 2 hours at room temperature, followed by 5 washes in PBS 1X-Tween 20 0.1% for 5-minute intervals. The blots were labelled with the secondary antibody Goat anti-rabbit IgG Star Bright Blue 520 (Table 5) for 1 hour at room temperature, followed by 5 washes in PBS 1X-Tween 20 0.1% for 5-minute intervals. The immunoblots were visualized on the ChemiDoc at suitable exposure times.

3. Immunofluorescence

Table 5 summarizes the different antibodies used in this work: cell cycle experiments (**section 1.4, Materials and Methods**), for western blot analysis (**section 2, Materials and Methods**) and for immunolabeling experiments (**section 4, Materials and Methods**). Wherever required, we have indicated all the antibody dilutions tested (black) and working dilutions used (red) in the lab for the following experiments.

Table 5: List of concentrations of primary and secondary antibodies.

Red text highlights the dilution and concentration of antibodies considered for respective techniques.

ANTIBODIES						
Catalogue No.	**Company**	**Primary Antibodies**	**Type**	**Western Blot**	**Immunofluorescence/ Flow cytometry**	**dSTORM**
BER and Chromatin proteins						
ab191413	Abcam	anti-**NTH1** (1.26mg/ml)	Rabbit monoclonal	1:500 [2.52 µg/ml] 1:1000 [1.26 µg/ml] 1:5000 [0.252 µg/ml]	1:150 [8.4 µg/ml] 1:500 [2.52 µg/ml]	1:150 [8.4 µg/ml] 1:500 [2.52 µg/ml]
ab236912	Abcam	anti-**NTH1** (4.61mg/ml)	Rabbit polyclonal	1:5000 [0.922 µg/ml]	1:100 [46.1 µg/ml] 1:500 [9.2 µg/ml] 1:1000 [4.61 µg/ml]	-
ab268072	Abcam	anti-**APE1** (0.2mg/ml)	Mouse monoclonal	1:1000 [0.2 µg/ml]	1:100 [2 µg/ml] 1:500 [0.4 µg/ml]	1:500 [0.4 µg/ml]
DNA lesions						
ab81299	Abcam	Anti-**gamma H2AX** (phospho S139)(0.73mg/ml)	Rabbit monoclonal	-	1:100 [7.3 µg/ml] 1:500 [1.5 µg/ml]	-
05-636	Merck	anti-phospho-Histone **H2A.X** (Ser139), clone JBW301 [1mg/ml]	Mouse monoclonal	-	1:500 [2 µg/ml]	-
ab1791	Abcam	Anti-**Histone H3** antibody **(Nuclear marker and ChIP grade)** (1mg/ml)	Rabbit polyclonal	-	1:10,000 [0.1 µmg/ml]	1:1000 [0.1 mg/ml]
ab14955	Abcam	Anti-**Histone H3** antibody **(phospho S10) (1mg/ml)**	Mouse monoclonal		1:10,000 [0.1 µg/ml]	1:2000 [0.5 µg/ml]
MABE71	Merck Millipore	**Anti-Histone antibody, Pan,** clone F152.C25.WJJ	Mouse monoclonal		1:2000	
ab48508	Abcam	anti-**8-Hydroxy-2'-deoxyguanosine** (1.2mg/ml)	Mouse monoclonal	-	1:2000 [0.6 µg/ml]	-
Catalogue No.	**Company**	**Secondary Antibodies**	**Type**	**Western Blot**	**Immunofluorescence**	**dSTORM**
12005870	BioRad	Star Bright Blue 520	Goat anti-rabbit polyclonal	1:2500		
AB_143165	Invitrogen	Alexa Fluor **488 (H+L)** (2mg/ml)	Goat α rabbit polyclonal		1:500 [4 µg/ml] 1:1000 [2 µg/ml]	
AB_2534069	Invitrogen	Alexa Fluor **488 (H+L)** (2mg/ml)	Goat α mouse polyclonal		1:500 [4 µg/ml] 1:1000 [2 µg/ml]	
AB_143157	Invitrogen	Alexa Fluor **568 (H+L)** (2mg/ml)	Goat α rabbit polyclonal		1:500 [4 µg/ml] 1:1000 [2 µg/ml] 1:5000 [0.4 µg/ml]	
AB_2534072	Invitrogen	Alexa Fluor **568 (H+L)** (2mg/ml)	Goat α mouse polyclonal		1:500 [4 µg/ml] 1:1000 [2 µg/ml]	
AB_2535814	Invitrogen	AlexaFluor **647 F(ab')2** (2mg/ml)	Goat α rabbit polyclonal		1:1000 [2 µg/ml]	1:500 [4 µg/ml]
FP-SC5110	Interchim	FluoProbes **647H (H+L)** (1mg/ml)	Donkey α rabbit polyclonal			1:100 [10 µg/ml] 1:500 [2 µg/ml]
20802	Biotium	**CF 568** IgG (H+L), Highly Cross-Adsorbed, CF® Dye Conjugates, - (1mg/ml)	Donkey anti-Mouse polyclonal			1:500 [2 µg/ml] 1:1000 [1 µg/ml] 1:2000 [0.5 µg/ml]
20819	Biotium	**CF 680** IgG (H+L), Highly Cross-Adsorbed, CF® Dye Conjugates, - CF 680 (1mg/ml)	Donkey anti-Mouse polyclonal			1:1000 [1 µg/ml] 1:2000 [0.5 µg/ml]

4. Sample preparation for microscopy experiments

4.1 Immunofluorescence of fixed samples

We placed 12 mm/ 18 mm poly-D-lysine (0.2mg/ml) coated coverglasses (1.5 or 1.5H grade) in either a 6-well plate or 35mm individual petriplates, containing 2-3 coverglasses per plate. 0.2 x 10^6 HeLa cells were seeded in 2 ml complete DMEM medium or FluoroBrite DMEM (dSTORM) per well overnight.

When indicated subcellular fractionation was carried out to remove the nucleoplasmic protein fraction, retaining only the chromatin-associated one. For subcellular fractionation, different buffers were tested:

- 1X cytoskeleton (CSK) buffer (100 mM NaCl, 300 mM sucrose, 10 mM PIPES pH 6.8, 3 mM $MgCl_2$, and protease inhibitors final concentration at 1X) supplemented with 0.2% or 0.5% Triton X-100.
- 1X PBX 1X, supplemented with 0.2% Triton X-100
- 1X CB buffer at pH 6.1 (10 mM 2-(N-morpholino) ethanesulfonic acid hydrate, 150 mM NaCl, 5 mM ethylene glycol tetraacetic acid, 5 mM $MgCl_2$, 5 mM glucose), supplemented with 0.2% Triton X-100.

By convention, in the manuscript, non-fractionated cells will be addressed as **NF cells** and the fractionated cells will be addressed as **F cells.**

NF and F cells were fixed in 4% paraformaldehyde (PFA in PBS, w/v, Electron Microscopy Sciences) for 10 minutes at room temperature (RT). Alternatively, to detect 8-oxoguanine, cells were fixed with methanol: acetone [1:1] for 10 minutes at -20ºC, followed by denaturation with 2N HCl for 45 minutes and neutralized with Tris-HCl for 5 minutes. Cells were then permeabilized with 0.2% TritonX-100 for 5 minutes and saturated with 3% BSA (Bovine Serum Albumin, Sigma-Aldrich) in PBS for 1 hour. Depending on the experiments, cells were immunolabelled with a primary antibody anti-NTH1 or anti-APE1 or anti- γH2AX or anti- 8oxoG for 1 hour at room temperature, followed by secondary antibody labelling using previously determined dilution factors (Table 5). Samples were kept in PBS 1X at 4°C until use. After immunolabelling, for confocal imaging, coverglasses were washed 3 times for 5-minute interval and for dSTORM imaging, coverglasses were washed 4 times for 5-minute intervals.

For dSTORM experiments, we have used F(ab')2 antibody. This antibody is smaller in size (5 to 7 nm) compared to the full-length antibody (~ 20 nm). The latter reduces the size of the detection complex (epitope-fluorophore distance) improving the localization precision. F(ab')2 tends to also reduce the background noise, leading to a better signal to noise ratio.

For confocal imaging, 10 µl of DAPI-Vectashield (Vectorlabs) mounting medium was applied on a microscopy slide. The coverglasses were flipped over the droplet with cells facing the mounting medium. The coverglasses were gently pressed to remove excess mounting medium and avoid formation of air bubbles. Once, the excess medium was removed, the coverglass was sealed with Picodent twinsil (Picodent 13001000).

Before mounting the coverglasses for dSTORM imaging experiments, they were first incubated with different fiducial markers such as, gold nanoparticles (AuNPs) for 1.5 hours (Sigma 753688), Nanodiamonds-WGA for 1 hour (Adámas Nanotechnologies) or even Qdot 655 streptavidin conjugates (Invitrogen Q10121MP) at 0.2 x 10^6 particles/µl. The coverglasses were post fixed with 4% PFA for 10 minutes. Coverglasses were immersed in an imaging Glox buffer [62.5 mM Tris, 12.5 mM NaCl, 12.5% D (+) Glucose, 0.01 mg/mL glucose oxidase, 0.8 µg/mL catalase], containing either 10- or 100-mM MEA (Sigma 30070) or 143 mM BME suitable for the photophysical properties of the fluorophore used. The imaging buffer allows to transfer most fluorophores to the non-fluorescent 'off' state, while maintaining a stochastic reactivation of a small subset to the 'on' state for a short period of time. Two factors, besides its photophysical properties, affect the photo switching behaviour of the fluorophore – concentration of thiol and oxygen scavenging system. 200 µl of imaging buffer was placed within adhesive silicone cover-well chambers attached to a microscopy slide (Electron Microscopy Sciences). The cover glass was flipped over with the cells facing the imaging buffer and sealed with Picodent twinsil to limit gas exchange.

4.2 Living samples

Two 18 mm poly-D-lysine (0.2mg/ml) coated coverglasses were placed in a 6-well plate. Each well was seeded with 0.1 x 10^6 cells and allowed to grow overnight in 2 ml FluoroBrite DMEM. Transfections were carried out with either p-NTH1-mEos4B or p-mEos4B-NLS plasmids as described in **section 1.2 of Materials and Methods**. mEos4B is a green to red photoconvertible fluorescent protein routinely used in single particle tracking experiments with living cells (Wulffele et al., 2022). Treatment with $KBrO_3$ was performed to prepare NT, T0 and T4 coverglasses (**section 1.3, Materials and Methods**). Cells were washed rapidly in warm FluoroBrite DMEM. The coverglass was flipped over with the cells facing Fluorobrite DMEM and sealed with Picodent twinsil to limit gas exchange.

5. Microscope setup and data acquisition

5.1 Spinning disk confocal fluorescence microscopy

Experiments were performed using an Olympus IX81 inverted microscope (Figure 26-left image), equipped with six diode lasers (Table 6), which allows acquisition in multiple fluorescence channels. Here the confocality is achieved by a combination of first, a collector disk composed of an

array of microlenses, that split and focuses the excitation beam through the pinholes of the second disk (Nipkow disk) placed so it is in the back focal plane of the emission beam. The resulting emission is thus filtered for confocality, reflected by a dichroic mirror of suitable characteristics, so the emission is directed to the camera, accelerating image acquisition with low phototoxicity and reduced background signal.

The microscope is equipped with a piezo z-stage (range 400 µm). The autofocus system (ZDC) acts on the Olympus z mechanism to find/ set the focal plane within a Z resolution, depending on the objective. This allows acquisition of 3D volumes of the sample. All images and Z scans were acquired using a 20x, air objective and 60x and 100x oil immersion objectives. Table 6A describes the calibration of pixel size based on the objective used. An iXon Ultra EMCCD 512 x 512 with 16 µm/px camera (Andor X7300) was used for acquisitions, that were recorded on the Metamorph software. Confocal microscopes are limited in resolution by the diffraction of light, which follow the Abbe's law.

$$d = \frac{\lambda}{2NA_{obj}}$$

where, d is the diffraction limit of light, λ is the wavelength of light and NA_{obj} is the numerical aperture. For example, an object emitting at 500 nm wavelength, which is observed using an objective with a numerical aperture of NA = 1.49, results in an achievable resolution of around 200 nm.

Table 6: (A) Calibrations details of image magnifications used during 3D acquisition of confocal images. (B) Laser properties and power densities used with different magnifications at the sample level during 3D acquisitions of confocal images.

A

Objectives	Type	Calibration (µm/ pixel)	N.A	Z resolution (µm) (depth of field)	Step size (µm)
20×	air	0.5984	0.8	1.56	1
60×	oil	0.2296	1.42	0.44	1
100×	oil	0.1323	1.49	0.40	0.5

B

Lasers	Digitizer	EM gain	Exposure	Power at sample (W/cm²)		
				20x	60x	100x
DIC	16 bit 10MHz	200	200	-	-	-
405	16 bit 10MHz	250	200	14.8	37	37
488	16 bit 10MHz	250	200	15.5	64.6	64.6
561	16 bit 10MHz	250	200	-	12.4	-
640	16 bit 10MHz	250	200	6.6	22	66

5.2 Single molecule localization microscopy (SMLM)

5.2.1 Overview of SMLM

In the early 2000s, advances in microscopy were spurred onward to overcome the diffraction barrier of the optical microscope (Miriklis et al., 2021). This led to the advent of super-resolution microscopy techniques (SRM), developed independently by three researchers Eric Betzig, William E. Moerner (SMLM) and Stefan W. Hell (STED), who shared the 2014 Nobel prize in Chemistry and brought light microscopy into the nanometer scale (Betzig et al., 2006; Rust et al., 2006). Single-Molecule Localization Microscopy (SMLM), is one of the three SRM techniques achieving nanoscale resolution between 10-20 nm (Lelek et al., 2021). This enables us to visualize small macromolecular structures and protein-protein interactions. We decided to use three SMLM approaches to spatially characterize the nuclear distribution and dynamics of the BER DNA glycosylase NTH1.

5.2.2 Principle of SMLM

Because of the limited resolution of conventional fluorescence microscopy (~200 nm resolution) (Betzig et al., 2006; Rust et al., 2006), it is not suitable to visualize the genomic organization at a nanoscale level. Recent studies utilize SMLM, a super-resolution (SR) technique that achieves a high spatial resolution of 10-20 nm, circumventing the problem of the diffraction limit of light and becoming the new bedrock for near-molecular resolution studies (Rahman et al., 2024). To study endogenous and overexpressed NTH1, two SMLM techniques have been employed during my thesis - dSTORM and PALM (Figure 25).

dSTORM (Direct Stochastic Optical Reconstruction Microscopy) involves immunolabelling cellular structures with antibody tagged photo-switchable fluorophores; the majority of these fluorophores is switched to the non-fluorescent dark state and only a small fraction is stochastically activated at each time interval, determining their positions with high localization accuracy in fixed cells (Betzig et al., 2006; Xu et al., 2017). On the other hand, PALM (PhotoActivated Localization Microscopy) utilises mainly photo transformable fluorescent proteins (PTFPs, e.g mEos4B in Figure 25), which are photoconverted or photoactivated with a low UV light intensity to the ON state. In the case of mEos4b, the protein is photoconverted from the initial green form (OFF state) to the red form (ON state), which is then excited to detect only the red emission, until the molecule is switched to a different transient OFF state or permanently bleached (Rust et al., 2006; B. Huang, 2010). In both PALM and dSTORM, only a small subset of fluorophores is activated to an 'on' state. This process is repeated 'n' times to map the localization of the fluorophores (Figure 25 - t_1, t_2…t_n). Finally, computational image processing reconstructs a composite image of all the localizations with their coordinates, in a spatial resolution of 10-20 nm (Betzig et al., 2006; Lelek et al., 2021).

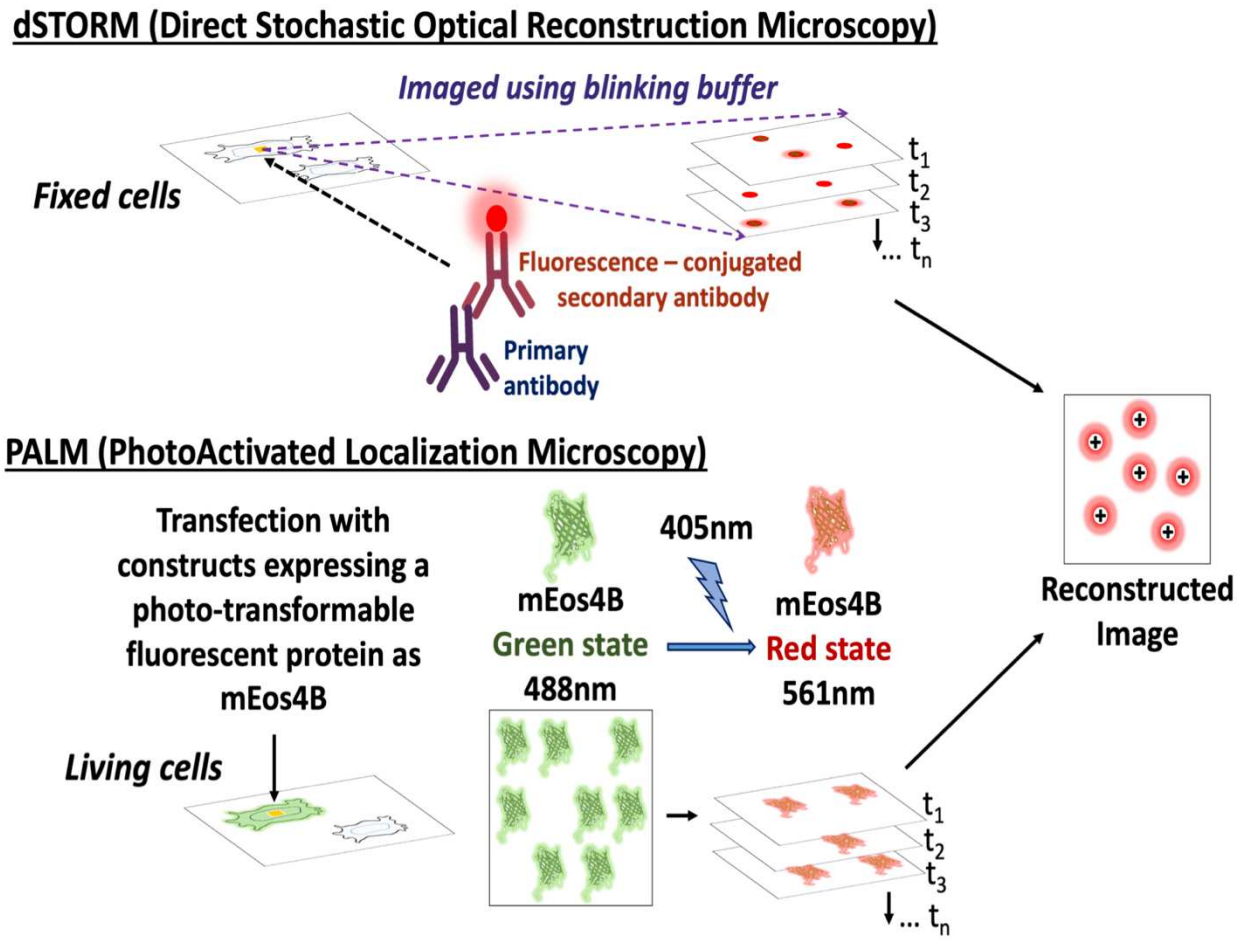


Figure 25: Schematic representation of SMLM (dSTORM and PALM) used in this thesis.
A fraction of fluorescent markers are stochastically activated at different time frames (t_1, t_2, t_3, t_n…) that are imaged successively. Each of these localizations are defined at a high precision using 2D gaussian

fitting. Then, image processing reconstructs all the fluorescence signals into a single image at a nanoscale resolution (reconstructed image).

5.2.3 The ABBELIGHT SAFe360 system

The M4D platform houses a commercial Abbelight SAFe360 system (Figure 26-right image). An Olympus IX83 inverted microscope is equipped with a 100x oil immersion 1.5 NA objective lens (UPLAPO100×OHR). Constant focus is ensured during acquisitions by an axial drift correction unit (IX3-ZDC2-830). The microscope is equipped with six lasers available in an Oxxius laser combiner (405, 488, 532, 561, 643 and 730 nm) and a module for homogeneous EPI/HiLo/TIRF illumination. The lasers and two cameras (Orca Fusion sCMOS camera by Hamamatsu) are controlled by Neo Live Imaging software (Abbelight) (Table 7). A large field of view with homogenous illumination and real time analysis provided by the NEO software provides fast acquisitions with real time analysis on 3D and multicolor imaging. The equipment of the Abbelight microscope allows to implement dSTORM, PALM and DNA-PAINT (Points Accumulation for Imaging in Nanoscale Topography) experiments.

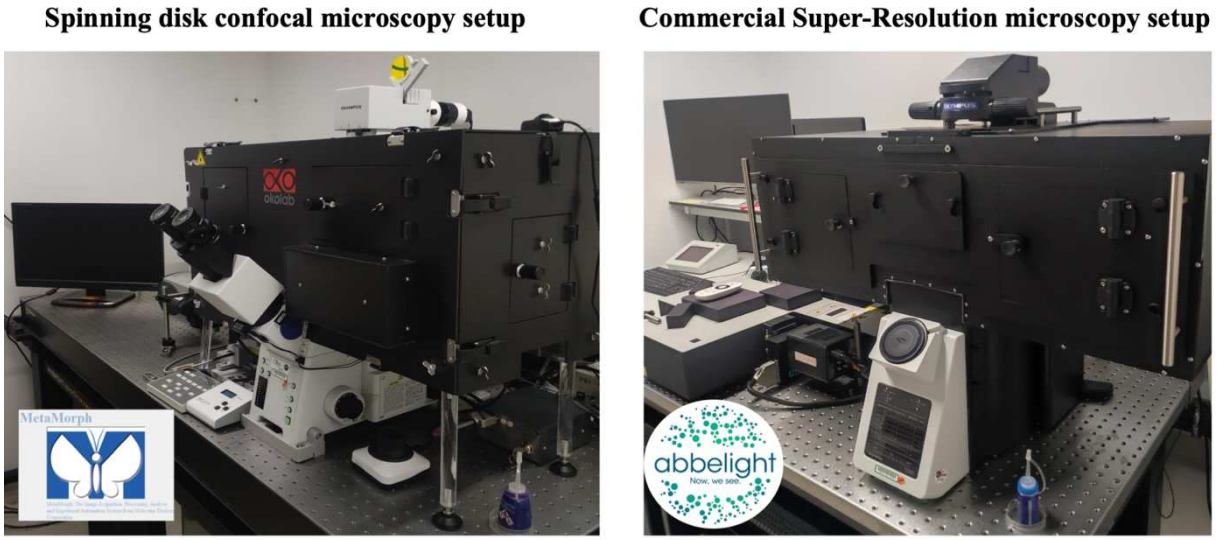


Figure 26: The microscopy setup in the M4D platform.
The spinning disk confocal microscope (left) controlled with Metamorph, and the commercial super-resolution setup, Abbelight SAFe360 (right), controlled with Neo Live Imaging.

5.2.4 dSTORM acquisitions

We employed dSTORM to first investigate, the distribution of NTH1 at the single – molecule level. Here, the sample was illuminated in HiLO (Highly inclined and laminated optical sheet) mode on the Abbelight Olympus microscope setup (Tokunaga et al., 2008). A 2D transmission and HiLO illuminated image were taken using a 100x high NA objective. A Di03-R405/488/561/635-t1 (Semrock) excitation dichroic mirror was used with a band pass filter FF01-698/70 (Semrock) to separate emission

and excitation light. A series of 40000 frames at an exposure of 60 ms was acquired using a high-power density of the 640 nm laser in EPI/HiLO illumination. In addition to this, to improve photo switching and maintain consistent localizations per frame, a continuous immunization of a weak 405 nm laser power was applied. Real-time reconstruction of the nuclear ROI was performed on the *Abbelight software Neo* and helped to follow the number of localizations per frame and photon count. Please refer the imaging parameters described in Table 7.

5.2.5 spt PALM acquisitions

SptPALM images of HeLa cells expressing either p-NTH1-mEos4B or p-mEos4B-NLS were taken under 27˚C, within a closed incubator chamber. First, we illuminated our sample with very low 488 laser power to be able to scan a large field of view with an exposure time of 100 ms, in search of medium to highly transfected cells. Once an optimal transfected cell was located, the field of view was narrowed and a 488 nm illuminated, and transmission light snapshot of the cell was taken. The 561 nm laser was switched on and continuously illuminated the sample during acquisition of 10000 frames at an exposure time of 10 ms (100 fps). The photoconversion of mEos4b relied on the intensity of the 405 nm laser, which was set at 3 mW/cm^2 and manually pulsed to maintain consistent localization density during acquisitions. Additionally, we also used weak 488 nm light to revert the dark states in the red form of mEos4b to their fluorescent state, thereby eliminating slow blinking and recording longer tracks with minimal track interruptions (De Zitter et al., 2019). The combination of Di03-R405/488/561/635-t1 dichroic mirror with either ET525/50m or ET600/50m band path filters (both from Chroma) were used to observe the green and the red form of mEos4b, respectively. Real-time reconstruction of the nuclear ROI with the Abbelight software Neo, helped to follow and monitor the number of localizations per frame. Please refer the imaging parameters described in Table 7.

Table 7: Hardware configurations and imaging parameters used during acquisitions on the Abbelight Olympus IXE.

Imaging parameters	dSTORM	DNA-PAINT	PALM
No. of fiducial markers per cell	2 to 5	2 to 5	2 to 5
Exposure (ms)	40	50	10
No. of Frames	40000	20000	10000
Illumination channel	HiLO/TIRF	Epi/ HiLO	Epi/ HiLO
640nm (W/cm^2)	1054.5	1051.8	-
561 nm (W/cm^2)	-	128.7	136.9
488 nm (W/cm^2)	-	-	9.3

6. Data analysis and statistics

6.1 Data analysis of confocal images

Images obtained by confocal imaging were processed and the fluorescence intensity measurements and segmentation steps were performed on the software IMARIS [Bitplane (Oxford Instrument) ™, V10.2). Z stacks were processed by selecting an ROI of 380 x 380 px from the center of the field of view (FOV), limiting discrepancies in the laser illumination found at the edges of the image. Our segmentation parameters were applied to all 20x and 100x magnified images.

6.1.1 2D and 3D nuclear segmentation

3D nuclei from 20x magnified images were segmented by automatic thresholding of the DAPI channel using the 'Surfaces' module on the IMARIS software. A Gaussian filter was applied with a surface area detail of 1.5 µm, and background subtraction of 0.2 µm, of allowing normalization of the DAPI fluorescence signal within the ROI which varied from image to image. To determine the borders of the segmentation mask, each nucleus was assigned a 'seed point', at the centre of the nucleus. The seed point was allowed to automatically grow till it detected the boundary of the nucleus, establishing an estimated nuclear diameter. Finally, nuclear masks are applied on nuclei within the ROI. Nuclei close to the edges of the ROI were excluded from the statistical data. These settings were applied to ~ 30 cells within the field of view and for more than 500 cells per condition. In a similar manner, 2D nuclear masks on HeLa nuclei from 100x magnified images were applied on the 488 nm channel to measure nuclear mean fluorescence intensity (NMFI).

6.1.2 2D NTH1 foci segmentation

Foci were segmented from single HeLa nuclei present on 100x magnified confocal images using the 'Surfaces' module of the IMARIS software. From each image, three nuclear Z slices were merged into a single 2D image with a Z depth of 1.5 µm. We used the 488 nm channel which captured immulabelled cells for endogenous NTH1. As illustrated in figure 27, first a manual threshold was applied to each 2D image (lower limit = 184 a.u.) with a surface smoothing detail of 0.1 µm and background subtraction of 0.2 µm and a seed point diameter of 0.264 µm. These settings were applied for 2-3 cells within the FOV and for a total of ~ 10 cells per condition.

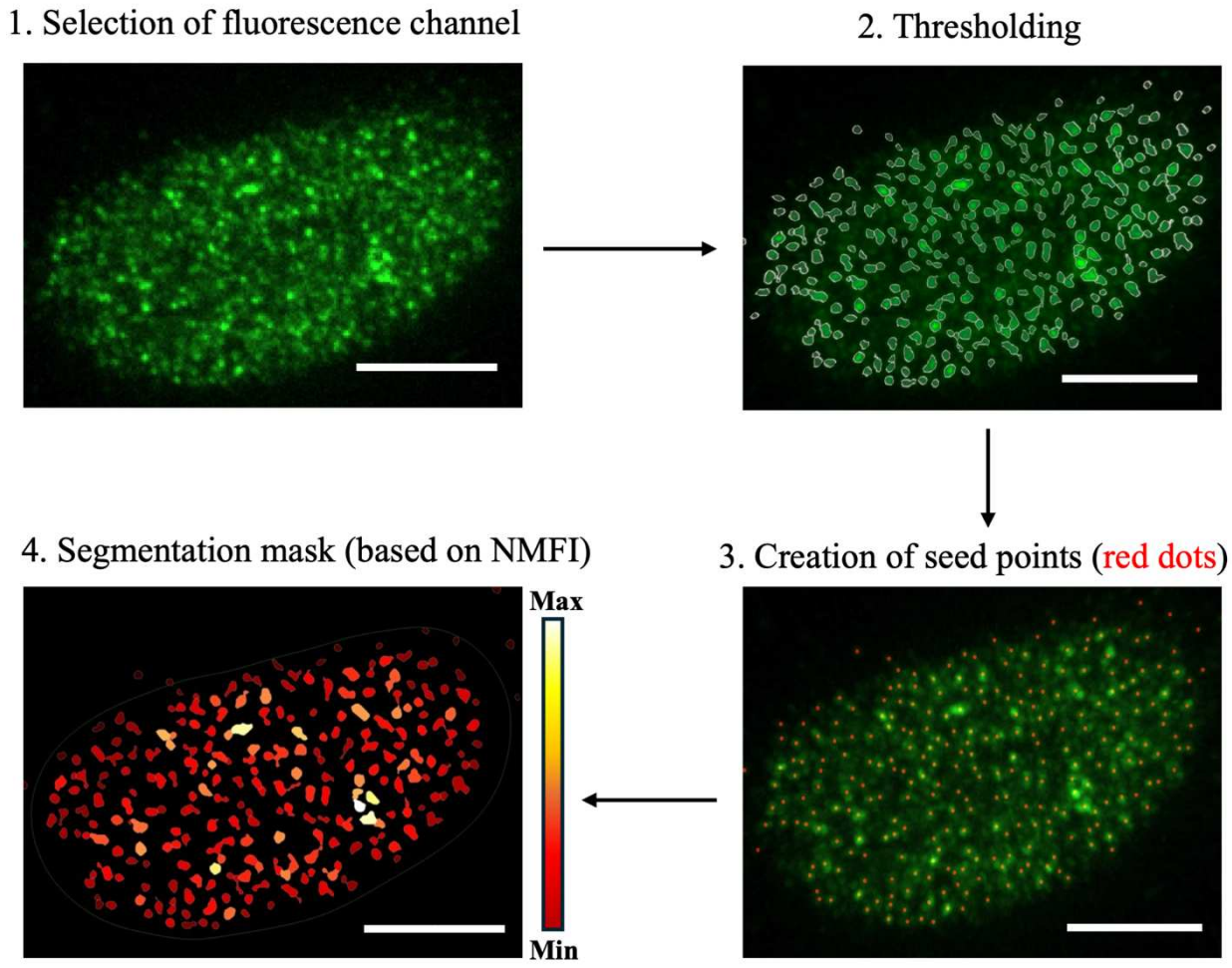


Figure 27: Flowchart for NTH1 foci segmentation optimized for HeLa cells.
1. Selection of the fluorescence channel (NTH1 labelling). 2. Thresholding the fluorescence signal. 3. Creation of 'seed points' as starting points to initiate automatic detection of foci and 4. Foci segmentation mask colour coded based on nuclear mean fluorescence intensity (NMFI) with respective colour bar. Scale is 5 µm.

6.1.3 Fluorescence intensity measurements

Nuclei masks were applied to the 488 nm fluorescent channel corresponding to the immunolabeled endogenous NTH. The mean fluorescence intensity of nuclear NTH1 was measured for ~ 500 segmented HeLa nuclei from 5 independent experiments. Similarly, the foci masks were applied to the 488 nm fluorescent channel. Characteristic features like the number of foci, the foci surface area, foci diameter, foci circularity and the mean NTH1 foci fluorescence intensity were measured for each focus and subsequently extracted for all foci within a HeLa nucleus. This data was collected for ~ 10 segmented HeLa nuclei from 2 independent experiments.

6.2 dSTORM

6.2.1 Reconstruction of super-resolved images

2D dSTORM images were reconstructed from 40000 frames (640 nm channel) and analysed with the ThunderSTORM plugin (Ovesný et al., 2014) (v1.3) in FIJI v2.9.0.

The camera setup included:

- Pixel size (nm) = 100
- Photoelectrons per A/D count = 0.23
- Quantum efficiency = 0.81
- Base level (A/D counts) = 99
- Readout noise (e^-/pixel) = 0.99

The following parameters were used to find and fit the signal emitted by each particle:

- Image filtering – Wavelet B-Spline (B spline order: 3.0 and B-spline scale: 2).
- Approximate localization of molecules – Local maximum method (Peak intensity threshold: 2*std (Wave.F1) and Connectivity: 8 neighbourhood)
- Sub-pixel localization of molecules – PSF: Integrated Gaussian method (Fitting radius: 5 px, Fitting method: Maximum likelihood, Initial sigma: 1.3 px).

After fitting, all the detected molecules are summarized in the Results table together with the parameters on the Gaussian fit (x, y coordinates of the centre, sigma, intensity and offset) and with the derived/ calculated parameters such as uncertainty or localization precision. During the post-processing, several filters were applied to discard artefacts and low-quality localizations. Sigma filtering (75 - 250 nm) was used to remove out of focus localizations and multi-emitters, while filtering by uncertainty (< 25 nm) allowed us to select the brightest and well localized molecules. To correct for the sample drift, we initially used fiducial markers (AuNPs or nanodiamonds, **see section 4.1**) and the following parameters in the ThunderSTORM plugin: max distance – 40 nm, min marker visibility ratio – 0.01, trajectory smoothing – 0.04. However, the latest dSTORM images were drift corrected on a GPU accelerated software known as COMET (Cost function Optimized Maximal overlap drift Estimation) *https://smlm.tools/* , developed by the team of *Dr. Mark Bates, University of Gothenburg, Germany*. The dataset was divided into equal parts containing a fixed number of localizations with a maximum drift of 200 nm in one direction. Final rendering of reconstructed SR images was magnified ten times (pixel size: 10 nm).

6.2.2 Cluster segmentation and quantification

To characterize NTH1 clusters, we used density-based clustering from the SR-Tesseler software developed by *Dr. Florian Levet at the Bordeaux Imaging Center, France* (Levet et al., 2015). Voronoi tessellation draws a perpendicular bisector between each pair of localizations. The intersection of all the bisectors divides the space into polygons with only one localization in each of them. The denser the localizations are, the smaller the Voronoi area occupied.

We then, applied different local density values and selected the best value that visibly encompassed clusters of NTH1. Figure 28 summarizes the steps involved in Voronoi Tessellation and an example of one density factor primarily tested for cluster segmentation. Final measurements of the number of clusters within a nucleus, cluster surface area, number of localizations within each cluster, their circularity and diameter were extracted.

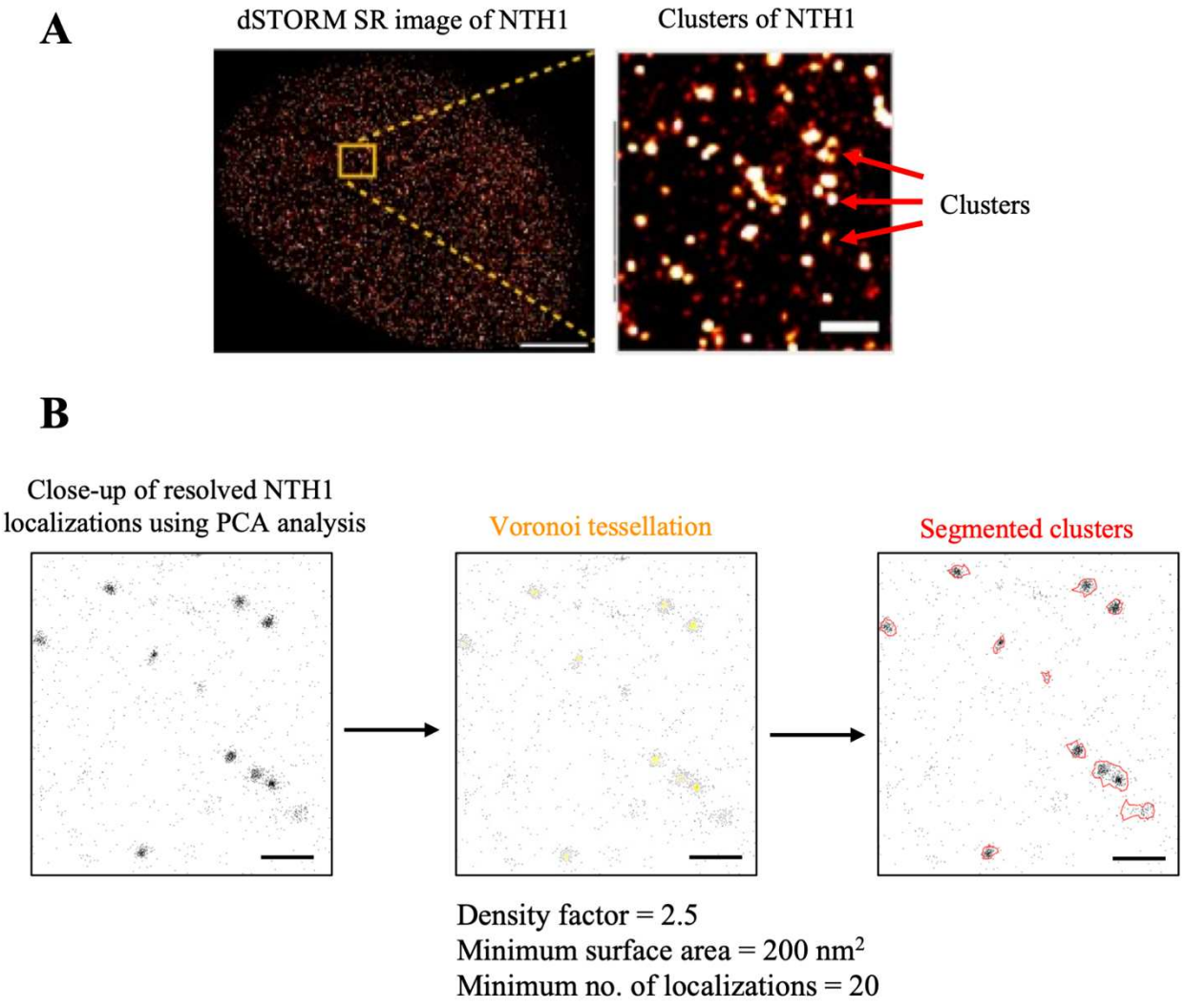


Figure 28: Voronoi tessellation analysis performed on reconstructed dSTORM images of HeLa nuclei using the SR-Tesseler algorithm.
(A) Reconstructed dSTORM images of HeLa nuclei showing the heterogenous distribution of NTH1 forming dense clusters of localizations (NTH1), were rendered as (B) 'seed points' (black) using the Point Cloud Analysis feature (PCA) on the software SR-Tesseler. Each seed point within a Voronoi surface area was assigned a local density (yellow) and segmentation of clusters was further performed by applying a density factor of 2.5, with a minimum number of 20 localizations and a minimum surface area of 200 nm^2 per cluster.

6.3 Single Particle Tracking (SPT) PALM

sptPALM experiments aim at gaining information about the cellular dynamics of molecules, in our case NTH1. The idea is to track individual molecules in cells to determine the Diffusion coefficients (D) of different populations of molecules, as a function of the cell state and subcellular localization. In our case, we were interested in populations of NTH1 molecules bound or not bound to DNA, as proteins interacting with a DNA lesion are expected to show almost no mobility (very low D), whereas a protein free in the cytoplasm will be more mobile (high D).

One of the earliest reviews on single-particle tracking describes the dynamic and heterogenous organization of the plasma membrane (Saxton, 1997). Due to its simple implementation with PALM, this technique became accessible to many laboratories and constantly improved the manner of reconstructing trajectories and calculating diffusion rates in 2D- or 3D systems. sptPALM uses reporters (e.g PCFPs) that provide excellent spatial localization precision (~ 27 nm) and high temporal resolution (~ 100 frames/s) with limited phototoxicity and biodegradation (Manzo & Garcia-Parajo, 2015). We combined SPT with PALM to trace individual molecules within HeLa nuclei and to follow real-time diffusion dynamics properties of NTH1, by measuring their diffusion coefficients. In short, a protein interacting with a DNA lesion is expected to show almost no mobility or a low diffusion coefficient whereas, a protein in search of DNA lesions would appear very mobile and have a higher diffusion coefficient. Therefore, applying this technique to live cells will allow us to investigate the dynamics of NTH1 in space and time, in response to oxidative stress.

6.3.1 Reconstruction of single molecule trajectories

PALM data was collected and reconstructed using the ThunderSTORM plugin (Figure 29). Here, we used the same camera settings as described previously (**section 5.2.1**), with a peak intensity threshold of 1.3*std (Wave.F1), due to low signal to noise ratio on acquisition. Here, our goal is to obtain long tracks at a high temporal resolution. By limiting the laser power density, we reduce the effect of photobleaching. This effect coupled with a short exposure time, results in low signal detection. Final rendering of reconstructed SR images was magnified ten times.

The *Swift* tracking algorithm [*http://bit.ly/swifttracking*; Endesfelder et al., manuscript in prep] was used to link the localizations between frames, to reconstruct 2D trajectories belonging to NTH1 molecules, diffusing throughout the nuclear landscape. The following tracking parameters were used: exp_displacement = 100 nm, p_bleach = 0.1, p_blink = 0, p_reappear = 0.5, precision = 25 nm, max_displacement = 1000 nm, max_displacement_pp = 1000 nm, max_blinking_duration = 2 frames and default values were used for the remaining parameters. A pruning step was introduced to iteratively eliminate excess connections per localization, resembling uncharacteristic motion behaviour within dense clusters of localizations. Parameters related to photophysics—such as the probabilities of bleaching, blinking, and reappearing (p_bleach, p_blink, p_reappear, and max_blinking_duration)—were adjusted to reflect the observed track. Maximum displacement or the probability of maximum displacement (max_displacement or max_displacement_pp) was determined arbitrarily, by the nuclear size and the right tail of the jump distance (JD) histogram measured for transfected cells. The expected displacement (exp_displacement) was selected to approximately match the peak of the mean jump distance histogram observed. We considered tracks with more than four localizations (n > 4) as valid trajectories, since shorter tracks contribute to molecules moving out of the focal plane or photobleached. *Swift* separates tracks based on motion transitions (e.g from immobile to diffusive) into segments. Notably, only a small fraction of tracks (~1–2%) contained more than one segment, suggesting that tracks were too short to see motion changes.

The following information was extracted from a custom-written MATLAB (MathWorks) code designed by *Dr. Dominique Bourgeois - Institut de Biologie Structurale* to extract the diffusion properties of NTH1 (**see next section 6.3.2**).

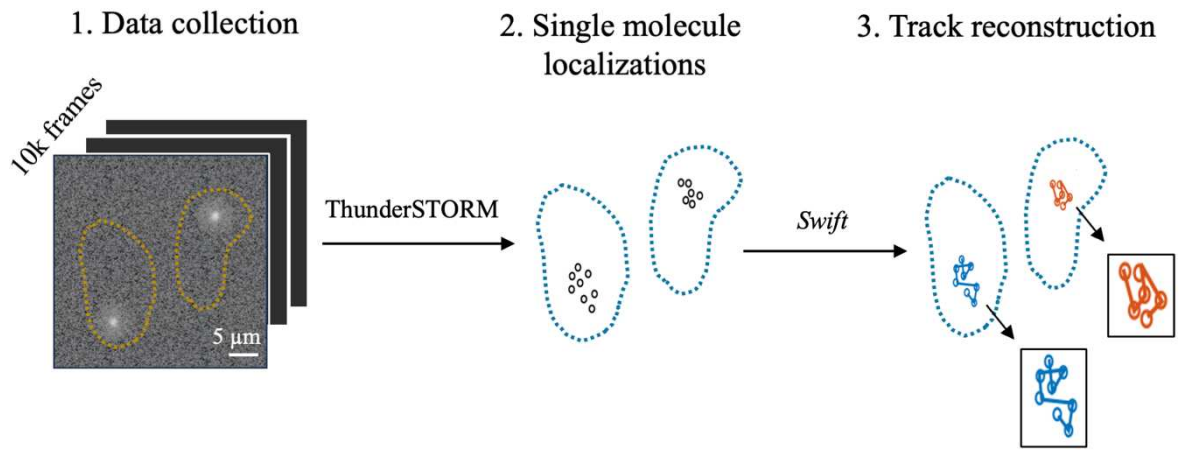


Figure 29: Flowchart of reconstruction of trajectories from single-molecule localizations.
Data is collected from 10000 frames to reconstruct a super-resolved image of NTH1 localizations using the FIJI plugin, ThunderSTORM. Next, the nucleus is selected as the ROI for reconstructing single-molecule trajectories (orange and blue) using the Swift program (close-up of a single trajectory).

6.3.2 Characterization of molecular dynamics from single molecule tracking analysis

To analyse single molecule tracks to extract Diffusion coefficients, two methods are commonly used: Mean Jump Distance (MJD) and Mean Squared Displacement (MSD). Each method has its own strengths and limitations.

The MJD measures the average distance a particle travels between consecutive frames within a trajectory (Lelek et al., 2021). It is less sensitive than MSD analysis to localization errors and outliers, as it uses the absolute distance rather than the squared distance. Analysis of MJD histograms can provide a first level of analysis defining, for example, the number of NTH1 populations, as illustrated in figure 30A-B. However, it is harder to extract quantitative parameters like the diffusion coefficient from MJD analysis, and it is also less effective at distinguishing between different types of motion (e.g., subdiffusion vs. superdiffusion) compared to the MSD.

One of the common methods used to estimate the diffusion coefficient of individual particles is by calculating the mean squared displacement (MSD). The MSD is the average of all squared distances between two localizations with a certain lag time, t_{lag} (Figure 30C), as shown in the formula below,

$$MSD\ (nt)= \frac{1}{l\text{-}n}\sum_{i=1}^{l-n}(x(i+n)\text{-}x(i))^2+(y(i+n)\text{-}y(i))^2$$

where, l is the length of the trajectory, n is the number of frames over which the molecule is tracked, and x(i) and y(i) are the coordinates at time t.

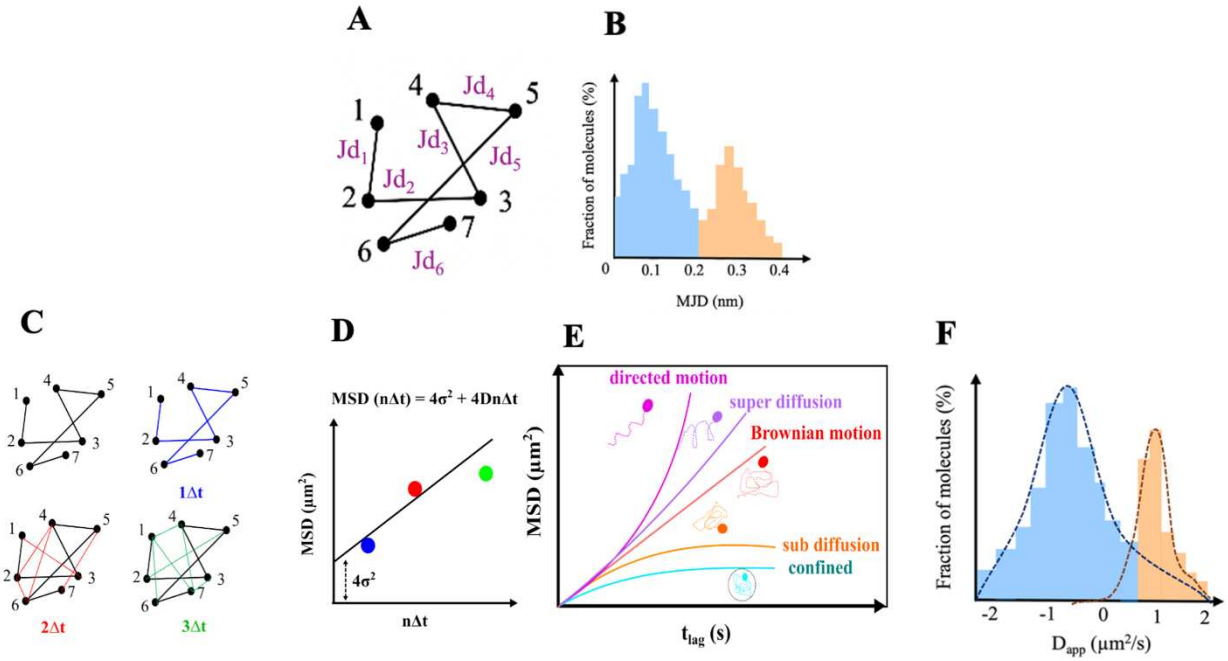


Figure 30: Principle of mean jump distance and MSD analysis for the measurement of diffusion coefficient.
(A) The path traced by an individual molecule from point 1 to point 7 with a jump distance of (Jd_1, Jd_2…Jd_6) over time and the average of all the JDs is the mean jump distance (MJD). (B) Mean jump distance (MJD) histogram helps to identify populations with different diffusion coefficients (in this example two populations indicated by two peaks) (C) The MSD nΔt of a 2D (D) The MSD scales linearly for freely diffusing molecules with a time lag and with an offset of ($4\sigma^2$) representing the localization uncertainty. The diffusion coefficient is obtained from the slope. (E) The relation between the MSD and lag time describes the type of diffusion dynamics of the molecule. (F) Apparent diffusion coefficient (D_{app}) for two populations fitted by a Gaussian curve where the blue peak indicates a slow-diffusing population and orange peak indicate a fast-diffusing population. Illustrations adapted from Jip Wulffele's thesis.

For freely diffusing molecules, MSD increases linearly with nΔt and the apparent diffusion coefficient (D_{app}), expressed in $\mu m^2/s$, corresponds to the slope of the MSD plot (Figure 30D). Moreover, by analyzing the shape of the MSD vs. time lag plot, one can distinguish between different modes of motion (Figure 30E). For example, an upward steep curve tells us the motion is directed and a sublinear curve that plateaus suggests subdiffusion or confinement. As with MJD histograms, by plotting the histogram distribution of D_{app} values derived from MSD analysis of individual trajectories, it is possible to discriminate between distinct populations having different diffusion coefficients **(**Figure 30F**).**

One limitation of MSD analysis is its sensitivity to localization errors and experimental noise, which can bias the results, especially when analyzing short trajectories. To minimize this, we restricted our analysis to longer trajectories (minimal of 4 localizations).

Apparent diffusion coefficients of single trajectories (Di*) were calculated from the mean squared jump distance as described by Stracy et al., 2021, using the above formula:

$$Di^{*}= \frac{1}{4n\Delta t}\sum_{i=1}^{n}[x(i\Delta t)\text{-}x(i\Delta t+\Delta t)]^2+[y(i\Delta t)\text{-}y(i\Delta t+\Delta t)]^2$$

where n is the number of displacements over which the mean squared jump distance is calculated, x(t) and y(t) are the coordinates of the molecule at time t and Δt is the frame time.

In our case, we hypothesize that, there are two populations of NTH1 molecules, one bound to the DNA, and one not bound to the DNA. Thus we performed fits on the MSD distribution of diffusion coefficients using the following equation defined by Stracy et al., 2021.

$$p(D_i)= \left[\frac{A_1}{6}*\left(\frac{4}{D_1}\right)^4*(D_i)^3*exp\left(\frac{\text{-}4D_i}{D_1}\right)\right]+\left[\frac{(1\text{-}A)}{6}*\left(\frac{4}{D_2}\right)^4*(D_i)^3*exp\left(\frac{\text{-}4D_i}{D_2}\right)\right]$$

where A and 1-A are the fraction of molecules found in each state. The states D_1 and D_2 were defined as immobile and mobile fraction of diffusing molecules respectively.

6.4 spt simulations using SMIS

SPT simulations were performed on the SMIS software (Bourgeois, 2023) , developed by *Dr. Dominique Bourgeois - Institut de Biologie Structurale*. Single Molecule Imaging Simulations or SMIS is a user-friendly GUI (Figure 31) simulator software package designed to not only simulate the complex photophysical behaviour of fluorophores, but to investigate and apply these complex models to advanced imaging. It incorporates a virtual widefield microscope, operating in multicolour and using 3D virtual samples. For our purposes, it can further be used to investigate the effect of confinement and exchange SMIS was employed to primarily confirm our spt experimental datasets -kinetics, combined with fluorophore-photophysical properties of mEos4B, to study its influence on accurate retrieval of diffusion coefficients and exchange kinetics between mixed populations of diffusing molecules. We used a virtual 3D HeLa cell model but conducted 2D processing steps like our 2D spt experimental data. For further details, on the simulation setup, **refer Results section 7** on integrating SPT simulations to elucidate NTH1 nuclear dynamics.

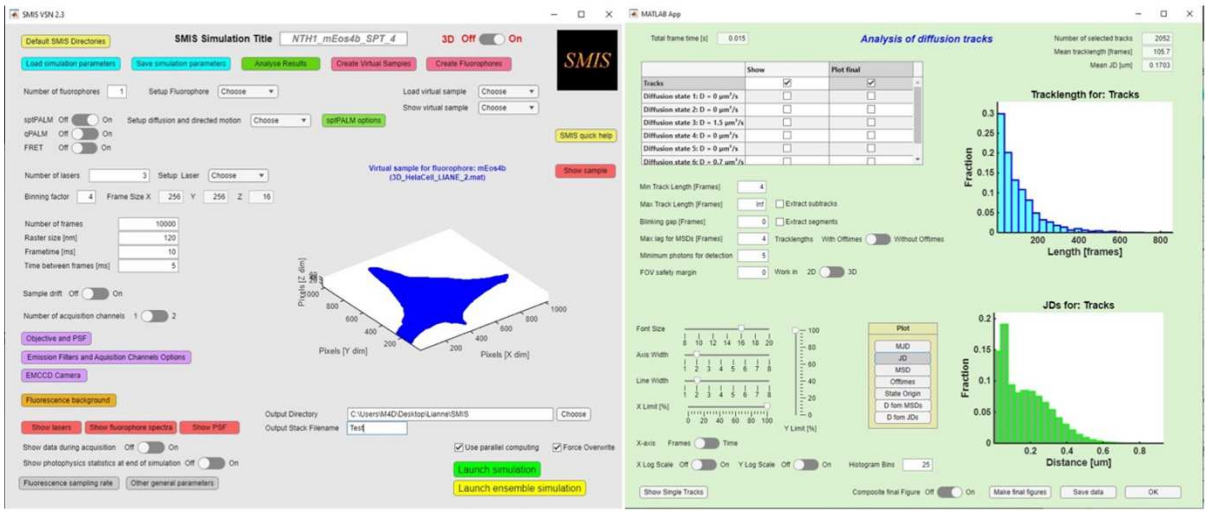


Figure 31: GUI interface of SMIS on the left and the interface for analysing diffusion tracks on the right.

7. Graphs and statistical analysis

All graphs, frequency distribution histograms, and statistical analysis was performed in GraphPad PRISM (v10). P values below 0.05 were considered as significant and are indicated in figures with asterisks as follows: * $0.01 < P < 0.05$; ** $0.001 < P < 0.01$; *** $0.0001 < P < 0.001$; **** $P < 0.0001$.

RESULTS

1. Heterogeneous nuclear distribution of NTH1 & existence of two nuclear pools.

Previous studies using GFP-tagged NTH1 or Myc-tagged-NTH1 described NTH1 as being primarily localized in the nucleus and in the mitochondria of eukaryotic cells (Takao et al., 1998; Luna et al., 2000; Ikeda et al., 2002; Campalans et al., 2005). However, the intranuclear distribution of endogenous NTH1 in eukarytic cells has not been further explored.

Our aim was to investigate the localization and distribution of NTH1 by immunofluorescence within fixed HeLa cells, using a 3D spinning disk confocal microscope, taking advantage of the reduced photo-toxicity and fast imaging rates. Moreover, we were able to analyse the distribution of endogenous NTH1 and not the overexpressed tagged version of NTH1, using a specific rabbit monoclonal and polyclonal anti-NTH1 antibodies available from Abcam (**in Table 5, Materials and Methods**). As a source of secondary antibodies, we used Goat anti-Rabbit IgG (H+L) labelled either with Alexa Fluor™ 488 or with Alexa Fluor™ 568. We tested several combinations of both primary NTH1 and secondary antibodies, to obtain the best immunofluorescence signal with low background, necessary for all further experiments.

Using either a monoclonal (Figure 32A) or a polyclonal (Figure 32B) antibody against NTH1, we performed immunofluorescence (IF) experiments to localize endogenous NTH1. Our images confirmed that NTH1 is localized in the nucleus and in the cytoplasm. In the cytoplasm, NTH1 displays a punctate distribution, probably reflecting its mitochondrial localization (see figure 32A-B, close-up images). In the nucleus, we noticed a heterogeneous nuclear distribution of NTH1, with one population of NTH1 forming foci and another more diffuse in the background as the analysis of multiple images revealed brighter endogenous nuclear NTH1 signal and low background noise (data not shown).

To validate the specificity of the monoclonal anti-NTH1 antibody, we knocked down endogenous NTH1 in HeLa cells using siRNA targeting NTH1 (see sequence in Material and Methods). The siRNA treatment was efficient, as evidenced by the reduced NTH1 signal detected by Western blot (Figure 32C, upper panel). In parallel, we also observed a 50% decrease in the mean nuclear fluorescence intensity (MNFI) in the Alexa 488 channel corresponding to NTH1 in these IF experiments (Figure 32C, lower panels). Finally, using a stable HeLa cell line knocked down for NTH1 (provided by Dr. Andriy Khobta), we confirmed the absence of NTH1 signal in both western blot analysis and IF labelled cells (Figure 32D). Both these validation approaches confirm the specificity of the NTH1 antibody and indicate that the antibody recognizes an epitope belonging to the endogenous NTH1

protein. The bright heterogeneous nuclear signal observed in our IF experiments thus undoubtedly corresponds to NTH1.

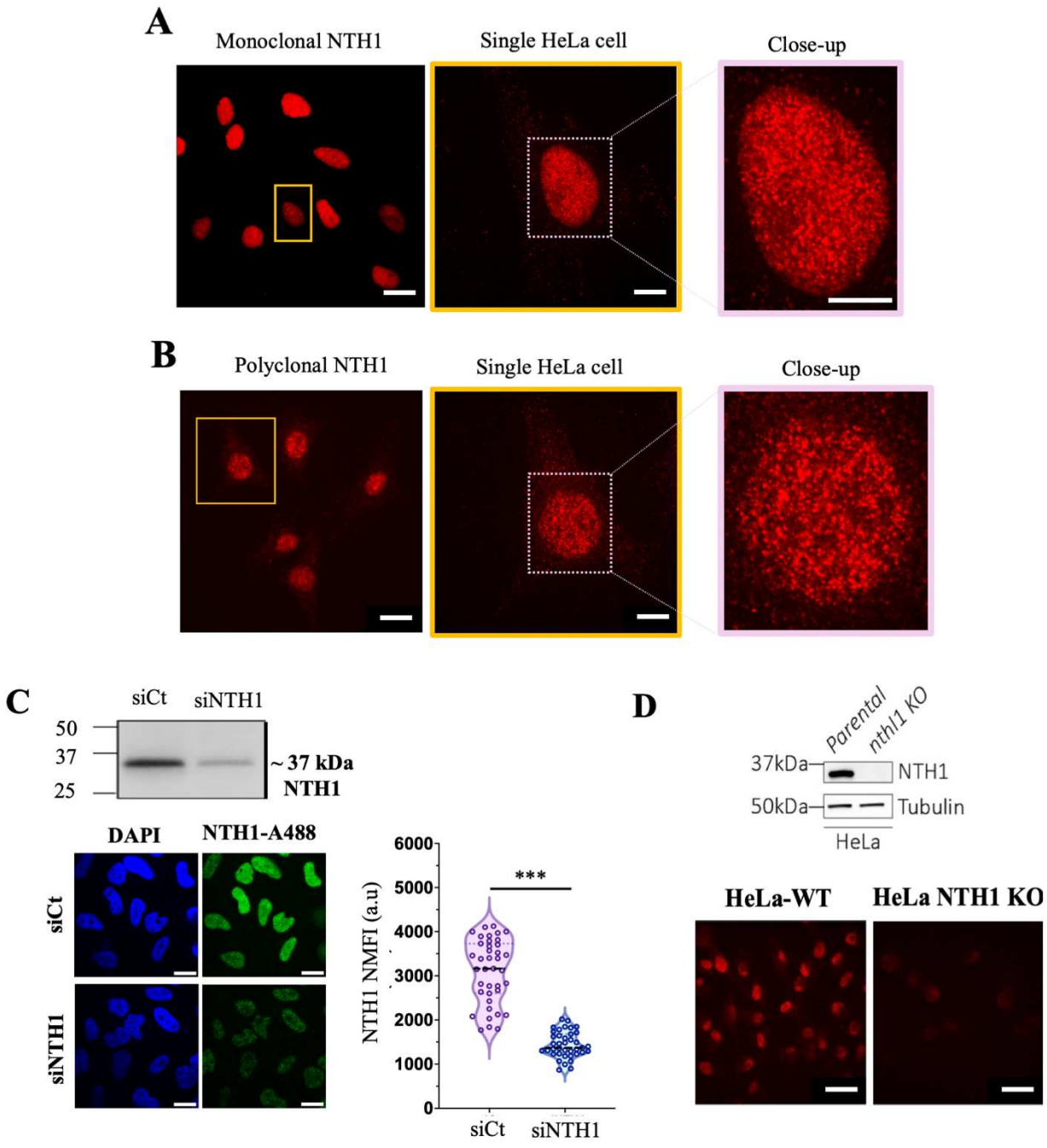


Figure 32: Detection of NTH1 by immunolabelling in HeLa cells of immunolabelling NTH1 and verification of labelling efficiency.

Nuclear and mitochondrial localization of NTH1 observed by immunolabelling with (A) primary monoclonal NTH1 antibody and secondary antibody labelled with– Alexa Fluor 568. (B) with primary polyclonal NTH1 antibody and secondary antibody labelled with– Alexa Fluor 568. The scale for the

*right panels is 20 µm, 60x magnification and the scale for the close-up panels of nuclei is 2 µm, 100x magnification. And close-up of HeLa nucleus at a scale of 5 µm. (C) HeLa cells transfected with scrambled siRNA (siCt) and siNTH1 show a 50% decrease in NTH1 signal after siRNA transfection in 50 HeLa cells. NMFI – Nuclear Mean Fluorescence Intensity (a.u). Scale = 20 µm, 40x magnification. Statistical analysis was performed using unpaired t-test where ***P< 0.001. Western blot confirms the specificity of NTH1 observed at 37 kDa molecular weight. (D) Immunofluorescence images of HeLa parental WT and NTH1 KO (-/-) HeLa cells. Scale: 20 µm, 20x magnification. Western blots performed by Pierre Carron (Institut de Biologie Structurale).*

2. NTH1 displays cell-cycle dependent expression.

In the literature, the expression of NTH1 is described as cell-cycle dependent. Using cell-cycle synchronized cells by serum starvation, NTH1 mRNA was shown to be low during the G1 phase of the cell cycle, reaching its maximum level during the S phase, then decreasing again during the G2 phase (Luna et al., 2000). To confirm these results, we took advantage of FUCCI HeLa cells expressing the G1 marker – Cdt1 and S/G2 marker – Geminin, fused respectively to mCherry and GFP (Sakaue-Sawano et al., 2011). We immunolabeled FUCCI HeLa cells with the anti-NTH1 antibody detected by an F(ab')2-Goat anti-Rabbit IgG (H+L) Cross-Adsorbed Secondary antibody labelled with Alexa Fluor™ 647.

From figure 33A, we observed a heterogeneous distribution of NTH1 within the nucleus of HeLa cells, like our previous findings. Moreover, during the S and G2 phases, the mean fluorescence intensity of NTH1 (370 a.u) was 1.2-fold higher than during the G1 phase (330 a.u), as seen in figure 33B. These results confirm that NTH1 is a cell-cycle regulated factor, although this regulation is only moderate.

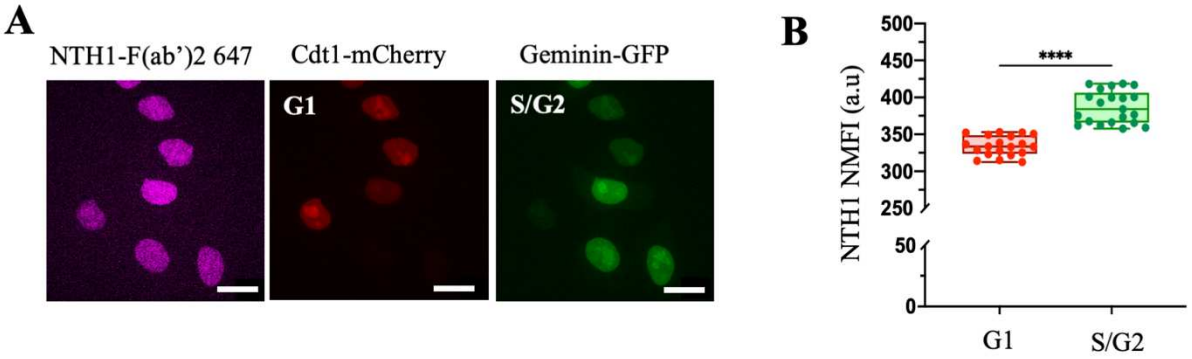


Figure 33: Expression of NTH1 during the cell cycle using FUCCI HeLa cells.
(A) Confocal images of FUCCI HeLa cells expressing Cdt1-mCherry (G1 cell cycle marker) and Geminin-GFP (S/G2 cell cycle marker) immunolabelled with NTH1 and F(ab') 647. Scale = 20 µm.

40x magnification. (B) Corresponding box and whisker plot of NTH1 signal in 20 HeLa cells during the G1 and S/ G2 cell cycle phases.

3. Subcellular fractionation reveals a chromatin-associated NTH1 fraction and a nucleoplasmic NTH1 fraction.

From our previous observations, the nuclear distribution profile of endogenous NTH1 in HeLa cells is composed of bright heterogeneously distributed foci and a more diffuse NTH1 signal in the nucleoplasm. We hypothesized that the NTH1 located in foci may represent chromatin-associated NTH1 (Amouroux et al., 2010; Lebraud et al., 2020). We thus decided to remove the diffuse nucleoplasmic fraction of NTH1 by treating the cells with different extraction buffers for different time periods, prior to performing NTH1 immunolabelling (Campalans et al., 2007; Amouroux et al., 2010; Robeska et al., 2024).

In figure 34A, we observed a 3.2-fold decrease in fluorescence intensity in cells fractionated with 0.2% Triton X100-1X PBS for 2 min, and in cells fractionated with 0.2% Triton X100- 1X CB (see section 4.1, Materials and Methods), a mild detergent with CSK, for 2 minutes compared to non-fractionated (NF) cells. However, a 1.8-and 2-fold (0.54 and 0.45) decrease of fluorescence was observed after treatment with 0.5% Triton X100-CSK, for 2 minutes and 5 minutes respectively. We selected the 0.5% Triton X100 – CSK extraction buffer composition and a treatment duration of 5 minutes, which seemed to be a good compromise. After treatment of the cells with 0.5% Triton X100 – CSK extraction buffer for 5 minutes at room temperature, we clearly see a decrease in the overall fluorescence intensity and subsequently find the NTH1 foci become more visible as a result of reduced background fluorescence signal (Figure 34B), demonstrating the successful elimination of the diffuse nucleoplasmic fraction of NTH1, which was found to contribute to ~ 40% of the total nuclear pool of NTH1.

Therefore, we concluded that two nuclear fractions of NTH1 exist: a chromatin – associated fraction present in the form of NTH1 foci and a diffuse nucleoplasmic fraction. Considering this significant observation, our next aim was to better characterise the NTH1 foci observed in the chromatin – associated fraction of NTH1 and evaluate the effects of oxidative stress on their distribution, size and number.

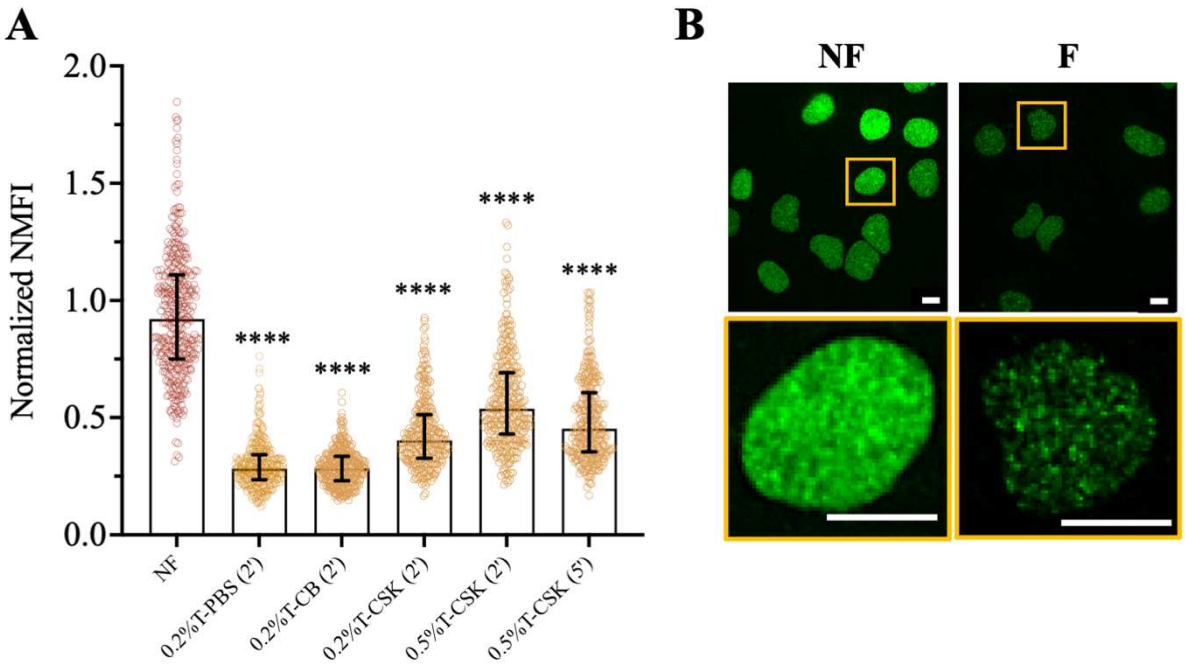


Figure 34: Isolation of chromatin-bound fraction of NTH1 by in cellulo fractionation.
*(A) HeLa cells treated with different triton (0.2% or 0.5% T) and cytoskeletal buffer compositions such as, phosphate saline buffer (PBS), (CB) and cytoskeletal buffer (CSK). Nuclear mean fluorescence intensity (NMFI). A one-way ANOVA – Kruskal Wallis test was performed on the non-parametric data and significance was measured as ****P < 0.0001 for an average of 332 cells per condition, compared to NF condition. (B) After selection of optimal buffer composition, HeLa cells were treated with 0.5% triton-CSK for 5 minutes at room temperature to isolate the chromatin – associated fraction of NTH1 and remove the nucleoplasmic fraction of the protein. A single cell is represented to demonstrate the efficiency of the detergent treatment on HeLa cells.*

4. Effects of various oxidizing agents on the nuclear distribution and abundance of NTH1

4.1 Cisplatin treatment mildly affects the distribution of NTH1 on chromatin

Previous studies have shown that NTH1 may be involved in the repair of DNA damage caused by cisplatin (Guay, Garand, et al., 2008; Kothandapani et al., 2011; Senarisoy et al., 2020; Kar et al., 2024), a commonly used chemotherapeutic agent that is known to react with DNA to form inter- and intra-strand crosslinks, but also to induce oxidative DNA damage.

First, we began by studying the effects of cisplatin on the nuclear levels of NTH1. Previous results obtained from our collaborators at the *CMBA platform (CEA-Grenoble)* showed a significant decrease in cell viability, when MCF7 cells were treated with cisplatin above a concentration of 10 µM for 48 hours (*Emmanuelle Soleilhac, CMBA platform, CEA Grenoble*). Based on these observations, we treated HeLa cells with cisplatin concentrations ranging from 0.3 µM to 10 µM for a period of 24 hours and measured the intensity of NTH1 signal by IF. We were able to detect DNA damage indicated by the presence of DSBs through the labelling of γH2AX foci, a well-known marker of DSBs. In Figure 35, we have chosen to show the images obtained after treatment of cells with 0.625 µM and 5 µM cisplatin, which are representative of the results obtained for the full range of cisplatin concentrations (Figure 35).

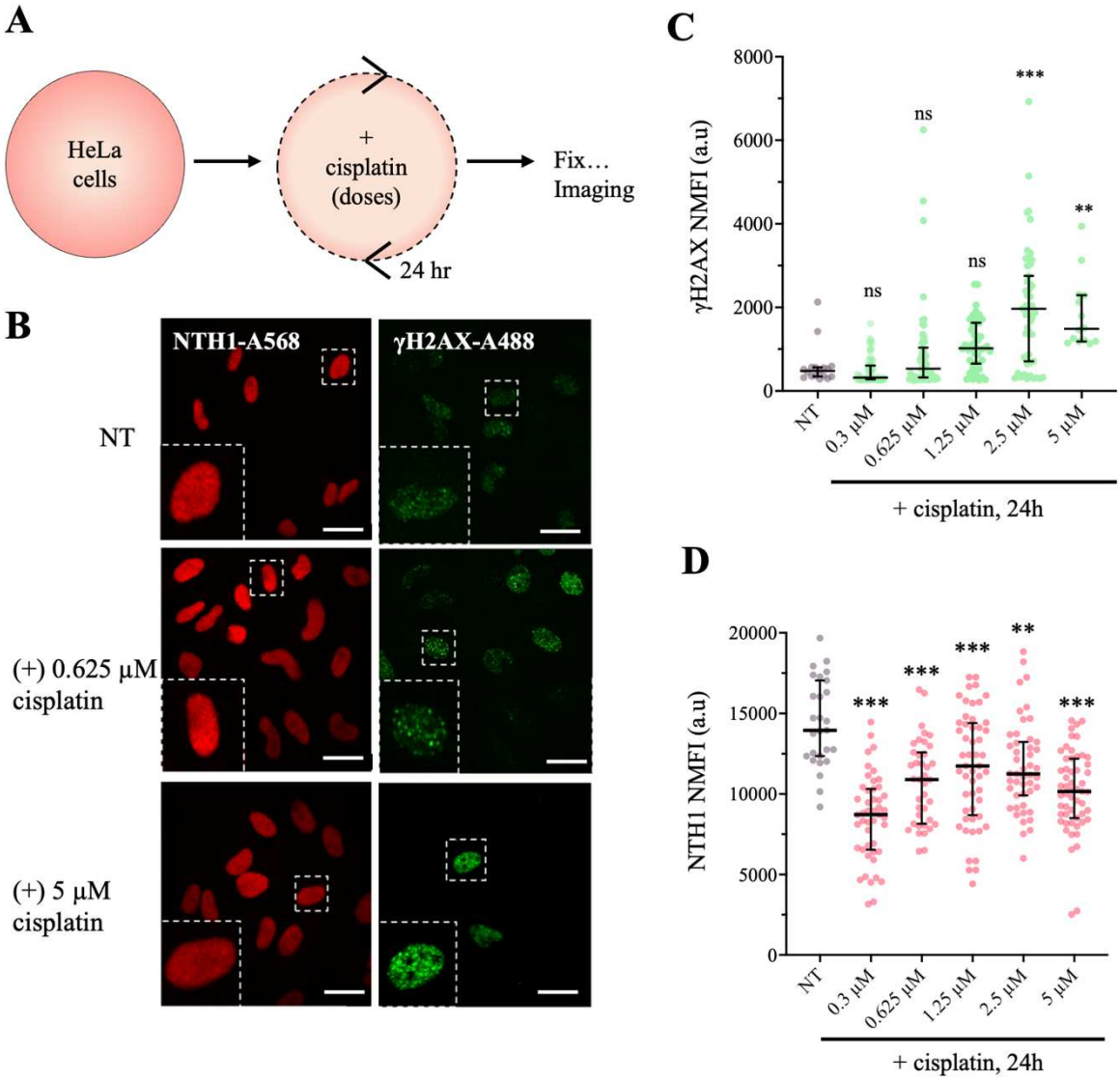


Figure 35: Dose- dependent effect of cisplatin on the nuclear level of NTH1 of HeLa cells.
(A) Schematic representation describing treatment plan of HeLa cells with a dose range of cisplatin for 24 hours. (B) HeLa cells stained for NTH1 (red) and γH2AX (green) before (non-treated) and after 24

*hours of treatment with 0.625 µM and 5 µM cisplatin. Close-up views of single cells show the effect of cisplatin indicated by increased levels of γH2AX foci and unchanged levels of NTH1. Images magnified by 40*x. *(C) Quantification of nuclear mean fluorescence intensity (NMFI) of γH2AX per HeLa cell nucleus, with the median represented as a bar for each dose and corresponding error bars as the interquartile range. (D) Quantification of NMFI of NTH1 per HeLa cell nucleus, with the median represented as a bar for each dose and corresponding error bars as the interquartile range. For both plots, a one-way ANOVA (Kruskal-Wallis) was performed and the significance measured as **P < 0.01, ***P < 0.001, compared to NT condition. N = 50 cells/ condition.*

In Figure 35B and 35C, we see that the signal of γH2AX increased after cisplatin treatment reaching a maximum at 2.5 µM cisplatin. As in our previous studies, NTH1 foci can be seen in both treated and non-treated conditions (Figure 35B). The nuclear mean fluorescence NTH1 signal (NMFI) decreases after treatment with low concentrations of cisplatin, but the effect is less noticeable at higher concentrations. In this experiment, it should be noted that the cells have not been fractionated, so the fluorescence intensity corresponds to the total NTH1 in the nucleus.

We next treated cells with 10 µM of cisplatin for different durations (Figure 36). Cells were fractionated (Figure 36C, 36F, 36G) or not (Figure 36B, 36D, 36E), fixed and immunolabelled with anti-NTH1 and anti-γH2AX. The NMFI was measured for each cell. At each time point, a control without any treatment with cisplatin was also performed (Figure 36D, 36F).

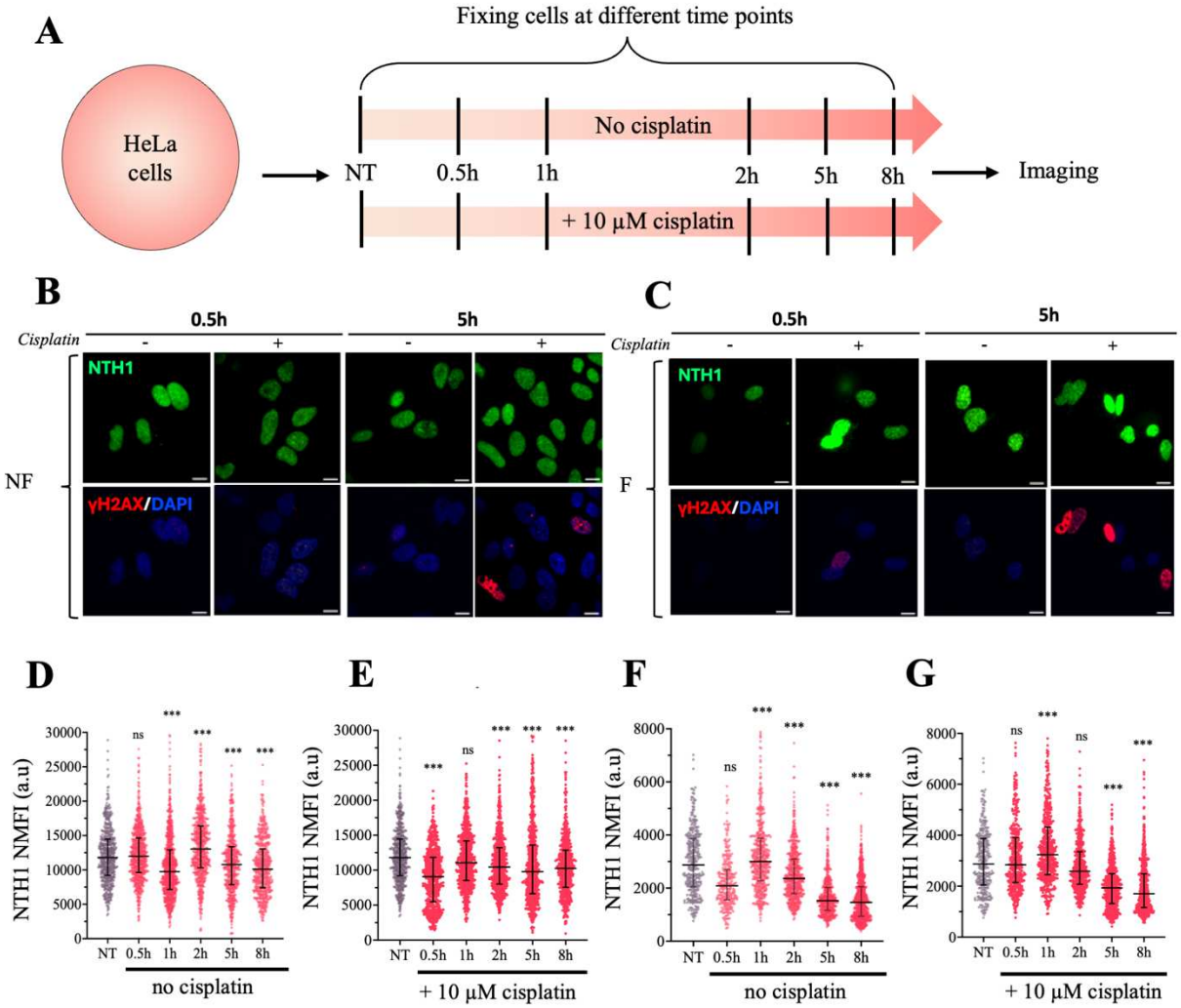


Figure 36: Comparison of the NTH1 expression levels in non-fractionated (NF) and fractionated (F) HeLa cells treated or not with cisplatin.

*(A) Schematic cartoon of the flow of the experiments. (B, C) NTH1 fluorescent signal in (-/+) subcellular fractionated HeLa cells cultivated without (-) or with 10 µM of cisplatin (+) for 0.5h and 5h. Scale = 10 µm. (D, E) Graphs representing the NMFI of NTH1 per HeLa cell nucleus in **NF** cells cultivated without (D) or with 10µM of cisplatin (E) and in **F** cells cultivated without (F) or with 10 µM of cisplatin (G). Lines represent the median and the interquartile range is represented by the error bars. N < 250 per time point. One-way ANOVA (Kruskal-Wallis) test on non-parametric data was performed with a significance of *** p<0.001, compared to NT condition.*

Without subcellular fractionation, we identified an increase in the γH2AX signal after 5 hours of treatment (Figure 36B) and the measurement of the NMFI, showed a ~2.1-fold increase in γH2AX after cisplatin treatment (data not shown). We concluded that cisplatin successfully induces DSBs in the DNA. However, there was no clear change in the levels of nuclear NTH1 over time (Figure 36B). This

is further highlighted in figure 36D, where even in the absence of cisplatin, the NTH1 signal fluctuates between the different time points (Figure 36D). Although we did not see any major change in the total NTH1 levels after cisplatin treatment, we reasoned that the nuclear pool of NTH1 may be redistributed in response to cisplatin treatment with an increased fraction of NTH1 being bound or associated to chromatin in order to repair the DNA lesions. Thus, we introduced a subcellular fractionation step after the treatment with cisplatin. After cisplatin treatment, cells were extracted for 2 minutes with a mild detergent (0.2% Triton X100 – PBS).

However, after cell fractionation, we observed similar γH2AX and NTH1 profiles. We indeed observed an increase in γH2AX signal as a function of time (data not shown), with γH2AX positive cells appearing after 5 hours of treatment. However, even in the absence of cisplatin treatment, we measured significant fluctuations of the NTH1 signal, rendering the interpretations of the results difficult, as we also observed a decrease of the NTH1 signal after treatment with cisplatin. In both coverglasses, after 0.5 and 8 hours of treatment, we observed an increase of the NTH1 chromatin-associated fraction between T0 and NT cells (Figures 36D, 36F and 36G), but for the other time points, the results were inconclusive.

To sum up, these first experiments allowed us to conclude that after a treatment of HeLa cells with 10 µM cisplatin, there is no obvious change in the global nuclear NTH1 levels or clear recruitment of NTH1 to the chromatin. This is likely due to the limited oxidative stress induced by cisplatin treatment.

4.2 Hydrogen peroxide treatment increases NTH1 recruitment to chromatin.

Hydrogen peroxide or H_2O_2 is not only produced intracellularly, but is also used externally as a potent oxidizing agent to investigate the effect of oxidative stress (Di Marzo et al., 2018). In figure 37A, the schematic flowchart describes the cells treated with 5 mM H_2O_2 supplemented or not with iron (II) sulphate ($FeSO_4$), where the Fe^{2+} combined with H_2O_2 generates hydroxyl radicals (OH^-), and is the basis of the Fenton reaction (Yang et al., 2006). This was followed by a recovery period in fresh media for 15 minutes before fractionating cells with 0.5% Triton X-100-CSK buffer for 5 minutes to remove the nucleoplasmic NTH1 fraction and retain only the chromatin-associated fraction prior to fixation and imaging.

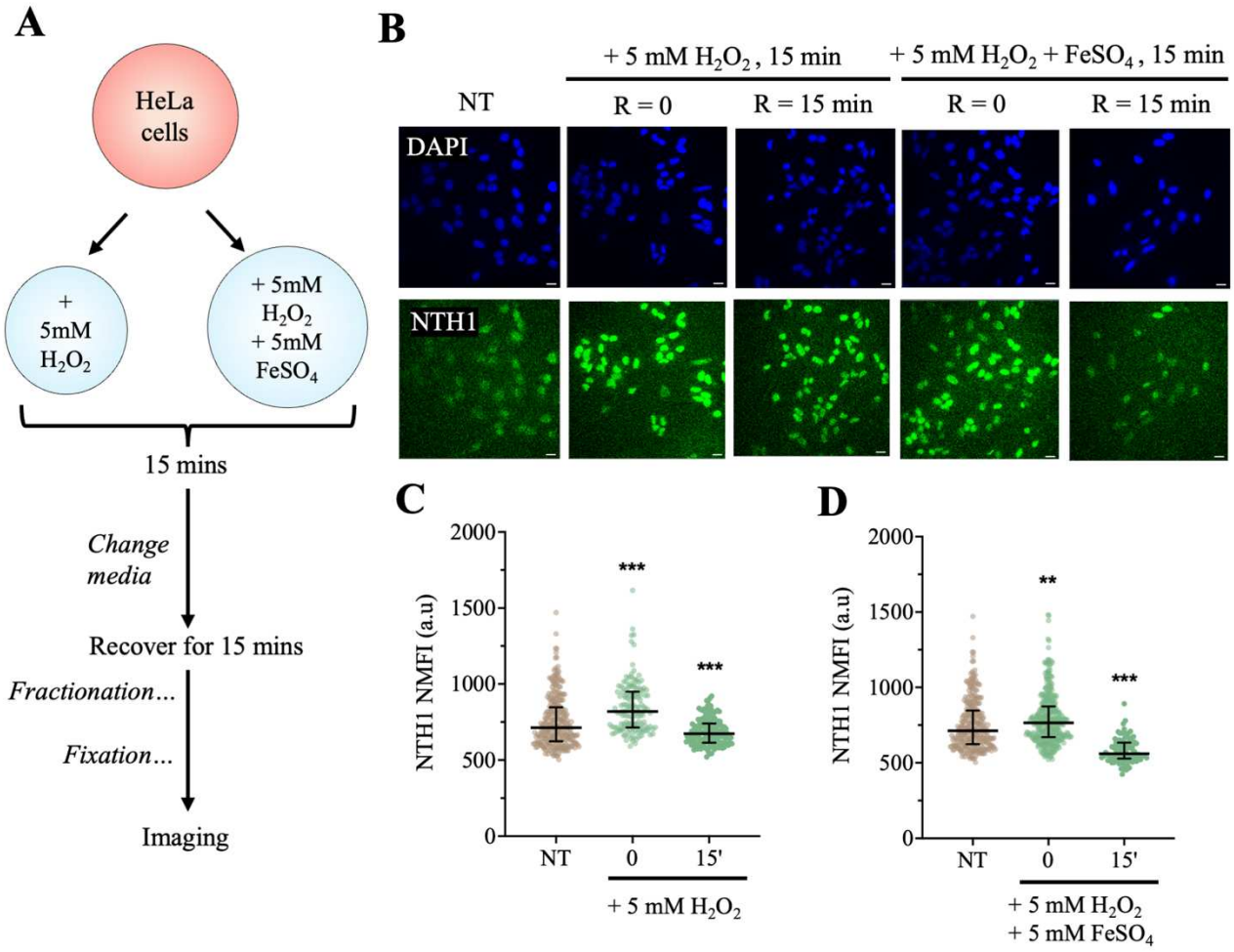


*Figure 37: Increase in chromatin-associated NTH1 levels after treatment with H_2O_2 (-/+) $FeSO_4$. (A) Schematic representation of treatment with 5 mM H_2O_2 (-/+) 5 mM $FeSO_4$, followed by recovering cells is fresh media for 15 minutes, before fractionation, fixation and imaging. (B) Image panel displaying DAPI and NTH1 channels of fractionated HeLa cell nuclei, treated H_2O_2 (-/+) $FeSO_4$, imaged before (NT), after treatment (R = 0) and post 15 minutes of recovery (R = 15 min). (C-D) Box and whisker plots showing the nuclear mean fluorescence intensity of NTH1 in **F** cells treated with H_2O_2 (-/+) $FeSO_4$, imaged before (NT), after treatment (R = 0) and post 15 minutes of recovery (R = 15 min). Here, the horizontal lines represent the median and the interquartile range is represented by the error bars. N < 200 per condition. One-way ANOVA (Kruskal-Wallis) test with Dunn's multiple comparisons was performed on data with a measured significance of **P < 0.002 and *** P < 0.001, compared to NT condition.*

Interestingly we observed a statistically significant increase (1.2-fold) in the chromatin-associated fraction of NTH1 after treatment with H_2O_2 *(-/+) $FeSO_4$* when comparing NT and R=0 conditions (Figure 37C). But 15 minutes after treatment, NTH1 levels were similar to those seen in NT cells, suggesting the effect was only transient (Figure 39C, 39D). This suggests that the recruitment of

NTH1 in response to H_2O_2-induced oxidative stress is rapid and that the damage is efficiently repaired leading to a subsequent release of NTH1 from the chromatin. Having confirmed that NTH1 responds to oxidative stress, we decided to test an alternative oxidizing agent, potassium bromate ($KBrO_3$), which has been previously used to study the effect of oxidative stress on the recruitment of other DNA glycosylases, including hOGG1, to sites of oxidative DNA damage (Amouroux et al., 2010).

4.3 $KBrO_3$ treatment increases recruitment of chromatin – associated NTH1

4.3.1 Dose-dependent effect of $KBrO_3$ on the survival of HeLa cells

To study the kinetics of NTH1 recruitment to chromatin in response to $KBrO_3$, we decided to take advantage of the previous work by Amouroux et al., 2010, that demonstrates the recruitment of OGG1 to the chromatin after oxidative DNA damage. As a preliminary experiment, we decided to test the effect of different concentrations of $KBrO_3$ on HeLa cells after 0.5h and 2h of treatment: 0, 40 mM, 80 mM, 100 mM, 200 mM and 400 mM (Figure 38A).

Treatment with $KBrO_3$ equal or higher to 100 mM for over 30 minutes led to apoptotic bleb formation, indicating cell death, which was not the case at a concentration of 40 mM of $KBrO_3$ for 0.5h. We also checked whether a treatment with $KBrO_3$ for 0.5h influences the cell cycle. Figure 38B shows that the percentage of cells in S-phase increases after 40 mM $KBrO_3$ treatment by 16.4% compared to the NT cells. However, when treating cells with 400 mM $KBrO_3$, an enrichment of cells in G2 phase was observed, suggesting a possible dysregulation of the cell cycle after $KBrO_3$ treatment. It is important to note that the Watson-Pragmatic model used by Floreada.io was used to fit the curves for the G1, S and G2 cell cycle phases is an approximation and that the percentage of cells in these phases are to be considered lightly.

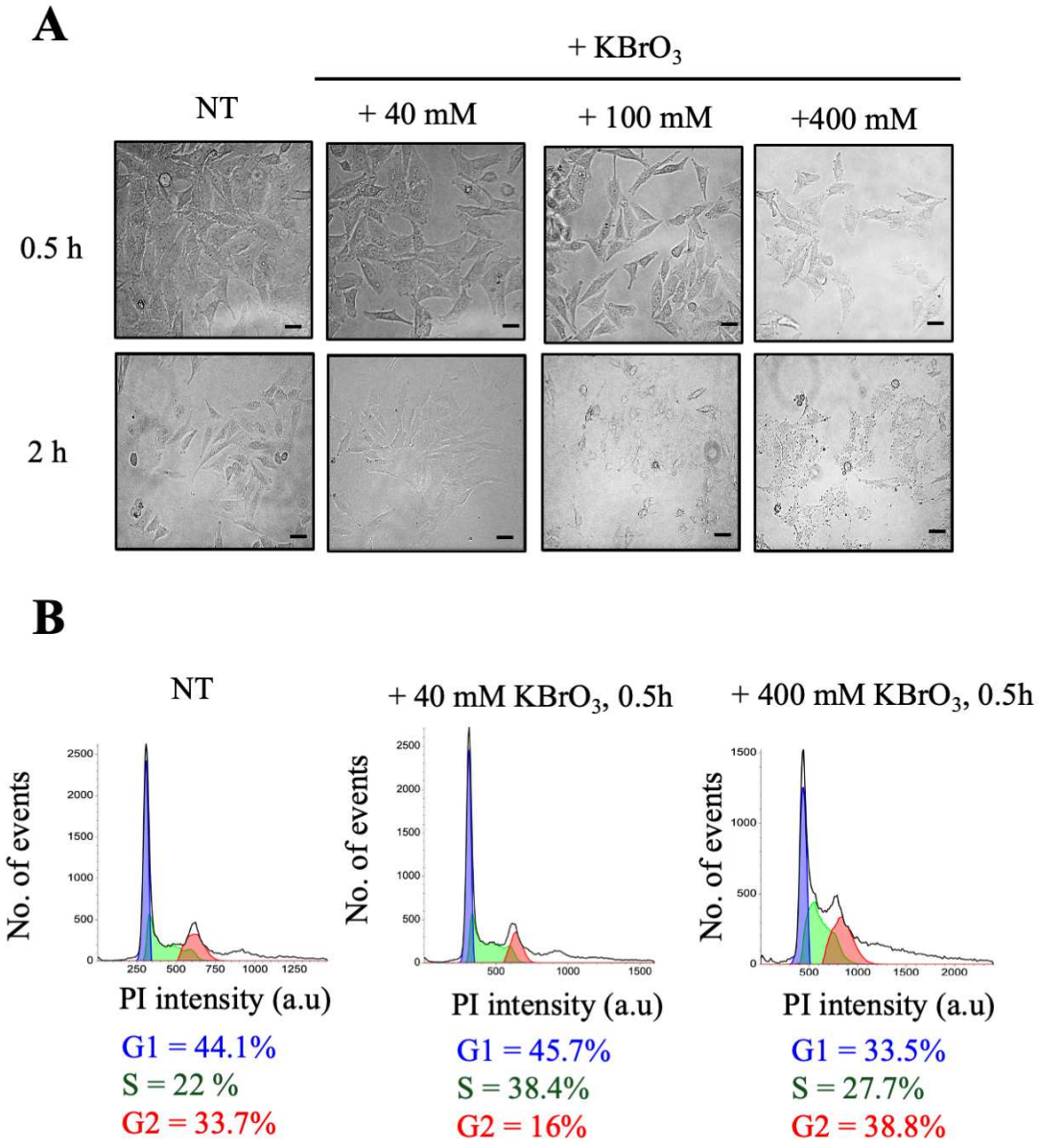


Figure 38: $KBrO_3$ treatment effects on the cell cycle and NTH1 chromatin recruitment in HeLa cells. (A) Bright-field images show dose- and time-dependent effect of $KBrO_3$ on the survival HeLa cells. (B) cell cycle analysis of HeLa cells treated with $KBrO_3$. *Propidium iodide (PI) histograms fitted with the Watson-Pragmatic model on G1, S and G2 cell cycle phases in non-treated (NT), 40 mM and 400 mM $KBrO_3$ treated HeLa cells, for 0.5h with corresponding percentage of cells in each cell cycle phase presented below each histogram. Image bars are 20 µm.*

4.3.2 Chromatin-associated NTH1 levels are significantly increased in response to $KBrO_3$ treatment

To assess the effects of $KBrO_3$ treatment on HeLa cells, we first treated cells with 40 mM $KBrO_3$ for 0.5h, after which they were recovered in DMEM, collected at different time points and fractionated with 0.5% Triton X100-CSK buffer to remove the nucleoplasmic protein fraction prior to fixation. In parallel, we also prepared samples to follow oxidative DNA damage, and more particularly 8oxoG accumulation by immunolabelling. 8oxoG is an oxidative base lesion repaired by OGG1 and is routinely used to monitor the extent of oxidative DNA damage (Figure 39B).

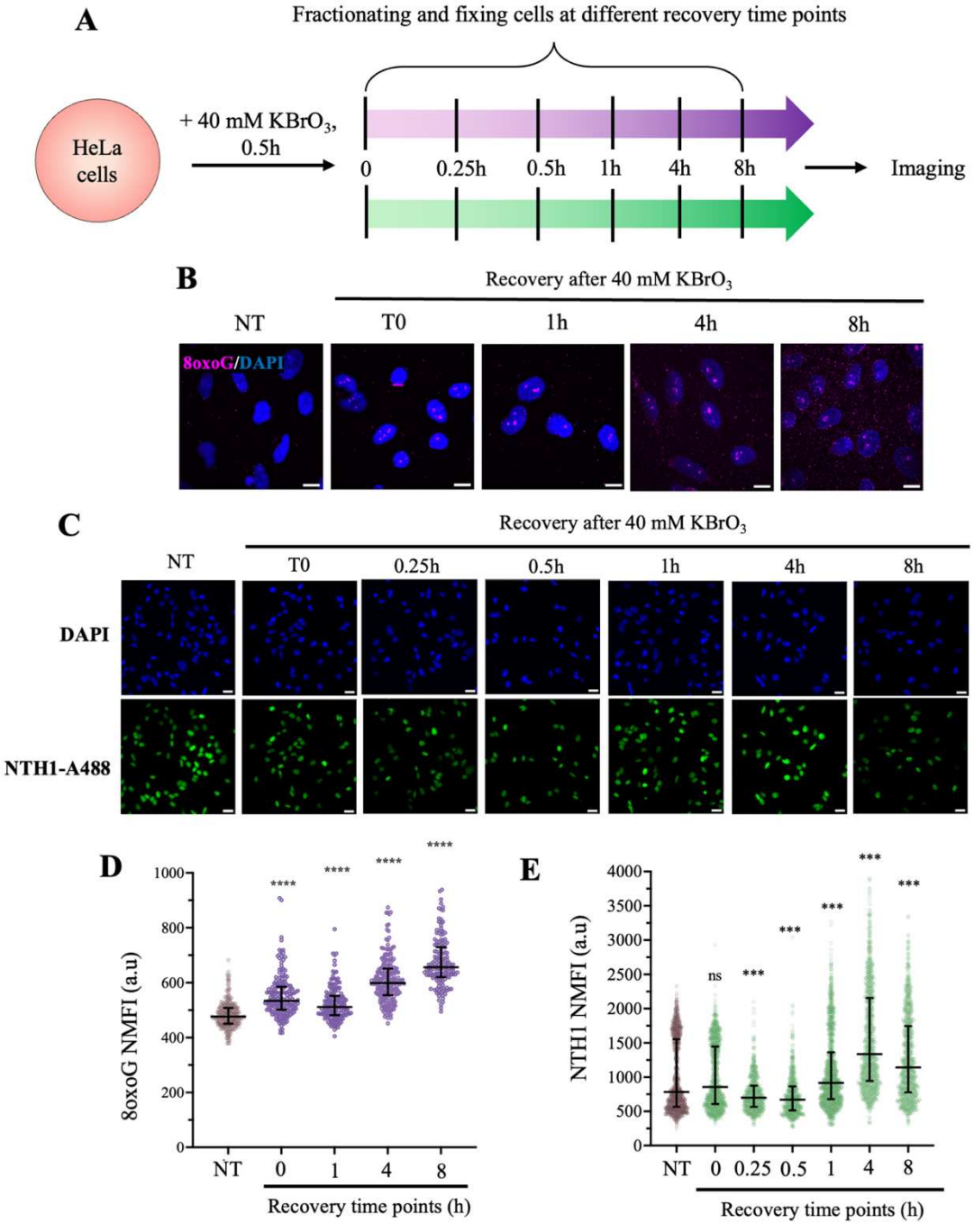


Figure 39: The NTH1 chromatin bound fraction increase after Recovery from an oxidative stress induced by $KBrO_3$ treatment.
*(A) Schematic diagram of the experiment design. HeLa cells were treated with 40 mM of $KBrO_3$ for 0.5h followed by different recovery periods. Then, subcellular fractionation, fixation and imaging either for 8oxoG (purple) or $KBrO_3$ (green) have been performed. (B) 8oxoG immunofluorescence images of labelling and DAPI overlay and (C) NTH1 immunofluorescence images labelling and DAPI in NT, T0 and TX post recovery. Scale = 20 µm. Scatter plot of (D) 8oxoG NMFI from N < 200 cells in each condition and of (E) NTH1 NMFI was measured for N < 1000 cells. Statistical analysis was performed using a one-way ANOVA (Kruskal-Wallis) test and Dunn's multiple comparisons test on non-parametric data with a significance of *P<0.05, **P<0.01 and *** P<0.001, compared to NT condition.*

Oxidative DNA damage was indeed detected following exposure to $KBrO_3$, with a marked increase in the levels of 8oxoG after 4 and 8 hours of treatment compared to NT cells (Figure 39B and 39D). Having confirmed that $KBrO_3$ induces oxidative DNA lesions repaired by the BER pathway, we proceeded to follow the kinetics of NTH1 accrual on damaged chromatin. Interestingly, in figure 39C and 39E, we observed oscillating NTH1 levels after treatment, during the first three recovery time points (0.25h, 0.5h and 1h). Following this, we observed a substantial (1.2-fold) increase of NTH1 nuclear mean fluorescence after a period of 4 hours of recovery compared to the control. This signal decreases slightly 8h after treatment. Thus, this data suggests that the highest levels of chromatin-associated NTH1 were observed 4h post-treatment. To determine whether this was a consequence of a redistribution of nuclear NTH1 or a net increase in the total amount of NTH1, we decided to embark on a deeper inspection of the effects of $KBrO_3$ treatment on the number and distribution of NTH1 foci.

4.3.3 Effects of $KBrO_3$ treatment on NTH1 foci formation.

In this section, we evaluated whether oxidative stress affects the foci distribution of chromatin-associated NTH1. To do so, we first attempted to segment NTH1 foci from 2D confocal images (Z depth of 1.5 µm with 3 Z slices merged) using the 'surfaces' feature in the IMARIS software (see Materials and Methods). Figure 40A illustrates the accuracy of foci segmentation on highly magnified confocal images (100x) and a summary of the defining characteristics of these foci are listed in table 9.

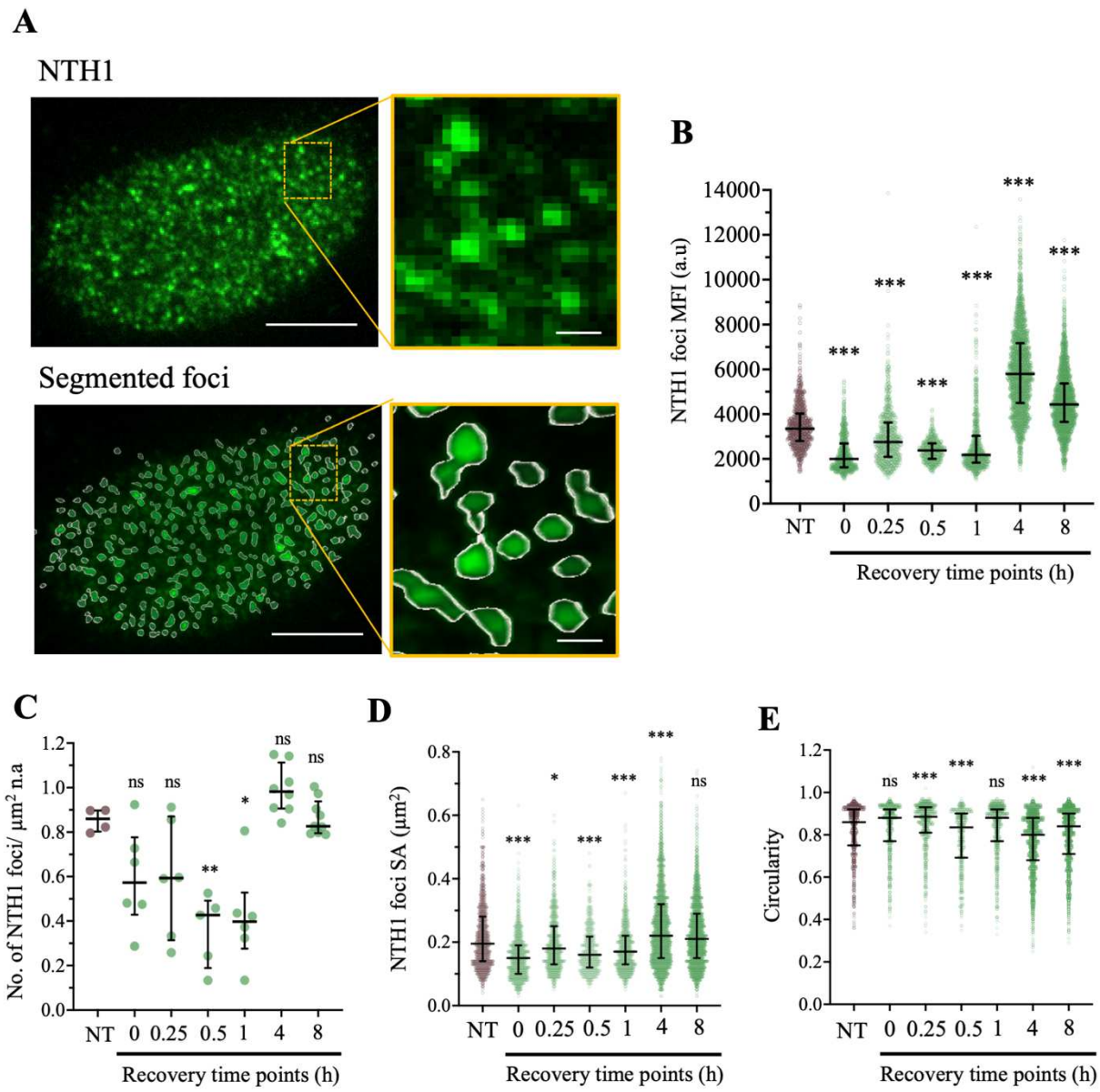


Figure 40: Effect of $KBrO_3$ on NTH1 foci formation.

*(A) Immunofluorescence images (Scale = 5 µm) of a representative NT HeLa cell immunolabelled for NTH1 and segmentation of NTH1 foci with closeups (Scale = 0.25 µm) . (B) Scatter plot of NTH1 mean foci fluorescence intensity (MFI) in each condition of $KBrO_3$ treatment. (C) Bar graph of the number of NTH1 foci per 1 μm^2 nuclear area (n.a). (D) Scatter plot of the surface area (SA) of NTH1 foci and (E) Scatter plot of the circularity of NTH1 foci in each condition. In each plot, the horizontal line represents the mean (C) or median (B, D, F), and the error bars represent the standard deviation (C) the interquartile range (B, D, F). N < 10 cells per condition. Statistical analysis was performed using a one-way ANOVA (Kruskal-Wallis) test and Dunn's multiple comparisons test on non-parametric data with a significance of *P<0.05, **P<0.01 and *** P<0.001, compared to NT condition.*

Individual NTH1 foci appear very bright, as measured by their mean fluorescence intensity, suggesting they likely contain numerous molecules of NTH1, packed into a tight space (~0.22 μm^2 in NT cells; Table 9). Figure 40B reveals a two phase response to oxidative DNA damage. First, we observe a marked reduction (~ 1.2-fold) in the mean NTH1 foci fluorescence intensity, just after treatment, that lasts for approximately 1-hour post-treatment (0.25 h, 0.5 h, and 1 h). Then, we observe a sharp (~ 2-fold) increase in NTH1 foci fluorescence 4 h post-treatment, which again starts to decline at the 8h timepoint, similar to our global measurement described in section 4.2, figure 39.

Table 9: Summary of the characteristics of NTH1 foci obtained from confocal images.
Here, the mean and standard deviation numbers highlighted in red represent the lowest values within the category measured and numbers highlighted in green represent the highest values within the category measured.

Conditions	Nuclear surface area (μm^2)	Mean fluorescence intensity (a.u)	No. of foci/ nuclear area (μm^{-2})	Mean surface area (μm^2)	Circularity
NT	266 ± 8.6	3493 ± 1009	0.85 ± 0.052	0.22 ± 0.11	0.82 ± 0.13
0	220 ± 38	***2252 ± 832***	0.59 ± 0.22	***0.16 ± 0.076***	0.83 ± 0.13
0.25h	226 ± 27	3020 ± 1359	0.59 ± 0.27	0.20 ± 0.091	0.85 ± 0.12
0.5h	269 ± 40	2380 ± 482	***0.36 ± 0.16***	0.17 ± .072	0.78 ± 0.14
1h	292 ± 73	2664 ± 1371	0.42 ± 0.22	0.18 ± 0.082	0.83 ± 0.13
4h	277 ± 48	***5923 ± 1907***	***0.99 ± 0.11***	***0.25 ± 0.13***	0.76 ± 0.14
8h	278 ± 57	4600 ± 1369	0.87 ± 0.080	0.23 ± 0.11	0.80 ± 0.14

Similarly, we observe a variation in the number of foci per nuclear area in response to oxidative stress, with an initial reduction from 0.85 foci/μm^2 in non-treated samples down to 0.36 foci/μm^2, 30 minutes after treatment. This decrease, which likely reflects a redistribution of NTH1 and more particularly a release of NTH1 from the foci, is then followed by a marked increase in the number of foci 4h post-treatment reaching a maximum of 0.99 foci/μm^2 (Figure 40C, Table 9). Although both the mean NTH1 fluorescence in foci and the number of foci follow the same trend, we do notice some differences. Indeed, 4h post-treatment, the number of foci is only slightly higher than in non-treated cells, while the mean fluorescence intensity is almost double, suggesting the foci formed 4h after treatment contain more NTH1 molecules (Figure 40C-D). This increased foci density may reflect the recruitment of NTH1 to sites of oxidative DNA damage. Additionally, Table 9 provides a closer inspection of the characteristics of these foci, revealing that the mean surface area and circularity of the foci remain relatively constant under all conditions, indicating that the overall size and shape remain largely unchanged.

5. Single-molecule localization microscopy reveals NTH1 clusters

Next, we wished to better understand how NTH1 molecules were distributed inside the nuclear NTH1 foci observed by confocal microscopy. Are they uniformly distributed inside the foci? Are they denser in some foci? As we were limited by the spatial resolution of conventional spinning disk confocal microscopy (~200 nm), we therefore, implemented the single – molecule localization microscopy (SMLM) technique, dSTORM, to achieve the highest possible spatial resolution (~10 nm), and to further resolve the nature and composition of the observed NTH1 foci.

5.1 Optimization of sample preparation for dSTORM imaging

Various studies have described the importance of sample preparation, especially in dSTORM (Xu et al., 2017; Clément et al., 2018). We put a lot of effort into optimizing our sample, data acquisition and processing pipelines to acquire high quality and robust data.

First, we optimized our immunolabelling step. We notably tested several working dilutions for our monoclonal anti-NTH1 antibody with suitable secondary fluorophores, routinely used for dSTORM imaging **(see Table 5 in Materials and Methods)**. To begin, we used the FluoroProbe 647 full-length antibody and were able to achieve our first high spatial resolution map of NTH1 distributed within HeLa cell nuclei. To improve our labelling efficiency and localization precision, we switched to the F(ab')2 647 antibody, thereby reducing the number of fluorophores attached to the IgG antibody from 5-7 fluorophores to 3-4 fluorophores.

Second, we tested different dSTORM buffers to assess the quality of the reconstructed images, as illustrated in figure 41. Imaging cells with buffers containing Glox supplemented with either 143 mM BME (β-mercaptoethanol) or 100 mM MEA (also, known as cystamine) yielded faster blinking events within a highly reduced environment. However, they simultaneously also caused higher background and shorter fluorophore lifetimes, leading to faster bleaching of the Alexa fluor 647 signal. In contrast, Vectashield provided higher number of blinking events, but caused high background signal and lower photon yield. In the end, we found that Glox supplemented with 10 mM MEA was the best compromise to maintain a reasonable number of blinking events per frame, which remained stable for long acquisitions, and limited background signal.

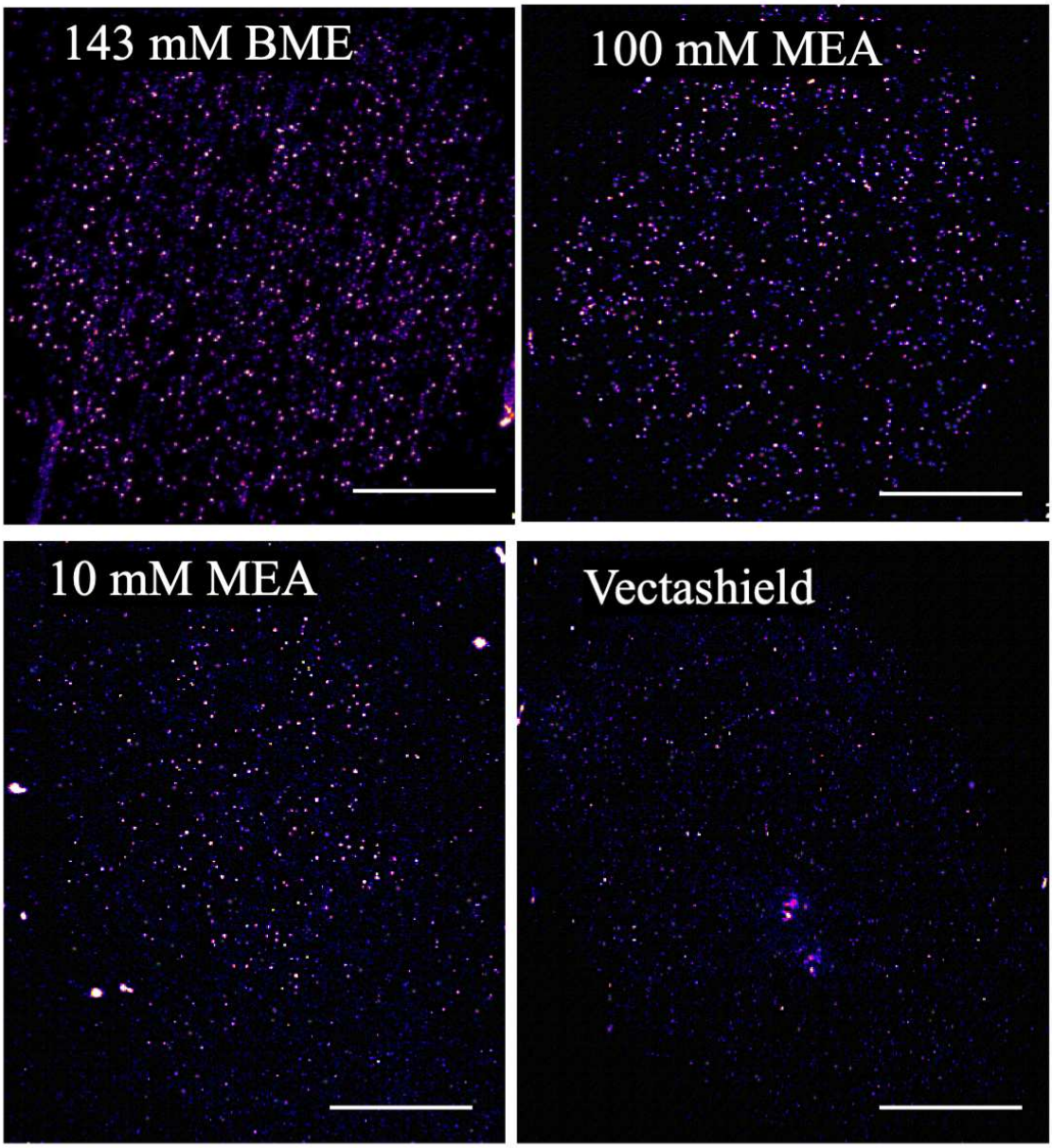


Figure 41: Buffer combinations and fiducial markers tested for dSTORM.
40000 frames were reconstructed to obtain a super-resolved image NTH1 localizations acquired using different dSTORM imaging buffers. Scale = 5 µm.

Our third task was to identify potential fiducial markers to facilitate 2D drift correction during the post processing steps. In short, we tested gold nanoparticles, nanodiamonds and Qdot 655 along with different buffer combinations. Nanodiamonds and Qdot 655 were limited to certain buffer compositions, Glox/MEA and Vectashield that provided very low resolution for NTH1 imaging. Instead, gold nanoparticles, which are commonly used with MEA were stable, but not during long acquisitions. To overcome these difficulties, we decided to omit the use of fiducials and rely instead on the use of

COMET, which efficiently corrects 2D drift in SMLM data **(see section 5.2.1, Materials and Methods)**.

5.2 Nuclear distribution of NTH1 reveals clusters within foci

After optimizing our sample preparation, we were able to reconstruct the first highly resolved images of nuclear NTH1 in non-fractionated (NF) HeLa cells. As in our confocal data, these super-resolved images revealed a punctate distribution of NTH1 across the nucleus (Figure 42). Thanks to the following close-up views, we confirmed that at least two populations of NTH1 can be seen in the nuclei of HeLa cells. Indeed, NTH1 molecules were found either sparsely distributed or forming dense clusters. As in our earlier experiments, subcellular fractionation resulted in a loss of a fraction of NTH1 localizations, likely corresponding to the nucleoplasmic fraction of NTH1 (Table 10).

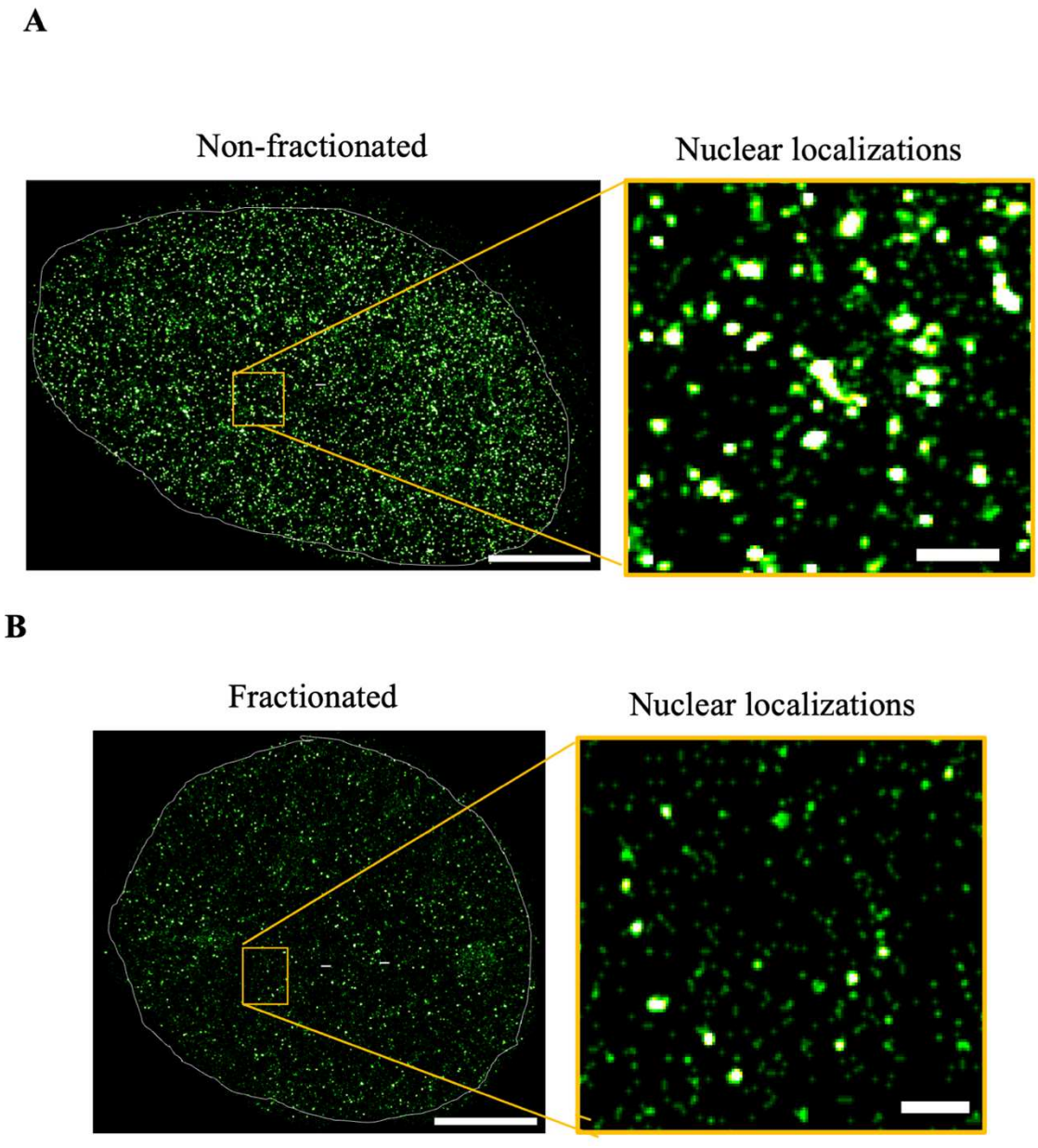


Figure 42: Nuclear distribution of NTH1 in non-fractionated and fractionated HeLa cells, by dSTORM. (A) Reconstructed dSTORM images (Scale = 5 µm) of a representative (A) non-fractionated HeLa cell and (B) fractionated HeLa cell, immunolabelled for NTH1 with F(ab')2 647 secondary antibody, with a closeup on the distribution of NTH1 nuclear localizations, highlighted by yellow squares (Scale = 0.5 µm).

Table 10: Comparing the mean and standard deviation of the localization properties between 10 non-fractionated (NF) and 8 fractionated (F) HeLa cells.

HeLa cells	Nuclei localizations/ μm^2 nuclear area	Sigma (nm)	Localization precision (nm)	Intensity (photons)
NF	512 ± 184	159 ± 9.8	12 ± 1.4	1894 ± 417
F	446 ± 162	157 ± 7.7	14 ± 2.5	1834 ± 33

We decided to investigate the characteristics of these NTH1 clusters in both fractionated and non-fractionated cells. To do this, we used one of the density-based clustering algorithm, known as Voronoi Tessellation provided by the software SR-Tesseller (Levet et al., 2015; Levet, 2023), to isloate heterogeneously dispersed clusters and extract their characteristics, including cluster density, area, shape and number.

We explored different combinations of the parameters, to visually confirm successful segmentation of clusters. Figure 42 illustrates two strategies we employed: (i) a one-level cluster segmentation, which relies on a high density factor of 2.5, and (ii) a two-level cluster segmentation. The latter involves an initial segmentation of clusters covering a larger surface area, characterized by a low density factor of 0.3, allowing to segment groups of clusters, similar in size to the foci observed in confocal images. In the next step, a higher density factor of 0.7 is applied to achieve a tighter segmentation within these groups, resolving them into individual clusters.

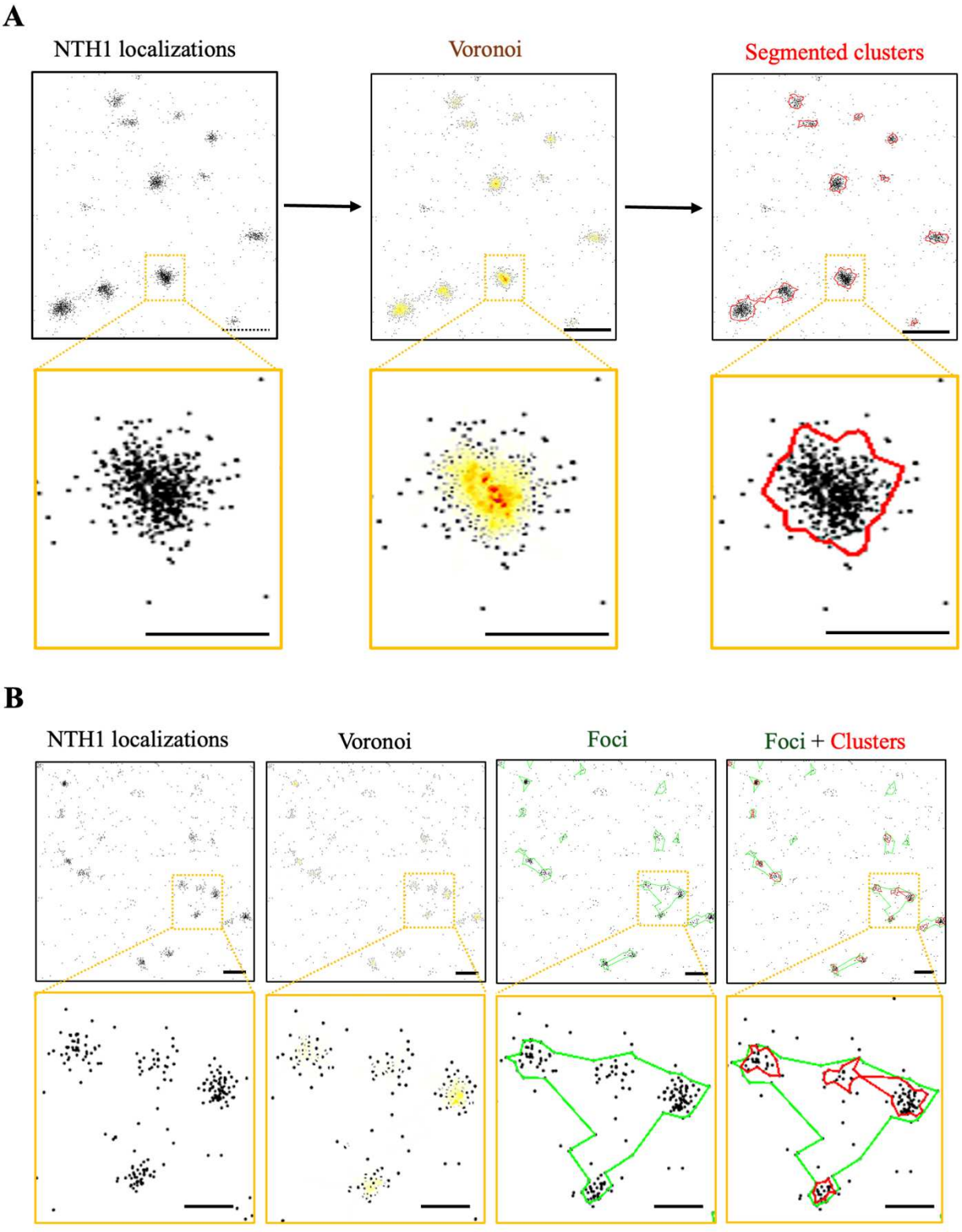


Figure 43: Voronoi tessellation applied on dSTORM images of NTH1 from fractionated HeLa cells. (A) Illustration of the 1-step direct segmentation of distinct, individual clusters of NTH1 localizations making use of a high-density factor (2.5), a minimum surface area of 200 nm^2 and a minimum number of localizations set to 20. Clusters highlighted in yellow represent Voronoi tessellation, prior to

segmentation (red). Scale = 0.2 µm. (B) Illustration of the 2-step segmentation of NTH1 clusters. First, each NTH1 localization (black dot) is assigned to a given area. Second, Voronoi tessellation is applied (yellow) to segment groups of clusters, termed as foci (green). For this purpose, a density factor of 0.3 was applied with a minimum surface area of 20 nm^2 and a minimum number of localizations set to 10. Finally, to further segment individual clusters within these groups (red), we applied a density factor of 0.7 with a minimum surface area of 20 nm^2 and a minimum number of localizations of 10. Overlay of segmentation mask of foci and clusters is shown. Scale = 0.2 µm. Both A and B show close-ups of individual NTH1 foci/ clusters at different stages of segmentation.

Both these strategies yielded similar results. For simplicity, we decided to adopt the one-level segmentation strategy for further analyses. On comparing the number of nuclear localizations, as seen in figure 43A, we found an average 1.4-fold reduction between non-fractionated and fractionated cells, affecting both the number of localizations within and outside of clusters. This is highlighted in figure 43B, were the proportion of localizations within clusters is 50% and decreases to ~ 40% after fractionation, suggesting that many NTH1 clusters are not tightly associated with the chromatin. Similarly, we observe a marked decrease in the number of clusters in fractionated cells (Figure 43C-D), When comparing the characteristics of clusters in non-fractionated and fractionated cells, we noticed that, although they exhibit similar shape (circularity), fractionated cells exhibit significantly larger clusters (1.7-fold higher surface area) than non-fractionated cells (Figures 43E-F-G).

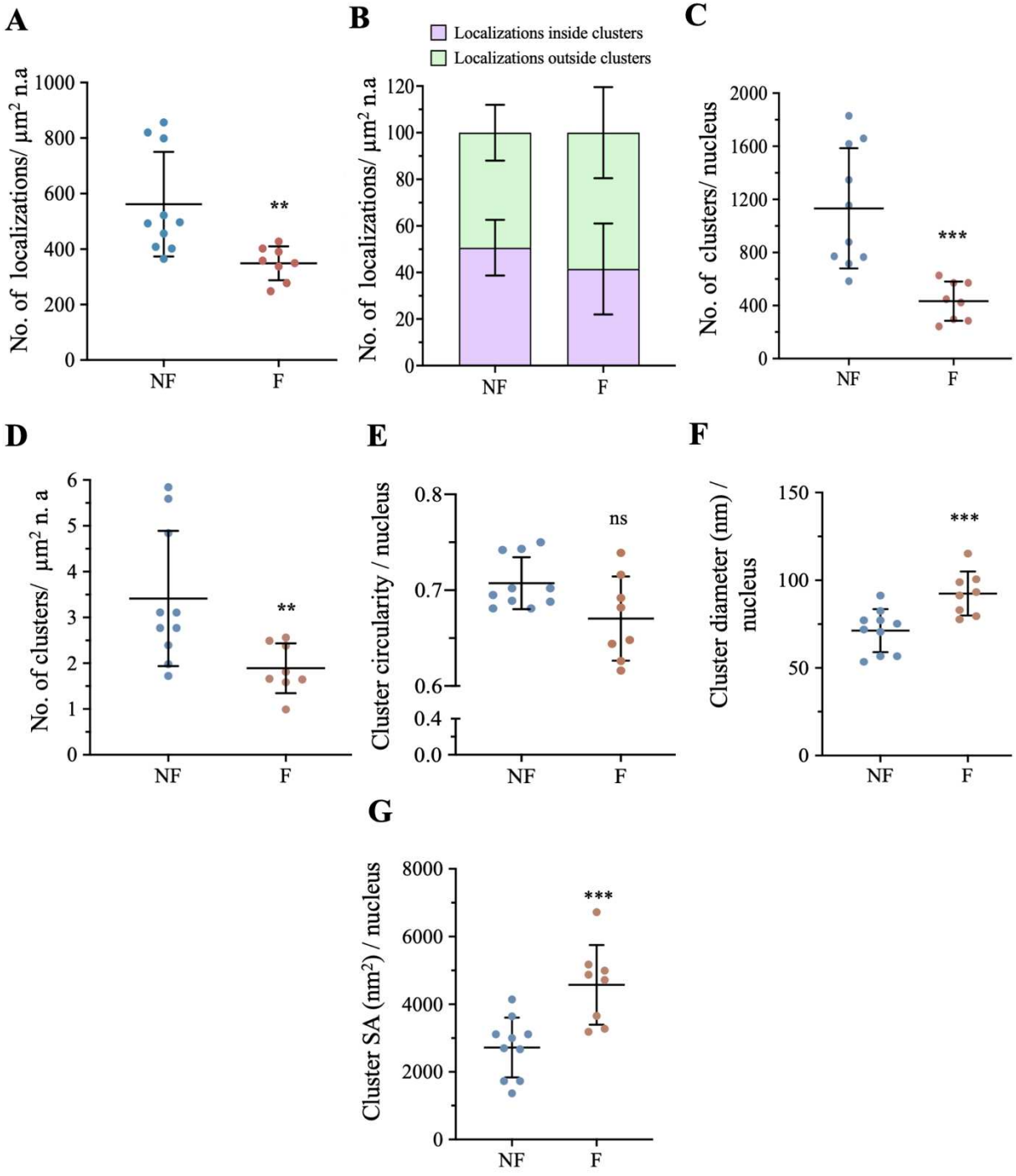


Figure 44: Characteristics of NTH1 clusters from non-fractionated and fractionated HeLa cells. The following graphs describe (A) The number of localizations per 1 µm² nuclear area (n.a) of nuclear localizations, (B) the percentage of localizations within clusters (purple) and localizations outside clusters (green) in non-fractionated (NF) and fractionated (F) HeLa cells. (C) the number of NTH1 clusters per nucleus, (D) the number of clusters per nuclear area for each nucleus, (E) the mean circularity of NTH1 clusters per nucleus, (F) the mean diameter of clusters per nucleus, (G) the mean surface area (SA) of clusters within each nucleus. 10 NF and 8 F cells were measured. In all graphs,

*the mean is represented by the bar and the error bar represents the standard deviation. Statistical analysis was performed using the Mann-Whitney unpaired t-test on non-parametric data with a significance of ns – non-significant, **P<0.001 and *** P<0.001, compared to the NF condition.*

A closer look at NTH1 clusters revealed a diverse density (i.e. number of localizations/μm^2) of clusters, as illustrated in figure 44A. We, therefore decided to classify NTH1 clusters into three classes, based on their densities: low density (0-0.025), medium density (0.025-0.05) and high density (> 0.05). In non-fractionated cells, all three types of NTH1 clusters could be seen, with medium density clusters being the most frequent. In fractionated cells, all types of clusters were also present, but their total number was reduced. High-density clusters were particularly impacted, suggesting that fractionation may partially disrupt NTH1 clusters, in addition to removing the freely diffusing nucleoplasmic fraction of NTH1 (Figure 44B). Interestingly, the mean surface area of all types of clusters was a little larger in fractionated versus non-fractionated cells (Figure 44C). While low and medium density clusters in fractionated cells exhibited slightly larger surface areas with a constant number of localizations, high-density clusters, in contrast, were found to be both larger and more enriched (1.3-fold increase) with NTH1 localizations after fractionation (Figure 44D).

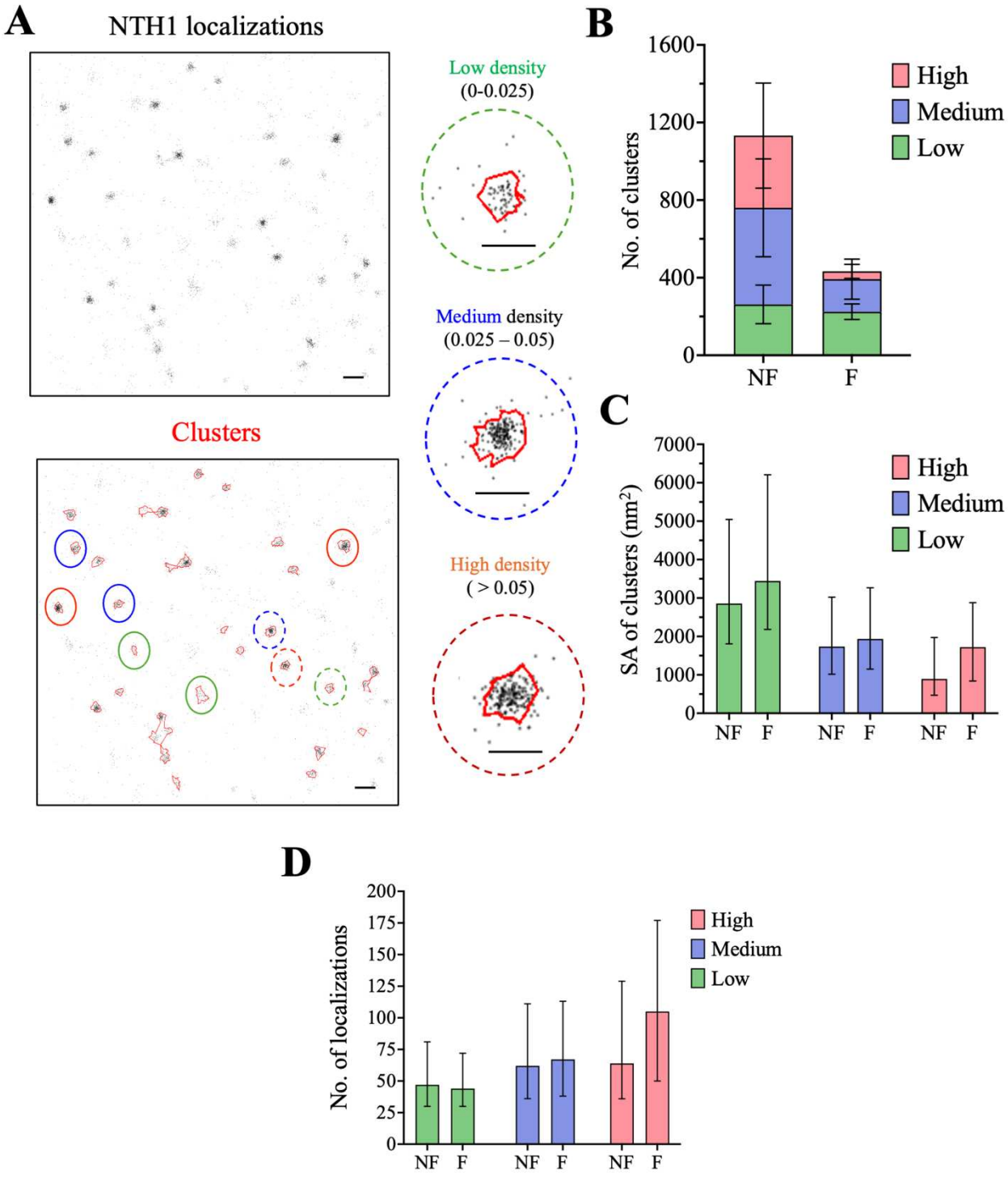


Figure 45: Characterization of NTH1 clusters based on different density classes.
(A) Voronoi tessellation of NTH1 clusters from fractionated HeLa cell nuclei and subsequent division of clusters, into three classes, based on their densities. Low density (green), medium density (blue) and high density (red) clusters are highlighted by respective coloured circles and an example of each is provided alongside. (B) Stacked bar graph describes distribution of NTH1 clusters based on the three density classes. (C) The surface area (nm^2) of NTH1 clusters and (D) the number of NTH1 localizations.

In graphs B, C, and D, the horizontal line is the mean and the error bar represents the standard deviation, considered for 10 non-fractionated (NF) and 8 fractionated (F) HeLa cells.

5.3 $KBrO_3$ induces a redistribution and increase in chromatin-associated NTH1

Next, we investigated the effects of oxidative stress on the nanoscale distribution of nuclear NTH1. We treated cells with $KBrO_3$ in a similar manner to our previous confocal experiments and applied our 1-step cluster segmentation parameters. We were able to maintain consistent imaging quality of our dSTORM images as seen in the localization precision values presented in table 11, providing us with a robust data set to perform our clustering analysis.

Figure 45 compares the total number of nuclear NTH1 localizations (Figure 45A), and the fraction of localizations present inside and outside NTH1 clusters for each condition (non-treated, immediately after treatment and at 15 minutes, 1h, 4h and 8h post-treatment; Figure 45B). An increase in the total number of NTH1 localizations was observed after treatment (Figure 45A). However we have high cell-to-cell variability as indicated by the large error bars. A 2-fold decrease in the number of localizations was subsequently observed at the early recovery time points - 0.25h and 1h, before returning to control levels 4h and 8h post recovery. Interestingly, we found that $KBrO_3$ treatment led to a reduced fraction of NTH1 localizations within clusters, decreasing from ~40% in untreated cells to ~25% in the T0 condition, while the remaining 75% were located outside the cluster boundaries (Figure 45B). This suggests a redistribution of NTH1 from the clusters to the nucleoplasm in the initial response to $KBrO_3$ induced oxidative stress. A steady increase in the fraction of localizations within clusters was then observed after this initial drop (from 0.25h to 1h), that appears to stabilize around 50% from 1h to 8h post treatment. This increased proportion of NTH1 within clusters indicates a possible recruitment of NTH1 to sites of oxidative DNA damage requiring repair.

Table 11: Comparing the mean and standard deviation of the localization properties between non-treated (NT), treated (T0) and cells recovering from treatment at different time points (TX).

Conditions (time in hours)	No. of cells	Sigma (nm)	Localization precision (nm)	Intensity (photons)
NT	8	157 ± 7.7	14 ± 2.5	1834 ± 33
0	7	154 ± 5.9	12 ± 1.4	2286 ± 164
0.25	5	155 ± 3.5	13 ± 1.5	1970 ± 466
1	5	155 ± 4.1	11 ± 1.5	2176 ± 560
4	7	154 ± 3.6	12 ± 1.6	2095 ± 496
8	7	156 ± 4.2	10 ± 0.38	2690 ± 132

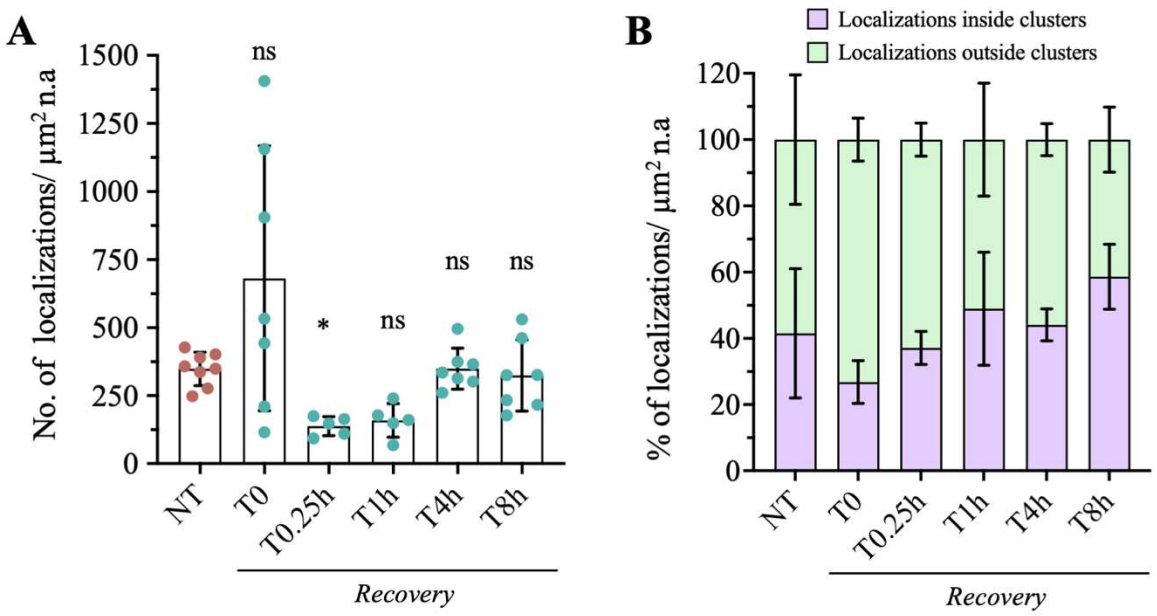


Figure 46: Comparing nuclear localizations inside and outside clusters.
*(A) The number of localizations per 1 µm² nuclear area (n.a) of nuclear localizations, where each dot represents the no. of localizations per nucleus, the bar represents the mean and the error bars represent the standard deviation. (B) The stacked bar graph describes the percentage of localizations within clusters (purple) and localizations outside clusters (green, where the bar represents the mean and the error bars represent the standard deviation. One-way ANOVA (Kruskal-Wallis) test (A) was performed for non-parametric data with *P < 0.01, and ns-non-significant, compared to NT condition. Measured for T0 and TX conditions.*

After implementing our clustering parameters, we extracted cluster characteristics from each data set (Figure 46). Figure 46A shows a marked reduction (30%) in the number of clusters per nucleus (decreasing from ~420 to ~300) between NT and $KBrO_3$ treated cells (T0). During the initial recovery time points (T0.25h and T1h), the number of clusters then remained fairly low around 300 clusters/nucleus and stable. After which, we observed an increase with a doubling at the 4h timepoint (~600 clusters/nucleus) and reaching a maximum of ~700 clusters/nucleus at the 8h post-treatment. After correcting these values for the nuclear area (Figure 46B), the same trend is observed. The cluster morphology determined by the circularity (~0.68) remained mostly constant in all conditions, with only a small decrease after 1h of recovery. Surprisingly, we discovered that the mean surface area of clusters immediately after treatment is 1.6 times higher than that of non-treated cells and rapidly returns to similar levels found in non – treated cells during the recovery time period (Figure 46D). The diameter of the clusters within NTH1 clusters also follows a similar trend, as seen in figure 46E. Taken together, these observations suggest that $KBrO_3$ leads to an initial decrease followed by a gradual increase in the number of NTH1 clusters in nuclei during the recovery phase, similar to what we observed for the foci

in our confocal images (Figure 40). The change in size and area of these clusters is however less pronounced than was observed for the foci.

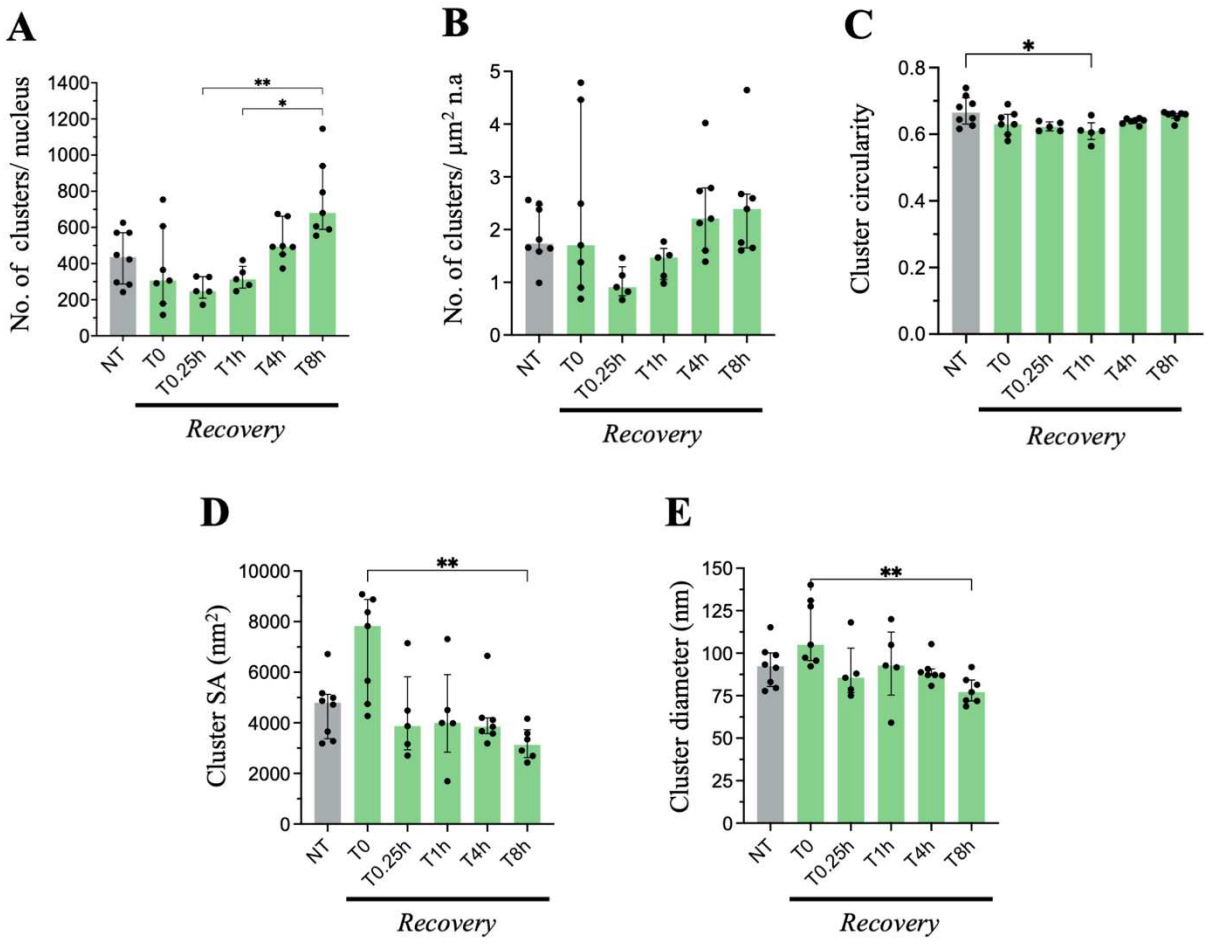


Figure 47: Characteristics of cluster features in $KBrO_3$ treated and recovered HeLa cells.
*The following graphs describe (A) the number of NTH1 clusters per nucleus, (B) the number of clusters per nuclear area (n.a) for each nucleus, (C) the mean circularity of NTH1 clusters per nucleus, (D) the mean surface area (SA) of clusters within each nucleus and (E) the mean diameter of clusters per nucleus, in fractionated HeLa cells treated with 40 mM $KBrO_3$ for 0.5h and further recovered in fresh media and fixed at different time points. In all graphs, each point represents clusters belonging to one nucleus, the median is represented by the bar and the error bar represents the interquartle range. The number of cells measured for clustering parameters are as follows: NT = 8; T0 = 7; T0.25h = 5; T1h = 5; T4h = 7; T8h = 7. Statistical analysis was performed using the one – way ANOVA (Kruskal-Wallis) and Dunn's multiple comparisons test on non-parametric data with a significance of **P<0.01 and *** P<0.001. P value bars on the graphs indicate only significant relationships between conditions, whereas the rest remain non-significant.*

Changes in the density of NTH1 localizations within these clusters could also be followed by classifying clusters, as described previously (Figure 44), into low- medium- and high-density clusters. Figure 47 displays a close-up of the cluster diversity observed after treatment (T0) and during the first (T0.25h) and last (T8h) recovery time points.

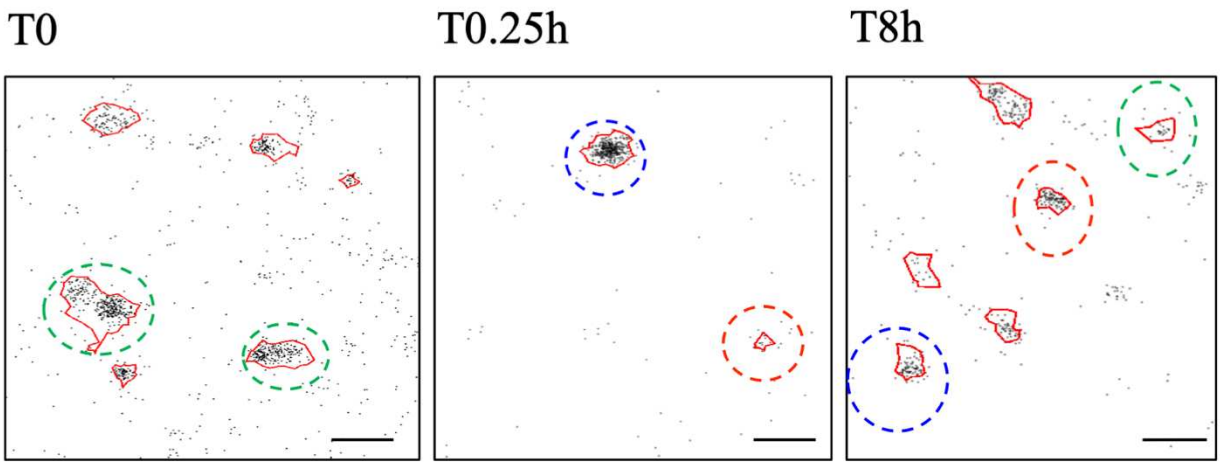


Figure 48: $KBrO_3$ effect on the distribution of NTH1 clusters.
Changes in the distribution of NTH1 clusters (red line) of NTH1 localizations (black dots) in $KBrO_3$-treated cells at T0, T0.25 and T8 respectively. Scale = 200 nm. NTH1 clusters were divided into three classes, based on their density (dashed circles). Low density clusters (green) range from 0-0.025. Medium density clusters (blue) range from 0.025-0.05. High density clusters were considered above 0.05 (red).

It is important to note that NTH1 was also localized in the nucleoli of some cells, irrespective of their treatment with $KBrO_3$. NTH1 clusters within nucleoli were exempted from the clustering analysis, due to the application of stringent clustering parameters. Apart from this, within the nuclear space, we observed a diverse density of clusters and implemented the same classification, previously established. The number of low-density clusters exhibited a slight decrease at the 0.25 and 1h timepoints after treatment, but were overall rather constant, while the medium- and high-density clusters showed an initial decrease, followed by a marked increase in their number at 4h and particularly 8h post-treatment (Figure 48A), when the number of high-density clusters was found to be ~4 times higher than that in non-treated cells.

On measuring the surface area of these clusters, we discovered that low density clusters remained at a consistent size of ~ 3200 nm^2 in all conditions. In contrast, the areas of medium and high-density clusters and the number of localizations per cluster followed a similar trend as the number of clusters. They showed an initial decrease followed by a steady increase during the 1h to 8h recovery period (Figure 48B-C).

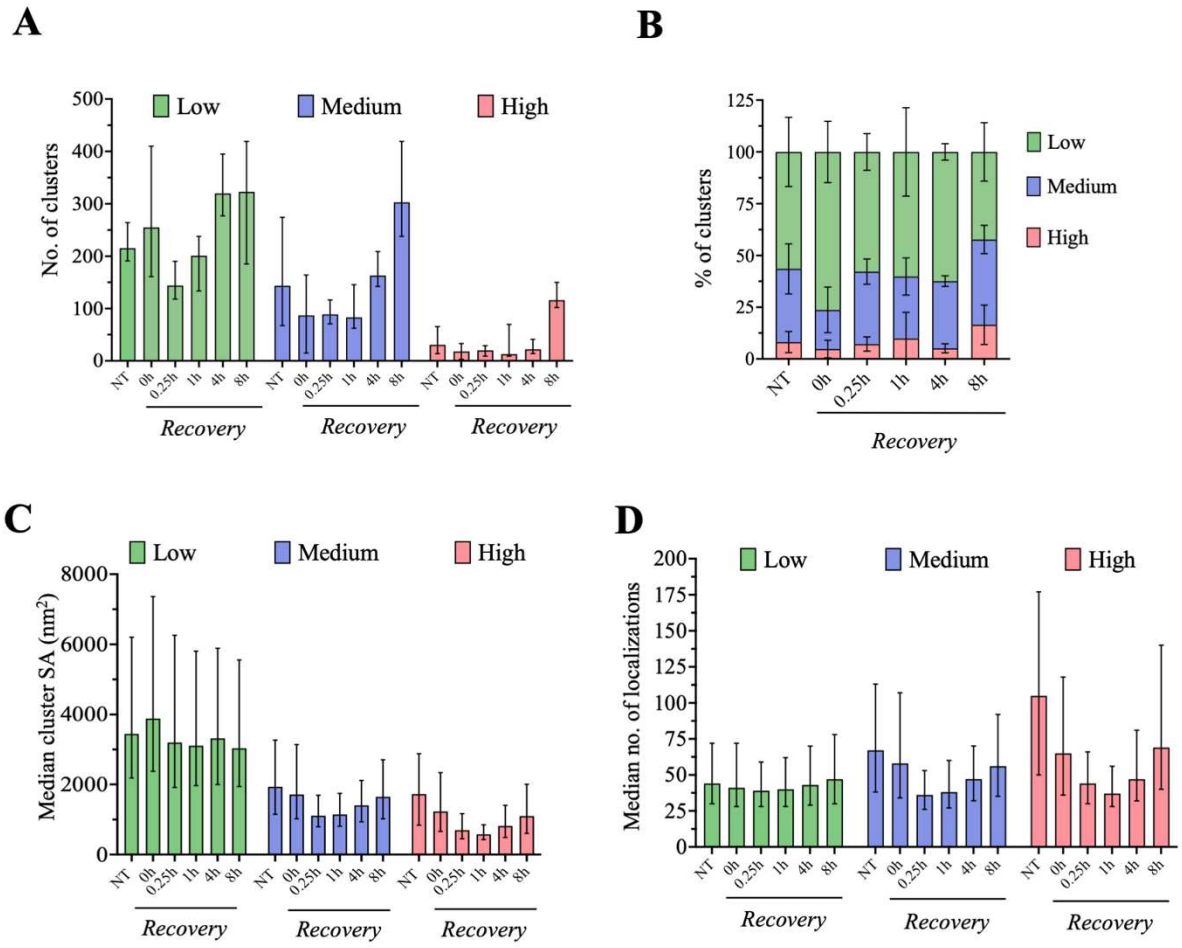


Figure 49: Characterisation of NTH1 cluster features based on different density classes in cells treated and recovered from $KBrO_3$.

(A) Bar graph describes the number of NTH1 clusters in three density classes. (B) Stacked bar graph describes the proportion of low, medium and high density NTH1 clusters. (C) The surface area (nm^2) of NTH1 clusters and (D) the number of NTH1 localizations. Bars represents the median and the error bars represent the interquartile range, measured for each condition, for the following number of cells: NT = 8; T0 = 7; T0.25h = 5; T1h = 5; T4h = 7; T8h = 7. Low density clusters (green) range from 0-0.025. Medium density clusters (blue) range from 0.025-0.05. High density clusters were considered above 0.05 (red).

In summary, our dSTORM images provided the first high-resolution map of NTH1 distribution within HeLa cell nuclei. NTH1 was found either sparsely distributed in the nucleoplasm or densely packed into clusters. Based on the respective characteristics of NTH1 foci observed in confocal microscopy and NTH1 clusters seen in dSTORM, we propose that NTH1 foci are likely composed of a minimum of two clusters. NTH1 localizations within these clusters and foci were found to redistribute in a two-phase response to oxidative stress, involving an initial reduction of the number of foci and

clusters and an increase in the amount of sparsely distributed NTH1 immediately after exposure to oxidative stress, followed by a gradual increase of the number and density of the foci and clusters during the following hours. The first phase may coincide with the search for DNA lesions, while the second phase is likely to coincide with the repair of the damaged DNA.

6. Investigating the dynamics of NTH1 by single-particle tracking PALM.

The third objective of this thesis was to investigate the dynamic behaviour of NTH1 in the nucleus of HeLa cells under normal and oxidative stress conditions. Similar studies have described the dynamics of OGG1 in HeLa cells (Campalans et al., 2007; D'Augustin et al., 2023) and of DNA repair proteins, such as RAD51, in yeast (Miné-Hattab et al., 2021), unlocking novel modes of diffusion within the nuclear environment. To do so, we turned to a second SMLM technique, single-particle tracking (spt) PALM, which has previously been used in the team to follow dynamics of DNA-interacting proteins in their native cellular environment (Floc'h et al., 2019; Vauclare et al., 2024).

6.1 Dynamics of NTH1 in untreated HeLa cells

To investigate the dynamic behaviour of NTH1 within HeLa cell nuclei, we set out to follow the dynamics of NTH1 fused to the widely used photoconvertible fluorescent protein, mEos4B, that is activated to an 'on' or 'green' state and photoconverts to the 'red' state on illumination with a 405 nm laser, at a low power density (>10 W cm^{-2}) (Wulffele et al., 2022). For this, we needed to transiently transfect HeLa cells to express NTH1-mEos4B.

We successfully transfected cells with a plasmid encoding NTH1-mEos4B. After 48 hrs of transfection, confocal images showed ~ 80 % transfection as illustrated in figure 49A. This was confirmed by detection of an intense band by Western Blot using our anti-NTH1 antibody, migrating at its expected molecular weight (~ 65 kDa), in addition to the previously detected endogenous NTH1, migrating at ~37kDa. As a control, we also transfected cells with a plasmid encoding mEos4B with a NLS signal to target it to the nucleus of HeLa cells and were able to obtain similar transfection efficiency (Figure 49B). The dynamic behavior of mEos4B-NLS within the nuclear space is expected to be very different from that of NTH1-mEos4B, since it should be largely free diffusing with no interaction with the chromatin.

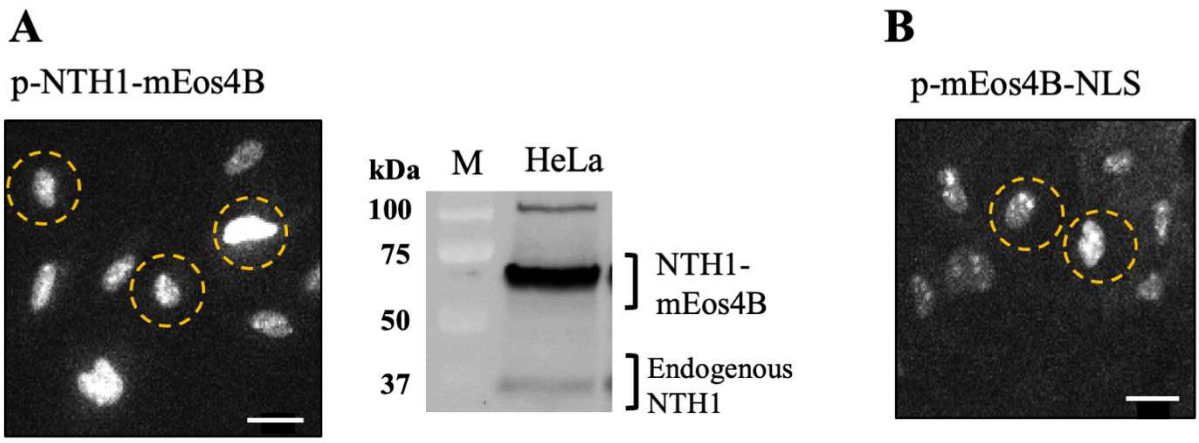


Figure 50: Efficiency of NTH1-mEos4B and mEos4B-NLS transfections in HeLa cells.
(A) Left: Transfected HeLa cells expressing variable levels of NTH1-mEos4B. Right: Western blot analysis of transfected HeLa cell extracts confirming high expression of NTH1-mEos4B at ~ 65 kDa compared to endogenous levels at 37 kDa. (B) HeLa cells transfected with mEos4B-NLS. Cells representing moderate to high transfection efficiency (circled in yellow) were considered for single particle tracking PALM. Images of photoconverted mEos4B using 568 nm illumination were taken under a confocal microscope. Scale = 20 µm.

Next, we setup spt experiments using live-cell PALM (PhotoActivated Localization Microscopy) imaging to study the dynamic behavior of NTH1. However, transfected cells, displayed heterogeneous levels of protein expression. In order to retrieve and reconstruct trajectories belonging to individual NTH1 molecules, we considered medium to highly transfected cells, providing nuclei with consistent ~ 7 NTH1 localizations/ frame or spt analysis.

Images were recorded at a frame rate of 10 ms for 10,000 frames, providing the ability to trace NTH1 in real-time, limiting motion blur. We used very low 405 nm laser power and 488 nm laser illumination to limit photobleaching and increase track length of molecules (**see section 5.3.1, Materials and Methods**). After data acquisition and image reconstruction, we performed trajectory reconstruction using the software *Swift*. Localizations were linked together in time, creating trajectories belonging to individual NTH1 molecules, as illustrated in figure 50. We only considered trajectories composed of at least four localizations appearing in consecutive frames, before bleaching, blinking or moving out of the focal plane. Data acquired on mEos4B-NLS transfected HeLa cells were processed using the same pipeline, yielding similar data quality (Table 12). However, because we analysed only three mEos4B-NLS transfected cells, compared to 10 NTH1-mEos4B transfected cells, we had fewer total number of tracks for the mEos4B-NLS construct. Table 12 summarizes the localization properties and number of recorded trajectories for both conditions.

Table 12: Localization properties of cells transfected with either NTH1-mEos4B (N=10) or mEos4B-NLS (N=3).

Conditions	No. of cells	No. of localizations/ nuclear area	Sigma (nm)	Localization precision (nm)	Intensity (photons)	Total no. of tracks
NTH1-mEos4B	10	317 ± 146	134 ± 4.6	27 ± 1.2	238 ± 37	341315
mEos4B-NLS	3	550 ± 403	136 ± 2.6	27 ± 0.15	247 ± 13	154709

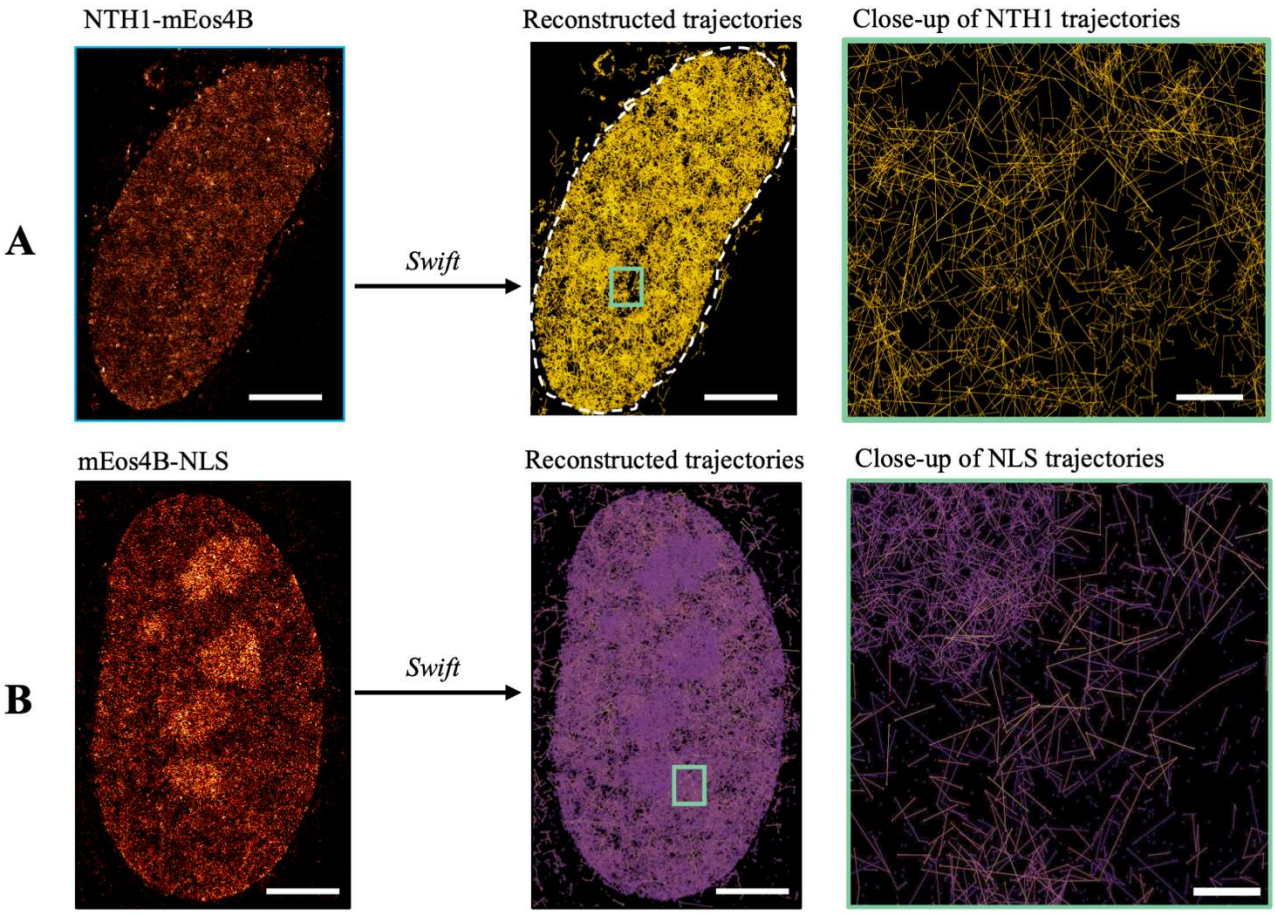


Figure 51: NTH1-mEos4B and mEos4B-NLS trajectories reconstructed using the Swift software. Left: Reconstruction of NTH1-mEos4B (A) and mEos4B-NLS (B) localizations. Middle: Single-molecule trajectories were then traced using the single-particle analysis software, Swift. Right: Close-up views of the distribution of NTH1-mEos4B (yellow) and mEos4B-NLS tracks (purple to orange). Nucleus image scale is 2 µm and the closeup is 500 nm.

On average, we obtained more localizations of mEos4B-NLS per nucleus than of NTH1-mEos4B (Figure 51A-B). However, the proportion of long, exploitable tracks (with >4 localizations) was almost the same in the two samples (Figure 51C), with just over 25% of tracks meeting this

criterium. Only these longer tracks were used for further analysis to determine the diffusion coefficients of NTH1-mEos4B and mEos4B-NLS molecules.

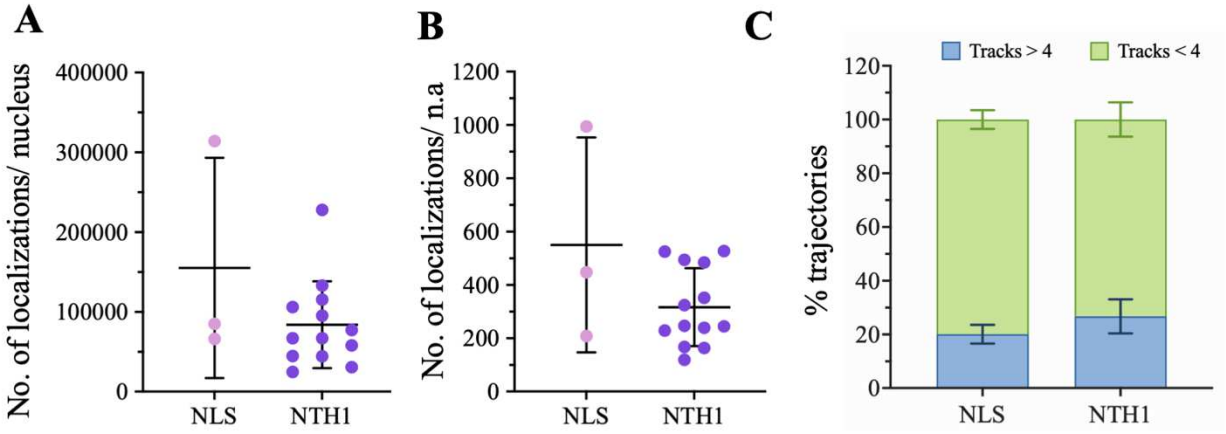


Figure 52: Comparison of the number of localizations per nucleus for NTH1-mEos4B and mEos4B-NLS transfected HeLa cells and the proportion of long (>4) tracks in both cases.
(A)-(B) Scatter plots illustrate the total number of NTH1-mEos4B (purple) and mEos4B-NLS (pink) localizations per nucleus (A) or per μm^2 nuclear area (B). Each dot represents one nucleus, the horizontal line is the mean and the error bars represent the standard deviation. No. of mEos4B-NLS transfected cells = 3; NTH1- mEos4B transfected cells = 10. (C) Stacked histograms illustrating the proportion of long (>4 frames; blue) and short (<4 frames; green) trajectories.

There are two approaches used to estimate the diffusion coefficient of a molecule: the mean jump distance (MJD) and the mean squared displacement (MSD). Histograms of the MJD distribution provided us with a first evaluation of the overall diffusion kinetics of NTH1-mEos4B and mEos4B-NLS in individual nuclei. Interestingly, we observed substantial cell-to-cell (Figure 52A), with some histograms displaying a narrow distribution of NTH1-mEos4B MJD values, and others being broader, suggesting there may be multiple diffusive populations. In contrast, histograms of the MJD distribution of mEos4B-NLS were more consistent across the three datasets.

Next, we plotted histogram distributions of apparent diffusion coefficients (D_{app}) of individual trajectories derived from MSD analysis and fitted them to either a one- or two-population Gaussian fit, to derive population diffusion coefficients. MSD histograms of NTH1-mEos4B molecules were best fitted to a two-population model, whereas MSD histograms of mEos4B-NLS were best fitted to a one-population model.

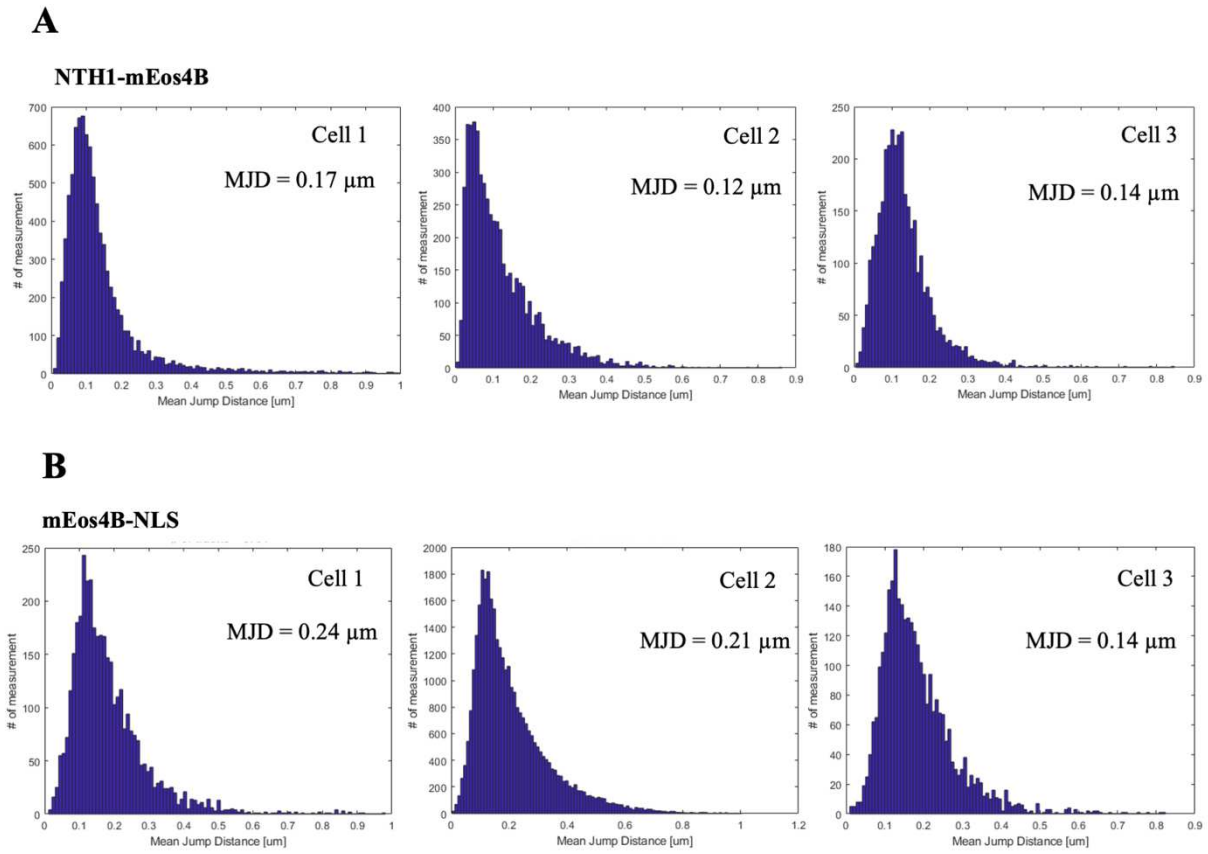


Figure 53: Mean jump distance (MJD) histograms measured for NTH1-mEos4B and mEos4B-NLS molecules.

Histograms of the MJD distribution of NTH1-mEos4B (A) and mEos4B-NLS (B) molecules in individual cells. The x-axis plots the MJD vs the number of trajectories in the y-axis. The mean MJD value for each cell is indicated.

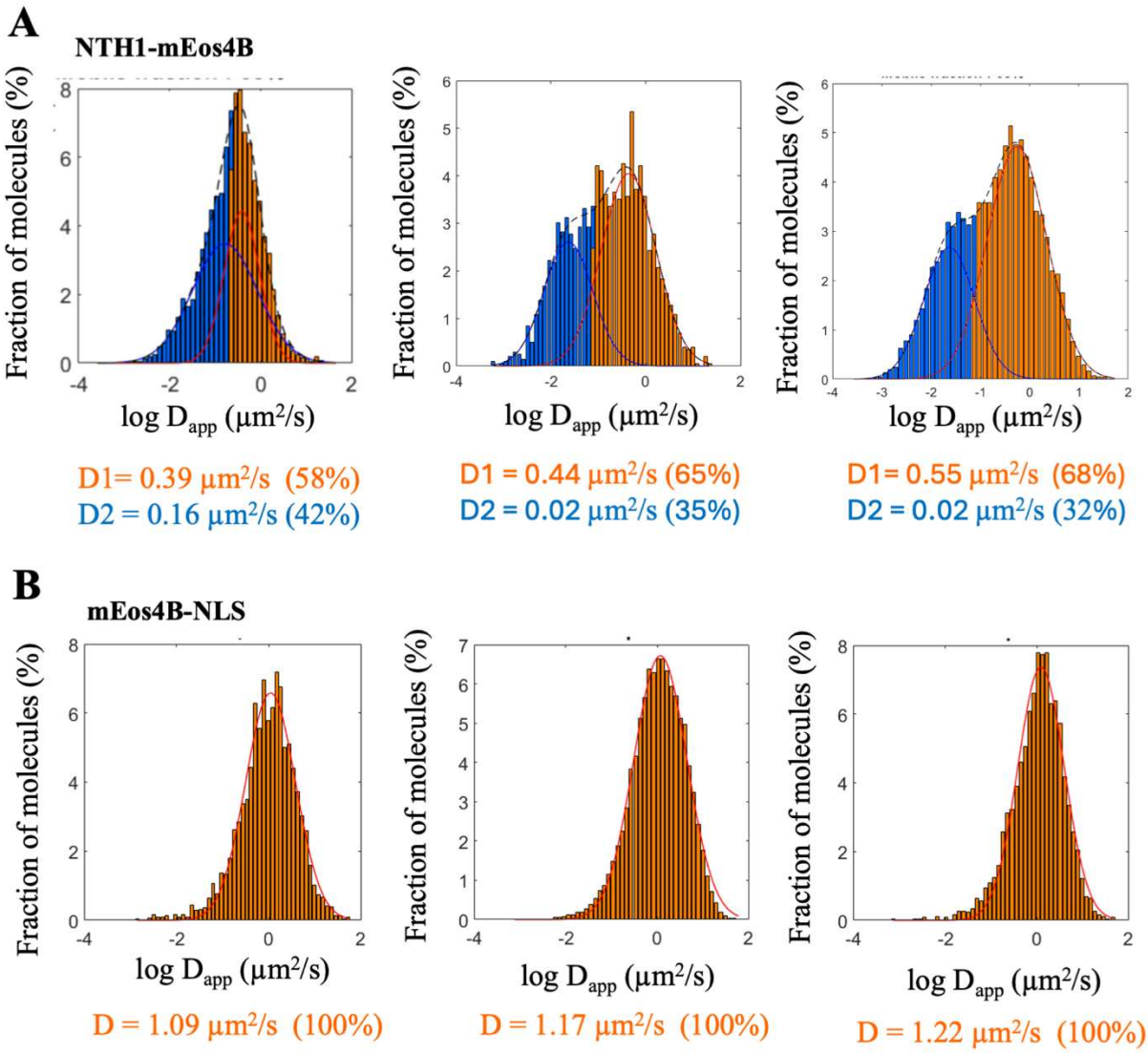


Figure 54: Apparent diffusion coefficient (D_{app}) histograms measured for NTH1-mEos4B and mEos4B-NLS molecules.

Single cell analysis of apparent diffusion coefficients (D_{app}) of NTH1-mEos4B (A) and mEos4B-NLS (B) molecules. (A) Representative D_{app} histograms of NTH1-mEos4B fitted to a two-population Gaussian fit ($R^2 < 0.98$) by interactively selecting the peak maximum, followed by the full width half maximum (FWHM) of each population in MATLAB. The more mobile population is coloured orange, while the slower population is coloured blue. (B) Representative D_{app} histograms of mEos4B-NLS fitted to one-population Gaussian fit (orange).

For NTH1-mEos4B molecules, as in the MJD histograms, we observed substantial cell-to-cell variability in the MSD histograms, with some histograms clearly exhibiting two peaks (i.e. two populations), while others were more homogeneous (Figure 53A). As a result, the derived diffusion coefficients (D1 and D2) were also quite variable, although the proportion of fast- and slow-diffusing

molecules remained quite constant. The fits nonetheless convincingly demonstrate the existence of two populations of diffusing NTH1 molecules in HeLa cell nuclei, with one largely immobile population (D2 ~0.14 $\mu m^2/s$) and a second more mobile population with an average diffusion coefficient (D1) ~0.67 $\mu m^2/s$. For mEos4B-NLS, we obtained a consistent diffusion coefficient of ~1.12 $\mu m^2/s$.

6.2 Dynamics of NTH1 in HeLa cells exposed to oxidative stress

HeLa cells expressing NTH1-mEos4B were treated with 40 mM $KBrO_3$ for 0.5h and then allowed to recover in fresh media for up to 4h. sptPALM analysis was performed on non-treated cells, immediately after $KBrO_3$ treatment (T0) and 4h post treatment (T4h). A minimum of 10 cells were analyzed for each condition. In response to $KBrO_3$ treatment, we observed a decrease in the number of NTH1-mEos4B localizations and consequently of the number of trajectories (1.4-fold from T0 to NT) at T0, followed by an increase at the 4h recovery time point (Table 13 and figure 54A). The number of localizations per nuclear area for T4h was still relatively low compared to that obtained in the NT condition. This is further highlighted in figure 55, in which the close-up view of the trajectories obtained at T4h reveals fewer and more clustered trajectories, reminiscent of the clusters observed by dSTORM. In all three conditions, we obtained ~ 20% of trajectories with a tracklength of more than 4, providing us with robust and reliable data to analyze the dynamics of NTH1-mEos4B.

Table 13: Localization properties of NTH1-mEos4B transfected cells in non-treated (NT), treated (T0) and recovered at 4h time point (T4h).

Conditions	No. of cells	No. of localizations/ nuclear area	Sigma (nm)	Localization precision (nm)	Intensity (photons)	Total no. of tracks
NT	10	317 ± 146	134 ± 4.6	27 ± 1.2	238 ± 37	341315
T0	16	175 ± 129	133 ± 4.3	28 ± 2.0	215 ± 37	242546
T4h	12	224 ± 140	133 ± 3.2	28 ± 1.4	222 ± 32	275342

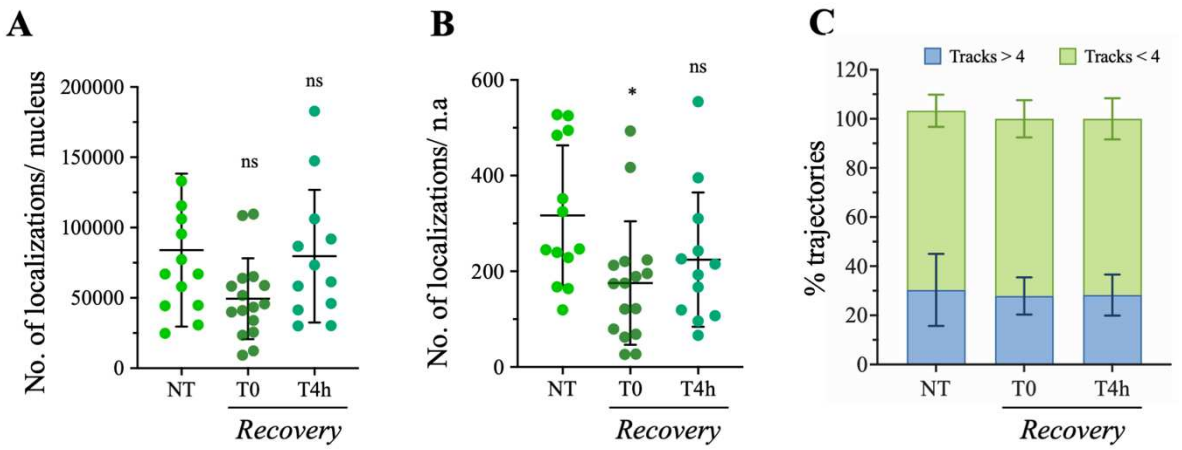


Figure 55: Comparing localization properties between non-treated, treated (T0) and 4h recovered NTH1-mEos4B transfected cells.

*(A) Scatter plot describes the total number of NTH1 localizations in non-treated (NT), treated (T0) and 4h recovered cells (T4h). (B) The number of localizations per μm^2 nuclear area and (C) the percentage of trajectories representing the proportion of tracks with localizations appearing in more than 4 frames. Each dot represents one nucleus, the horizontal line is the mean and the error bars represent the standard deviation. NT = 10; T0 = 16; T4h = 12. One – way ANOVA (Kruskal-Wallis) test performed on non-parametric data were the significance measured is ns – non-significant, *P<0.05 compared to NT condition.*

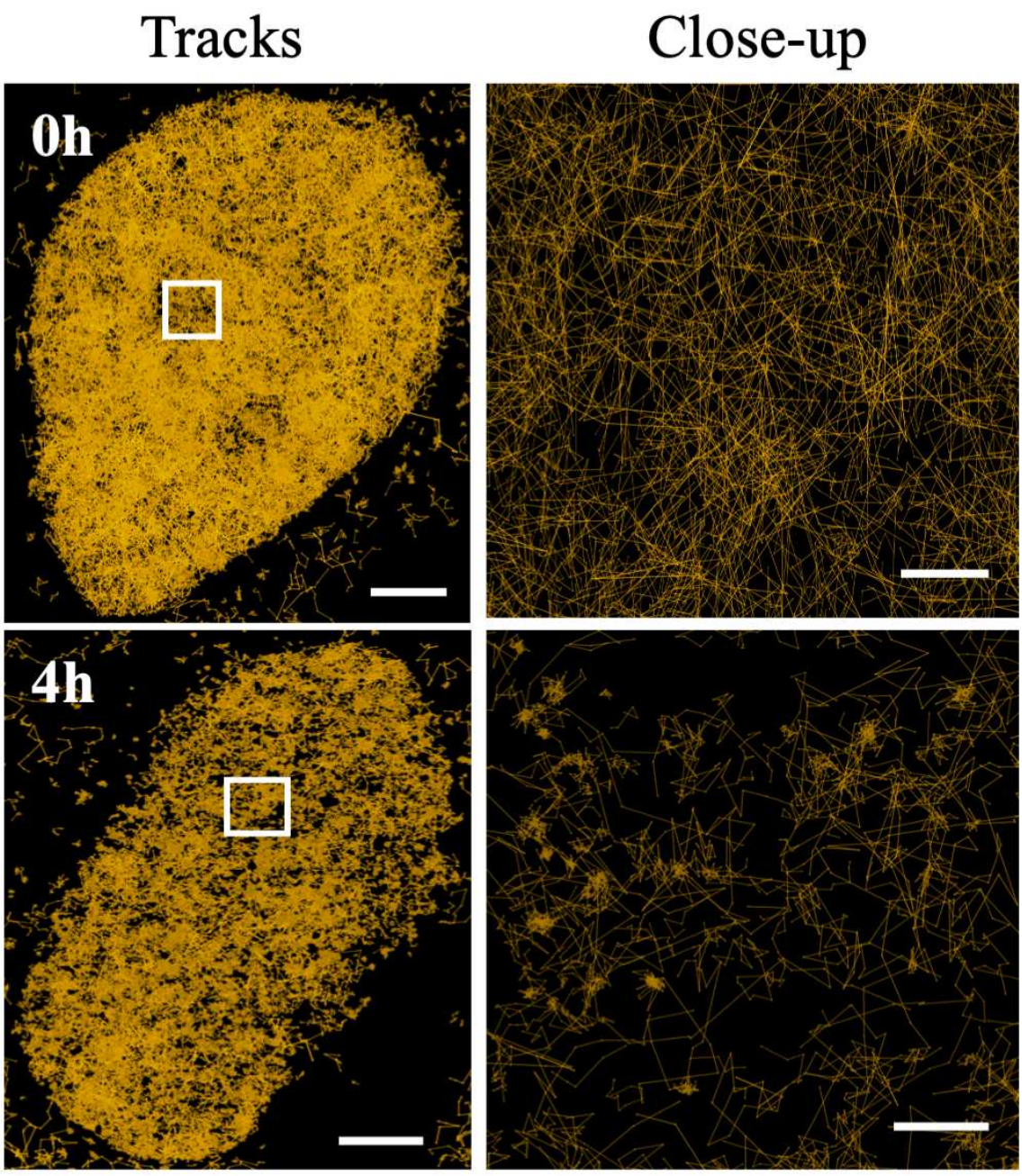


Figure 56: $KBrO_3$ alters the diffusion kinetics of NTH1.
Reconstructed tracks of single NTH1-mEos4B molecules derived from sptPALM imaging of transiently transfected HeLa cell nuclei treated with 40mM $KBrO_3$ for 0.5h (0h) and another treated cell allowed to recover for 4h (T4h) (Scale = 5 µm). Right: close-up view of the tracks within a given ROI (white box) (Scale = 0.2 µm).

MJD distribution histograms of NTH1-mEos4B molecules were calculated for each cell in all three conditions (Figure 57). As in our experiments in the absence of $KBrO_3$, we here again observed a high cell-to-cell variability after treatment with $KBrO_3$ (Figure 56 and 57). The cell variability is more prominent in cells recovered at T4h, suggesting cells may be at different stages of recovery from $KBrO_3$

treatment. Interestingly, we could nonetheless observe that histograms in the T0 condition were quite different from those obtained for non-treated and 4h recovery samples, displaying a much broader distribution and a higher mean MJD (0.15 µm at T0 compared 0.13 µm in NT and 0.13 µm at T4h), indicating a change in the dynamic behavior of NTH1-mEos4B.

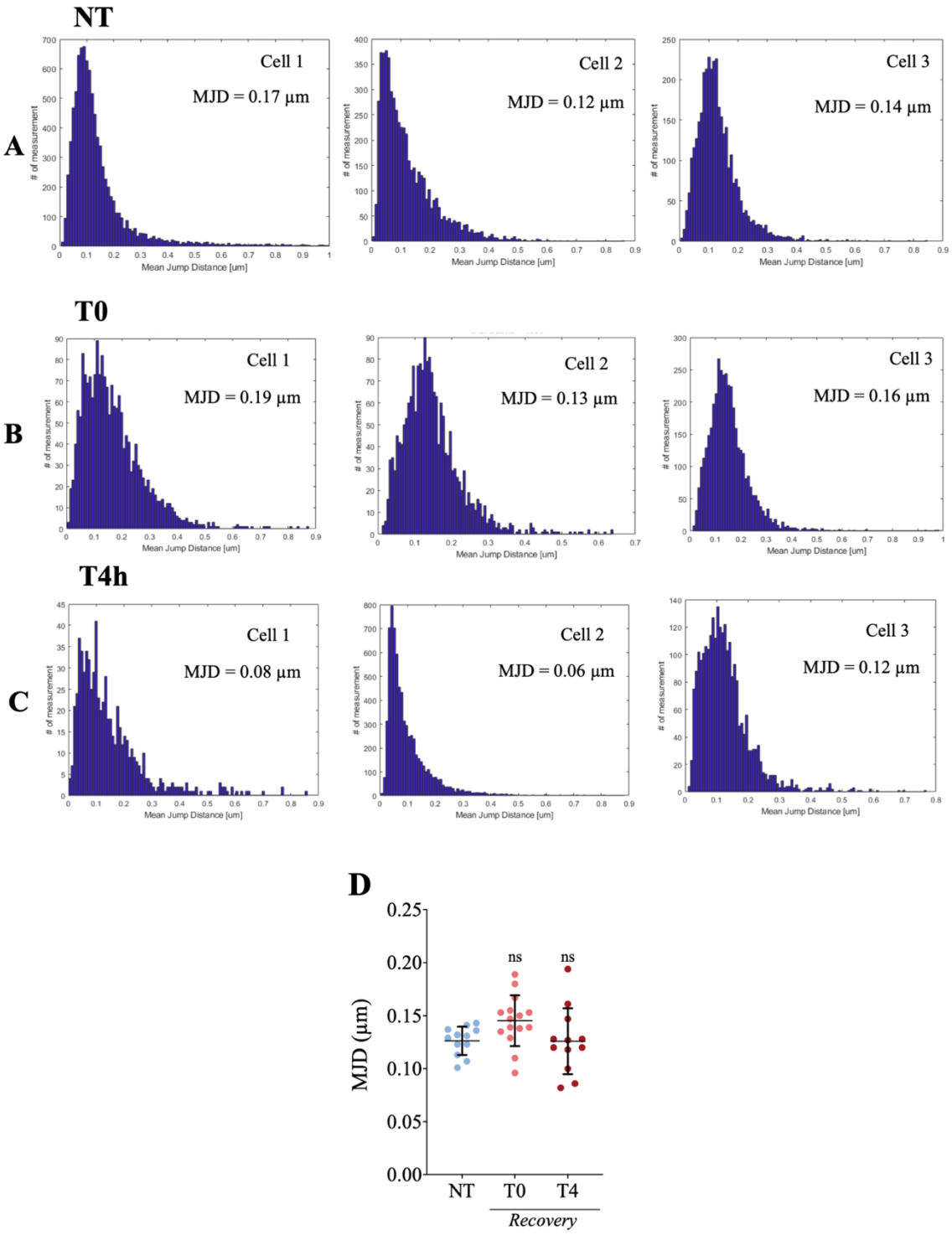


Figure 57: Mean jump distance (MJD) histograms of NTH1-mEos4B measured for (A) NT cells, (B) T0 cells and (C) T4 cells.
(A, B, C) NTH1-mEos4B transfected single cell analysis panels of MJD histograms for (A) non-nontreated-NT (B) treated cells-T0 and (C) cells recovered at T4h after treatment), with the mean MJD provided per histogram. The x-axis plots the MJD vs the number of trajectories in the y-axis. (D) Mean MJD of NTH1-mEos4B in NT cells (n = 12), T0 cells (n = 16) and T4 cells (n = 13 nuclei) taken from 4 independent experiments. Here, error bars represent the median and interquartile range. A one-way ANOVA analysis (Kruskal-Wallis) was performed on non-parametric data and significance was compared to the non-treated control cells (NT). The P values are indicated above each condition, where ns = non-significant.

Next, we extracted and fitted the MSD-derived D_{app} distribution histograms for NTH1-mEos4B using a two-population fit, as before (Figure 58A-B-C). Despite substantial cell-to-cell variation, we observed (i) an increase in the diffusion coefficient and proportion of the 'fast'-diffusing population of NTH1-mEos4B (D1) at T0, and (ii) a decrease in the mobility and an increased proportion of the slow-diffusing population of NTH1-mEos4B (D2) molecules in treated cells after 4h of recovery (Figure 58B-C).

Indeed, in NT cells, we established that there were two populations of NTH1-mEos4B (Figure 58D-F).: a slow – moving population with a diffusion coefficient (D2) of 0.17 $\mu m^2/s$ accounting for ~40% of the molecules and a fast-moving population (D1) diffusing at 0.67 $\mu m^2/s$ accounting for ~60% of the molecules. Immediately after treatment, we observed an increase in the diffusion coefficient and proportion of D1 now accounting for ~75% of the molecules with an average diffusion coefficient of 1 $\mu m^2/s$, while the slow diffusing population (0.15 $\mu m^2/s$) exhibited similar diffusion coefficients, but only accounted for 25% of the molecules. Remarkably, 4h post treatment, the diffusion coefficient and proportion of the more mobile NTH1-mEos4B molecules was very similar to that found in non-treated cells (0.72 $\mu m^2/s$ and ~60%), while the mean diffusion coefficient of the slow-diffusing fraction is markedly reduced to a value below 0.10 $\mu m^2/s$.

Altogether, this data provides strong evidence for a change in the dynamic behavior of NTH1-mEos4B in HeLa cells exposed to oxidative stress involving an increased mobility of a fraction of the molecules immediately after treatment, which may result from a potential dissociation of NTH1 molecules from the chromatin and their engagement in a 3D search for DNA lesions, followed by the appearance of a largely immobile population, which may correspond to NTH1 molecules tightly bound to their substrate lesions.

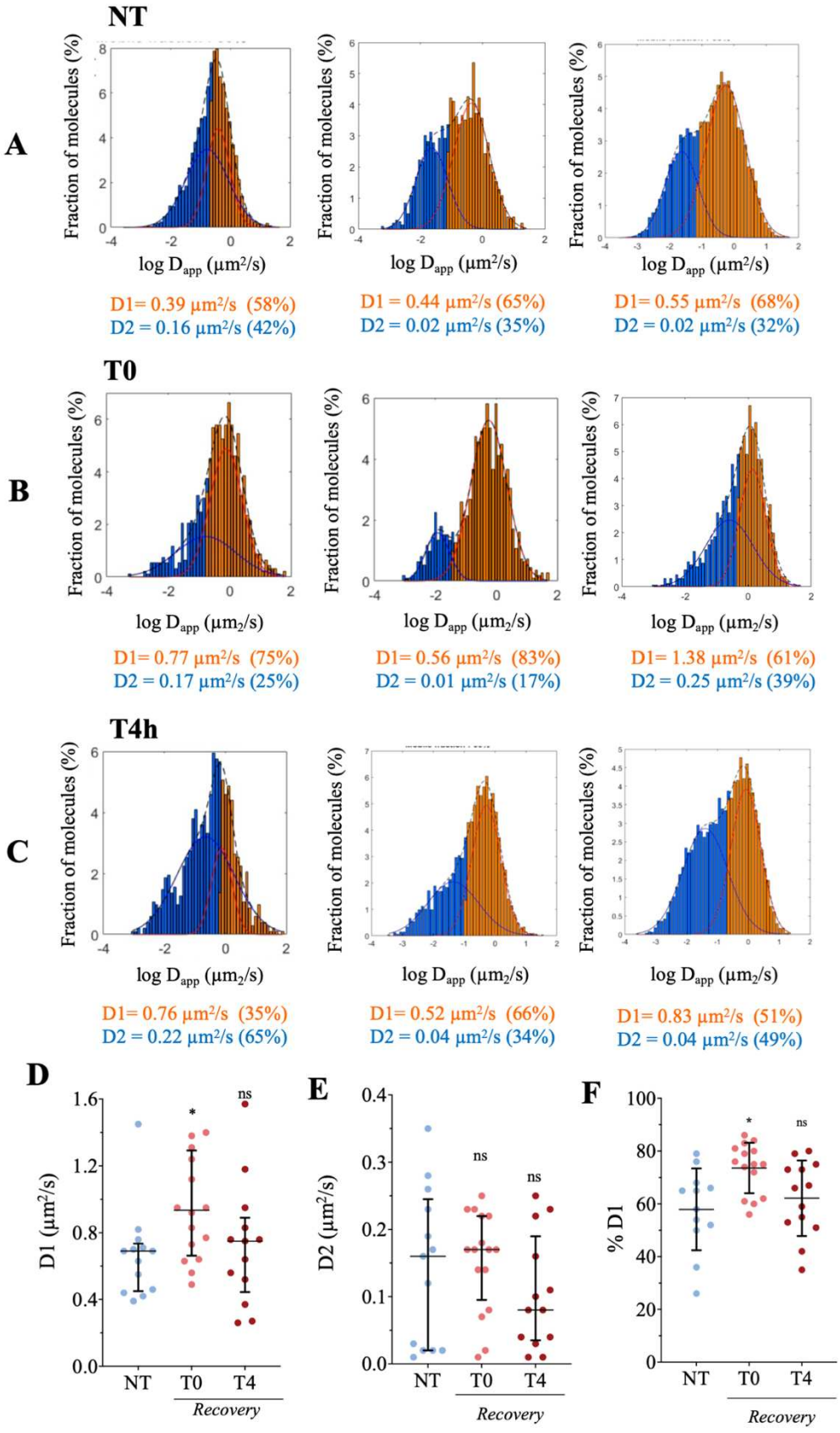


Figure 58: Apparent diffusion coefficient (D_{app}) histograms of NTH1-mEos4B measured in (A) NT, (B) T0 cells and (C) T4 cells.

*The x-axis plots the apparent diffusion coefficient in log scale vs fraction of molecules (%) in the y-axis. (D) Median D_{app} for fast moving NTH1-mEos4B molecules (D1) and (E) Median D_{app} for slow moving NTH1 molecules (D2). (F) the median percentage of fast moving (D1) NTH1-mEos4B molecules in NT cells (n = 12), T0 cells (n = 16) and T4 cells (n = 13 nuclei). Error bars represent the median and interquartile range. A one-way ANOVA analysis (Kruskal-Wallis) was performed on non-parametric data and significance was compared to the non-treated control cells (NT). The P values are indicated above each condition, where ns = non-significant, *P < 0.05.*

6.3 Integrating SPT simulations to elucidate NTH1 nuclear dynamics

To help us interpret the sptPALM data obtained for NTH1, we leveraged the single molecule simulating software, SMIS, to generate simulated trajectories under controlled conditions that mirror our experimental setup. This allowed us to account for critical parameters such as localization error, exposure time, and track length (tuned by laser power densities) and to build reference distributions for both Brownian and multi-state diffusion profiles. By directly comparing simulated and experimental NTH1 trajectories, we were able to validate our diffusion analysis pipeline, correct for technical biases, and start testing different mechanistic models distinguishing between freely diffusing, weakly- DNA bound and tightly DNA-bound populations, based on Stracy et al., 2021.

SMIS simulations were setup within a 3D virtual HeLa cell, were a 2D focal plane was considered. Here, diffusion of 5000 NTH1 molecules was measured across 1000 frames at a frametime of 10 ms, only within the nucleus. We applied similar imaging conditions to our experimental setup. The 405 nm laser and 488 nm laser were switched 'on' between frames to increase the rate of photoconversion and provide longer tracks. In order to validate our experimental data, we entered diffusion coefficients derived from our experimental data for the two NTH1 populations found within the nucleus. The obtained tracks were processed using the same pipeline as was used for the experimental data, yielding MJD and MSD distribution histograms (Figure 57 and 58) from which fractional populations and overall apparent diffusion coefficients could be derived.

The ground truth data described in figure 58 shows that we were able to successfully validate the presence of two NTH1 populations in the NT condition: 49% of fast-diffusing fraction moving at 0.66 $\mu m^2/s$ and 51% of slow-diffusing NTH1 fraction moving at 0.08 $\mu m^2/s$, with a MJD of 0.11 µm, recapitulates very well our experimental sptPALM data. Similarly, in the case of treated cells, the simulated data recapitulates well the data we obtained experimentally at T0: 49% of fast-diffusing NTH1 molecules were moving at 0.95 $\mu m^2/s$ whereas the slow-diffusing NTH1 fraction was moving at 0.18 $\mu m^2/s$.

These simulations bring further support for a model in which two NTH1 populations differing in their diffusion rates and MJD can co-exist in the nuclei of HeLa cells.

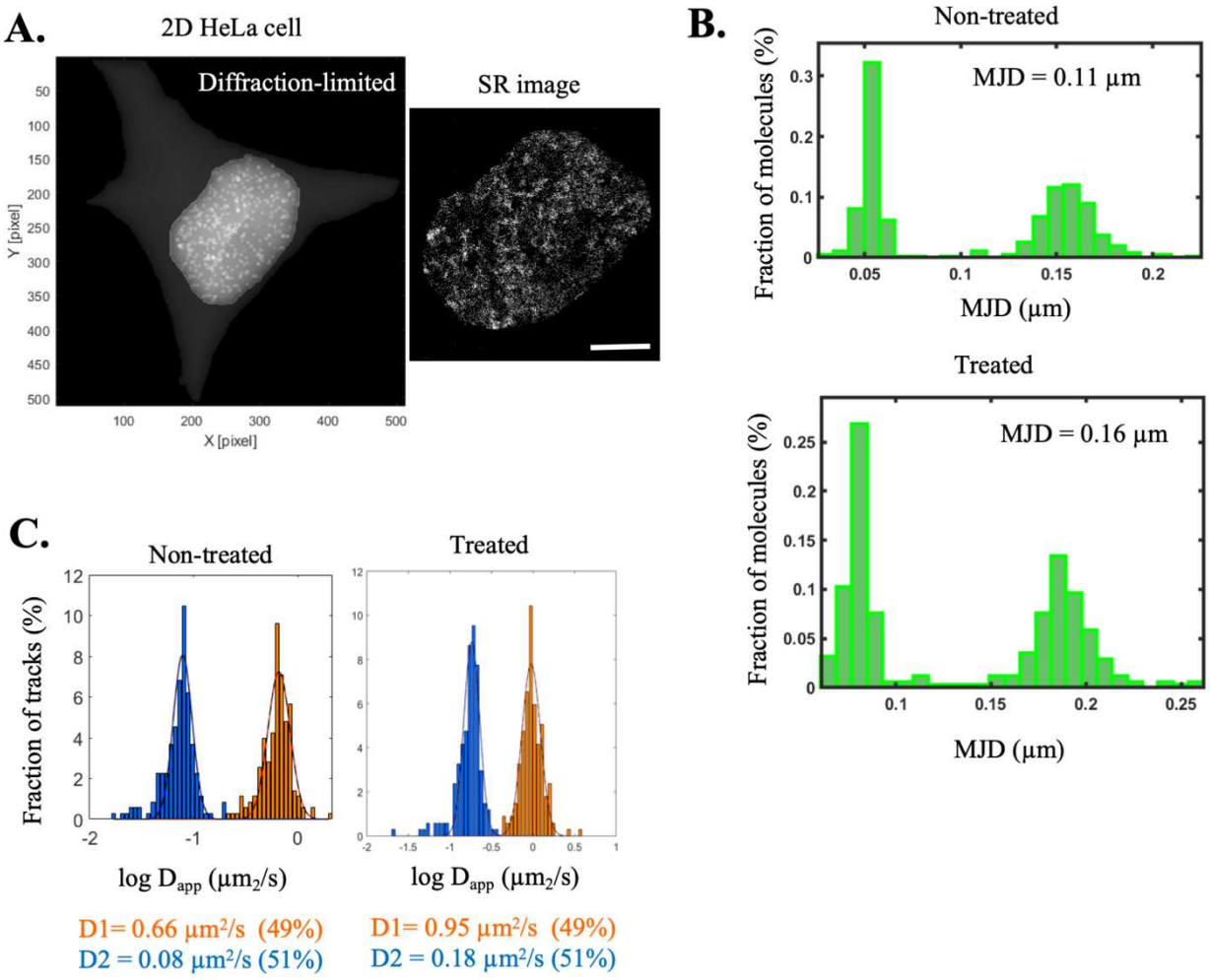


Figure 59: Ground-truth diffusion kinetics for NTH1 simulated in HeLa cell nuclei before and after $KBrO_3$ treatment.

(A) *Representative diffraction-limited image of a virtual 2D HeLa cell generated for simulating the diffusion kinetics of NTH1. A super-resolved image of the HeLa cell nucleus based on spt settings performed on SMIS. Scale = 5 µm.* (B) *The MJD histograms for non-treated and treated conditions with a mean MJD measured.* (C) *Apparent diffusion coefficient (D_{app}) measured from 2-fit Gaussian model of two simulated NTH1 populations in non-treated and treated conditions, based on input diffusion coefficient values. Here the number of molecules diffusing in each population is 50%.*

Closer inspection of our sptPALM data revealed NTH1 clusters consistent with confocal and dSTORM observations in fixed cells. Within these clusters, multiple overlapping trajectories were detected (Figure 62A), with diffusion coefficients ranging from 0.05–1 µm²/s, reflecting variable molecular density and dynamics. Trajectories located outside of clusters (Figure 62B) typically showed faster diffusion rates, indicating compartment-specific mobility and possibly confinement effects. Although further analysis was limited by time, detailed investigation of diffusion kinetics, residence times, and their changes under oxidative stress would provide valuable insight into NTH1 dynamics across nuclear compartments.

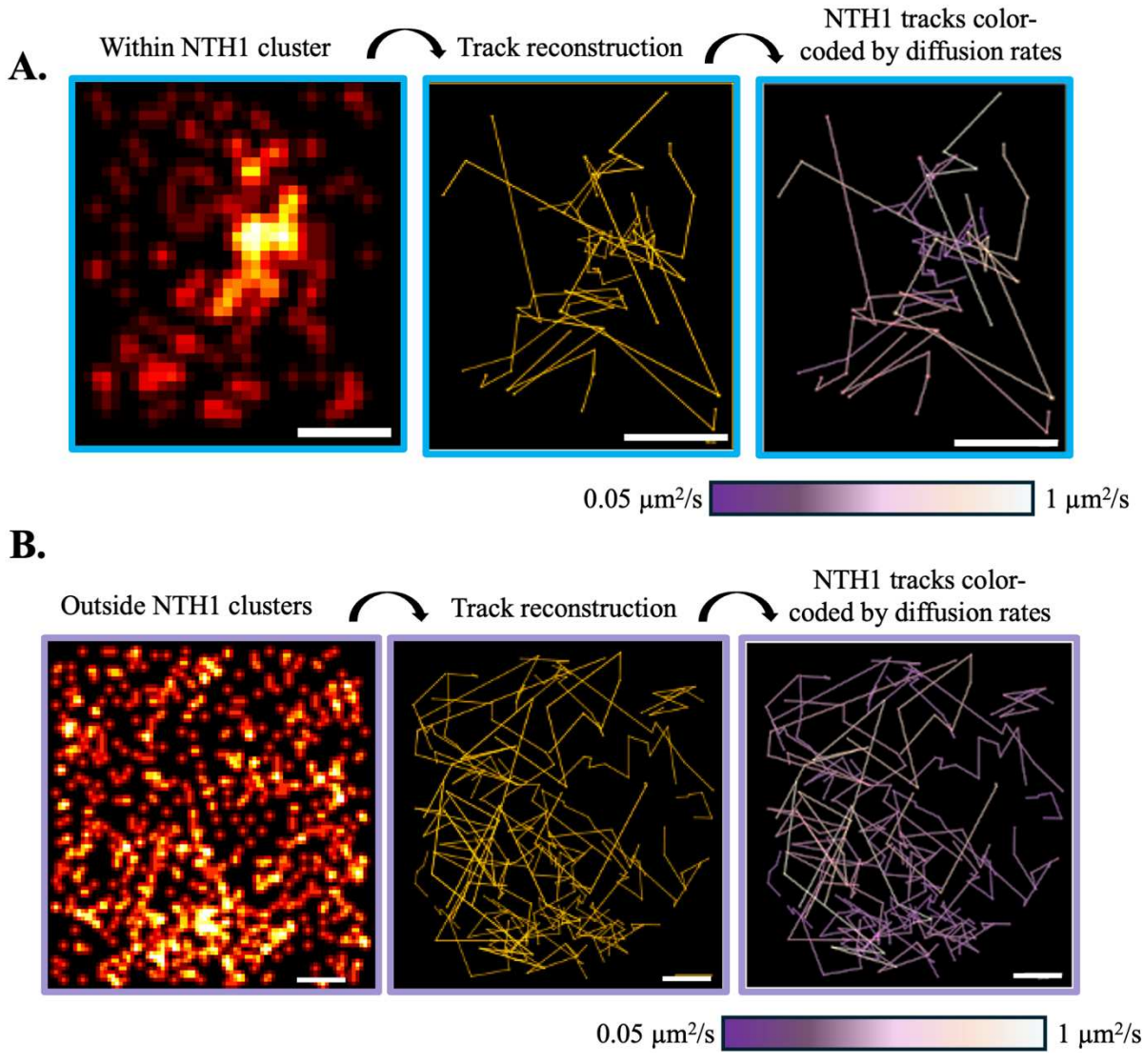


Figure 60: Preliminary attempt to reconstruct spt trajectories of diffusing NTH1 inside and outside NTH1 clusters.

Image panel displays the reconstructed single-molecule image of NTH1 measured in living cells. Scale = 2 µm. (A) The blue box highlights a representative NTH1 cluster and (B) the purple box shows a close of NTH1 localizations outside clusters and the. The nucleus is considered as the ROI (region of interest),

using the software SWIFT designed to reconstruct trajectories (yellow) observed within the nucleus. A close-up of the distribution of these tracks. Close up scale = 0.2 µm.

We have already performed a few trials of sptPALM simulations using the software SMIS, to verify and correctly interpret our experimental spt data. This very helpful tool offers the possibility of designing experiments within a virtual 3D HeLa nucleus, to avoid the limitations of motion blur, confinement and short tracks, frequently problematic when dealing with 2D sptPALM data. Additionally, SMIS allows us to virtually create multiple diffusion states with defined exchange rates, comparable to assigning different cellular compartments and follow the exchange of molecules between each compartment (Bourgeois, 2023). Beyond the simulations presented in the results section, we also attempted to simulate NTH1 dynamics in a virtual HeLa cell with two compartments: the nucleoplasm and 300–400 clusters (diameter set to ~120 nm) per nucleus. Both compartments contained fast- and slow-diffusing NTH1, assumed to exchange equally. The simulations produced histograms that qualitatively resembled more our experimental data (with poorly separated populations of NTH1 molecules), probably because this simulation allowed for exchange between the slow and fast-diffusing populations (Figure 61A). However, the derived mobility characteristics (MJD and apparent diffusion coefficients from MSD analysis) were much less consistent with our experimental data. The MJD showed a slight MJD peak shift (~0.12 → 0.14 µm) and decreased diffusion rates (D_1 = 0.37, D_2 = 0.34 µm²/s) in non-treated cells, while only one population (0.54 µm²/s) appeared after treatment (Figure 61B). High exchange rates and the distribution of both slow and fast-diffusing molecules in both compartments may be the cause of these discrepancies. This suggests we still need to refine the model to better recapitulate our experimental data.

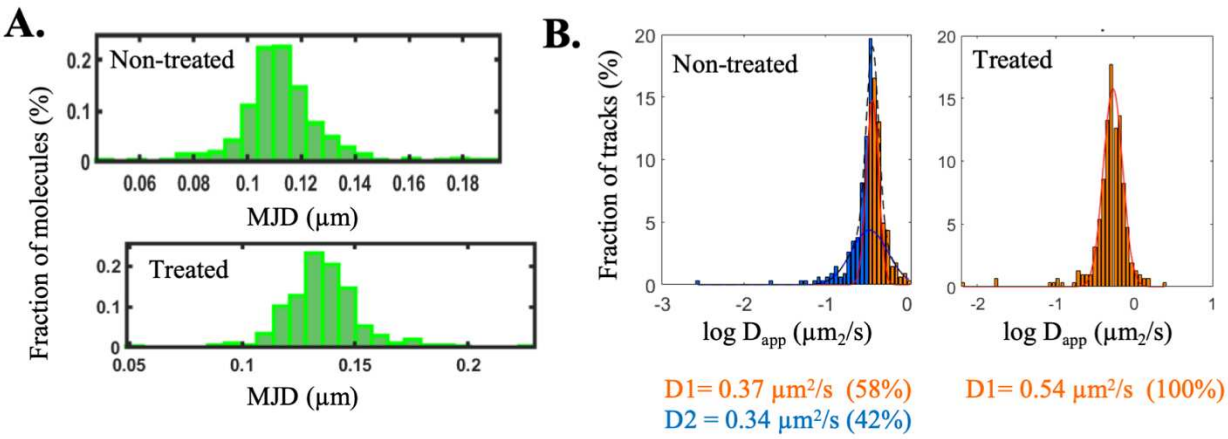


Figure 61: Exchange rates between two diffusing NTH1 populations
(A) MJD histograms show the fraction of NTH1 molecules travelling between the nucleus and NTH1 clusters. (B) Apparent diffusion coefficient (D_{app}) extracted from 2-fit Gaussian model describes the fraction of tracks for two NTH1 populations; D1 and D2 respectively, in a simulated non-treated cell and a cell treated with 40 mM $KBrO_3$ for 0.5h.

However, simulations have limitations too, as they cannot fully replicate experimental complexity or environmental effects. Despite these constraints, simulations remain a powerful tool to test model accuracy, refine photophysical models, improve analysis pipelines, and guide the interpretation of experimental data. For instance, in the future, simulations could be used to define parameters best suited for quantitative PALM (qPALM) on molecular counting.

DISCUSSION & PERSPECTIVES

DISCUSSION

The first objective of my PhD was to establish the nuclear distribution of endogenous NTH1 in HeLa cells using a combination of 3D confocal imaging and 2D dSTORM to achieve the highest spatial and temporal resolution. Our 3D confocal images performed on NTH1 immunolabelled cells reveals that endogenous NTH1 forms heterogeneously distributed foci within the nucleus of HeLa cells. These foci were further analyzed by fractionating the cells with mild detergent treatment prior to fixation to separate chromatin-associated from soluble nucleoplasmic NTH1 fractions. While the total NTH1 signal drops by about 50% after fractionation, the foci remain visible. These results suggest for the first time that nuclear NTH1 can be found in two populations: (i) a chromatin-associated fraction forming foci that may represent chromatin nanodomains or biocondensates, where BER DNA repair takes place and (ii) a more sparsely distributed soluble nucleoplasmic fraction. Each of these populations are in equal proportion in the nucleus. The chromatin-bound punctate foci contrast with the uniform nuclear distribution previously reported for overexpressed NTH1 tagged with eGFP (Luna et al., 2000; Campalans et al., 2007).

We next concentrated our effort on the characterization of the chromatin-associated forms of NTH1, working on fractionated cells. We obtained reconstructed dSTORM images that provide the first nanoscale cartography of NTH1 (<10 nm of resolution), confirming the existence of at least two forms of NTH1, one distributed sparsely throughout the nucleus and another organized into NTH1 clusters. We used different computational tools to further analyze our NTH1 foci and clusters. Our analysis of IMARIS-segmented foci, summarized in table 14, reveals an average of ~ 230 discrete foci per nucleus in non treated HeLa cells, each with an average surface area of 0.2 µm² and regular circular morphology. This indicates a non-random organization of endogenous NTH1 within the nuclear environment.

Table 14: Summary of NTH1 foci characteristics. Highlighted in bold italic red are low values and in bold italic green are high values for each parameter.

Foci characteristics								
Parameter	**Description**	**Non-treated**	**Immediately after $KBrO_3$**	**Early recovery**	**Intermediate recovery**			**Late recovery**
			T0	**T0.25 h**	**T0.5 h**	**T1 h**	**T4 h**	**T8 h**
Number of foci per nucleus	Average total foci detected	227 ± 6.9	129 ± 53	130 ± 52	***97 ± 49***	127 ± 78	***276 ± 68***	240 ± 55
Foci per nuclear area (foci/µm²)	Density of foci across nuclear surface	0.85 ± 0.052	0.59 ± 0.22	0.59 ± 0.27	***0.36 ± 0.16***	0.42 ± 0.22	***0.99 ± 0.11***	0.87 ± 0.080
Mean foci surface area (µm²)	Average size of foci	0.22 ± 0.11	***0.16 ± 0.076***	0.20 ± 0.091	0.17 ± .072	0.18 ± 0.082	***0.25 ± 0.13***	0.23 ± 0.11
Mean foci fluorescence (a.u)	Average foci fluorescence intensity	3493 ± 1009	***2252 ± 832***	3020 ± 1359	2380 ± 482	2664 ± 1371	***5923 ± 1907***	4600 ± 1369
Foci circularity	Average regularity of foci	0.82 ± 0.13	0.83 ± 0.13	***0.85 ± 0.12***	0.78 ± 0.14	0.83 ± 0.13	***0.76 ± 0.14***	0.80 ± 0.14

We then implemented Voronoi tessellation to analyze NTH1 clustering in our dSTORM data (Levet et al., 2015; Levet, 2023). Each foci was estimated to contain on average two clusters, with a total of ~400 clusters per nucleus with an average surface area of 0.005 µm² (Table 15). Clusters varied in density, with medium/high-density clusters making up 50% and low-density clusters the remaining 50% in fractionated cells. Figure 62A provides a schematic of NTH1 spatial organization within HeLa cell nuclei.

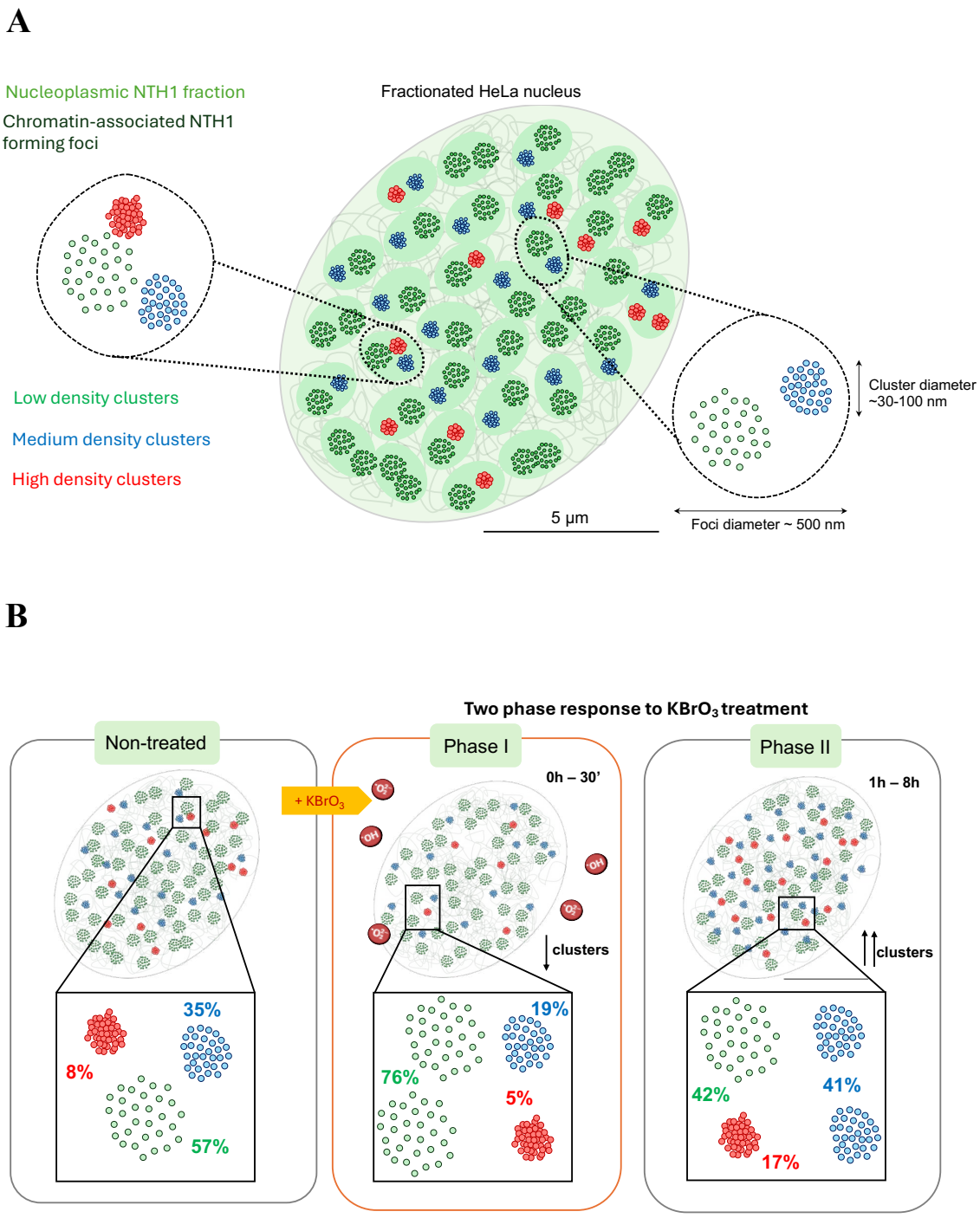


Figure 62: Illustration of the nuclear organization and distribution of endogenous NTH1 changes in the distribution and composition of NTH1 clusters in response to oxidative stress.

(A) In a HeLa nucleus, two fractions of NTH1 have been identified: a nucleoplasmic fraction (light green) and a chromatin-associated fraction (green). Chromatin-associated NTH1 fraction is composed of NTH1 foci (~ 500 nm) heterogeneously distributed throughout the nuclear space. Further resolving these NTH1 foci revealed that they are composed of 2 or clusters of NTH1 molecules (~30-100 nm). These clusters are sparse and dense in nature, distributed hetergeneously throughout the nuclear space. (B) Image panels represent the evolution of the distribution of NTH1 clusters based on their density, before (non-treated) and in response to $KBrO_3$ treatment. A two phase response to $KBrO_3$ treatment was observed – phase I (0h-30') follows a global decrease in number of clusters and in phase II (1h-8h), we observed a subsequent increase in number of medium and high density clusters. Low density clusters are indicated in green dots/ circles, medium density clusters are indicated in blue dots/ circles and high density clusters are indicated in red dots/ circles, with corresponding percentage in each condition.

Table 15: Summary of NTH1 cluster characteristics. Highlighted in bold red are low values and in bold italised green are high values for each parameter.

Cluster characteristics							
Parameter	**Description**	**Non-treated**	**Immediately after $KBrO_3$**	**Early recovery**	**Intermediate recovery**		**Late recovery**
			T0	**T0.25 h**	**T1 h**	**T4 h**	**T8 h**
Number of clusters per nucleus	Average total clusters detected	432 ± 147	374 ± 229	***263 ± 65***	322 ± 66	520 ± 109	***758 ± 42***
Clusters per nuclear area (clusters/µm²)	Density of clusters across nuclear surface	1.9 ± 0.54	2.3 ± 1.7	***1 ± 0.31***	1.4 ± 0.32	2.4 ± 0.88	***2.5 ± 1.1***
Mean cluster surface area (nm²)	Average surface area per cluster	4574 ± 1177	***6976 ± 2030***	4276 ± 1744	4298 ± 2004	4176 ± 1141	***3187 ± 636***
Mean cluster diameter (nm)	Estimated lateral dimension	92 ±13	***113 ± 20***	89 ± 20	94 ± 22	90 ± 7.6	***78 ± 8.2***
Mean number of NTH1 localizations / cluster	Average number of localizations	150 ± 84	176 ± 138	***51 ± 14***	72 ± 24	155 ± 42	***190 ± 87***
Cluster circularity	Average regularity of foci	0.67 ± 0.044	0.63 ± 0.037	0.62 ± 0.014	***0.61 ± 0.033***	0.64 ± 0.0085	***0.65 ± 0.014***

While these results clearly demonstrate that endogenous NTH1 forms discrete and non-randomly organized clusters within the nucleus, the functional significance of these structures remains an open question. In particular, it is unclear what biological role NTH1 clusters serve and how their formation contributes to the efficiency, regulation, or coordination of base excision repair *in vivo*. One possibility is that these clusters correspond to specialized repair hubs or chromatin nanodomains that locally concentrate BER factors, thereby facilitating efficient lesion recognition and processing. Alternatively, NTH1 clustering may reflect transient sequestration or regulatory storage of the enzyme, or arise from chromatin-dependent constraints on NTH1 mobility within the nuclear environment. Elucidating the functional purpose of these NTH1 clusters therefore emerges as one of the next steps towards understanding how spatial organization contributes to NTH1-mediated repair of oxidative DNA damage.

The second objective of my PhD was to explore the changes in the distribution of chromatin-associated NTH1 in response to oxidative stress using 3D confocal imaging and 2D dSTORM. We conducted a first set of experiments to find the best oxidizing agent to observe a redistribution of NTH1 after oxidative stress. We first treated HeLa cells with cisplatin, but these experiments gave inconclusive results due to either technical issues or to the limited oxidizing strength of cisplatin that was perhaps insufficient to induce a clear BER response.

Subsequently, we subjected the HeLa cells to two potent oxidizing agents, namely H_2O_2 or $KBrO_3$, which are well-known to induce the recruitment of OGG1 DNA glycosylase to chromatin. For both of these agents, our 3D confocal images confirmed an increase of NTH1 association with chromatin after treatment. We decided to pursue working with the strongest oxidizing agent, i.e. $KBrO_3$, also because several recent studies conducted on another BER DNA glycosylase, OGG1, had made use of this oxidizing agent (Campalans et al., 2005; Amouroux et al., 2010; Lebraud et al., 2020). To facilitate comparison with these earlier studies, we therefore implemented a similar framework to investigate the recruitment of NTH1 to chromatin. Segmentation of 3D confocal images and dSTORM images allowed us to follow the spatial and temporal evolution of the foci and clusters (tables 14 and 15). We noticed a similar trend for all the analyzed parameters involving a two-phase response. First, immediately after exposure to oxidative stress, chromatin-associated levels of NTH1 as well as the total number of NTH1 foci and clusters per nucleus were found to decrease. Second, between 4 and 8h post-treatment, chromatin-associated levels of NTH1 along with the number and density of NTH1 foci and clusters increased significantly, suggesting a major re-organization of NTH1 in response to oxidative DNA damage (Figure 62B), resulting in its recruitment to defined nuclear foci, which we speculate may be sites of DNA damage.

This biphasic behavior suggests that NTH1 clusters are functionally regulated, damage-responsive assemblies: the early reduction in cluster number and density may reflect transient cluster

disassembly that enhances NTH1 mobility and facilitates a genome-wide search for oxidative lesions, while the later enrichment of medium- and high-density clusters may correspond to the stabilization of NTH1 at selected chromatin sites undergoing active repair. Together, these observations support a speculative model in which NTH1 clusters dynamically balance rapid lesion detection with localized concentration of repair activity during base excision repair.

Besides clusters, NTH1 molecules were also found sparsely distributed in the nucleoplasm. The dispersed molecules may serve as a reservoir of DNA repair factors. Interestingly, the balance between nucleoplasmic and clustered NTH1 changed markedly after oxidative stress: 74% of localizations were outside clusters just after $KBrO_3$ treatment, compared to 59% in untreated cells, suggesting that NTH1 molecules may have been released from existing clusters, possibly as a result of local re-organization of the chromatin induced by oxidative DNA damage (García Fernández et al., 2025). In addition, during recovery, clustered NTH1 increased steadily between T0.25h and T8h, indicating dynamic exchange between diffusive and chromatin-associated states or the synthesis of new protein.

The fact that our assesssment of NTH1 clusters relies on data originating from immunolabelling of NTH1 constitutes a limitation to perform a more quantitative evaluation of the exact compositions of NTH1 clusters. Our data provides precise information on the number of NTH1 localizations in nuclei and in clusters, but converting this value to the number of NTH1 molecules is far from being straight forward. This indeed depends on the labelling density, fluorescence lifetime and reactivation cycles of the fluorophore, and a single molecule may account for multiple localizations close to the true localization precision, as highlighted by the work of Varga et al., 2019 on γH2AX. To achieve reliable molecule quantification, dSTORM could be combined with calibration-based approaches such as using DNA origami standards or endogenous reference proteins of known stoichiometry to correct for labeling efficiency and fluorophore reactivation. Additionally, applying photophysical correction models or Bayesian cluster analysis would help estimate the true number of NTH1 molecules per cluster. Together, these quantitative strategies would overcome current limitations of immunolabeling and allow a more accurate assessment of NTH1 organization at the nanoscale.

Additionally, our dSTORM data is limited to a 2D XY plane. In the future, extending our NTH1 cluster analysis to 3D dSTORM would enable quantitative characterization of cluster structure, distribution, and composition within the nuclear volume.

Another major limitation in the field of BER is the lack of suitable tools to induce site-specific oxidative DNA damage. Indeed, $KBrO_3$ induces random oxidative base lesions throughout the genome, but their exact nature, amount, and locations remain unknown. Consequently, it is unclear whether NTH1 clusters mark sites of oxidative DNA damage. To address this, we are collaborating with *Dr. Jean-Luc Ravanat's lab (CEA, Grenoble)* to characterize the nature and abundance of oxidized bases formed in HeLa cells after a 0.5 h treatment with 40 mM $KBrO_3$. This will also allow monitoring of

lesion repair kinetics and correlating them with NTH1 redistribution. Comparing these kinetics in NTH1 KO cells will further clarify NTH1's role in the repair process. In the future, the use of molecular tools such as CRISPR-fused ROS producing enzymes such as KillerRed or D-amino acid oxidase (DAAO) that generates H_2O_2 (Van Soest et al., 2024) locally upon D-alanine addition guided to specific genomic loci by suitable guide RNAs, will enable to assess NTH1 distribution and dynamics in specific chromatin contexts for instance, providing key insight into the influence of chromatin organization on the function and dynamics of DNA glycosylases.

Indeed, *in vivo* factors such as chromatin compaction, molecular crowding and DNA accessibility strongly influence diffusion and lesion recognition, as demonstrated in FRAP and live-cell imaging of hOGG1, rapidly accumulating at sites of DNA damage induced by intense laser light treatment (D'Augustin et al., 2020, 2023). By measuring the kinetics of recruitment and residence times at repair sites, it is possible to gain insight into the kinetics of assembly/disassembly of repair complexes in heterogeneous nuclear environments (Schaich & Van Houten, 2021). Performing such experiments on NTH1 would also be very insightful.

Changes in the NTH1 distribution observed in confocal and dSTORM imaging support a dynamic behavior of NTH1. **The third objective of my PhD** was to investigate the dynamics of NTH1 at the single-molecule level using sptPALM, before and after exposure to oxidative stress. We followed the trajectories of single molecules of NTH1 fused to mEos4B in non-treated cells and in T0 and T4h post $KBrO_3$ treatment. In NT cells, analysis of the apparent diffusion coefficients of NTH1-mEos4B molecules, revealed two populations: a slow diffusing population with a diffusion coefficient (D2) of 0.13 $\mu m^2/s$ representing ~40% of the molecules, likely chromatin-bound, and a faster diffusing population (D1) exhibiting an average apparent diffusion coefficient of 0.67 $\mu m^2/s$ representing ~60% of the molecules, which may correspond to either transiently bound or freely diffusing NTH1 in the nucleoplasm. A summary of our findings is presented in table 16. After treatment with $KBrO_3$, we observed that both populations evolved differently, with an increase of the percentage of D1 populations, together with an increase of its diffusion coefficient immediately after treatment (T0), while the D2 population remained stable (Figure 63). 4h post treatment, however, the apparent diffusion coefficient of D1 returned to its basal level and in contrast, the slower population (D2) showed a reduced apparent diffusion coefficient. We did however observe a large cell-to-cell variability in our data, so interpretation of these current results should be done with caution, and additional experiments should be performed to consolidate these findings. These results nonetheless indicate that NTH1 changes its diffusion behavior in response to oxidative stress, reflecting transitions between transient and stable chromatin binding states. Incorporating additional intermediate recovery time points would provide a better understanding of the changes in mobility of NTH1 molecules induced by oxidative stress. Our results globally align with earlier observations on DNA repair factors, such as OGG1, and TDG which have been studied using various techniques and have been shown to engage in multiple diffusion modes (Blainey, Van

Oijen, et al., 2006 ; Miné-Hattab et al., 2021 ; D'Augustin et al., 2023 ; Heyza et al., 2023 ; Schnable et al., 2024).

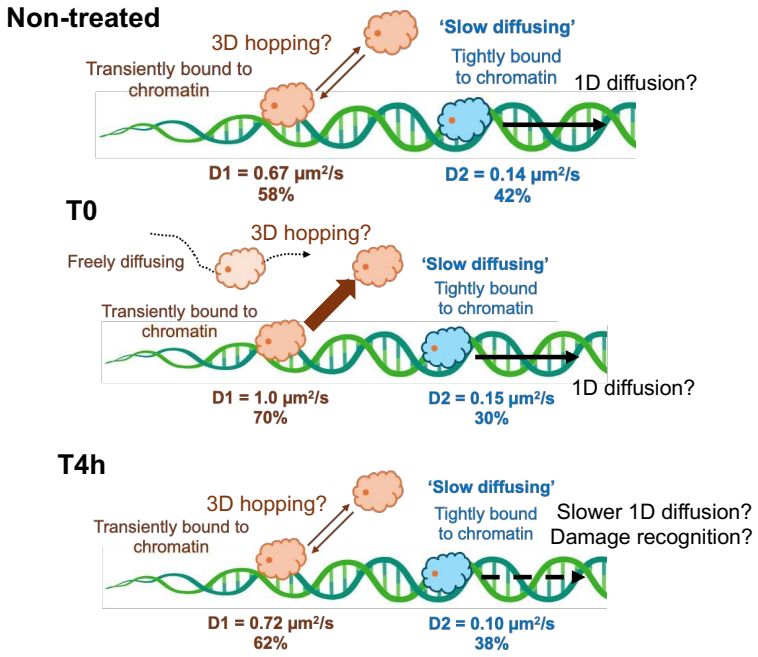


Figure 63: Schematic illustration of diffusion properties of NTH1 in non-treated and $KBrO_3$ treated cells.

Non-treated HeLa cells exhibit equal proportions of slow (blue) and fast-diffusing (orange) NTH1 molecules, exibiting a possible 1D diffusion and 3D hopping diffusion mechanism, respectively. Upon treatment with 40 mM KBrO3 for 0.5h, there is a 30% increase in the proportion of fast-diffusing NTH1 population (orange) and an increased apparent diffusion coefficient, suggesting a freely diffusing population of NTH1, transiently activating a search mode to detect oxidative DNA lesions within the genome. At 4h post treatment, the search mode appears to be over and instead we observe the accumulation of largely immobile NTH1 molecules (blue) which may correspond to sites of DNA repair.

Table 16: Summary of sptPALM data recorded for NTH1 molecules in HeLa nuclei before and after exposure to $KBrO_3$.

Highlighted in bold red are low values and in bold italised green are high values for each parameter.

Diffusion kinetics of NTH1			
Parameters	**NT**	**Early recovery**	**Late recovery**
		T0	**T4h**
No. of localizations per nucleus	***83985 ± 54373***	***49418 ± 28779***	79669 ± 47134
No. of localizations/ μm^2 nuclear area	***317 ± 146***	***175 ± 129***	224 ± 140
Total no. of tracks	***341315***	***242546***	275342
% of tracks > 4	***30.3 ± 14.7***	***27.9 ± 7.6***	28.3 ± 8.4
Mean MJD	***0.13 ± 0.013***	***0.15 ± 0.024***	0.13 ± 0.031
Average rate of fast - diffusing molecules ($\mu m^2/s$)	***0.67 ± 0.27***	***1.0 ± 0.40***	0.72 ± 0.37
Average rate of slow-diffusing molecules ($\mu m^2/s$)	0.14 ± 0.12	***0.15 ± 0.074***	***0.10 ± 0.085***
Mean % of fast - diffusing molecules	***58 ± 16***	***74 ± 9.5***	62 ± 14
Mean % of slow-diffusing molecules	***42 ± 16***	***30 ± 16***	39 ± 15

Single-particle tracking PALM has provided crucial first evidence to the unique diffusion dynamics of individual NTH1 molecules. It is important to note that, in our experiments, single particle tracking came with many technical and biological limitations:

(i) Since we use live cells for tracking, cells can be at different phases of the cell cycle which might slightly effect the diffusion rates of NTH1. This is observed with cell-to-cell variability in the diffusion kinetics in normal HeLa cells, described in figure 57 and 58.

(ii) The HeLa cell line used in our spt experiments showed low traces of endogenous NTH1 protein levels (Figure 50). The influence of the endogenous protein levels may result in discrepancies with MJD and diffusion rates. Therefore, tracking of NTH1 would be confirmed with the use of transfected NTH1 knockout (KO) HeLa cell lines, already present in the lab and currently being tested.

(iii) For our spt experiments, we imaged cells in 2D. This creates localization precision errors and motion blur due to the limitation of imaging in one focal plane. Molecules constantly diffuse in and out of the focal plane which causes shorter trajectories.

(iv) Within the nucleus, exists a crowded environment, causing confinement of the molecule. Trajectories shorten due to obstacles or nuclear boundaries and do not provide a true trajectory of the protein.

To partially compensate for limitations (iii) and (iv), we manually supplied a low power density of 405 nm laser and a constant low power density of 488 nm laser to increase tracklengths (**see Materials and Methods**).

Performing sptPALM-PAINT experiments on live HeLa cells expressing NTH1-mEos4B and labelled with Si-Hoeschst dye, would also help correlate NTH1 dynamics with chromatin structure.

CONCLUSION

Altogether, this work demonstrates the complex and heterogeneous nuclear distribution and dynamics of NTH1 and how these are modulated in response to oxidative stress. Figure 64 illustrates a comprehensive summary of our findings. For the first time, we discovered two fractions of NTH1 – a soluble nucleoplasmic and a chromatin associated fraction. Our spt PALM data suggests that the nucleoplasmic fraction is more mobile than the chromatin associated one. The chromatin associated one can be transiently or tightly bound to chromatin depending on the diffusion coefficients. Our dSTORM data reveals that this NTH1 population consists of accumulated NTH1 localizations forming clusters at different densities. In response to oxidative stress induced by potassium bromate, NTH1 exhibits a two-phase response. During the early recovery stage, reduced cluster number and increased diffusion of transiently bound chromatin fraction suggests a release of NTH1 from chromatin and possibly chromatin remodelling at sites of DNA damage while NTH1 undergoes 3D diffusion in search for its substrates. During the late recovery stage, we observed an increase in medium and high-density clusters comprising a tight chromatin bound fraction of NTH1 with decreased mobility. This suggests a recruitment of NTH1 to sites of oxidative damage on chromatin, initiating repair. Longer recovery time points could provide answers on whether NTH1 returns to distribution levels observed in non-treated cells suggesting completion of the repair process.

Using complementary imaging strategies across different resolution scales will be key to further explore NTH1 organization and dynamics. High-resolution live-cell imaging has been used to show that chromatin loci undergo constrained local diffusion within ~1 µm, enabling regulated molecular interactions. Techniques like MINFLUX single-particle tracking (Mazzocca et al., 2025) extend temporal resolution from microseconds to seconds, revealing subdiffusive chromatin motion (~300–500 nm) that limits long-range interactions. Furthermore, incorporating *in vitro* optical tweezers can further probe NTH1–chromatin interactions by applying precise mechanical forces to measure binding strength and dynamic responses at the single-molecule level (Schaich et al., 2024). Together with advanced

super-resolution microscopy, improved labeling, and computational modeling, these approaches will enable a multi-scale understanding of NTH1 dynamics in relation to chromatin organization, DNA repair, and nuclear function.

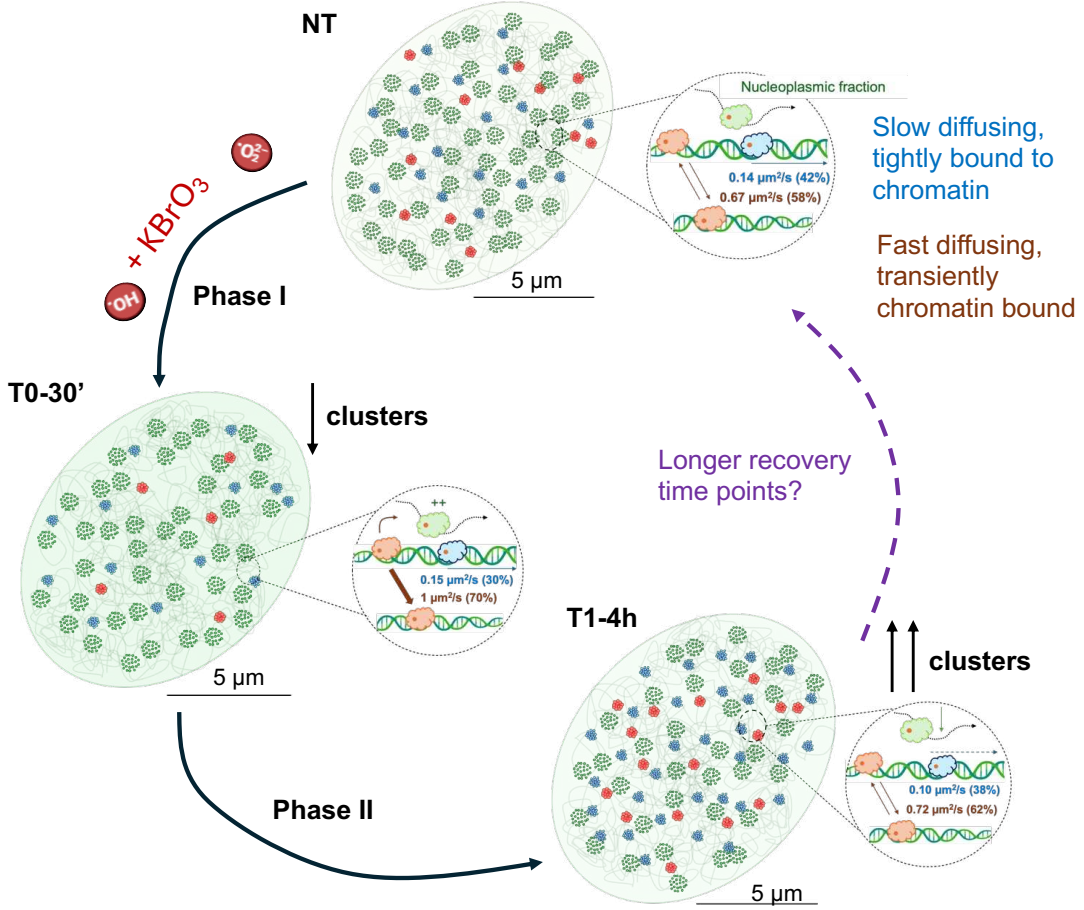


Figure 64: Illustration of our findings on the nuclear distribution and dynamics of NTH1 before and after oxidative stress.

Our work has contributed to fundamental and translational research aimed at gaining new insights into the spatial and temporal distribution and dynamics of NTH1. We have shown that the balance between the different populations of NTH1 is altered in response to oxidative stress, in favor of NTH1 chromatin-bound foci. These findings provide substantial evidence for the tight spatial and temporal regulation of NTH1, and more broadly, BER activity, in cells, paving the way for new research and therapeutic opportunities, notably in the context of cancer. Comparing the detailed cartography of nuclear NTH1 in various tumor types, in both drug-resistant and -sensitive cells, before and after exposure to oxidative stress or chemotherapeutic agents, may allow us to identify characteristic NTH1 molecular signatures that may be used for prognostic or diagnostic purposes. Coupled with the analysis of the dynamics of NTH1 in such cells, these studies will provide valuable information regarding the involvement of the BER pathway in cancer etiology and in the cellular response of cells to anti-cancer drugs, that could guide the use and design of personalized therapy.

FUTURE PERSPECTIVES

From this work, we established a spatiotemporal cartography of the nuclear distribution and dynamics of NTH1 in isolation within HeLa cells. However, within the highly crowded and heterogeneous nuclear environment, DNA repair is orchestrated through the coordinated actions of multiple repair factors, on different chromatin states. Future studies would therefore benefit from elucidating how the existence of these NTH1 clusters functionally and dynamically interacts with other components of the base excision repair (BER) pathway, as well as how its repair activity is modulated by chromatin organization and accessibility. Addressing these questions, both in the presence and absence of DNA damage, will be essential for a more comprehensive understanding of oxidative DNA damage repair *in vivo*.

1. NTH1 in the context of BER partners

Following the distribution and dynamics of other BER factors together with those of NTH1 will help establish an integrated cartography of BER pathway activation in response to oxidative stress. Initial experiments were performed in that sense during my thesis. We notably compared the spatial distribution of NTH1 with that of APE1, a key BER AP endonuclease responsible for cleaving abasic sites generated following base excision (Krokan & Bjoras, 2013). It is interesting to note that, although both proteins are thought to act sequentially in the BER pathway, we observed little to no spatial overlap (colocalization) between NTH1 and APE1, either in non-treated (NT) conditions or following oxidative stress induced by $KBrO_3$ treatment (Figure 65A).

Quantitative analysis (Figure 65B) showed that APE1 levels slightly increased immediately after treatment (T0; ~1500 a.u.) but dropped ~2-fold by T1h (~750 a.u.) and remained low, with only a modest rise at T4h (~1000 a.u.). Spatially, APE1 formed punctate foci at T1h that decreased by T4h, appearing independent of NTH1 clusters (Figure 65C). These results suggest transient, spatially segregated redistribution of APE1 in response to oxidative stress, indicating distinct temporal phases from NTH1 during BER. Early intensity increases at T0 may reflect immediate engagement post-damage. As APE1 is also involved in the redox regulation of transcription factors involved in cellular proliferation, stress response and inflammation (Chaudhari et al., 2021; Gautam et al., 2023; Kladova et al., 2018), our results may reveal its dual functions. Higher temporal resolution or live-cell imaging could help clarify the sequential recruitment and interplay between NTH1 and APE1.

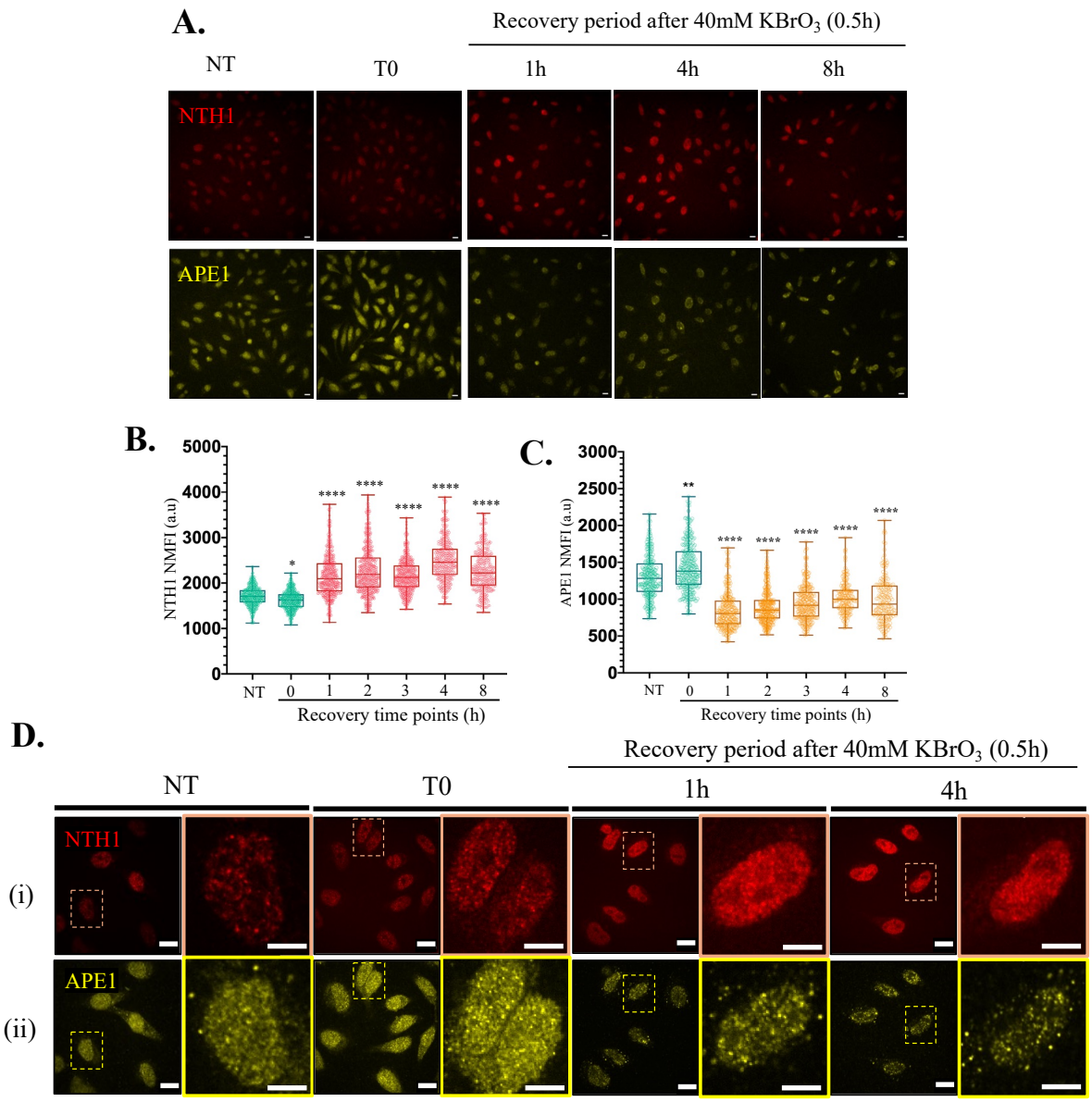


Figure 65: Co-immunofluorescence of NTH1 and APE1 before and after $KBrO_3$ treatment.
*(A) Confocal images of NTH1 and APE1 labelling after $KBrO_3$ treatment. Here, NT = Non – treated; T represents cells treated with 40mM $KBrO_3$ for 0.5h. Cells were allowed to recover in DMEM at indicated recovery time points before fractionation with CSK to remove soluble protein fraction. Scale bar: 10 µm. (B) Nuclear mean fluorescence intensities (NMFI) of NTH1 and APE1 respectively observed for 250 cells. A one-way ANOVA test (Kruskal-Wallis) test was perfomed on non-parametric data and significance was measured with *P < 0.05 , ****P < 0.001, compared to NT. (C) Representative immunolfuorescence images show the redistribution of NTH1 (i) and APE1 (ii) after 1h and 4h of recovery from $KBrO_3$ treatment in HeLa cells. Scale = 10 µm. Cells magnified in corresponding conditions show the redistribution of NTH1 (i) and APE1 (ii) foci for a single-cell. Scale = 5 µm.*

To further investigate the nuclear dynamics and distribution of NTH1 upon exposure to oxidative stress, future studies using targeted DNA damage induction (e.g., laser microirradiation or CRISPR-guided ROS production) and other live-cell single-molecule imaging (eg. MINFLUX), which allow to reach 1 to 3 nm spatial resolution could be used. In parallel, multi-color super-resolution imaging or proximity-based assays could determine whether clusters recruit other BER factors, while functional perturbation through NTH1 mutants or chromatin modification could reveal whether clustering is necessary for efficient oxidative lesion repair. Together, such approaches will be crucial for understanding how NTH1 clusters integrate within the larger BER network and contribute to the spatial and temporal coordination and regulation of BER *in vivo*.

2. NTH1 in the context of chromatin

It is important to highlight how our work opens new perspectives for studying NTH1 within the context of chromatin. Understanding how NTH1 is distributed across different chromatin compartments is one of the central questions that arises from our data. While dSTORM allowed us to resolve NTH1 in nanoscale clusters, we still don't know how these clusters relate to higher-order chromatin features. This could be tested by performing colocalization experiments with cohesin, which organizes chromatin loops, or by dual colour dSTORM imaging of NTH1 together with histone markers or DNA labelling dyes.

We performed a preliminary investigation of the nuclear organization of NTH1 relative to chromatin by first examining the global distribution of Histone H3 in non-fractionated HeLa cells, building on previous super-resolution studies of its variants H3.1 and H3.3 (Clément et al., 2018). We implemented two-colour dSTORM to resolve NTH1 and H3 at the single-molecule level and optimized our immunolabelling procedure using a mouse polyclonal anti-H3 antibody recognized by an Alexa Fluor 568-coupled secondary antibody for confocal microscopy or an CF680 or CF568-coupled secondary antibody for dSTORM, (Figure 66A-B). We have tested both sequential labelling for the conditions NTH1 with F(ab')2 647 coupled secondary antibody and H3 with CF568-coupled secondary antibody and spectral demixing strategies with NTH1 with F(ab')2 647 coupled secondary antibody and H3 with CF680-coupled secondary antibody. For Histone H3 labelling with CF568-coupled secondary antibody proved inefficient (Figure 66C-i) and affected NTH1 detection. But the CF680-based approach enabled clear visualization of NTH1 relative to this chromatin marker, revealing only limited colocalization between NTH1 and Histone H3 (Figure 66C-ii).

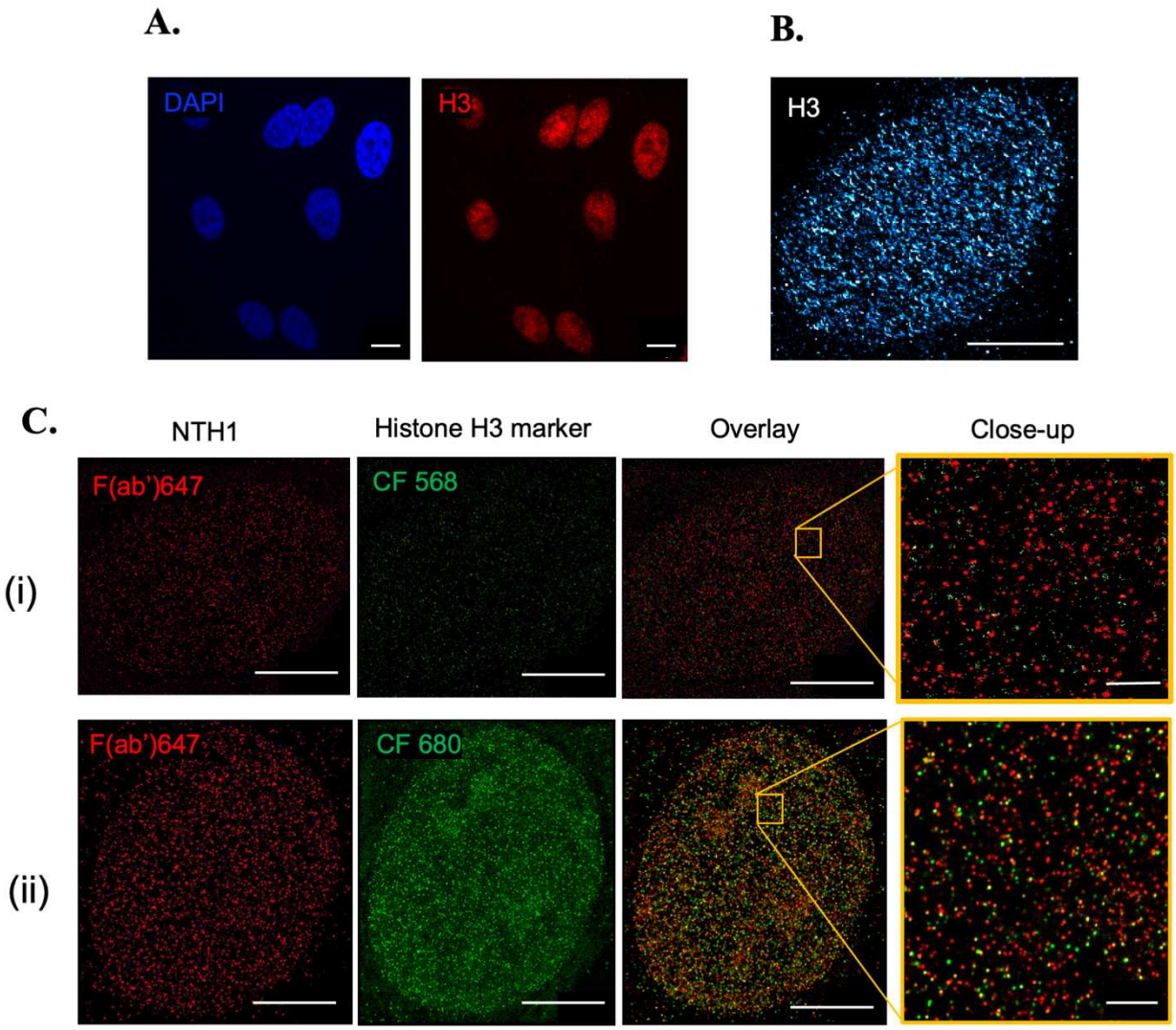


Figure 66: Optimization of Histone H3 by confocal and dSTORM, followed by 2-colour imaging strategies with NTH1.

(A) DAPI and mouse polyclonal anti-Histone H3 labelled with AF568-coupled secondary antibody immunofluorescence images obtained by confocal microscopy. Scale – 20 µm. (B) dSTORM reconstructured image of mouse polyclonal anti-Histone H3 labelled with CF680-coupled secondary antibody. Scale = 5 µm. (C) 2-colour imaging of NTH1 and Histone H3 by (i) Sequential labelling of NTH1 with F(ab')2 647-coupled secondary antibody and Histone H3 with CF568-coupled secondary antibody and (ii) Spectral demixing of NTH1 with F(ab')647-coupled secondary antibody and Histone H3 with CF680-coupled secondary antibody. Scale = 5 µm. Overlaid images of both NTH1 and Histone H3 are shown alongside with a close-up on the distribution of their localizations within the nuclear space. Scale = 0.5 µm.

However, reproducing this data for fractionated HeLa cells proved problematic due to very few localizations captured for Histone H3. As figure 67 demonstrates, we discovered that after subcellular fractionation, the Histone H3 signal was drastically reduced, leading to uneven labelling efficiency (a 11-fold decrease from 2865 a.u in NF to 245.3 a.u in F cells). We decided to test another histone antibody - mouse monoclonal pan nuclear Histone H1, kindly provided by *Dr. Guillermo Orsi (Institut pour l'Avancée des Biosciences),* which maintained labelling efficiency after fractionation. Further investigations utilizing fractionated HeLa cells now need to be performed to observe the effect of oxidative stress on the distribution of NTH1 in relation to this chromatin marker.

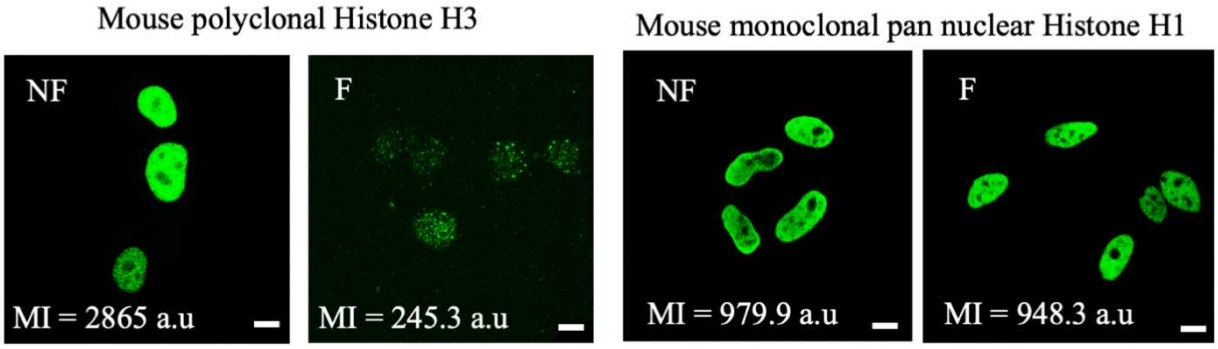


Figure 67: Testing compatibility of fractionation step on Histone H3 immunolabelled HeLa cell nuclei. Comparing fractionated (F) and non-fractionated (NF) HeLa nuclei with immunolabelled mouse polyclonal anti-Histone H3 and mouse monoclonal pan nuclear anti-Histone H1. The mean fluorescence intensity (MI) values are provided below each image as an estimate for 20 cells measured per condition. Scale = 20 µm.

Multiplexed dSTORM imaging is inherently challenging due to fluorophore photophysics, spectral overlap, and rapid photobleaching, especially when targeting high-density nuclear proteins such as NTH1 and Histone H3 (Rust et al., 2006; Xu et al., 2017). To overcome these limitations and achieve robust multi-target imaging, we also implemented DNA-PAINT, which provides precise single-molecule localization with improved control over labelling and imaging conditions (Nieves et al., 2018). Using optimized imager strands (ATTO 655 and Cy3B), shown in figure 68A, we were able to reproduce NTH1 distribution profiles comparable to single-colour dSTORM and perform two-colour imaging with chromatin labelled directly using Janelia 549, offering a more homogeneous representation of the genome compared to histone-based labelling (Figure 68B). This strategy also circumvents histone labelling, which restricts observations to nucleosome-occupied regions and may not reflect DNA

accessibility at linker DNA, nucleosome-depleted regions, or actively transcribed and damage-prone sites.

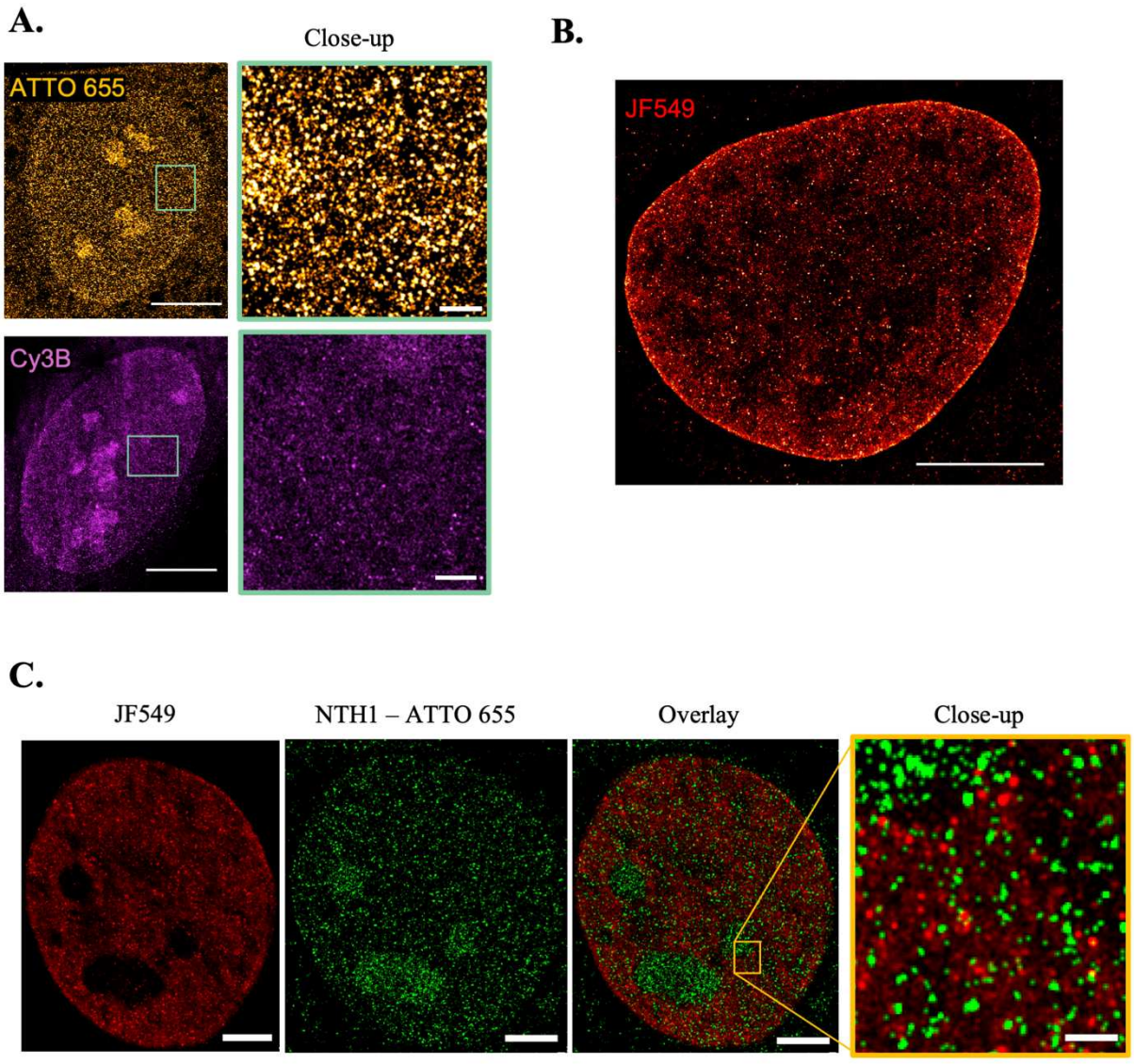


Figure 68. Distribution of NTH1 and chromatin label Janelia 549 by DNA-PAINT.
(A) NTH1 molecules site specifically conjugated to a single-stranded DNA docking strand. The imager strand was either labelled with ATTO655 or Cy3B fluorophores, shown with a close-up of distribution in HeLa cell nuclei. (B) PAINT image of HeLa cell nucleus with chromatin label Janelia 549 (JF549). (C) 2-colour imaging of NTH1 with imager strand labelled with ATTO 655 fluorophore, and the chromatin label, JF549. Overlaid image shows close-up of distribution of nuclear localizations for NTH1 with chromatin. All images have a scale of 5 µm with the close-up images of a scale = 0.5 µm.

DNA-PAINT revealed that NTH1 exhibits a heterogeneous and punctate distribution throughout the nucleus, including within nucleoli, consistent with previous dSTORM observations, while chromatin appeared more homogeneous with occasional punctate clusters likely corresponding to compacted regions (Figure 68A-B). Notably, there was little co-localization between NTH1 and the chromatin label, suggesting that NTH1 preferentially associates with nucleosome-depleted or more accessible DNA regions rather than densely packed chromatin (Figure 68C). The very first experiments performed after exposure to oxidative stress induced by $KBrO_3$ revealed visible chromatin compaction immediately after treatment, which persisted and appeared visibly disjointed after a 4h recovery (Figure 69). These experiments need to be reproduced and confirmed. Chromatin compaction is likely to influence the recruitment and spatial organization of NTH1, potentially modulating its access to damaged DNA sites.

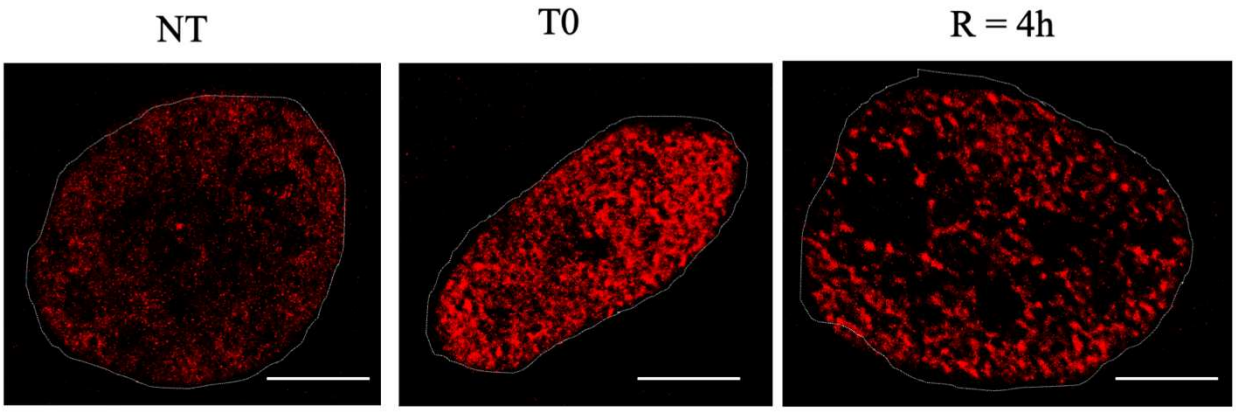


Figure 69. Redistribution of NTH1 and effect of $KBrO_3$ on chromatin.
Reconstructed dSTORM imaging of chromatin labelled with Janelia 549 (labels minor grooves of DNA) observed in non-treated (NT), treated (T0) and cells recovered in fresh DMEM for 4h after $KBrO_3$ treatment (R=4h). Scale = 5 µm.

Low NTH1 labelling efficiency in these experiments limited the number of detectable localizations, highlighting the need for further optimization and reproducing data to confirm DNA-PAINT labelling and imaging parameters. Taken together, these new findings begin to unravel the dynamic interplay between chromatin architecture and NTH1 localization, suggesting that oxidative stress alters nuclear landscapes in ways that may shape the activity and targeting of BER proteins. This also has the potential to develop better quantitative analysis using qPAINT (quantitative), to count proteins since we know the number of docking strands per protein. This is in contrast with our dSTORM data from which it is very difficult to relate the number of localizations to the number of NTH1 molecules within clusters.

Our sptPALM data shows NTH1 diffusing at different diffusion rates likely reflecting interactions with chromatin subregions. Using simulators like SMIS would allow us to evaluate how NTH1 transitions between fast, slow, and transiently bound states and if these states are chromatin

compartment specific. A recent preprint by Xiang et al., 2025 used a point cloud single molecule diffusivity mapping (pc-SMdM) to reveal how the highly heterogenous nucleus influences the mobility of OGG1 within different intranuclear compartments. They confirm previous results that OGG1 demonstrates a two-state kinetic model: highly mobile (loosely bound) and less mobile (tightly bound) influenced by the intranuclear compartments (Amouroux et al., 2010; D'Augustin et al., 2022). Not only does OGG1 exhibit two kinetic states, but also that its proportion changes indicating different repair efficiencies followed in different intranuclear compartments. Increased chromatin compaction causes OGG1 to favour a 1D sliding mechanism and alternatively, a 3D hopping approach in the presence of an induced net positive charge (Xiang et al., 2025). The two-state kinetics does indeed, reflect our observations with the diffusion dynamics of NTH1. However, it is speculative whether its two-state kinetics is influenced by intranuclear compartments and further modulated by a net positive charge of the enzyme. To investigate this, we could employ a combination of PALM and dSTORM imaging, to track NTH1 in regions annotated as heterochromatin versus euchromatin, or even in transcriptionally active versus inactive domains. This subsequent mapping of intranuclear compartments over single-particle NTH1 trajectories would allow us to correlate whether the dynamics of these kinetic states change depending on the intranuclear compartment and map potential sites of increased repair activity indicated by slow or static diffusion of NTH1. These changes in electrostatic properties, chromatin compaction and molecular diffusion of NTH1 would allow us to bridge our understanding between the nuclear architecture, molecular diffusion and enzymatic dynamics of DNA glycosylases. Finally, oxidative damage is known to reshape both chromatin organisation and repair dynamics. This would provide a more mechanistic understanding of how the cell coordinates different chromatin states with base excision repair.

These perspectives could represent the next steps toward understanding NTH1 not just as a DNA glycosylase, but as a repair protein whose function is fundamentally shaped by its chromatin environment.

BIBLIOGRAPHY

Ahel, D., Hořejší, Z., Wiechens, N., Polo, S. E., Garcia-Wilson, E., Ahel, I., Flynn, H., Skehel, M., West, S. C., Jackson, S. P., Owen-Hughes, T., & Boulton, S. J. (2009). Poly(ADP-ribose)–Dependent Regulation of DNA Repair by the Chromatin Remodeling Enzyme ALC1. *Science*, *325*(5945), 1240–1243. https://doi.org/10.1126/science.1177321

Alemasova, E. E., Moor, N. A., Naumenko, K. N., Kutuzov, M. M., Sukhanova, M. V., Pestryakov, P. E., & Lavrik, O. I. (2016). Y-box-binding protein 1 as a non-canonical factor of base excision repair. *Biochimica et Biophysica Acta (BBA) - Proteins and Proteomics*, *1864*(12), 1631–1640. https://doi.org/10.1016/j.bbapap.2016.08.012

Almeida, K. H., & Sobol, R. W. (2007). A unified view of base excision repair: Lesion-dependent protein complexes regulated by post-translational modification. *DNA Repair*, *6*(6), 695–711. https://doi.org/10.1016/j.dnarep.2007.01.009

Almouzni, G., & Cedar, H. (2016). Maintenance of Epigenetic Information. *Cold Spring Harbor Perspectives in Biology*, *8*(5), a019372. https://doi.org/10.1101/cshperspect.a019372

Amouroux, R., Campalans, A., Epe, B., & Radicella, J. P. (2010). Oxidative stress triggers the preferential assembly of base excision repair complexes on open chromatin regions. *Nucleic Acids Research*, *38*(9), 2878–2890. https://doi.org/10.1093/nar/gkp1247

Apelt, K., Lans, H., Schärer, O. D., & Luijsterburg, M. S. (2021). Nucleotide excision repair leaves a mark on chromatin: DNA damage detection in nucleosomes. *Cellular and Molecular Life Sciences*, *78*(24), 7925–7942. https://doi.org/10.1007/s00018-021-03984-7

Arnould, C., Rocher, V., Saur, F., Bader, A. S., Muzzopappa, F., Collins, S., Lesage, E., Le Bozec, B., Puget, N., Clouaire, T., Mangeat, T., Mourad, R., Ahituv, N., Noordermeer, D., Erdel, F., Bushell, M., Marnef, A., & Legube, G. (2023). Chromatin compartmentalization regulates the response to DNA damage. *Nature*, *623*(7985), 183–192. https://doi.org/10.1038/s41586-023-06635-y

Averill-Bates, D. A. (2023). The antioxidant glutathione. In *Vitamins and Hormones* (Vol. 121, pp. 109–141). Elsevier. https://doi.org/10.1016/bs.vh.2022.09.002

Bai, M., Ti, D., Mei, Q., Liu, J., Yan, X., Chen, D., Li, X., Wu, Z., & Han, W. (2020). The Role of Posttranslational Modifications in DNA Repair. *BioMed Research International*, *2020*(1). https://doi.org/10.1155/2020/7493902

Baiken, Y., Kanayeva, D., Taipakova, S., Groisman, R., Ishchenko, A. A., Begimbetova, D., Matkarimov, B., & Saparbaev, M. (2021). Role of Base Excision Repair Pathway in the Processing of Complex DNA Damage Generated by Oxidative Stress and Anticancer Drugs. *Frontiers in Cell and Developmental Biology*, *8*, 617884. https://doi.org/10.3389/fcell.2020.617884

Banani, S. F., Lee, H. O., Hyman, A. A., & Rosen, M. K. (2017). Biomolecular condensates: Organizers of cellular biochemistry. *Nature Reviews Molecular Cell Biology*, *18*(5), 285–298. https://doi.org/10.1038/nrm.2017.7

Bancaud, A., Huet, S., Daigle, N., Mozziconacci, J., Beaudouin, J., & Ellenberg, J. (2009). Molecular crowding affects diffusion and binding of nuclear proteins in heterochromatin and reveals the fractal organization of chromatin. *The EMBO Journal*, *28*(24), 3785–3798. https://doi.org/10.1038/emboj.2009.340

Barth, R., Bystricky, K., & Shaban, H. A. (2020). Coupling chromatin structure and dynamics by live super-resolution imaging. *Science Advances*, *6*(27), eaaz2196. https://doi.org/10.1126/sciadv.aaz2196

Basu, A., & Krishnamurthy, S. (2010). Cellular Responses to Cisplatin-Induced DNA Damage. *Journal of Nucleic Acids*, *2010*, 1–16. https://doi.org/10.4061/2010/201367

Belhadj, S., Quintana, I., Mur, P., Munoz-Torres, P. M., Alonso, M. H., Navarro, M., Terradas, M., Piñol, V., Brunet, J., Moreno, V., Lázaro, C., Capellá, G., & Valle, L. (2019). NTHL1 biallelic mutations seldom cause colorectal cancer, serrated polyposis or a multi-tumor phenotype, in absence of colorectal adenomas. *Scientific Reports*, *9*(1). https://doi.org/10.1038/s41598-019-45281-1

Bellacosa, A. (2001). Role of *MED1* (*MBD4*) Gene in DNA repair and human cancer. *Journal of Cellular Physiology*, *187*(2), 137–144. https://doi.org/10.1002/jcp.1064

Bessho, T. (1999). Nucleotide excision repair 3' endonuclease XPG stimulates the activity of base excision repairenzyme thymine glycol DNA glycosylase. *Nucleic Acids Research*, *27*(4), 979–983. https://doi.org/10.1093/nar/27.4.979

Betzig, E., Patterson, G. H., Sougrat, R., Lindwasser, O. W., Olenych, S., Bonifacino, J. S., Davidson, M. W., Lippincott-Schwartz, J., & Hess, H. F. (2006). Imaging Intracellular Fluorescent Proteins at Nanometer Resolution. *Science*, *313*(5793), 1642–1645. https://doi.org/10.1126/science.1127344

Blainey, P. C., Luo, G., Kou, S. C., Mangel, W. F., Verdine, G. L., Bagchi, B., & Xie, X. S. (2009). Nonspecifically bound proteins spin while diffusing along DNA. *Nature Structural & Molecular Biology*, *16*(12), 1224–1229. https://doi.org/10.1038/nsmb.1716

Blainey, P. C., Van Oijen, A. M., Banerjee, A., Verdine, G. L., & Xie, X. S. (2006). A base-excision DNA-repair protein finds intrahelical lesion bases by fast sliding in contact with DNA. *Proceedings of the National Academy of Sciences*, *103*(15), 5752–5757. https://doi.org/10.1073/pnas.0509723103

Boldinova, Khairullin, Makarova, & Zharkov. (2019). Isoforms of Base Excision Repair Enzymes Produced by Alternative Splicing. *International Journal of Molecular Sciences*, *20*(13), 3279. https://doi.org/10.3390/ijms20133279

Bourgeois, D. (2023). Single molecule imaging simulations with advanced fluorophore photophysics. *Communications Biology*, *6*(1), 53. https://doi.org/10.1038/s42003-023-04432-x

Bowden, N. A. (2014). Nucleotide excision repair: Why is it not used to predict response to platinum-based chemotherapy? *Cancer Letters*, *346*(2), 163–171. https://doi.org/10.1016/j.canlet.2014.01.005

Cadet, J., & Wagner, J. R. (2013). DNA Base Damage by Reactive Oxygen Species, Oxidizing Agents, and UV Radiation. *Cold Spring Harbor Perspectives in Biology*, *5*(2), a012559–a012559. https://doi.org/10.1101/cshperspect.a012559

Caldecott, K. W. (2024). Causes and consequences of DNA single-strand breaks. *Trends in Biochemical Sciences*, *49*(1), 68–78. https://doi.org/10.1016/j.tibs.2023.11.001

Campalans, A., Amouroux, R., Bravard, A., Epe, B., & Radicella, J. P. (2007). UVA irradiation induces relocalisation of the DNA repair protein hOGG1 to nuclear speckles. *Journal of Cell Science*, *120*(1), 23–32. https://doi.org/10.1242/jcs.03312

Campalans, A., Kortulewski, T., Amouroux, R., Menoni, H., Vermeulen, W., & Radicella, J. P. (2013). Distinct spatiotemporal patterns and PARP dependence of XRCC1 recruitment to single-strand break and base excision repair. *Nucleic Acids Research*, *41*(5), 3115–3129. https://doi.org/10.1093/nar/gkt025

Campalans, A., Marsin, S., Nakabeppu, Y., O'Connor, T. R., Boiteux, S., & Radicella, J. P. (2005). XRCC1 interactions with multiple DNA glycosylases: A model for its recruitment to base excision repair. *DNA Repair*, *4*(7), 826–835. https://doi.org/10.1016/j.dnarep.2005.04.014

Carré-Simon, À., & Fabre, E. (2021). 3D Genome Organization: Causes and Consequences for DNA Damage and Repair. *Genes*, *13*(1), 7. https://doi.org/10.3390/genes13010007

Carroll, B. L., Zahn, K. E., Hanley, J. P., Wallace, S. S., Dragon, J. A., & Doublié, S. (2021). Caught in motion: Human NTHL1 undergoes interdomain rearrangement necessary for catalysis. *Nucleic Acids Research*, *49*(22), 13165–13178. https://doi.org/10.1093/nar/gkab1162

Chae, Y. K., Anker, J. F., Carneiro, B. A., Chandra, S., Kaplan, J., Kalyan, A., Santa-Maria, C. A., Platanias, L. C., & Giles, F. J. (2016). Genomic landscape of DNA repair genes in cancer. *Oncotarget*, *7*(17), 23312–23321. https://doi.org/10.18632/oncotarget.8196

Chan, M. K., Ocampo-Hafalla, M. T., Vartanian, V., Jaruga, P., Kirkali, G., Koenig, K. L., Brown, S., Lloyd, R. S., Dizdaroglu, M., & Teebor, G. W. (2009). Targeted deletion of the genes encoding NTH1 and NEIL1 DNA N-glycosylases reveals the existence of novel carcinogenic oxidative damage to DNA. *DNA Repair*, *8*(7), 786–794. https://doi.org/10.1016/j.dnarep.2009.03.001

Chapman, J. R., Sossick, A. J., Boulton, S. J., & Jackson, S. P. (2012). BRCA1-associated exclusion of 53BP1 from DNA damage sites underlies temporal control of DNA repair. *Journal of Cell Science*, *125*(15), 3529–3534. https://doi.org/10.1242/jcs.105353

Chapman, J. R., Taylor, M. R. G., & Boulton, S. J. (2012). Playing the End Game: DNA Double-Strand Break Repair Pathway Choice. *Molecular Cell*, *47*(4), 497–510. https://doi.org/10.1016/j.molcel.2012.07.029

Chatterjee, N., & Walker, G. C. (2017). Mechanisms of DNA damage, repair, and mutagenesis. *Environmental and Molecular Mutagenesis*, *58*(5), 235–263. https://doi.org/10.1002/em.22087

Chaudhari, S., Ware, A. P., Jayaram, P., Gorthi, S. P., El-Khamisy, S. F., & Satyamoorthy, K. (2021). Apurinic/Apyrimidinic Endonuclease 2 (APE2): An ancillary enzyme for contextual base excision repair mechanisms to preserve genome stability. *Biochimie*, *190*, 70–90. https://doi.org/10.1016/j.biochi.2021.07.006

Chen, A., Stadulis, S. E., deLeuze, K., & Gibney, P. A. (2024). Evaluating cellular roles and phenotypes associated with trehalose degradation genes in *Saccharomyces cerevisiae*. *G3: Genes, Genomes, Genetics*, *14*(11). https://doi.org/10.1093/g3journal/jkae215

Chen, B.-C., & Lin, H.-Y. (2022). Deletion of NTH1 and HSP12 increases the freeze–thaw resistance of baker's yeast in bread dough. *Microbial Cell Factories*, *21*(1). https://doi.org/10.1186/s12934-022-01876-4

Chen, Z., & Tyler, J. K. (2022). The Chromatin Landscape Channels DNA Double-Strand Breaks to Distinct Repair Pathways. *Frontiers in Cell and Developmental Biology*, *10*, 909696. https://doi.org/10.3389/fcell.2022.909696

Chiolo, I., Altmeyer, M., Legube, G., & Mekhail, K. (2025). Nuclear and genome dynamics underlying DNA double-strand break repair. *Nature Reviews Molecular Cell Biology*, *26*(7), 538–557. https://doi.org/10.1038/s41580-025-00828-1

Chiou, Y.-Y., Hu, J., Sancar, A., & Selby, C. P. (2018). RNA polymerase II is released from the DNA template during transcription-coupled repair in mammalian cells. *Journal of Biological Chemistry*, *293*(7), 2476–2486. https://doi.org/10.1074/jbc.ra117.000971

Clément, C., Orsi, G. A., Gatto, A., Boyarchuk, E., Forest, A., Hajj, B., Miné-Hattab, J., Garnier, M., Gurard-Levin, Z. A., Quivy, J.-P., & Almouzni, G. (2018). High-resolution visualization of

H3 variants during replication reveals their controlled recycling. *Nature Communications*, *9*(1), 3181. https://doi.org/10.1038/s41467-018-05697-1

Cook, J. C., & Delaney, S. (2022). The Domino Effect: Nucleosome Dynamics and the Regulation of Base Excision Repair Enzymes. *DNA*, *2*(4), 248–263. https://doi.org/10.3390/dna2040018

Cunningham, R. P., Asahara, H., Bank, J. F., Scholes, C. P., Salerno, J. C., Surerus, K., Munck, E., McCracken, J., Peisach, J., & Emptage, M. H. (1989). Endonuclease III is an iron-sulfur protein. *Biochemistry*, *28*(10), 4450–4455. https://doi.org/10.1021/bi00436a049

Dantzer, F., Schreiber, V., Niedergang, C., Trucco, C., Flatter, E., Rubia, G. D. L., Oliver, J., Rolli, V., Ménissier-de Murcia, J., & De Murcia, G. (1999). Involvement of poly(ADP-ribose) polymerase in base excision repair. *Biochimie*, *81*(1–2), 69–75. https://doi.org/10.1016/S0300-9084(99)80040-6

Das, S., Chattopadhyay, R., Bhakat, K. K., Boldogh, I., Kohno, K., Prasad, R., Wilson, S. H., & Hazra, T. K. (2007). Stimulation of NEIL2-mediated oxidized base excision repair via YB-1 interaction during oxidative stress. *The Journal of Biological Chemistry*, *282*(39), 28474–28484. https://doi.org/10.1074/jbc.M704672200

D'Augustin, O. (2022). *Caractérisation de la dynamique de l'ADN glycosylase OGG1 et de résidus responsables de son interaction avec l'ADN en cellules vivantes* [PhD Thesis].

D'Augustin, O., Gaudon, V., Siberchicot, C., Smith, R., Chapuis, C., Depagne, J., Veaute, X., Busso, D., Di Guilmi, A.-M., Castaing, B., Radicella, J. P., Campalans, A., & Huet, S. (2022). *Identification of key residues of the DNA glycosylase OGG1 controlling efficient DNA scanning and recruitment to oxidized bases in living cells* [Preprint]. Cell Biology. https://doi.org/10.1101/2022.11.04.515179

D'Augustin, O., Gaudon, V., Siberchicot, C., Smith, R., Chapuis, C., Depagne, J., Veaute, X., Busso, D., Di Guilmi, A.-M., Castaing, B., Radicella, J. P., Campalans, A., & Huet, S. (2023). Identification of key residues of the DNA glycosylase OGG1 controlling efficient DNA sampling and recruitment to oxidized bases in living cells. *Nucleic Acids Research*, *51*(10), 4942–4958. https://doi.org/10.1093/nar/gkad243

D'Augustin, O., Huet, S., Campalans, A., & Radicella, J. P. (2020). Lost in the Crowd: How Does Human 8-Oxoguanine DNA Glycosylase 1 (OGG1) Find 8-Oxoguanine in the Genome? *International Journal of Molecular Sciences*, *21*(21), 8360. https://doi.org/10.3390/ijms21218360

Davie, J. R. (1996). The Nuclear Matrix and the Regulation of Chromatin Organization and Function. In *International Review of Cytology* (Vol. 162, pp. 191–250). Elsevier. https://doi.org/10.1016/S0074-7696(08)61232-2

De Zitter, E., Thédié, D., Mönkemöller, V., Hugelier, S., Beaudouin, J., Adam, V., Byrdin, M., Van Meervelt, L., Dedecker, P., & Bourgeois, D. (2019). Mechanistic investigation of mEos4b reveals a strategy to reduce track interruptions in sptPALM. *Nature Methods*, *16*(8), 707–710. https://doi.org/10.1038/s41592-019-0462-3

Demple, B. (n.d.). *Repair of Oxidative Damage to DNA: Enzymology and Biology*.

Dey, P., & Bhattacherjee, A. (2019). Mechanism of Facilitated Diffusion of DNA Repair Proteins in Crowded Environment: Case Study with Human Uracil DNA Glycosylase. *The Journal of Physical Chemistry B*, *123*(49), 10354–10364. https://doi.org/10.1021/acs.jpcb.9b07342

Di Marzo, N., Chisci, E., & Giovannoni, R. (2018). The Role of Hydrogen Peroxide in Redox-Dependent Signaling: Homeostatic and Pathological Responses in Mammalian Cells. *Cells*, *7*(10), 156. https://doi.org/10.3390/cells7100156

Dizdaroglu, M. (2005). Base-excision repair of oxidative DNA damage by DNA glycosylases. *Mutation Research/Fundamental and Molecular Mechanisms of Mutagenesis*, *591*(1–2), 45–59. https://doi.org/10.1016/j.mrfmmm.2005.01.033

Dizdaroglu, M., Coskun, E., & Jaruga, P. (2017). Repair of oxidatively induced DNA damage by DNA glycosylases: Mechanisms of action, substrate specificities and excision kinetics. *Mutation Research/Reviews in Mutation Research*, *771*, 99–127. https://doi.org/10.1016/j.mrrev.2017.02.001

Dizdaroglu, M., Laval, J., & Boiteux, S. (1993). Substrate specificity of the Escherichia coli endonuclease III: Excision of thymine- and cytosine-derived lesions in DNA produced by

radiation-generated free radicals. *Biochemistry*, *32*(45), 12105–12111. https://doi.org/10.1021/bi00096a022

Dou, H., Theriot, C. A., Das, A., Hegde, M. L., Matsumoto, Y., Boldogh, I., Hazra, T. K., Bhakat, K. K., & Mitra, S. (2008). Interaction of the Human DNA Glycosylase NEIL1 with Proliferating Cell Nuclear Antigen. *Journal of Biological Chemistry*, *283*(6), 3130–3140. https://doi.org/10.1074/jbc.M709186200

Drost, J., Van Boxtel, R., Blokzijl, F., Mizutani, T., Sasaki, N., Sasselli, V., De Ligt, J., Behjati, S., Grolleman, J. E., Van Wezel, T., Nik-Zainal, S., Kuiper, R. P., Cuppen, E., & Clevers, H. (2017). Use of CRISPR-modified human stem cell organoids to study the origin of mutational signatures in cancer. *Science*, *358*(6360), 234–238. https://doi.org/10.1126/science.aao3130

Duan, M., Ulibarri, J., Liu, K. J., & Mao, P. (2020). Role of Nucleotide Excision Repair in Cisplatin Resistance. *International Journal of Molecular Sciences*, *21*(23), 9248. https://doi.org/10.3390/ijms21239248

Ebert, C., Simon, N., Schneider, S., & Carell, T. (2017). Structural Insights into the Recognition of N^2-Aryl- and C8-Aryl DNA Lesions by the Repair Protein XPA/Rad14. *ChemBioChem*, *18*(14), 1379–1382. https://doi.org/10.1002/cbic.201700169

Elsakrmy, N., Zhang-Akiyama, Q.-M., & Ramotar, D. (2020). The Base Excision Repair Pathway in the Nematode Caenorhabditis elegans. *Frontiers in Cell and Developmental Biology*, *8*. https://doi.org/10.3389/fcell.2020.598860

Fahrer, J., & Christmann, M. (2023). DNA Alkylation Damage by Nitrosamines and Relevant DNA Repair Pathways. *International Journal of Molecular Sciences*, *24*(5), 4684. https://doi.org/10.3390/ijms24054684

Ferrand, J., Plessier, A., & Polo, S. E. (2021). Control of the chromatin response to DNA damage: Histone proteins pull the strings. *Seminars in Cell & Developmental Biology*, *113*, 75–87. https://doi.org/10.1016/j.semcdb.2020.07.002

Ferrand, J., Rondinelli, B., & Polo, S. E. (2020). Histone Variants: Guardians of Genome Integrity. *Cells*, *9*(11), 2424. https://doi.org/10.3390/cells9112424

Fijen, C., & Rothenberg, E. (2021). The evolving complexity of DNA damage foci: RNA, condensates and chromatin in DNA double-strand break repair. *DNA Repair*, *105*, 103170. https://doi.org/10.1016/j.dnarep.2021.103170

Floc'h, K., Lacroix, F., Servant, P., Wong, Y.-S., Kleman, J.-P., Bourgeois, D., & Timmins, J. (2019). Cell morphology and nucleoid dynamics in dividing Deinococcus radiodurans. *Nature Communications*, *10*(1), 3815. https://doi.org/10.1038/s41467-019-11725-5

Freinbichler, W., Colivicchi, M. A., Stefanini, C., Bianchi, L., Ballini, C., Misini, B., Weinberger, P., Linert, W., Varešlija, D., Tipton, K. F., & Della Corte, L. (2011). Highly reactive oxygen species: Detection, formation, and possible functions. *Cellular and Molecular Life Sciences*, *68*(12), 2067–2079. https://doi.org/10.1007/s00018-011-0682-x

Freudenthal, B. D. (2017). Base excision repair of oxidative DNA damage from mechanism to disease. *Frontiers in Bioscience*, *22*(9), 1493–1522. https://doi.org/10.2741/4555

Friedberg, E. C., McDaniel, L. D., & Schultz, R. A. (2004). The role of endogenous and exogenous DNA damage and mutagenesis. *Current Opinion in Genetics & Development*, *14*(1), 5–10. https://doi.org/10.1016/j.gde.2003.11.001

Friedman, J. I., & Stivers, J. T. (2010). Detection of Damaged DNA Bases by DNA Glycosylase Enzymes. *Biochemistry*, *49*(24), 4957–4967. https://doi.org/10.1021/bi100593a

Fromme, J. C. (2003). Structure of a trapped endonuclease III-DNA covalent intermediate. *The EMBO Journal*, *22*(13), 3461–3471. https://doi.org/10.1093/emboj/cdg311

Fromme, J. C., Banerjee, A., & Verdine, G. L. (2004). DNA glycosylase recognition and catalysis. *Current Opinion in Structural Biology*, *14*(1), 43–49. https://doi.org/10.1016/j.sbi.2004.01.003

Fu, D., Calvo, J. A., & Samson, L. D. (2012). Balancing repair and tolerance of DNA damage caused by alkylating agents. *Nature Reviews Cancer*, *12*(2), 104–120. https://doi.org/10.1038/nrc3185

Fudenberg, G., Imakaev, M., Lu, C., Goloborodko, A., Abdennur, N., & Mirny, L. A. (2016). Formation of Chromosomal Domains by Loop Extrusion. *Cell Reports*, *15*(9), 2038–2049. https://doi.org/10.1016/j.celrep.2016.04.085

Galick, H. A., Kathe, S., Liu, M., Robey-Bond, S., Kidane, D., Wallace, S. S., & Sweasy, J. B. (2013). Germ-line variant of human NTH1 DNA glycosylase induces genomic instability and cellular

transformation. *Proceedings of the National Academy of Sciences*, *110*(35), 14314–14319. https://doi.org/10.1073/pnas.1306752110

García Fernández, F., Huet, S., & Miné-Hattab, J. (2023). Multi-Scale Imaging of the Dynamic Organization of Chromatin. *International Journal of Molecular Sciences*, *24*(21), 15975. https://doi.org/10.3390/ijms242115975

García Fernández, F., Park, J., Chapuis, C., Pinto Jurado, E., Imburchia, V., Smith, R., José Longarini, E., Taddei, A., Hubert, C., Sokolovska, N., Matić, I., Huet, S., & Miné-Hattab, J. (2025). Single nucleosome imaging reveals principles of transient multiscale chromatin reorganization triggered by histone ADP-ribosylation at DNA lesions. *Nature Communications*, *16*(1), 6652. https://doi.org/10.1038/s41467-025-61834-7

Gautam, A., Fawcett, H., Burdova, K., Brazina, J., & Caldecott, K. W. (2023). APE1-dependent base excision repair of DNA photodimers in human cells. *Molecular Cell*, S1097276523007359. https://doi.org/10.1016/j.molcel.2023.09.013

Georgieva, D., Wang, N., Taglialatela, A., Jerabek, S., Reczek, C. R., Lim, P. X., Sung, J., Du, Q., Horiguchi, M., Jasin, M., Ciccia, A., Baer, R., & Egli, D. (2024). BRCA1 and 53BP1 regulate reprogramming efficiency by mediating DNA repair pathway choice at replication-associated double-strand breaks. *Cell Reports*, *43*(4), 114006. https://doi.org/10.1016/j.celrep.2024.114006

Ghodgaonkar, M. M., Lazzaro, F., Olivera-Pimentel, M., Artola-Borán, M., Cejka, P., Reijns, M. A., Jackson, A. P., Plevani, P., Muzi-Falconi, M., & Jiricny, J. (2013). Ribonucleotides Misincorporated into DNA Act as Strand-Discrimination Signals in Eukaryotic Mismatch Repair. *Molecular Cell*, *50*(3), 323–332. https://doi.org/10.1016/j.molcel.2013.03.019

Ghosh, S., & Ghosh, A. (2021). Activation of DNA damage response signaling in mammalian cells by ionizing radiation. *Free Radical Research*, *55*(8), 814–827. https://doi.org/10.1080/10715762.2021.1876853

Gibson, B. A., Doolittle, L. K., Schneider, M. W. G., Jensen, L. E., Gamarra, N., Henry, L., Gerlich, D. W., Redding, S., & Rosen, M. K. (2019). Organization of Chromatin by Intrinsic and

Regulated Phase Separation. *Cell*, *179*(2), 470-484.e21. https://doi.org/10.1016/j.cell.2019.08.037

Goffart, S., Tikkanen, P., Michell, C., Wilson, T., & Pohjoismäki, J. L. O. (2021). The Type and Source of Reactive Oxygen Species Influences the Outcome of Oxidative Stress in Cultured Cells. *Cells*, *10*(5), 1075. https://doi.org/10.3390/cells10051075

Gorman, J., Chowdhury, A., Surtees, J. A., Shimada, J., Reichman, D. R., Alani, E., & Greene, E. C. (2007). Dynamic Basis for One-Dimensional DNA Scanning by the Mismatch Repair Complex Msh2-Msh6. *Molecular Cell*, *28*(3), 359–370. https://doi.org/10.1016/j.molcel.2007.09.008

Gorman, J., & Greene, E. C. (2008). Visualizing one-dimensional diffusion of proteins along DNA. *Nature Structural & Molecular Biology*, *15*(8), 768–774. https://doi.org/10.1038/nsmb.1441

Granéli, A., Yeykal, C. C., Robertson, R. B., & Greene, E. C. (2006). Long-distance lateral diffusion of human Rad51 on double-stranded DNA. *Proceedings of the National Academy of Sciences*, *103*(5), 1221–1226. https://doi.org/10.1073/pnas.0508366103

Greenberg, M. M. (2012). The Formamidopyrimidines: Purine Lesions Formed in Competition With 8-Oxopurines From Oxidative Stress. *Accounts of Chemical Research*, *45*(4), 588–597. https://doi.org/10.1021/ar2002182

Grolleman, J. E., De Voer, R. M., Elsayed, F. A., Nielsen, M., Weren, R. D. A., Palles, C., Ligtenberg, M. J. L., Vos, J. R., Ten Broeke, S. W., De Miranda, N. F. C. C., Kuiper, R. A., Kamping, E. J., Jansen, E. A. M., Vink-Börger, M. E., Popp, I., Lang, A., Spier, I., Hüneburg, R., James, P. A., … Kuiper, R. P. (2019). Mutational Signature Analysis Reveals NTHL1 Deficiency to Cause a Multi-tumor Phenotype. *Cancer Cell*, *35*(2), 256-266.e5. https://doi.org/10.1016/j.ccell.2018.12.011

Guay, D., Evoy, A.-A., Paquet, E., Garand, C., Bachvarova, M., Bachvarov, D., & Lebel, M. (2008). The strand separation and nuclease activities associated with YB-1 are dispensable for cisplatin resistance but overexpression of YB-1 in MCF7 and MDA-MB-231 breast tumor cells generates several chemoresistance signatures. *The International Journal of Biochemistry & Cell Biology*, *40*(11), 2492–2507. https://doi.org/10.1016/j.biocel.2008.04.011

Guay, D., Garand, C., Reddy, S., Schmutte, C., & Lebel, M. (2008). The human endonuclease III enzyme is a relevant target to potentiate cisplatin cytotoxicity in Y-box-binding protein-1 overexpressing tumor cells. *Cancer Science*, *99*(4), 762–769. https://doi.org/10.1111/j.1349-7006.2008.00739.x

Gupta, S., You, P., SenGupta, T., Nilsen, H., & Sharma, K. (2021). Crosstalk between Different DNA Repair Pathways Contributes to Neurodegenerative Diseases. *Biology*, *10*(2), 163. https://doi.org/10.3390/biology10020163

Hammons, G. (1997). Metabolism of carcinogenic heterocyclic and aromatic amines by recombinant human cytochrome P450 enzymes. *Carcinogenesis*, *18*(4), 851–854. https://doi.org/10.1093/carcin/18.4.851

Han, J., Yu, M., Bai, Y., Yu, J., Jin, F., Li, C., Zeng, R., Peng, J., Li, A., Song, X., Li, H., Wu, D., & Li, L. (2020). Elevated CXorf67 Expression in PFA Ependymomas Suppresses DNA Repair and Sensitizes to PARP Inhibitors. *Cancer Cell*, *38*(6), 844-856.e7. https://doi.org/10.1016/j.ccell.2020.10.009

Hans, F., Senarisoy, M., Bhaskar Naidu, C., & Timmins, J. (2020). Focus on DNA Glycosylases—A Set of Tightly Regulated Enzymes with a High Potential as Anticancer Drug Targets. *International Journal of Molecular Sciences*, *21*(23), 9226. https://doi.org/10.3390/ijms21239226

Hashimoto, H. (2014). Structural and mutation studies of two DNA demethylation related glycosylases: MBD4 and TDG. *BIOPHYSICS*, *10*(0), 63–68. https://doi.org/10.2142/biophysics.10.63

Haynes, B., Saadat, N., Myung, B., & Shekhar, M. P. V. (2015). Crosstalk between translesion synthesis, Fanconi anemia network, and homologous recombination repair pathways in interstrand DNA crosslink repair and development of chemoresistance. *Mutation Research/Reviews in Mutation Research*, *763*, 258–266. https://doi.org/10.1016/j.mrrev.2014.11.005

Hegde, M. L., Hazra, T. K., & Mitra, S. (2008). Early steps in the DNA base excision/single-strand interruption repair pathway in mammalian cells. *Cell Research*, *18*(1), 27–47. https://doi.org/10.1038/cr.2008.8

Heo, S., Kim, S., & Kang, D. (2020). The Role of Hydrogen Peroxide and Peroxiredoxins throughout the Cell Cycle. *Antioxidants*, *9*(4), 280. https://doi.org/10.3390/antiox9040280

Heyza, J. R., Mikhova, M., Bahl, A., Broadbent, D. G., & Schmidt, J. C. (2023). Systematic analysis of the molecular and biophysical properties of key DNA damage response factors. *eLife*, *12*, e87086. https://doi.org/10.7554/eLife.87086

Hoencamp, C., & Rowland, B. D. (2023). Genome control by SMC complexes. *Nature Reviews Molecular Cell Biology*, *24*(9), 633–650. https://doi.org/10.1038/s41580-023-00609-8

Hsieh, P. (2001). Molecular mechanisms of DNA mismatch repair. *Mutation Research/DNA Repair*, *486*(2), 71–87. https://doi.org/10.1016/s0921-8777(01)00088-x

Hsieh, P., & Yamane, K. (2008). DNA mismatch repair: Molecular mechanism, cancer, and ageing. *Mechanisms of Ageing and Development*, *129*(7–8), 391–407. https://doi.org/10.1016/j.mad.2008.02.012

Hsieh, P., & Zhang, Y. (2017). The Devil is in the details for DNA mismatch repair. *Proceedings of the National Academy of Sciences*, *114*(14), 3552–3554. https://doi.org/10.1073/pnas.1702747114

Hu, J., De Souza-Pinto, N. C., Haraguchi, K., Hogue, B. A., Jaruga, P., Greenberg, M. M., Dizdaroglu, M., & Bohr, V. A. (2005). Repair of Formamidopyrimidines in DNA Involves Different Glycosylases. *Journal of Biological Chemistry*, *280*(49), 40544–40551. https://doi.org/10.1074/jbc.m508772200

Huang, B. (2010). Super-resolution optical microscopy: Multiple choices. *Current Opinion in Chemical Biology*, *14*(1), 10–14. https://doi.org/10.1016/j.cbpa.2009.10.013

Huang, H., Lin, S., Garcia, B. A., & Zhao, Y. (2015). Quantitative Proteomic Analysis of Histone Modifications. *Chemical Reviews*, *115*(6), 2376–2418. https://doi.org/10.1021/cr500491u

Huang, R., & Zhou, P.-K. (2021). DNA damage repair: Historical perspectives, mechanistic pathways and clinical translation for targeted cancer therapy. *Signal Transduction and Targeted Therapy*, *6*(1), 254. https://doi.org/10.1038/s41392-021-00648-7

Huang, Y., & Li, G.-M. (2020). DNA mismatch repair in the chromatin context: Mechanisms and therapeutic potential. *DNA Repair*, *93*, 102918. https://doi.org/10.1016/j.dnarep.2020.102918

Hubers, L., Skjetne, A. M., Luna, L., Lefol, Y., Lund, S. O., Wågbø, A. M., Renaudin, X., Polster, A., Berg-Eriksen, A. K., Naranjo-Galindo, F. J., Campalans, A., Visnes, T., Nilsen, H. L., & Montaldo, N. P. (2024). *Functional Impact of Nth-like DNA glycosylase on Mitochondrial Dynamics*. https://doi.org/10.1101/2024.10.10.617535

Ikeda, S., Biswas, T., Roy, R., Izumi, T., Boldogh, I., Kurosky, A., Sarker, A. H., Seki, S., & Mitra, S. (1998). Purification and Characterization of Human NTH1, a Homolog ofEscherichia coli Endonuclease III. *Journal of Biological Chemistry*, *273*(34), 21585–21593. https://doi.org/10.1074/jbc.273.34.21585

Ikeda, S., Kohmoto, T., Tabata, R., & Seki, Y. (2002). Differential intracellular localization of the human and mouse endonuclease III homologs and analysis of the sorting signals. *DNA Repair*, *1*(10), 847–854. https://doi.org/10.1016/S1568-7864(02)00145-3

Jackson, S. P., & Bartek, J. (2009). The DNA-damage response in human biology and disease. *Nature*, *461*(7267), 1071–1078. https://doi.org/10.1038/nature08467

Jacobs, A. L., & Schär, P. (2012). DNA glycosylases: In DNA repair and beyond. *Chromosoma*, *121*(1), 1–20. https://doi.org/10.1007/s00412-011-0347-4

Jensen, N. M., Dalsgaard, T., Jakobsen, M., Nielsen, R. R., Sørensen, C. B., Bolund, L., & Jensen, T. G. (2011). An update on targeted gene repair in mammalian cells: Methods and mechanisms. *Journal of Biomedical Science*, *18*(1), 10. https://doi.org/10.1186/1423-0127-18-10

Johnstone, C. P., Wang, N. B., Sevier, S. A., & Galloway, K. E. (2020). Understanding and Engineering Chromatin as a Dynamical System across Length and Timescales. *Cell Systems*, *11*(5), 424–448. https://doi.org/10.1016/j.cels.2020.09.011

Kar, A., Degtyareva, N. P., & Doetsch, P. W. (2024). Human NTHL1 expression and subcellular distribution determines cisplatin sensitivity in human lung epithelial and non-small cell lung cancer cells. *NAR Cancer*, *6*(1), zcae006. https://doi.org/10.1093/narcan/zcae006

Karahalil, B., De Souza-Pinto, N. C., Parsons, J. L., Elder, R. H., & Bohr, V. A. (2003). Compromised Incision of Oxidized Pyrimidines in Liver Mitochondria of Mice Deficient in NTH1 and OGG1 Glycosylases. *Journal of Biological Chemistry*, *278*(36), 33701–33707. https://doi.org/10.1074/jbc.m301617200

Kawanishi, S., & Murata, M. (2006). Mechanism of DNA damage induced by bromate differs from general types of oxidative stress. *Toxicology*, *221*(2–3), 172–178. https://doi.org/10.1016/j.tox.2006.01.002

Kciuk, M., Marciniak, B., Mojzych, M., & Kontek, R. (2020). Focus on UV-Induced DNA Damage and Repair—Disease Relevance and Protective Strategies. *International Journal of Molecular Sciences*, *21*(19), 7264. https://doi.org/10.3390/ijms21197264

Kellner, V., & Luke, B. (2020). Molecular and physiological consequences of faulty eukaryotic ribonucleotide excision repair. *The EMBO Journal*, *39*(3), e102309. https://doi.org/10.15252/embj.2019102309

Kemmerich, K., Dingler, F. A., Rada, C., & Neuberger, M. S. (2012). Germline ablation of SMUG1 DNA glycosylase causes loss of 5-hydroxymethyluracil- and UNG-backup uracil-excision activities and increases cancer predisposition of Ung−/−Msh2−/− mice. *Nucleic Acids Research*, *40*(13), 6016–6025. https://doi.org/10.1093/nar/gks259

Kim, H., & Pak, Y. (2024a). Free Energy Landscape of Lesion Recognition by Human 8-Oxoguanine DNA N-Glycosylase 1: Mechanistic Insights into Detection and Processing of 8-Oxoguanine in DNA. *The Journal of Physical Chemistry B*, *128*(49), 12133–12142. https://doi.org/10.1021/acs.jpcb.4c07073

Kim, H., & Pak, Y. (2024b). Three-State Diffusion Model of DNA Glycosylase Translocation along Stretched DNA as Revealed by Free Energy Landscapes at the All-Atom Level. *Journal of Chemical Theory and Computation*, *20*(6), 2666–2675. https://doi.org/10.1021/acs.jctc.4c00043

Kladova, O. A., Bazlekowa-Karaban, M., Baconnais, S., Piétrement, O., Ishchenko, A. A., Matkarimov, B. T., Iakovlev, D. A., Vasenko, A., Fedorova, O. S., Le Cam, E., Tudek, B., Kuznetsov, N. A., & Saparbaev, M. (2018). The role of the N-terminal domain of human apurinic/apyrimidinic endonuclease 1, APE1, in DNA glycosylase stimulation. *DNA Repair*, *64*, 10–25. https://doi.org/10.1016/j.dnarep.2018.02.001

Klungland, A., Höss, M., Gunz, D., Constantinou, A., Clarkson, S. G., Doetsch, P. W., Bolton, P. H., Wood, R. D., & Lindahl, T. (1999). Base Excision Repair of Oxidative DNA Damage Activated by XPG Protein. *Molecular Cell*, *3*(1), 33–42. https://doi.org/10.1016/s1097-2765(00)80172-0

Konis, S. M. R., Hughes, J. R., & Parsons, J. L. (2022). TRIM26 Maintains Cell Survival in Response to Oxidative Stress through Regulating DNA Glycosylase Stability. *International Journal of Molecular Sciences*, *23*(19), 11613. https://doi.org/10.3390/ijms231911613

Kornberg, R. D. (1974). Chromatin Structure: A Repeating Unit of Histones and DNA: Chromatin structure is based on a repeating unit of eight histone molecules and about 200 DNA base pairs. *Science*, *184*(4139), 868–871. https://doi.org/10.1126/science.184.4139.868

Kornberg, R. D., & Lorch, Y. (1999). Twenty-Five Years of the Nucleosome, Fundamental Particle of the Eukaryote Chromosome. *Cell*, *98*(3), 285–294. https://doi.org/10.1016/S0092-8674(00)81958-3

Kothandapani, A., Dangeti, V. S. M. N., Brown, A. R., Banze, L. A., Wang, X.-H., Sobol, R. W., & Patrick, S. M. (2011). Novel Role of Base Excision Repair in Mediating Cisplatin Cytotoxicity. *Journal of Biological Chemistry*, *286*(16), 14564–14574. https://doi.org/10.1074/jbc.M111.225375

Krokan, H. E., & Bjoras, M. (2013). Base Excision Repair. *Cold Spring Harbor Perspectives in Biology*, *5*(4), a012583–a012583. https://doi.org/10.1101/cshperspect.a012583

Kumar, N., Theil, A. F., Roginskaya, V., Ali, Y., Calderon, M., Watkins, S. C., Barnes, R. P., Opresko, P. L., Pines, A., Lans, H., Vermeulen, W., & Van Houten, B. (2022). Global and transcription-coupled repair of 8-oxoG is initiated by nucleotide excision repair proteins. *Nature Communications*, *13*(1), 974. https://doi.org/10.1038/s41467-022-28642-9

Kumar, R., Horikoshi, N., Singh, M., Gupta, A., Misra, H. S., Albuquerque, K., Hunt, C. R., & Pandita, T. K. (2013). Chromatin modifications and the DNA damage response to ionizing radiation. *Frontiers in Oncology*, *2*. https://doi.org/10.3389/fonc.2012.00214

Larson, A. G., Elnatan, D., Keenen, M. M., Trnka, M. J., Johnston, J. B., Burlingame, A. L., Agard, D. A., Redding, S., & Narlikar, G. J. (2017). Liquid droplet formation by HP1α suggests a role for phase separation in heterochromatin. *Nature*, *547*(7662), 236–240. https://doi.org/10.1038/nature22822

Lebraud, E., Pinna, G., Siberchicot, C., Depagne, J., Busso, D., Fantini, D., Irbah, L., Robeska, E., Kratassiouk, G., Ravanat, J.-L., Epe, B., Radicella, J. P., & Campalans, A. (2020). Chromatin recruitment of OGG1 requires cohesin and mediator and is essential for efficient 8-oxoG removal. *Nucleic Acids Research*, *48*(16), 9082–9097. https://doi.org/10.1093/nar/gkaa611

Lelek, M., Gyparaki, M. T., Beliu, G., Schueder, F., Griffié, J., Manley, S., Jungmann, R., Sauer, M., Lakadamyali, M., & Zimmer, C. (2021). Single-molecule localization microscopy. *Nature Reviews Methods Primers*, *1*(1), 39. https://doi.org/10.1038/s43586-021-00038-x

Levet, F. (2023). Optimizing Voronoi-based quantifications for reaching interactive analysis of 3D localizations in the million range. *Frontiers in Bioinformatics*, *3*, 1249291. https://doi.org/10.3389/fbinf.2023.1249291

Levet, F., Hosy, E., Kechkar, A., Butler, C., Beghin, A., Choquet, D., & Sibarita, J.-B. (2015). SR-Tesseler: A method to segment and quantify localization-based super-resolution microscopy data. *Nature Methods*, *12*(11), 1065–1071. https://doi.org/10.1038/nmeth.3579

Limpose, K. L., Trego, K. S., Li, Z., Leung, S. W., Sarker, A. H., Shah, J. A., Ramalingam, S. S., Werner, E. M., Dynan, W. S., Cooper, P. K., Corbett, A. H., & Doetsch, P. W. (2018). Overexpression of the base excision repair NTHL1 glycosylase causes genomic instability and early cellular hallmarks of cancer. *Nucleic Acids Research*, *46*(9), 4515–4532. https://doi.org/10.1093/nar/gky162

Lindahl, T. (1993). Instability and decay of the primary structure of DNA. *Nature*, *362*(6422), 709–715. https://doi.org/10.1038/362709a0

Lindahl, T., & Barnes, D. E. (2000). Repair of Endogenous DNA Damage. *Cold Spring Harbor Symposia on Quantitative Biology*, *65*(0), 127–134. https://doi.org/10.1101/sqb.2000.65.127

Liu, M., Doublié, S., & Wallace, S. S. (2013). Neil3, the final frontier for the DNA glycosylases that recognize oxidative damage. *Mutation Research/Fundamental and Molecular Mechanisms of Mutagenesis*, *743–744*, 4–11. https://doi.org/10.1016/j.mrfmmm.2012.12.003

Liu, X., Choudhury, S., & Roy, R. (2003). In Vitro and in Vivo Dimerization of Human Endonuclease III Stimulates Its Activity. *Journal of Biological Chemistry*, *278*(50), 50061–50069. https://doi.org/10.1074/jbc.M309997200

Liu, X., & Roy, R. (2001). Mutation at Active Site Lysine 212 to Arginine Uncouples the Glycosylase Activity from the Lyase Activity of Human Endonuclease III. *Biochemistry*, *40*(45), 13617–13622. https://doi.org/10.1021/bi011053b

Lovell, M. A., Xie, C., & Markesbery, W. R. (2000). Decreased base excision repair and increased helicase activity in Alzheimer's disease brain. *Brain Research*, *855*(1), 116–123. https://doi.org/10.1016/S0006-8993(99)02335-5

Luger, K. (1997). *Crystal structure of the nucleosome core particle at 2.8 A˚ resolution*. *389*.

Lukianova, O. A., & David, S. S. (2005). A role for iron–sulfur clusters in DNA repair. *Current Opinion in Chemical Biology*, *9*(2), 145–151. https://doi.org/10.1016/j.cbpa.2005.02.006

Luna, L., Bjørås, M., Hoff, E., Rognes, T., & Seeberg, E. (2000). Cell-cycle regulation, intracellular sorting and induced overexpression of the human NTH1 DNA glycosylase involved in removal of formamidopyrimidine residues from DNA. *Mutation Research/DNA Repair*, *460*(2), 95–104. https://doi.org/10.1016/S0921-8777(00)00015-X

Madders, E. C. E. T., & Parsons, J. L. (2020). Base Excision Repair in Chromatin and the Requirement for Chromatin Remodelling. In D. O. Zharkov (Ed.), *Mechanisms of Genome Protection and Repair* (Vol. 1241, pp. 59–75). Springer International Publishing. https://doi.org/10.1007/978-3-030-41283-8_5

Maher, R. L., Prasad, A., Rizvanova, O., Wallace, S. S., & Pederson, D. S. (2013). Contribution of DNA unwrapping from histone octamers to the repair of oxidatively damaged DNA in nucleosomes. *DNA Repair*, *12*(11), 964–971. https://doi.org/10.1016/j.dnarep.2013.08.010

Manuelidis, L. (1985). Individual interphase chromosome domains revealed by in situ hybridization. *Human Genetics*, *71*(4), 288–293. https://doi.org/10.1007/BF00388453

Manzo, C., & Garcia-Parajo, M. F. (2015). A review of progress in single particle tracking: From methods to biophysical insights. *Reports on Progress in Physics*, *78*(12), 124601. https://doi.org/10.1088/0034-4885/78/12/124601

Marenstein, D. R., Chan, M. K., Altamirano, A., Basu, A. K., Boorstein, R. J., Cunningham, R. P., & Teebor, G. W. (2003). Substrate Specificity of Human Endonuclease III (hNTH1). *Journal of Biological Chemistry*, *278*(11), 9005–9012. https://doi.org/10.1074/jbc.m212168200

Marenstein, D. R., Ocampo, MariaT. A., Chan, MichaelK., Altamirano, A., Basu, AshisK., Boorstein, RobertJ., Cunningham, R. P., & Teebor, GeorgeW. (2001). Stimulation of Human Endonuclease III by Y Box-binding Protein 1 (DNA-binding Protein B). *Journal of Biological Chemistry*, *276*(24), 21242–21249. https://doi.org/10.1074/jbc.m101594200

Marsden, C. G., Jaruga, P., Coskun, E., Maher, R. L., Pederson, D. S., Dizdaroglu, M., & Sweasy, J. B. (2020). Expression of a germline variant in the N-terminal domain of the human DNA glycosylase NTHL1 induces cellular transformation without impairing enzymatic function or substrate specificity. *Oncotarget*, *11*(24), 2262–2272. https://doi.org/10.18632/oncotarget.27548

Marteijn, J. A., Lans, H., Vermeulen, W., & Hoeijmakers, J. H. J. (2014). Understanding nucleotide excision repair and its roles in cancer and ageing. *Nature Reviews Molecular Cell Biology*, *15*(7), 465–481. https://doi.org/10.1038/nrm3822

Mastrocola, A. S., Kim, S. H., Trinh, A. T., Rodenkirch, L. A., & Tibbetts, R. S. (2013). The RNA-binding Protein Fused in Sarcoma (FUS) Functions Downstream of Poly(ADP-ribose) Polymerase (PARP) in Response to DNA Damage. *Journal of Biological Chemistry*, *288*(34), 24731–24741. https://doi.org/10.1074/jbc.M113.497974

Mazzocca, M., Narducci, D. N., Grosse-Holz, S., & Matthias, J. (2025). *Chromatin Dynamics are Highly Subdiffusive Across Seven Orders of Magnitude*.

McSwiggen, D. T., Mir, M., Darzacq, X., & Tjian, R. (2019). Evaluating phase separation in live cells: Diagnosis, caveats, and functional consequences. *Genes & Development*, *33*(23–24), 1619–1634. https://doi.org/10.1101/gad.331520.119

Mei, C., Lei, L., Tan, L.-M., Xu, X.-J., He, B.-M., Luo, C., Yin, J.-Y., Li, X., Zhang, W., Zhou, H.-H., & Liu, Z.-Q. (2020). The role of single strand break repair pathways in cellular responses to camptothecin induced DNA damage. *Biomedicine & Pharmacotherapy*, *125*, 109875. https://doi.org/10.1016/j.biopha.2020.109875

Menoni, H., Wienholz, F., Theil, A. F., Janssens, R. C., Lans, H., Campalans, A., Radicella, J. P., Marteijn, J. A., & Vermeulen, W. (2018). The transcription-coupled DNA repair-initiating protein CSB promotes XRCC1 recruitment to oxidative DNA damage. *Nucleic Acids Research*, *46*(15), 7747–7756. https://doi.org/10.1093/nar/gky579

Miné-Hattab, J., Heltberg, M., Villemeur, M., Guedj, C., Mora, T., Walczak, A. M., Dahan, M., & Taddei, A. (2021). Single molecule microscopy reveals key physical features of repair foci in living cells. *eLife*, *10*, e60577. https://doi.org/10.7554/eLife.60577

Miriklis, E. L., Rozario, A. M., Rothenberg, E., Bell, T. D. M., & Whelan, D. R. (2021). Understanding DNA organization, damage, and repair with super-resolution fluorescence microscopy. *Methods and Applications in Fluorescence*, *9*(3), 032002. https://doi.org/10.1088/2050-6120/abf239

Misteli, T. (2001). Protein Dynamics: Implications for Nuclear Architecture and Gene Expression. *Science*, *291*(5505), 843–847. https://doi.org/10.1126/science.291.5505.843

Misteli, T. (2020). The Self-Organizing Genome: Principles of Genome Architecture and Function. *Cell*, *183*(1), 28–45. https://doi.org/10.1016/j.cell.2020.09.014

Mitra, J., Guerrero, E. N., Hegde, P. M., Liachko, N. F., Wang, H., Vasquez, V., Gao, J., Pandey, A., Taylor, J. P., Kraemer, B. C., Wu, P., Boldogh, I., Garruto, R. M., Mitra, S., Rao, K. S., & Hegde, M. L. (2019). Motor neuron disease-associated loss of nuclear TDP-43 is linked to DNA double-strand break repair defects. *Proceedings of the National Academy of Sciences*, *116*(10), 4696–4705. https://doi.org/10.1073/pnas.1818415116

Mittag, T., & Pappu, R. V. (2022). A conceptual framework for understanding phase separation and addressing open questions and challenges. *Molecular Cell*, *82*(12), 2201–2214. https://doi.org/10.1016/j.molcel.2022.05.018

Moe, E., Silveira, C. M., Zuccarello, L., Rollo, F., Stelter, M., De Bonis, S., Kulka-Peschke, C., Katz, S., Hildebrandt, P., Zebger, I., Timmins, J., & Todorovic, S. (2022). Human endonuclease III/NTH1: Focusing on the [4Fe–4S] cluster and the N-terminal domain. *Chemical Communications*, *58*(90), 12568–12571. https://doi.org/10.1039/D2CC03643F

Murakami, T., Nagai, M., Miyazaki, K., Morimoto, N., Ohta, Y., Kurata, T., Takehisa, Y., Kamiya, T., & Abe, K. (2007). Early decrease of mitochondrial DNA repair enzymes in spinal motor neurons of presymptomatic transgenic mice carrying a mutant SOD1 gene. *Brain Research*, *1150*, 182–189. https://doi.org/10.1016/j.brainres.2007.02.057

Nakamura, H., & Takada, K. (2021). Reactive oxygen species in cancer: Current findings and future directions. *Cancer Science*, *112*(10), 3945–3952. https://doi.org/10.1111/cas.15068

Nakamura, T., Okabe, K., Hirayama, S., Chirifu, M., Ikemizu, S., Morioka, H., Nakabeppu, Y., & Yamagata, Y. (2021). Structure of the mammalian adenine DNA glycosylase MUTYH: Insights into the base excision repair pathway and cancer. *Nucleic Acids Research*, *49*(12), 7154–7163. https://doi.org/10.1093/nar/gkab492

Nieves, D. J., Gaus, K., & Baker, M. A. B. (2018). DNA-Based Super-Resolution Microscopy: DNA-PAINT. *Genes*, *9*(12), 621. https://doi.org/10.3390/genes9120621

Nozaki, T., Imai, R., Tanbo, M., Nagashima, R., Tamura, S., Tani, T., Joti, Y., Tomita, M., Hibino, K., Kanemaki, M. T., Wendt, K. S., Okada, Y., Nagai, T., & Maeshima, K. (2017). Dynamic Organization of Chromatin Domains Revealed by Super-Resolution Live-Cell Imaging. *Molecular Cell*, *67*(2), 282-293.e7. https://doi.org/10.1016/j.molcel.2017.06.018

Obmolova, G., Ban, C., Hsieh, P., & Yang, W. (2000). Crystal structures of mismatch repair protein MutS and its complex with a substrate DNA. *Nature*, *407*(6805), 703–710. https://doi.org/10.1038/35037509

O'Brie, P. J., & Ellenberger, T. (2003). Human Alkyladenine DNA Glycosylase Uses Acid−Base Catalysis for Selective Excision of Damaged Purines. *Biochemistry*, *42*(42), 12418–12429. https://doi.org/10.1021/bi035177v

Odell, I. D., Wallace, S. S., & Pederson, D. S. (2013). Rules of engagement for base excision repair in chromatin. *Journal of Cellular Physiology*, *228*(2), 258–266. https://doi.org/10.1002/jcp.24134

Odstrcil, R. E., Dutta, P., & Liu, J. (2024). Enhanced Sampling for Conformational Changes and Molecular Mechanisms of Human NTHL1. *The Journal of Physical Chemistry Letters*, *15*(11), 3206–3213. https://doi.org/10.1021/acs.jpclett.4c00161

Osman, F., Bjørås, M., Alseth, I., Morland, I., McCready, S., Seeberg, E., & Tsaneva, I. (2003). A new *Schizosaccharomyces pombe* base excision repair mutant, *nth1*, reveals overlapping pathways for repair of DNA base damage. *Molecular Microbiology*, *48*(2), 465–480. https://doi.org/10.1046/j.1365-2958.2003.03440.x

Ovesný, M., Křížek, P., Borkovec, J., Švindrych, Z., & Hagen, G. M. (2014). ThunderSTORM: A comprehensive ImageJ plug-in for PALM and STORM data analysis and super-resolution imaging. *Bioinformatics*, *30*(16), 2389–2390. https://doi.org/10.1093/bioinformatics/btu202

Oyama, M., Wakasugi, M., Hama, T., Hashidume, H., Iwakami, Y., Imai, R., Hoshino, S., Morioka, H., Ishigaki, Y., Nikaido, O., & Matsunaga, T. (2004). Human NTH1 physically interacts with p53 and proliferating cell nuclear antigen. *Biochemical and Biophysical Research Communications*, *321*(1), 183–191. https://doi.org/10.1016/j.bbrc.2004.06.136

Pachkowski, B. F., Tano, K., Afonin, V., Elder, R. H., Takeda, S., Watanabe, M., Swenberg, J. A., & Nakamura, J. (2009). Cells deficient in PARP-1 show an accelerated accumulation of DNA single strand breaks, but not AP sites, over the PARP-1-proficient cells exposed to MMS. *Mutation Research/Fundamental and Molecular Mechanisms of Mutagenesis*, *671*(1–2), 93–99. https://doi.org/10.1016/j.mrfmmm.2009.09.006

Parteka-Tojek, Z., Zhu, J. J., Lee, B., Jodkowska, K., Wang, P., Aaron, J., Chew, T.-L., Banecki, K., Plewczynski, D., & Ruan, Y. (2022). Super-resolution visualization of chromatin loop folding

in human lymphoblastoid cells using interferometric photoactivated localization microscopy. *Scientific Reports*, *12*(1), 8582. https://doi.org/10.1038/s41598-022-12568-9

Patel, A., Lee, H. O., Jawerth, L., Maharana, S., Jahnel, M., Hein, M. Y., Stoynov, S., Mahamid, J., Saha, S., Franzmann, T. M., Pozniakovski, A., Poser, I., Maghelli, N., Royer, L. A., Weigert, M., Myers, E. W., Grill, S., Drechsel, D., Hyman, A. A., & Alberti, S. (2015). A Liquid-to-Solid Phase Transition of the ALS Protein FUS Accelerated by Disease Mutation. *Cell*, *162*(5), 1066–1077. https://doi.org/10.1016/j.cell.2015.07.047

Pettersen, H. S., Sundheim, O., Gilljam, K. M., Slupphaug, G., Krokan, H. E., & Kavli, B. (2007). Uracil–DNA glycosylases SMUG1 and UNG2 coordinate the initial steps of base excision repair by distinct mechanisms. *Nucleic Acids Research*, *35*(12), 3879–3892. https://doi.org/10.1093/nar/gkm372

Pidugu, L. S., Servius, H. W., Espinosa, K. B., Cook, M. E., Varney, K. M., & Drohat, A. C. (2024). Sumoylation of thymine DNA glycosylase impairs productive binding to substrate sites in DNA. *Journal of Biological Chemistry*, *300*(11), 107902. https://doi.org/10.1016/j.jbc.2024.107902

Pinto, C., Guerra, J., Pinheiro, M., Escudeiro, C., Santos, C., Pinto, P., Porto, M., Bartosch, C., Silva, J., Peixoto, A., & Teixeira, M. R. (2023). Combined germline and tumor mutation signature testing identifies new families with NTHL1 tumor syndrome. *Frontiers in Genetics*, *14*. https://doi.org/10.3389/fgene.2023.1254908

Poepsel, S., Kasinath, V., & Nogales, E. (2018). Cryo-EM structures of PRC2 simultaneously engaged with two functionally distinct nucleosomes. *Nature Structural & Molecular Biology*, *25*(2), 154–162. https://doi.org/10.1038/s41594-018-0023-y

Pommier, Y., Nussenzweig, A., Takeda, S., & Austin, C. (2022). Human topoisomerases and their roles in genome stability and organization. *Nature Reviews Molecular Cell Biology*, *23*(6), 407–427. https://doi.org/10.1038/s41580-022-00452-3

Prasad, A., Wallace, S. S., & Pederson, D. S. (2007). Initiation of Base Excision Repair of Oxidative Lesions in Nucleosomes by the Human, Bifunctional DNA Glycosylase NTH1. *Molecular and Cellular Biology*, *27*(24), 8442–8453. https://doi.org/10.1128/MCB.00791-07

Putnam, C. D. (2021). Strand discrimination in DNA mismatch repair. *DNA Repair*, *105*, 103161. https://doi.org/10.1016/j.dnarep.2021.103161

Radman, M. (1975). Endonuclease III: An Endonuclease from Escherichia coli That Introduces Single Polynucleotide Chain Scissions in Ultraviolet-Irradiated DNA. In P. C. Hanawalt & R. B. Setlow (Eds.), *Molecular Mechanisms for Repair of DNA* (pp. 197–200). Springer US. https://doi.org/10.1007/978-1-4684-2895-7_24

Rahman, F., Augoustides, V., Tyler, E., Daugird, T. A., Arthur, C., & Legant, W. R. (2024). *Mapping the nuclear landscape with multiplexed super-resolution fluorescence microscopy*. https://doi.org/10.1101/2024.07.27.605159

Rao, K. S., Annapurna, V. V., & Raji, N. S. (n.d.). *DNA Polymerase-ϰ May Be the Main Player for Defective DNA Repair in Aging Rat Neurons*.

Rathnaiah, G., & Sweasy, J. B. (2025). Protein–Protein Interactions in Base Excision Repair. *Biomolecules*, *15*(6), 890. https://doi.org/10.3390/biom15060890

Ray Chaudhuri, A., & Nussenzweig, A. (2017). The multifaceted roles of PARP1 in DNA repair and chromatin remodelling. *Nature Reviews Molecular Cell Biology*, *18*(10), 610–621. https://doi.org/10.1038/nrm.2017.53

Ricci, M. A., Manzo, C., García-Parajo, M. F., Lakadamyali, M., & Cosma, M. P. (2015). Chromatin Fibers Are Formed by Heterogeneous Groups of Nucleosomes In Vivo. *Cell*, *160*(6), 1145–1158. https://doi.org/10.1016/j.cell.2015.01.054

Robeska, E., Lalanne, K., Vianna, F., Sutcu, H. H., Khobta, A., Busso, D., Radicella, J. P., Campalans, A., & Baldeyron, C. (2024). Targeted nuclear irradiation with a proton microbeam induces oxidative DNA base damage and triggers the recruitment of DNA glycosylases OGG1 and NTH1. *DNA Repair*, *133*, 103610. https://doi.org/10.1016/j.dnarep.2023.103610

Rodriguez, J., & Larson, D. R. (2020). Transcription in Living Cells: Molecular Mechanisms of Bursting. *Annual Review of Biochemistry*, *89*(1), 189–212. https://doi.org/10.1146/annurev-biochem-011520-105250

Rodriguez, Y., Duan, M., Wyrick, J. J., & Smerdon, M. J. (2018). A cassette of basic amino acids in histone H2B regulates nucleosome dynamics and access to DNA damage. *Journal of Biological Chemistry*, *293*(19), 7376–7386. https://doi.org/10.1074/jbc.ra117.000358

Rong, Z., Tu, P., Xu, P., Sun, Y., Yu, F., Tu, N., Guo, L., & Yang, Y. (2021). The Mitochondrial Response to DNA Damage. *Frontiers in Cell and Developmental Biology*, *9*. https://doi.org/10.3389/fcell.2021.669379

Rowley, M. J., & Corces, V. G. (2018). Organizational principles of 3D genome architecture. *Nature Reviews Genetics*, *19*(12), 789–800. https://doi.org/10.1038/s41576-018-0060-8

Roy, S. (2017). Impact of UV Radiation on Genome Stability and Human Health. In S. I. Ahmad (Ed.), *Ultraviolet Light in Human Health, Diseases and Environment* (Vol. 996, pp. 207–219). Springer International Publishing. https://doi.org/10.1007/978-3-319-56017-5_17

Rust, M. J., Bates, M., & Zhuang, X. (2006). Sub-diffraction-limit imaging by stochastic optical reconstruction microscopy (STORM). *Nature Methods*, *3*(10), 793–796. https://doi.org/10.1038/nmeth929

Sakaue-Sawano, A., Kobayashi, T., Ohtawa, K., & Miyawaki, A. (2011). Drug-induced cell cycle modulation leading to cell-cycle arrest, nuclear mis-segregation, or endoreplication. *BMC Cell Biology*, *12*(1), 1–12. https://doi.org/10.1186/1471-2121-12-2

Sampath, H., McCullough, A. K., & Lloyd, R. S. (2012). Regulation of DNA glycosylases and their role in limiting disease. *Free Radical Research*, *46*(4), 460–478. https://doi.org/10.3109/10715762.2012.655730

Sangermano, F., Delicato, A., & Calabrò, V. (2020). Y box binding protein 1 (YB-1) oncoprotein at the hub of DNA proliferation, damage and cancer progression. *Biochimie*, *179*, 205–216. https://doi.org/10.1016/j.biochi.2020.10.004

Sarmini, L., Meabed, M., Emmanouil, E., Atsaves, G., Robeska, E., Karwowski, B. T., Campalans, A., Gimisis, T., & Khobta, A. (2023). Requirement of transcription-coupled nucleotide excision repair for the removal of a specific type of oxidatively induced DNA damage. *Nucleic Acids Research*, *51*(10), 4982–4994. https://doi.org/10.1093/nar/gkad256

Sarre, A., Stelter, M., Rollo, F., De Bonis, S., Seck, A., Hognon, C., Ravanat, J.-L., Monari, A., Dehez, F., Moe, E., & Timmins, J. (2019). The three Endonuclease III variants of Deinococcus radiodurans possess distinct and complementary DNA repair activities. *DNA Repair*, *78*, 45–59. https://doi.org/10.1016/j.dnarep.2019.03.014

Saxton, M. J. (1997). Single-particle tracking: The distribution of diffusion coefficients. *Biophysical Journal*, *72*(4), 1744–1753. https://doi.org/10.1016/S0006-3495(97)78820-9

Schaich, M. A., Schnable, B. L., Kumar, N., Roginskaya, V., Jakielski, R. C., Urban, R., Zhong, Z., Kad, N. M., & Van Houten, B. (2023). Single-molecule analysis of DNA-binding proteins from nuclear extracts (SMADNE). *Nucleic Acids Research*, *51*(7), e39–e39. https://doi.org/10.1093/nar/gkad095

Schaich, M. A., & Van Houten, B. (2021). Searching for DNA Damage: Insights From Single Molecule Analysis. *Frontiers in Molecular Biosciences*, *8*. https://doi.org/10.3389/fmolb.2021.772877

Schaich, M. A., Weaver, T. M., Roginskaya, V., Freudenthal, B. D., & Van Houten, B. (2024). Single-molecule analysis of purified proteins and nuclear extracts: Insights from 8-oxoguanine glycosylase 1. *DNA Repair*, *134*, 103625. https://doi.org/10.1016/j.dnarep.2024.103625

Schnable, B. L., Schaich, M. A., Roginskaya, V., Leary, L. P., Weaver, T. M., Freudenthal, B. D., Drohat, A. C., & Van Houten, B. (2024). Thymine DNA glycosylase combines sliding, hopping, and nucleosome interactions to efficiently search for 5-formylcytosine. *Nature Communications*, *15*(1), 9226. https://doi.org/10.1038/s41467-024-53497-7

Senarisoy, M., Barette, C., Lacroix, F., De Bonis, S., Stelter, M., Hans, F., Kleman, J.-P., Fauvarque, M.-O., & Timmins, J. (2020). Förster Resonance Energy Transfer Based Biosensor for Targeting the hNTH1–YB1 Interface as a Potential Anticancer Drug Target. *ACS Chemical Biology*, *15*(4), 990–1003. https://doi.org/10.1021/acschembio.9b01023

SenGupta, T., Palikaras, K., Esbensen, Y. Q., Konstantinidis, G., Galindo, F. J. N., Achanta, K., Kassahun, H., Stavgiannoudaki, I., Bohr, V. A., Akbari, M., Gaare, J., Tzoulis, C., Tavernarakis, N., & Nilsen, H. (2021). Base excision repair causes age-dependent

accumulation of single-stranded DNA breaks that contribute to Parkinson disease pathology. *Cell Reports*, *36*(10), 109668. https://doi.org/10.1016/j.celrep.2021.109668

Sergeeva, S. V., Loshchenova, P. S., Oshchepkov, D. Yu., & Orishchenko, K. E. (2024). Crosstalk between BER and NHEJ in XRCC4-Deficient Cells Depending on hTERT Overexpression. *International Journal of Molecular Sciences*, *25*(19), 10405. https://doi.org/10.3390/ijms251910405

Shao, X., Lv, N., Liao, J., Long, J., Xue, R., Ai, N., Xu, D., & Fan, X. (2019). Copy number variation is highly correlated with differential gene expression: A pan-cancer study. *BMC Medical Genetics*, *20*(1). https://doi.org/10.1186/s12881-019-0909-5

Shaw, A., Ajit, K., & Gullerova, M. (2024). *Y RNA-derived fragments in a complex with YBX1 modulate PARP1 residency at DNA double strand breaks*. https://doi.org/10.1101/2024.06.18.599493

Slyskova, J., Muniesa-Vargas, A., da Silva, I. T., Drummond, R., Park, J., Häckes, D., Poetsch, I., Ribeiro-Silva, C., Moretton, A., Heffeter, P., Schärer, O. D., Vermeulen, W., Lans, H., & Loizou, J. I. (2023). Detection of oxaliplatin- and cisplatin-DNA lesions requires different global genome repair mechanisms that affect their clinical efficacy. *NAR Cancer*, *5*(4), zcad057. https://doi.org/10.1093/narcan/zcad057

Slyskova, J., Sabatella, M., Ribeiro-Silva, C., Stok, C., Theil, A. F., Vermeulen, W., & Lans, H. (2018). Base and nucleotide excision repair facilitate resolution of platinum drugs-induced transcription blockage. *Nucleic Acids Research*, *46*(18), 9537–9549. https://doi.org/10.1093/nar/gky764

Song, Q., Hu, Y., Yin, A., Wang, H., & Yin, Q. (2022). DNA Holliday Junction: History, Regulation and Bioactivity. *International Journal of Molecular Sciences*, *23*(17), 9730. https://doi.org/10.3390/ijms23179730

Spegg, V., & Altmeyer, M. (2021). Biomolecular condensates at sites of DNA damage: More than just a phase. *DNA Repair*, *106*, 103179. https://doi.org/10.1016/j.dnarep.2021.103179

Spruijt, E. (2023). Open questions on liquid–liquid phase separation. *Communications Chemistry*, *6*(1), 23. https://doi.org/10.1038/s42004-023-00823-7

Stracy, M., Schweizer, J., Sherratt, D. J., Kapanidis, A. N., Uphoff, S., & Lesterlin, C. (2021). Transient non-specific DNA binding dominates the target search of bacterial DNA-binding proteins. *Molecular Cell*, *81*(7), 1499-1514.e6. https://doi.org/10.1016/j.molcel.2021.01.039

Ström, C. E., Mortusewicz, O., Finch, D., Parsons, J. L., Lagerqvist, A., Johansson, F., Schultz, N., Erixon, K., Dianov, G. L., & Helleday, T. (2011). CK2 phosphorylation of XRCC1 facilitates dissociation from DNA and single-strand break formation during base excision repair. *DNA Repair*, *10*(9), 961–969. https://doi.org/10.1016/j.dnarep.2011.07.004

Su, J.-H., Zheng, P., Kinrot, S. S., Bintu, B., & Zhuang, X. (2020). Genome-Scale Imaging of the 3D Organization and Transcriptional Activity of Chromatin. *Cell*, *182*(6), 1641-1659.e26. https://doi.org/10.1016/j.cell.2020.07.032

Su, S., Zhang, Y., & Liu, P. (2020). Roles of Ubiquitination and SUMOylation in DNA Damage Response. *Current Issues in Molecular Biology*, 59–84. https://doi.org/10.21775/cimb.035.059

Szabo, Q., Donjon, A., Jerković, I., Papadopoulos, G. L., Cheutin, T., Bonev, B., Nora, E. P., Bruneau, B. G., Bantignies, F., & Cavalli, G. (2020). Regulation of single-cell genome organization into TADs and chromatin nanodomains. *Nature Genetics*, *52*(11), 1151–1157. https://doi.org/10.1038/s41588-020-00716-8

Takao, M. (2002). Novel nuclear and mitochondrial glycosylases revealed by disruption of the mouse Nth1 gene encoding an endonuclease III homolog for repair of thymine glycols. *The EMBO Journal*, *21*(13), 3486–3493. https://doi.org/10.1093/emboj/cdf350

Takao, M., Aburatani, H., Kobayashi, K., & Yasui, A. (1998). Mitochondrial targeting of human DNA glycosylases for repair of oxidative DNA damage. *Nucleic Acids Research*, *26*(12), 2917–2922. https://doi.org/10.1093/nar/26.12.2917

Thayer, M. M., Ahern, H., Xing, D., Cunningham, R. P., & Tainer, J. A. (1995). Novel DNA binding motifs in the DNA repair enzyme endonuclease III crystal structure. *The EMBO Journal*, *14*(16), 4108–4120. https://doi.org/10.1002/j.1460-2075.1995.tb00083.x

Thompson, L. H., Busch, D. B., Brookman, K., Mooney, C. L., & Glaser, D. A. (1981). Genetic diversity of UV-sensitive DNA repair mutants of Chinese hamster ovary cells. *Proceedings of the National Academy of Sciences*, *78*(6), 3734–3737. https://doi.org/10.1073/pnas.78.6.3734

Tiwari, V., Buvarp, E., Borbolis, F., Puligilla, C., Croteau, D. L., Palikaras, K., & Bohr, V. A. (2024). Loss of DNA glycosylases improves health and cognitive function in a *C. elegans* model of human tauopathy. *Nucleic Acids Research*, *52*(18), 10965–10985. https://doi.org/10.1093/nar/gkae705

Tokunaga, M., Imamoto, N., & Sakata-Sogawa, K. (2008). Highly inclined thin illumination enables clear single-molecule imaging in cells. *Nature Methods*, *5*(2), 159–161. https://doi.org/10.1038/nmeth1171

Vallabhaneni, H., O'Callaghan, N., Sidorova, J., & Liu, Y. (2013). Defective Repair of Oxidative Base Lesions by the DNA Glycosylase Nth1 Associates with Multiple Telomere Defects. *PLoS Genetics*, *9*(7), e1003639. https://doi.org/10.1371/journal.pgen.1003639

Van Soest, D. M. K., Polderman, P. E., Den Toom, W. T. F., Keijer, J. P., Van Roosmalen, M. J., Leyten, T. M. F., Lehmann, J., Zwakenberg, S., De Henau, S., Van Boxtel, R., Burgering, B. M. T., & Dansen, T. B. (2024). Mitochondrial H2O2 release does not directly cause damage to chromosomal DNA. *Nature Communications*, *15*(1), 2725. https://doi.org/10.1038/s41467-024-47008-x

Varga, D., Majoros, H., Ujfaludi, Z., Erdélyi, M., & Pankotai, T. (2019). Quantification of DNA damage induced repair focus formation *via* super-resolution dSTORM localization microscopy. *Nanoscale*, *11*(30), 14226–14236. https://doi.org/10.1039/C9NR03696B

Vauclare, P., Wulffelé, J., Lacroix, F., Servant, P., Confalonieri, F., Kleman, J.-P., Bourgeois, D., & Timmins, J. (2024). Stress-induced nucleoid remodeling in Deinococcus radiodurans is associated with major changes in Heat Unstable (HU) protein dynamics. *Nucleic Acids Research*, *52*(11), 6406–6423. https://doi.org/10.1093/nar/gkae379

Vidal, A. E. (2001). Mechanism of stimulation of the DNA glycosylase activity of hOGG1 by the major human AP endonuclease: Bypass of the AP lyase activity step. *Nucleic Acids Research*, *29*(6), 1285–1292. https://doi.org/10.1093/nar/29.6.1285

Villaseñor, R., & Baubec, T. (2021). Regulatory mechanisms governing chromatin organization and function. *Current Opinion in Cell Biology*, *70*, 10–17. https://doi.org/10.1016/j.ceb.2020.10.015

Walker, R., Joo, J. E., Mahmood, K., Clendenning, M., Preston, S. G., Joseland, S., Pope, B. J., Murillo, B. V., Pachter, N., Sweet, K., Groves, A., Gleeson, M., Bernatowicz, K., Andrews, L., Healey, E., Gallinger, S., Grant, R. C., Win, A. K., Hopper, J. L., … Buchanan, D. D. (n.d.). *Adenomas from individuals with pathogenic biallelic variants in the MUTYH and NTHL1 genes demonstrate base excision repair tumour mutational signature profiles similar to colorectal cancers, expanding potential diagnostic and variant classification applications*.

Wallace, S. S. (2014). Base excision repair: A critical player in many games. *DNA Repair*, *19*, 14–26. https://doi.org/10.1016/j.dnarep.2014.03.030

Weren, R. D. A., Ligtenberg, M. J. L., Kets, C. M., De Voer, R. M., Verwiel, E. T. P., Spruijt, L., Van Zelst-Stams, W. A. G., Jongmans, M. C., Gilissen, C., Hehir-Kwa, J. Y., Hoischen, A., Shendure, J., Boyle, E. A., Kamping, E. J., Nagtegaal, I. D., Tops, B. B. J., Nagengast, F. M., Geurts Van Kessel, A., Van Krieken, J. H. J. M., … Hoogerbrugge, N. (2015). A germline homozygous mutation in the base-excision repair gene NTHL1 causes adenomatous polyposis and colorectal cancer. *Nature Genetics*, *47*(6), 668–671. https://doi.org/10.1038/ng.3287

Williams, S. C., & Parsons, J. L. (2018). NTH1 Is a New Target for Ubiquitylation-Dependent Regulation by TRIM26 Required for the Cellular Response to Oxidative Stress. *Molecular and Cellular Biology*, *38*(12), e00616-17. https://doi.org/10.1128/MCB.00616-17

Wulffele, J., Thédié, D., Glushonkov, O., & Bourgeois, D. (2022). mEos4b Photoconversion Efficiency Depends on Laser Illumination Conditions Used in PALM. *The Journal of Physical Chemistry Letters*, *13*(22), 5075–5080. https://doi.org/10.1021/acs.jpclett.2c00933

Xiang, L., Zhao, J., Deng, J., Zhao, Z., Yuan, Q., Huang, W., Zhang, L.-S., Jiang, S., Yu, M., Li, G., & Xu, K. (2025). *Local Chromatin Organization and Net Charge Modulate DNA Glycosylase Efficiency in Live Cells*. https://doi.org/10.21203/rs.3.rs-6816177/v1

Xu, J., Ma, H., & Liu, Y. (2017). Stochastic Optical Reconstruction Microscopy (STORM). *Current Protocols in Cytometry*, *81*(1). https://doi.org/10.1002/cpcy.23

Yang, N., Chaudhry, M. A., & Wallace, S. S. (2006). Base excision repair by hNTH1 and hOGG1: A two edged sword in the processing of DNA damage in γ-irradiated human cells. *DNA Repair*, *5*(1), 43–51. https://doi.org/10.1016/j.dnarep.2005.07.003

Yue, X., Bai, C., Xie, D., Ma, T., & Zhou, P.-K. (2020). DNA-PKcs: A Multi-Faceted Player in DNA Damage Response. *Frontiers in Genetics*, *11*, 607428. https://doi.org/10.3389/fgene.2020.607428

Zhai, Z., Meng, F., Kuang, J., & Pei, D. (2025). Phase Separation in Chromatin Organization and Human Diseases. *International Journal of Molecular Sciences*, *26*(11), 5156. https://doi.org/10.3390/ijms26115156

Zharkov, D. O., Mechetin, G. V., & Nevinsky, G. A. (2010). Uracil-DNA glycosylase: Structural, thermodynamic and kinetic aspects of lesion search and recognition. *Mutation Research/Fundamental and Molecular Mechanisms of Mutagenesis*, *685*(1–2), 11–20. https://doi.org/10.1016/j.mrfmmm.2009.10.017

APPENDICES

Appendix 1: List of resources used during the thesis.

Reagent or Resource	Source	Identifier
Cell Lines		
HeLa (HeLa IBS)	ATCC (American Type Culture collection)	No. CCL2
HeLa NTH1 double knockout (HeLa NTH1 -/- KO), Germany		
FUCCI HeLa system 1 (Geminin-GFP, Cdt1-mCherry)	Molecular Probes - Premo *BacMam 2.0*	P36237
Chemicals and Media		
DPBS (-Ca^{2+}, -Mg^{2+}) (Dulbecco's phosphate-buffered saline)	Gibco	14190-094
Cystamine	Sigma	30070
Poly-D-lysine hydrobromide	Sigma	P7886
Glycerol 99.5%	VWR	24388
Catalase from bovin liver (21850 units/mg)	Sigma	753688
Glucose Oxidase from Aspergillus niger (225970 units/g)	Sigma	15710
Nanodiamonds (wheat germ agglutinin)	Adàmas Technologies	NDNV100nmHiWGA2ml
Gold nanoparticles (100 nm diameter)	Sigma	753688
16% Paraformaldehyde solution EM grade	Electron Microscopy Sciences	15710
Bovine Serum Albumin	Sigma	A2153
Trypsin-EDTA (0.05%), phenol red	Gibco	25300-054
DMEM 1X + Glutamax , phenol red	Gibco	31966-021
Opti-MEM 1X (reduced serum medium)	Gibco	31985-047
FluoroBrite DMEM, no phenol red	Gibco	A18967-01
Triton X100	ICN Biomedicals Inc	2249E
Tween 20	Euromedex	2001-B
Complete™, EDTA-free Protease Inhibitor Cocktail	Roche	5056489001
Picodent twinsil	Picodent	13 001 000
Algorithms and Softwares		
MACSQuantify software	Miltenyl Biotec	RRID: SCR_020943
Fiji	https://fiji.sc/	RRID: SCR_002285
Prism	GraphPad 10	
Imaris	Oxford Instruments	RRID: SCR_007370
SWIFT	http://bit.ly/swifttracking	
Floreada.io	https://floreada.io/	
COMET	https://www.smlm.tools/	
SR-Tesseler	https://github.com/flevet/SR-Tesseler	
Metamorph	Molecular Devices	RRID: SCR_002368
Kits		
Massive-SDAB-FAST 1-PLEX	Massive Photonics	